Laboratori Nazionali di Frascati

LNF-94/028 (IR)
3 Giugno 1994

The KLOE Collaboration

THE KLOE CENTRAL DRIFT CHAMBER

ADDENDUM TO THE KLOE TECHNICAL PROPOSAL

PACS.: 11.30.Er; 13.20.Eb; 13.20.Jf; 29.40.Gx; 29.40.Vj

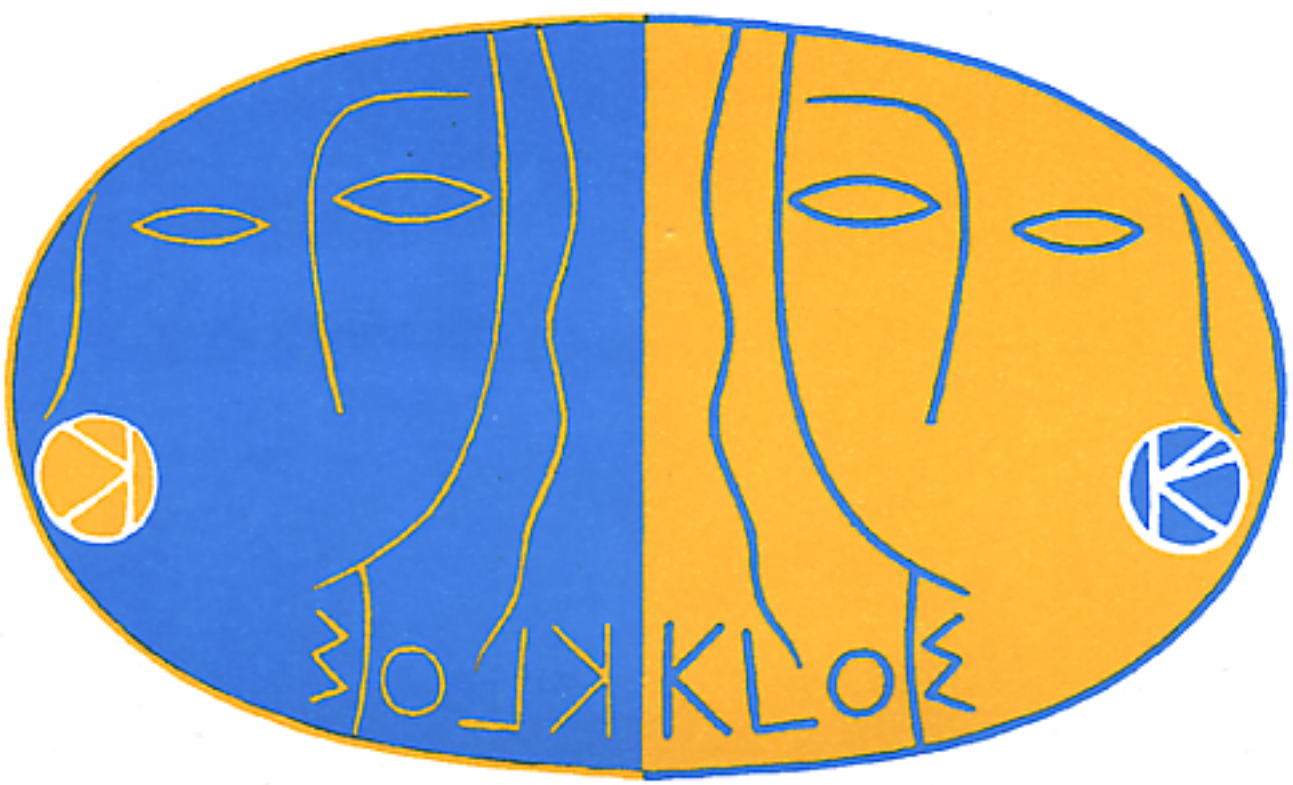

Servizio Documentazione
dei Laboratori Nazionali di Frascati
P.O. Box, 13 - 00044 Frascati (Italy)

THE KLOE CENTRAL DRIFT CHAMBER
ADDENDUM TO THE KLOE TECHNICAL PROPOSAL

The KLOE Collaboration

A. Aloisio[e], A. Andryakov[b], A. Antonelli[b], M. Antonelli[b], F. Anulli[h], D. Babusci[b], C. Bacci[h], R. Baldini-Ferroli[b], G. Barbiellini[l], M. Barone[h], K. Barth[c], V. Baturin[e], H. Beker[h], S. Bellucci[b], G. Bencivenni[b], S. Bertolucci[b], C. Bini[h], C. Bloise[b], V. Bocci[i], V. Bolognesi[g], F. Bossi[b], P. Branchini[i], L. Bucci[h], A. Calcaterra[b], R. Caloi[h], P. Campana[b], G. Capon[b], M. Carboni[b], G. Cataldi[d], N. Cavallo[e], L. Cerrito[i], M. Cerù[h], F. Cervelli[g], F. Cevenini[e], G. Chiefari[e], M. Cordelli[b], P. Creti[d], S. D'Angelo[i], F. Donno[b], R. De Sangro[b], P. De Simone[b], G. De Zorzi[h], A. Denig[c], G. Di Cosimo[h], A. Di Domenico[h], E. Drago[e], V. Elia[d], O. Erriquez[a], A. Farilla[a], G. Felici[b], A. Ferrari[g], M. L. Ferrer[b], G. Finocchiaro[b], D. Fiore[e], P. Franzini[i,f], A. Gaddi[b], C. Gatto[e], P. Gauzzi[h], E. Gero[b], S. Giovanella[h], E. Gorini[d], F. Grancagnolo[d], W. Grandegger[b], E. Graziani[i], U. v. Hagel[c], R. Haydar[b], M. Imhof[c], M. Incagli[g], C. Joram[c], L. Keeble[b], W. Kim[k], W. Kluge[c], F. Lacava[h], G. Lanfranchi[h], P. Laurelli[b], J. Lee-Franzini[b,k], A. Martini[b], A. Martinis[l], M. M. Massai[g], R. Messi[i], L. Merola[e], A. Michetti[h], S. Miscetti[b], S. Moccia[b], F. Murtas[b], G. P. Murtas[b,e], M. Napolitano[e], E. Pace[b], G. F. Palamà[d], M. Panareo[d], L. Paoluzi[i], A. Parri[h], E. Pasqualucci[i], M. Passaseo[h], A. Passeri[i], V. Patera[b], F. Pelucchi[b], E. Petrolo[h], M. C. Petrucci[h], M. Piccolo[b], M. Pollack[k], L. Pontecorvo[h], M. Primavera[d], F. Ruggieri[a], P. Santantonio[b], R. D. Schamberger[k], F. Scuri[l], A. Smilzo[e], S. Spagnolo[d], M. Spinetti[b], E. Spiriti[i], C. Stanescu[i], L. Tortora[i], P. M. Tuts[f], E. Valente[h], P. Valente[b], G. Venanzoni[g], S. Veneziano[h], X. L. Wang[b], S. Weseler[c], R. Wieser[c], S. Wölfle[b], A. Zallo[b]

[a] Dipartimento di Fisica dell'Università e Sezione INFN, Bari

[b] Laboratori Nazionali di Frascati dell'INFN, Frascati

[c] Institut für Experimentelle Kernphysik, Universität Karlsruhe

[d] Dipartimento di Fisica dell'Università e Sezione INFN, Lecce

[e] Dipartimento di Scienze Fisiche dell'Università e Sezione INFN, Napoli

[f] Physics Department, Columbia University, New York

[g] Dipartimento di Fisica dell'Università e Sezione INFN, Pisa

[h] Dipartimento di Fisica dell'Università e Sezione INFN, Roma I

[i] Dipartimento di Fisica dell'Università e Sezione INFN, Roma II

[j] Istituto Superiore di Sanità and Sezione INFN, ISS, Roma.

[k] Physics Department, State University of New York at Stony Brook.

[l] Dipartimento di Fisica dell'Università e Sezione INFN, Trieste/Udine

THE KLOE COLLABORATION

THE KLOE CENTRAL DRIFT CHAMBER

ADDENDUM TO THE KLOE TECHNICAL PROPOSAL

ABSTRACT

We present in the following a design of the central tracking chamber for the KLOE detector. Included are extensive report on test results gleaned from prototype tests, experience with construction of a full length sector prototype, and detailed reports on simulation of the chamber performances.

TABLE OF CONTENTS

1. INTRODUCTION

The design of the large tracking chamber for the KLOE detector is driven for the most part by the following considerations:

1. Maximizing the homogeneity and isotropy of the active tracking volume because of the long decay path of the K_L and the isotropic angular distribution of the charged decay products.
2. Achieving a high and a well controlled efficiency for the reconstruction of $K_L \to \pi^+\pi^-$ decays.
3. Maximize, without forgetting the points above, the fiducial volume for decay detection, to obtain the largest event sample for a given delivered luminosity.
4. Optimized resolution at low momentum values.
5. Minimize the number of wires, both sense and field, in order to ease the difficulties of building a transparent chamber shell, minimize multiple scattering and maintain the electronics channels count within reasonable limits.

The above consideration have lead quite naturally to the choice of helium plus hydrocarbons for the chamber gas.[1] We also chose to use aluminum for the field wires,[2] both to reduce multiple scattering and tension on the end walls. The most promising material for construction of the chamber shell appears at the moment to be carbon fiber-resin composites, which in addition to having high tensile strength, are easily shaped as required and economical. Aluminum alloys are a possible solution.

The basic cell configuration chosen is almost square. In order to fill uniformly the sensitive volumes, we follow the original Helena proposal[3] of avoiding axial wires. Using only stereo wires, allows us to realize a structure for which the wire's inward displacement at the chamber center is constant far all layers. The resulting stereo angle, alternatingly positive and negative, varies with radius from 50 to 120 mr, moving outward. At our extremely low expected multiplicities, this choice does not affect accuracy and efficiency.

The chamber optimization work is largely based on extensive Monte Carlo simulation work and results obtained with small prototypes exposed to a pion beam at the Paul Scherrer Institüt, Villigen, Switzerland. The simulation results are given in detail in chapter 9 and the complete analysis of the test beam data can be found in appendices 3, 4 and 5.

While the single track losses are smaller for a 2×2 cm^2 cell, the overall loss for full $K_L \to \pi^+\pi^-$ reconstruction increases from 3.1% to 4.6% with a 3×3 cm^2 cell. Given the large difference in number of wires for the two cases, $(3/2)^2=2.25$, we feel that the larger cell is an acceptable compromise. Concerning the number of sense wires, there is no conclusive evidence at present in favor of using a ratio field:sense of 3:1 or 2:1. The space-time relation for the latter is less uniform than for the former, requiring in the end more computer time for track reconstruction. This is of course true only for some special orientations of the tracks and is quite minor on average.

A possible configuration, assuring good tracking also for $K_S \to \pi^+\pi^-$ decays, might consist of twelve layers in the inner part of the chamber with 1.5×1.5 cm^2 cells, followed by 3×3 cells.

The number of cell layers for this case is 61 for a total number of cells of ~13,000. This choice cannot yet be considered final at the moment, but is not too far from an optimal configuration.

In order to acquire first hand experience about all problems concerning materials, stringing procedure, gas tightness, signal and HV, etc. we have built a full length prototype. The prototype, built with carbon fiber plates furnished by STESALIT A. G. of Zullwil, Switzerland, is 3 m long with 1 m^2 end plates. It has 500 cell with the whole stereo ahgle range. The construction of the prototype has been plagued by many delays but no real difficulties were otherwise encounterd. It has been invaluable for acquiring experience about all phases of the project.

2. GEOMETRICAL STRUCTURE AND WIRES

2.1 CELL

Uniform filling of the $r-\phi$ plane with minimal cell changes along z can be obtained with, almost, square cells arranged in circular layers, using only alternating stereo wires. Each plane of sense wires is enclosed by a plane of field wires running parallel and plane with wires skewed at twice the stereo angle. In order to minimize multiple scattering and mechanical tension on the end plates, as well as simplifying chamber stringing, the ratio R_{fs} of the number of field to sense wires in a cell, must be chosen as 2:1 or 3:1. Wire aging improves with increasing R_{fs} while transparency decreases and the overall tension increases. In the following we discuss the worse case of 3:1.

As mentioned in the introduction we chose a cell of 3 cm height by π cm width at z=0. Also, to improve the reconstruction efficiency for tracks at the chamber entrance, *i.e.* from K_S decays, we intend to split each cell of the six inner layers into 4 smaller cells of $1.5\times\pi/2$ cm^2.

The radius r_i of the ith layer of sense wires is given by $r_i = R_1 + h(i-1)$ where R_1 is the radius of the first layer and h the cell height. The number of sense wires in a layer is given by:

$$n_{si} = 2\pi r_i/w = \begin{cases} 4\times r_i & \text{if } w = \pi/2 \\ 2\times r_i & \text{if } w = \pi \end{cases}$$

With R_1=26 cm the total numbers of sense plus field wires are N_{SW}=11935 and N_{FW}= 36575 for a homogeneous "3 cm structure", while N$_{SW}$=13195 and N_{FW}=40537 for a "mixed structure", *i.e.* ~10% more. The number of guard wires required for a uniform gain is 213 at the inner radius of 26.5 cm and 804 at the outer radius of 193 cm.

The effect of the wires on the transparency of the chamber is not negligible. A gas mixture of 90% He (X$_0$=5300 m) and 10% C_4H_{10} (X$_0$=170 m) has a radiation length of about 1300 m. The wires, considered uniformily spread in the chamber volume, reduce the radiation length to a value of about 900 m (equivalent X$_0$ = 3000 m) with a partial contribution of 62% from the 80 μm Al field wires, including nickel flashing to insure surface conductivity, and 38% to the 25 μm W sense wires.

2.2 LAYER STRUCTURE

Stereo wires, *i.e.* non axial wires, move radially inward, going from the end plates to the chamber center at z=0, with a maximum displacement δ. A minimal distortion of the cell can be obtained by fixing the inward displacement at a constant value of δ=1 cm at the centre of the chamber for all wires. The stereo angle ϵ_i, for all wires at a given radius r$_i$ on the endplates, is:

$$\epsilon_i = \arctan\left(\frac{2\delta\sqrt{(2r_i/\delta)-1}}{L(r_i)}\right)$$

where $L(r_i)$ is the distance between the two endplates at radius r_i. This choice ensures that the cell height is constant along the z axis, whereas its width increases from the centre of the chamber towards the two endplates, by an increment proportional to δ/n_{s_i}. The choice $\delta = 1$ cm is a compromise between z accuracy, minimal distortion of the cell and loss of active volume.

Consecutive layers have stereo angles of opposite signs. This results in a cell varying shape along z which affects both the time to space relation and the uniformity of the gain along the chamber axis. Nevertheless there is a periodicity in the electrostatic configuration of a cell along z, given by:

$$P = (w/2)\cos\varepsilon_{is}/\sin(\varepsilon_{is} + \varepsilon_{i+1f})$$

where ε_{is} and ε_{i+1f} are the angles of a sense wire in the ith layer and of a field wire in the next layer at a larger radius.

The total number of layers is 55 in the structure with 3 cm $\times\pi$ cm cells only and 61 in the "mixed structure". Tables 2.1 and 2.2 give the radius at the chamber center, the stereo angle, the number of wires, the diameter and the voltage of the wires for the inner and the outer layers, for the two chamber configurations. Difficulties in pattern recognition due to this full stereo structure are not expected for KLOE, because of the low track multiplicity.

Layer	R at z=0	ε mr	Wire μm	# of wires	H. V. V
Inner wall	25				0
Guard	25.5	53.3	80	213	750
1st field	26.0	53.8	80	165	0
1st sense	27.5	55.2	25	55	1850
2st field	29.0	56.5	80	183	0
2st sense	30.5	57.9	25	61	1850
...	...	...	...	...	...
...	...	...	...	...	...
55th field	188.0	118.0	80	1137	0
55th sense	189.5	118.3	25	379	1850
56th field	191.0	118.6	80	770	0
Guard	192.0	118.8	80	804	750
Outer wall	194				0

Tab. 2.1. Layer structure for a cell size of ~3 cm and conical end-plates.

Layer	R at z=0	ε mr	Wire μm	# of wires	H. V.
Inner wall	25				0
Guard	25.5	53.3	80	213	800
1st field	26.0	53.8	80	321	0
1st sense	26.75	54.5	25	107	1650
2nd field	27.5	55.2	80	339	0
2nd sense	28.25	55.9	25	113	1650
...	...	...	...	...	...
...	...	...	...	...	...
61st field	188.0	118.0	80	1137	0
61st sense	189.5	118.3	25	379	1850
62nd field	191.0	118.6	80	770	0
Guard	192.0	118.8	80	804	750
Outer wall	194				0

Tab. 2.2. Layer coordinates for a mixed cell structure and conical end-plates.

2.3 WIRES

Tests performed on small prototypes have proven that a charge density ~15 nCoul/m is adequate to achieve $5{\cdot}10^4$-10^5 gas gain. Given a geometrical configuration of the cell, wire diameters and distances between wires, this constraint determines the choice of high voltage on the sense wires. Since within a cell the charge on the anode wire is equal to the total charge on the cathode wires, for fixed gain and number of field wires per sense wire, ageing effects set a lower limit on the field wire diameter. In the DAΦNE low radiation environment and in the helium atmosphere of the KLOE drift chamber, 25 kV/cm is an extremely conservative limit for the electric field on the cathode surface.[4] In the adopted cell configuration (sense wire diameter of 25 μm, field wire diameter of 80 μm, cell size 3 cm$\times\pi$ cm, ratio of field wires to sense wires 3:1), the expected gain value is achieved with a high voltage of 1800 V for the case of 1.5 cm wide cells and 1950 V for the 3 cm cells. The corresponding values of electric field on the field wires and on the sense wires are, respectively, 20 kV/cm and 170 kV/cm.

Under these conditions, charge density and, therefore, gain variations on the sense wires, as a function of the azimuthal angle along a layer and of the radial distance, are of the order of a few parts in a thousands at any given longitudinal cross section. Of the same order of magnitude are also the variations due to the changing shape and width of the cell along the wires because of the stereo angles. Variations in the first and last layers would be ~5–7%. Guard wires can remove this small effect.

The effects of the B-field on the drifting electrons (Lorentz angle) should be more contained in the helium based gas mixtures than in the corresponding argon mixtures, because of the reduced values of drift velocity. We plan, however, to test the small prototypes 0.1 and 0.2 in a magnetic field on a beam test at CERN in order to investigate possible worsening of the spatial resolution and of the cell efficiency due to a more complex space-time relation.

3. MECHANICAL DESIGN

3.1 Chamber Structure

A special requirement of the KLOE chamber is that all its walls must have the lowest possible thickness in order to minimize photon conversions before the electromagnetic calorimeter as well as multiple scattering and energy losses of charged particles entering the chamber. The preamplifiers, mounted on the chamber end plates must be included in this considerations.

While some bending of the end plates can be acceptable,[5] flat plates are unacceptably thick. Thin conical or spherical plates can easily carry the load of the wires, with deformations of $\mathcal{O}(1\text{ mm})$.[6] The plate deformation under load is strongly helped by properly attaching the plate outer rim to a torsionally stiff ring.

Non flat end plates introduce a large gap between end wall and calorimeter, in a region with magnetic field. As a result photon conversions in the wall introduce an error in the determination of the photon impact point, an error which is quadratic in the gap.[7]

The mechanical structure of the Kloe drift chamber is shown in figs. 3.1 and 3.2. The end plates are kept apart by twelve rods (stringers), fig. 3.3 attached to the outer ring. Gas seal is completed by twelve panels which will be mounted after chamber stringing and an inner cylinder. This last is attached to the end plates via two rings at the center of the plates which also provide support for the low β insertion. Panels and inner cylinder carry no loads in our chamber design. In the following we briefly describe the chamber components.

3.2 Chamber Components

End plates. Two shapes have been studied for the end plates: conical with a half opening angle of 80° and spherical with a radius of 9.76 m. Both plates have the same axial deformation under load, ~1.5 mm and the same effective plate–calorimeter gap, corresponding to an error in impact point of ~1.8 cm for converted photons. Two materials have likewise been examined. An aluminum alloy with Young modulus E=7000 kg/mm^2, is suitable for a 5 mm thick plate, equivalent to $0.055X_0$. Isotropic carbon fiber-epoxy composites,[8] E=3900 kg/mm^2 allows us to build an 8 mm end plate, equivalent to $0.03X_0$. Both solutions would not degrade significantly the calorimeter response.[9]

Carbon fiber–resin composites have a very large Young modulus, E~18000 kg/mm^2, but essentially in one direction only. In the solution studied the carbon fiber end plate is built piling up preimpregnated layers of fibers and epoxy (every 1 mm consisting of 4 layers each 0.25 mm thick), rotated with respect to the previous one by 45 degrees. The essentially isotropic plate, should have a Young modulus of about 4000 kg/mm^2. The end plates of the large prototype-I have been built in this way. A small material sample was found to be isotropic and the Young modulus measured to be E=3900 kg/mm^2, see appendix A2. 20–30% higher strength can be obtained inserting some layers of a better, more expensive, carbon fiber type. The Young modulus values above take into account a reduction of ~8% due to the holes in the plates.

Stiffening and inner rings. The cross section of the stiffening and inner rings and their position with respect to the endplate are shown in fig. 3.3. Since the stiffening ring is subject only to torsional stresses, a unidirectional carbon fiber-epoxy composite material, E=18000 kg/mm^2,

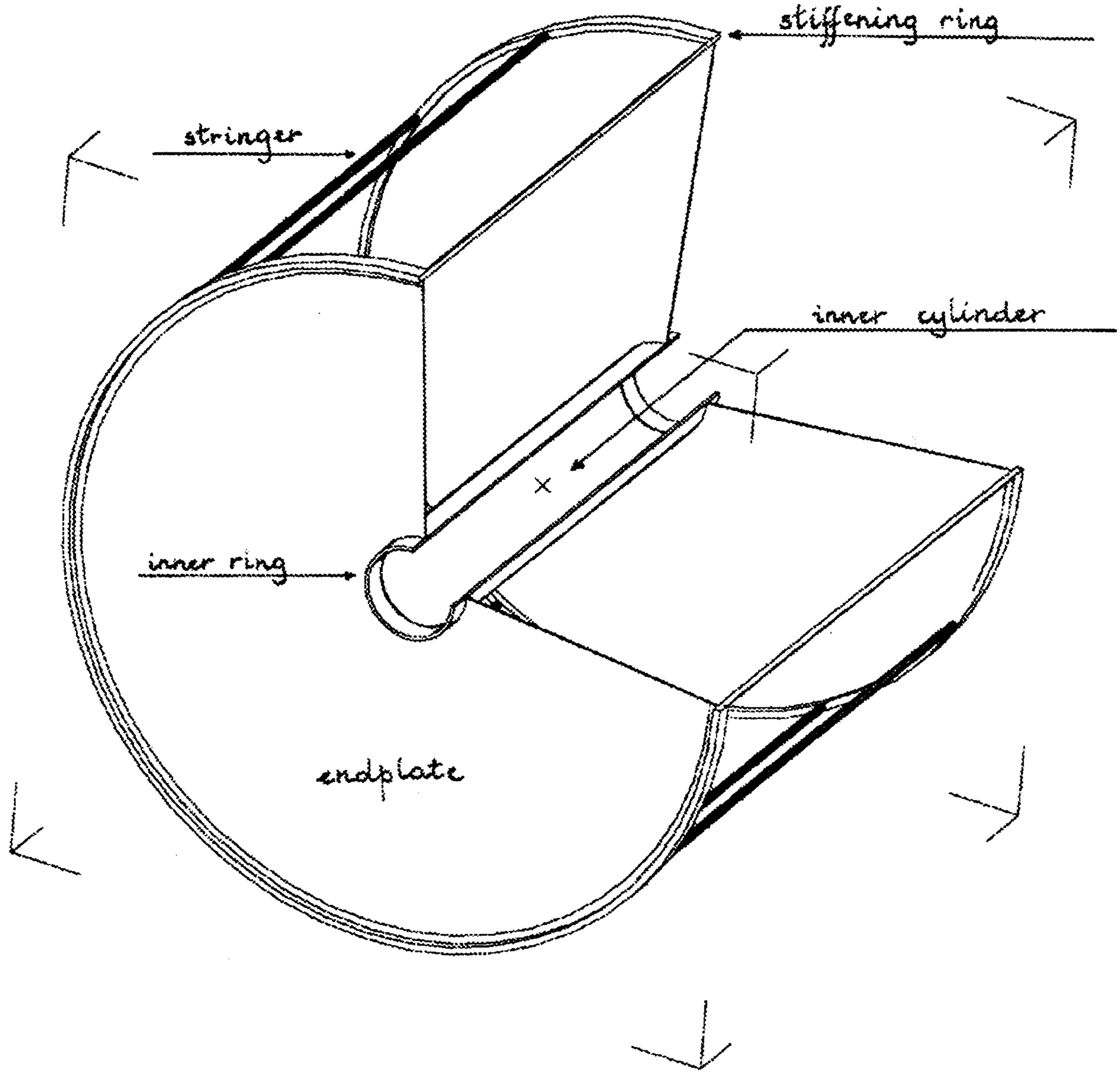

Fig. 3.1. Sketch of the mechanical structure of the KLOE drift chamber.

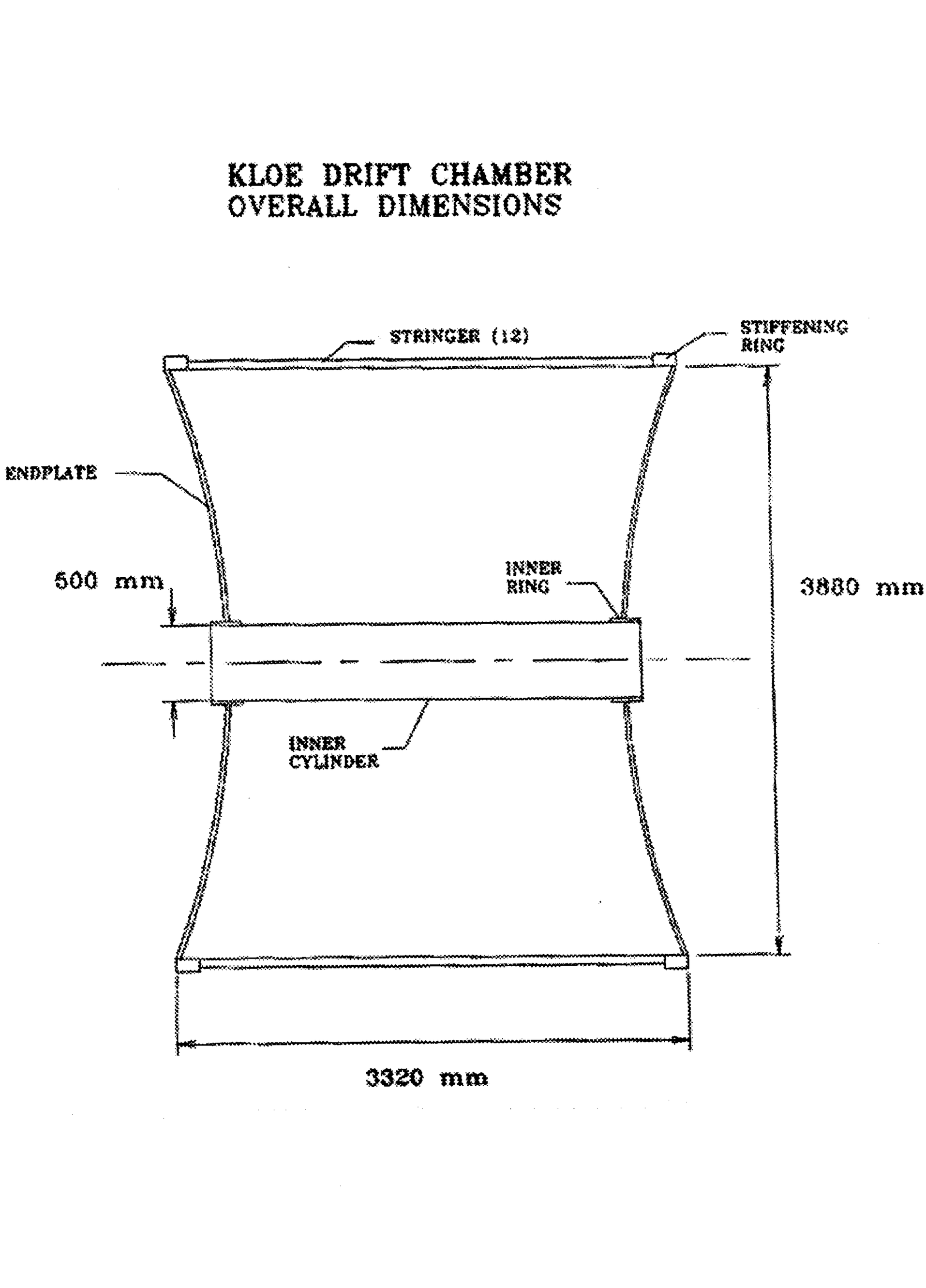

Fig. 3.2. Overall dimensions of the KLOE drift chamber.

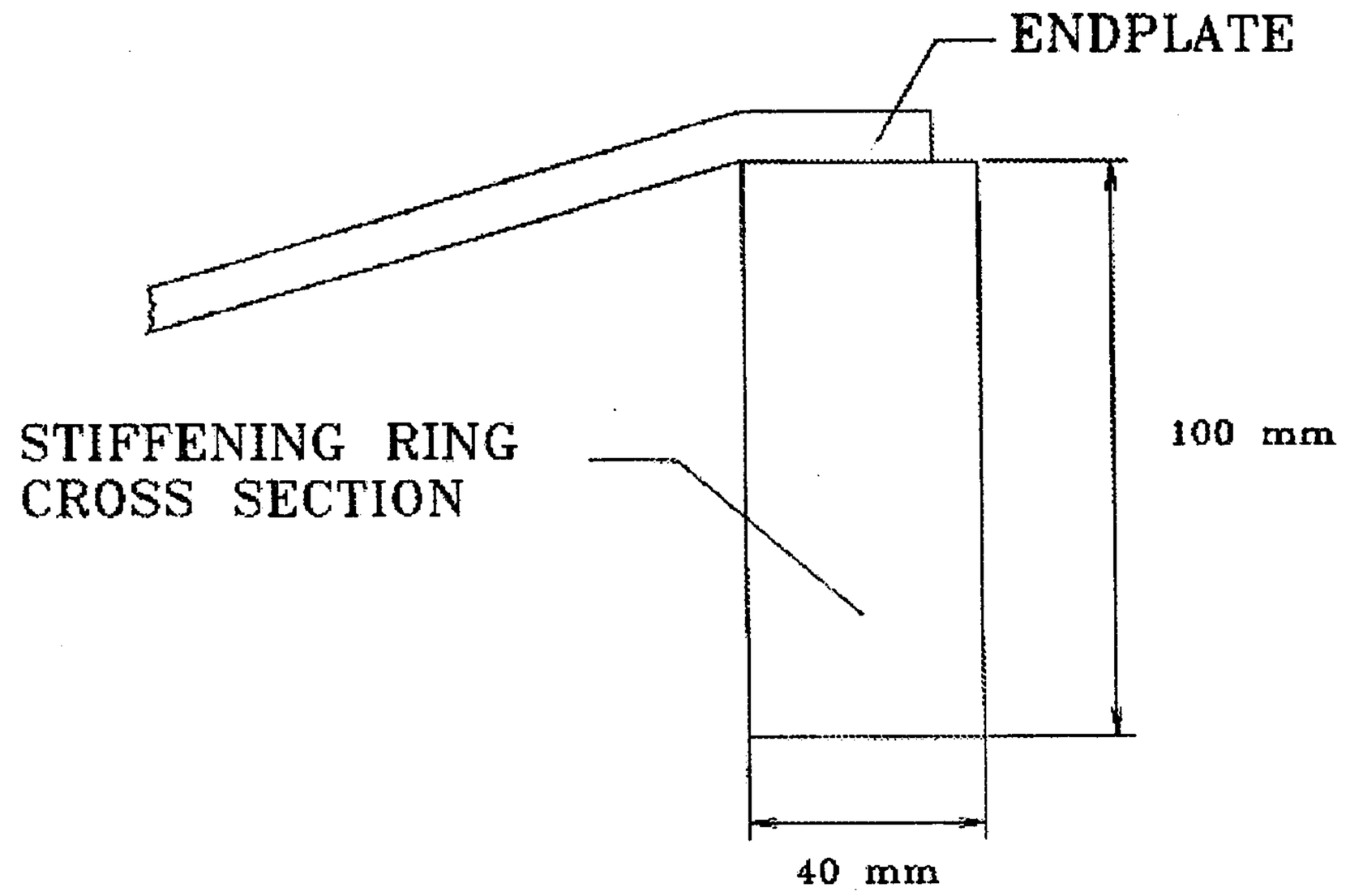

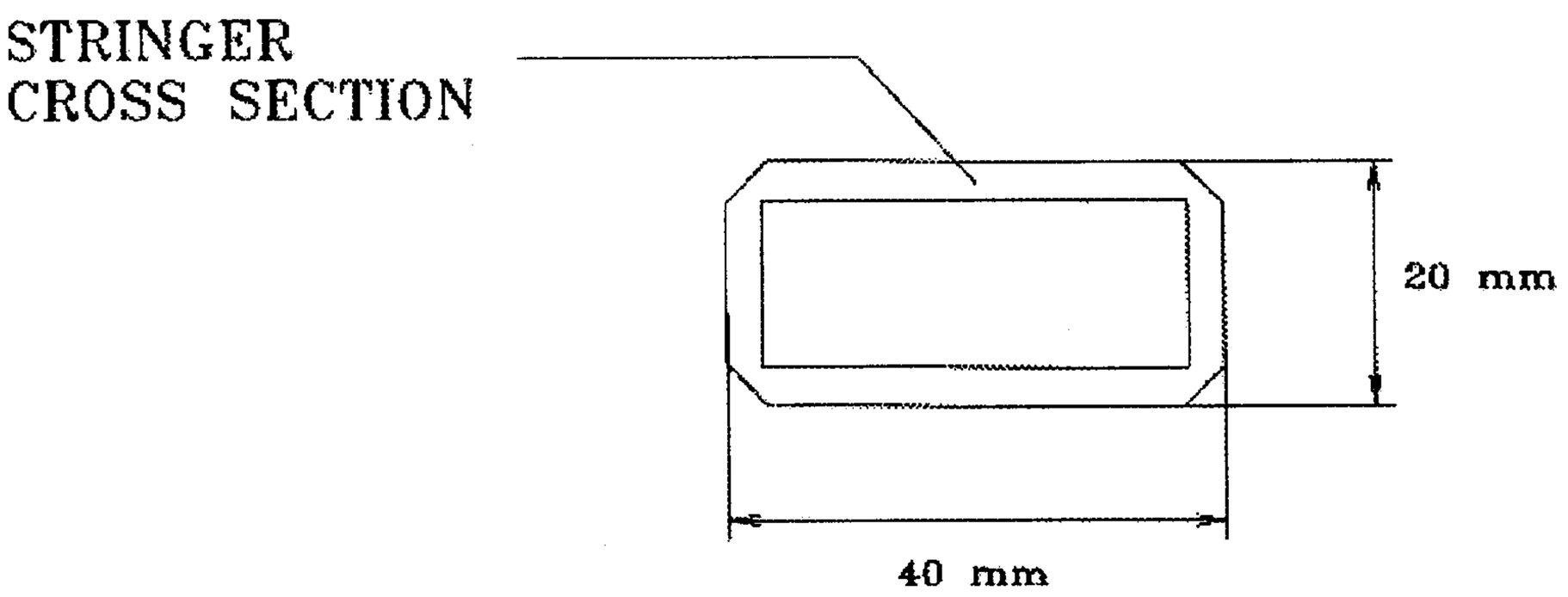

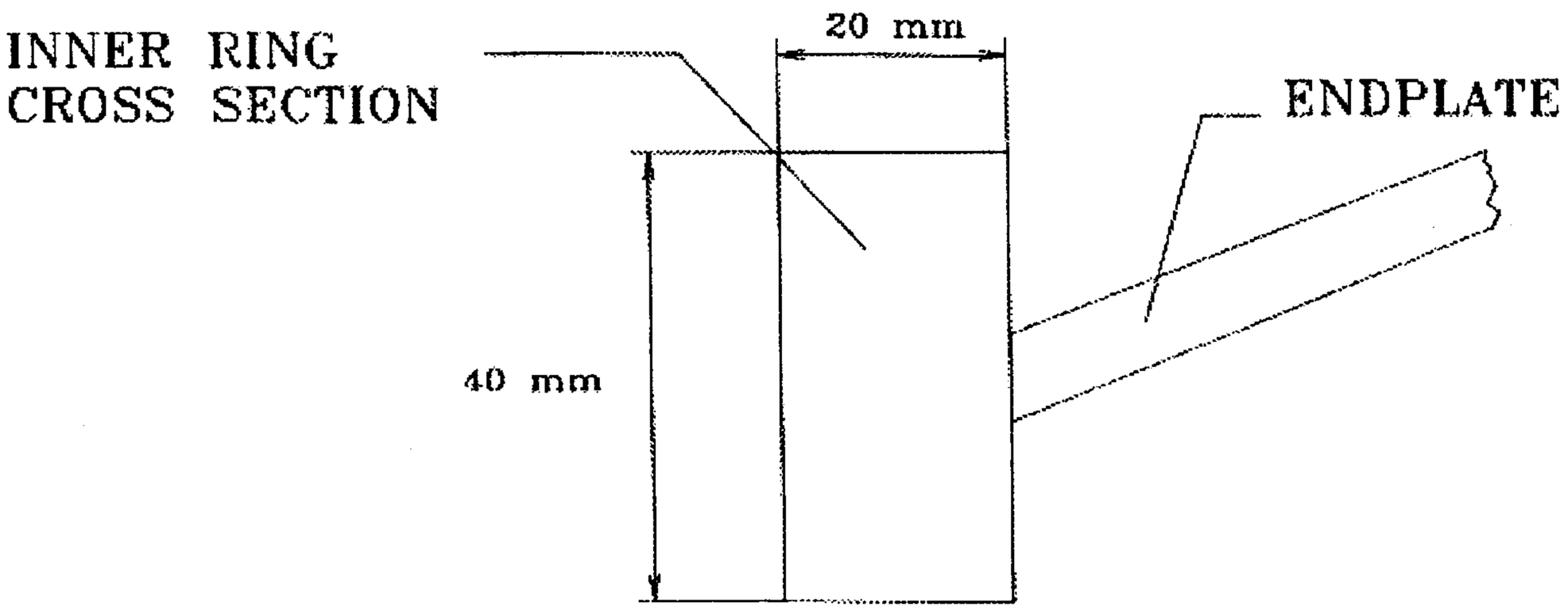

Fig. 3.3. Stiffening rings.

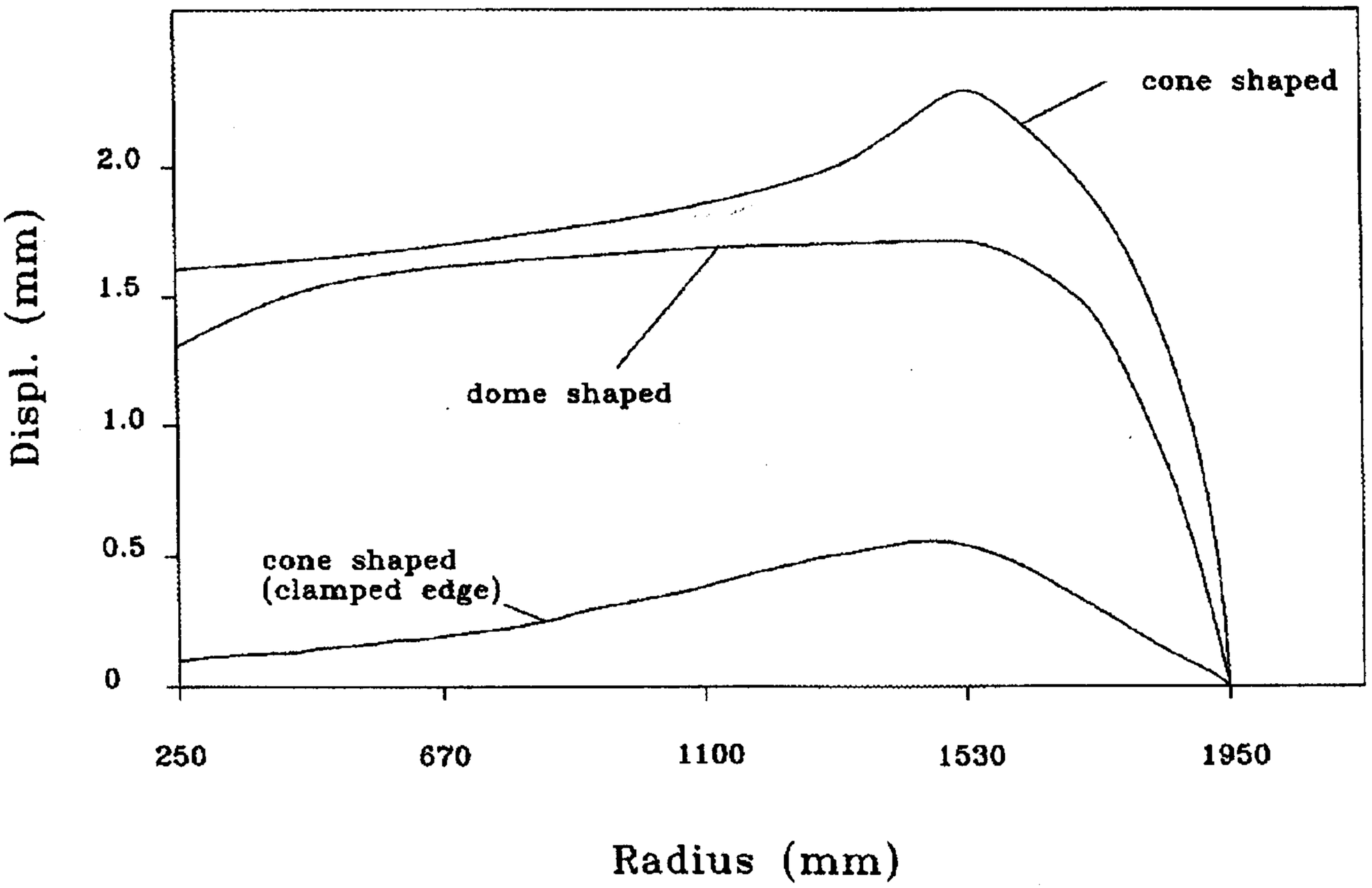

Fig. 3.4. Longitudinal deformations of the end plates vs radius for conical and dome shapes. The limiting case of a perfecly clamped outer rim is also shown.

is the best choice. Photons from K_L decays in the fiducial volume have a 2.9% probability of encountering the ring and cross 0.15 ± 0.07 X_0. A more sophisticated solution consists of two concentric rings, coupled in such a way that deformations are transferred to the external ring, during the stringing progresses. The deformation becomes <0.5 mm, as shown in fig. 3.4.

The inner rings allow us to attach the inner cylinder and to a less extent to reduce the deformations of the inner part of the endplate. They also transfer the weight of the R.E.C. quads to the end plates and to the detector structure.

Rods and panels. The cross section of a rod is also in fig. 3.3. It ensures stability under the compression load under which the rods are working. A unidirectional composite is appropriate here. A 3 mm thickness of composite is adequate for the panels.

Inner cylinder. The detection of charged kaons and of pions from K_S decays requires that the inner cylinder be very thin. A possible solution is a carbon fiber cylinder 700 μm thick.

3.3 Static analysis

A static analysis of the chamber structure has been carried out with the finite element computer code Ansys 4.4A in order to determine deformations and the stresses. The axial deformations of dome and cone shaped, carbon-fiber end plates are shown in fig. 3.4. The maximum displacements are similar, 2.2 and 1.7 mm for conical and spherical shapes respectively, with a smoother behaviour in the latter case. The dome shape might be harder to manufacture. Similar results are obtained for aluminum. We also show the deformation of a cone whose outer rim is ideally constrained. In all cases deformations and stresses are well below the elastic limits of the materials.

4. WIRING AND STRINGING TEST AND TOOLS

4.1 Wire and feed-through coupling tests

The large number of wires in the KLOE chamber requires a thorough check of the wire characteristic (yield strength, ultimate tensile strength...) and an exaustive test of the feed-through behaviour that must guarantee a very reliable clamping of the wires over the expected chamber lifetime. For this reason a systematic study of the wire/feed-through coupling as a function of the pin material, the pin hole diameter and the crimping size has been performed.[10] The phenomenon of creeping in the wire, as well as the long-term stability of the wire/feed-through connections, were also studied.

Due to the wire choice the most reliable wire clamping method is to crimp the pin. This method allows us to reach very good wire positioning ($\leq \pm 20$ μm) in the plane parallel to the crimped area.

The foreseen stringing tension is $\sim$ 80 g for the field and $\sim$ 60 g for the sense wires respectively.

Concerning the feed-through material the main requirements are good cutting and machining properties and proper ductility. In particular, in order to have a good wire/pin coupling on the crimped area, the hardness of the feed-through should be lower than, or at least comparable with the wire. For this reason an aluminum alloy feed-through for the aluminum wire and a copper feed-through for the tungsten one have been chosen.

The feed-through prototype, shown in fig. 4.1, consists of two concentric mini-tubes: the internal one used to clamp the wire, the external one for the electrical HV connections and/or the front end electronic cards. The de-coupling of the mechanical and the electrical function of the feed-through makes it more reliable.

The feed-through/wire clamping has been performed by means of a manual crimping tool (fig. 4.2). The crimping size, defined as the thickness of the pin after crimping, is adjustable (0.5 mm - 0.8 mm) by changing the crimping jaws. A motorized version of this tool has been also designed and succesfully operated. The crimping size uniformity obtained with this tool, measured on a sample of crimped pins of about 600 pieces, is at a level of less than $\pm$ 0.01 mm.

The wire/feed-through coupling has been studied as a function of the crimping size by means of a wire stressing device, recording the tension value at which the wire breaks and the occured failure type. A wire/feed-through coupling is defined as a "good one" when bringing the wire to its ultimate tensile it breaks in the middle, "bad one" when wire slips through the pin or breaks near the pin.

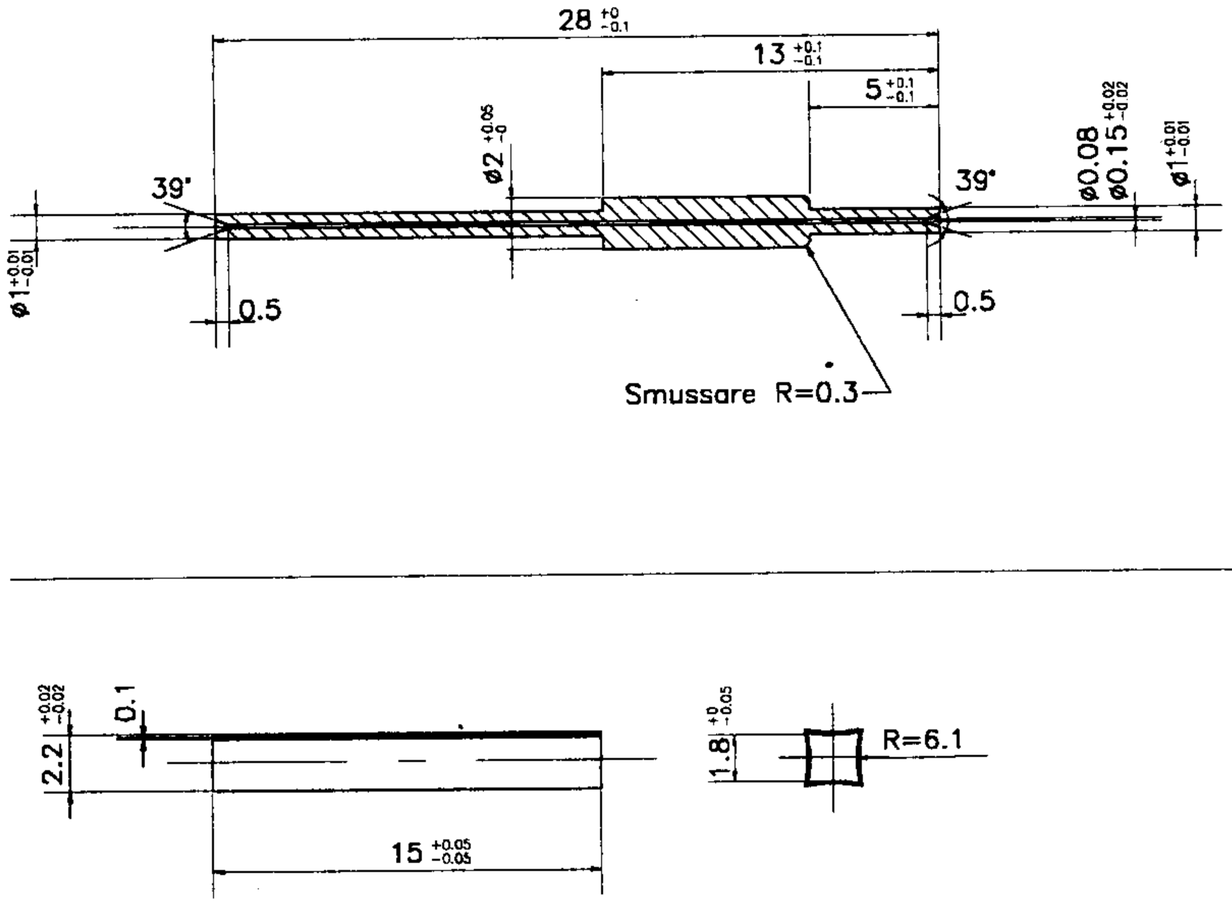

Fig. 4.1. Feed-Through design.

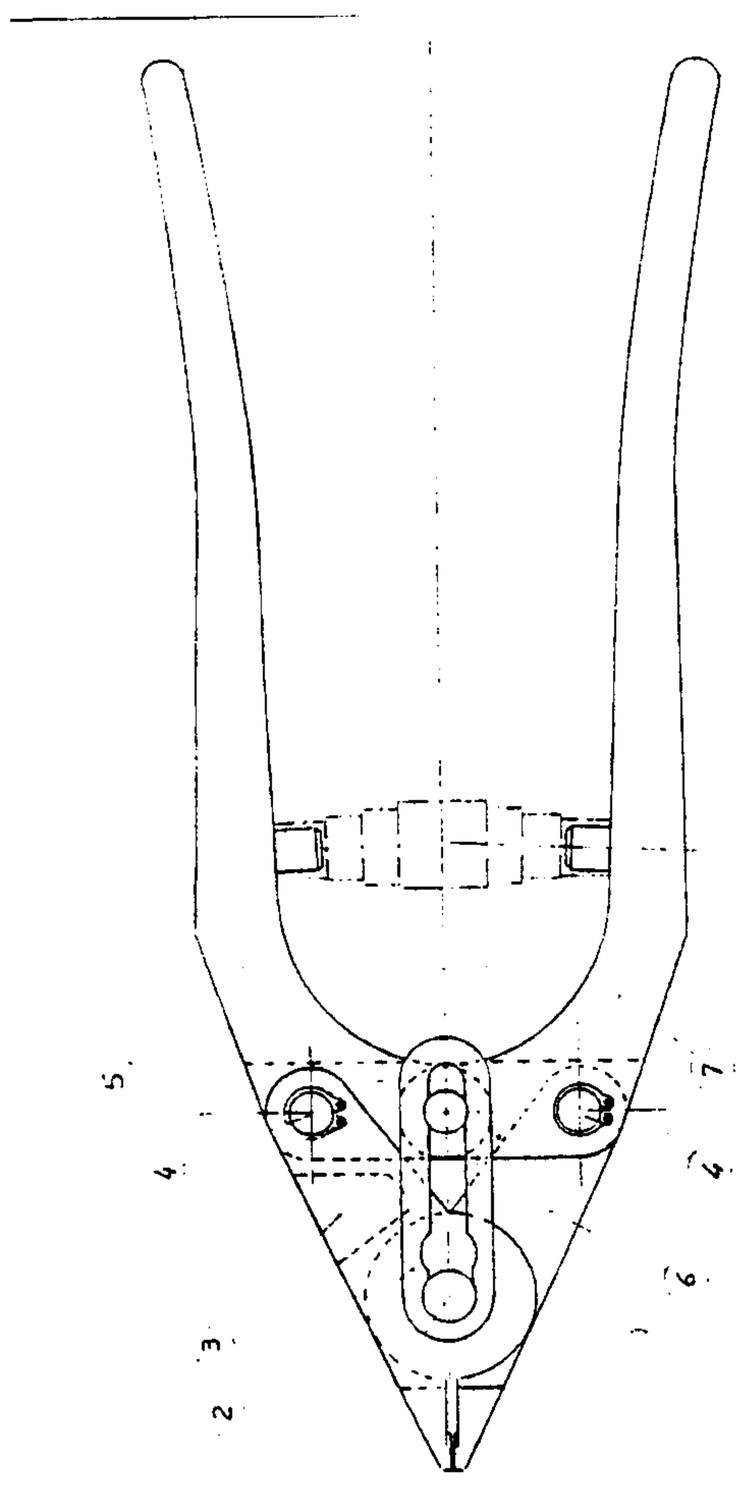

Fig. 4.2. Manual crimping tool design used in the wire/feed-through tests.

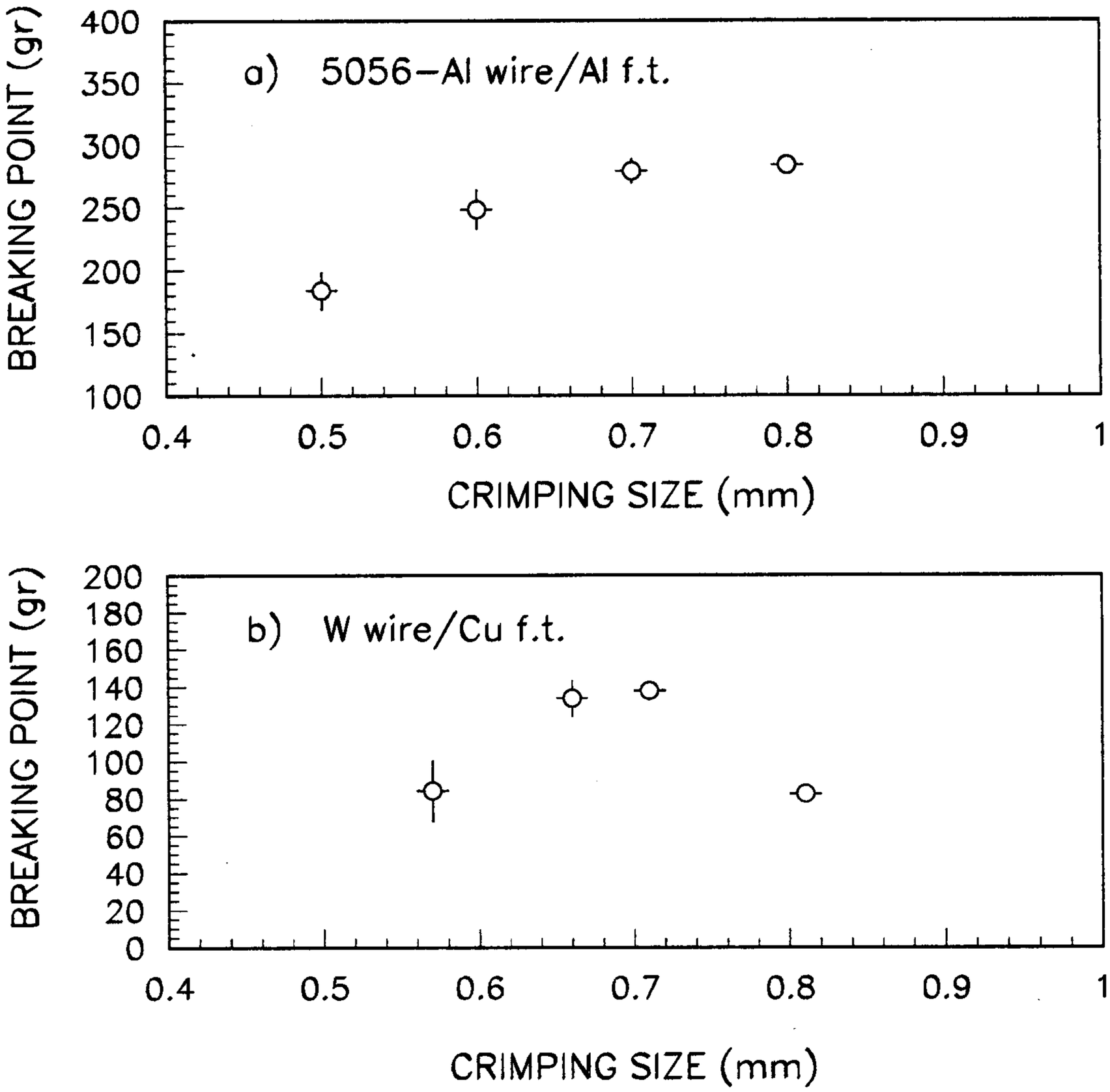

Fig. 4.3. Wire breaking point as a function of the crimping size for a) the aluminum wire and b) the tungsten one.

In fig. 4.3a the results obtained for the 5056 - gold plated aluminum wire and the Al feed-through are shown. For small crimping size, $\leq$0.6 mm, wire breaks near the crimped area at tension values less than the wire's ultimate tensile strength. For crimping size around 0.7 mm wires break mostly in the middle (58 times out 60) at a tension value comparable with the wire ultimate tensile strength. For crimping size around 0.8 mm wire starts to slip (6 times out 60) through the pin at tension values comparable with its ultimate tensile strength. Test at crimping size greater than 0.8 mm have not been performed, but it is quite likely that in this case the wire will slip at lower tension values.

The same kind of test has been repeated for the tungsten wire using the copper feed-through. The results, reported in fig. 4.3b, show that, with respect to the aluminum wire/Al feed-through coupling, a narrower safe crimping region is found. The safe region of the tungsten/copper feed-through ($\sim$0.7 mm) is coincident with the one of the aluminum wire/feed-through.

Taking into account that in the KLOE drift chamber all the wires are to be strung at stereo

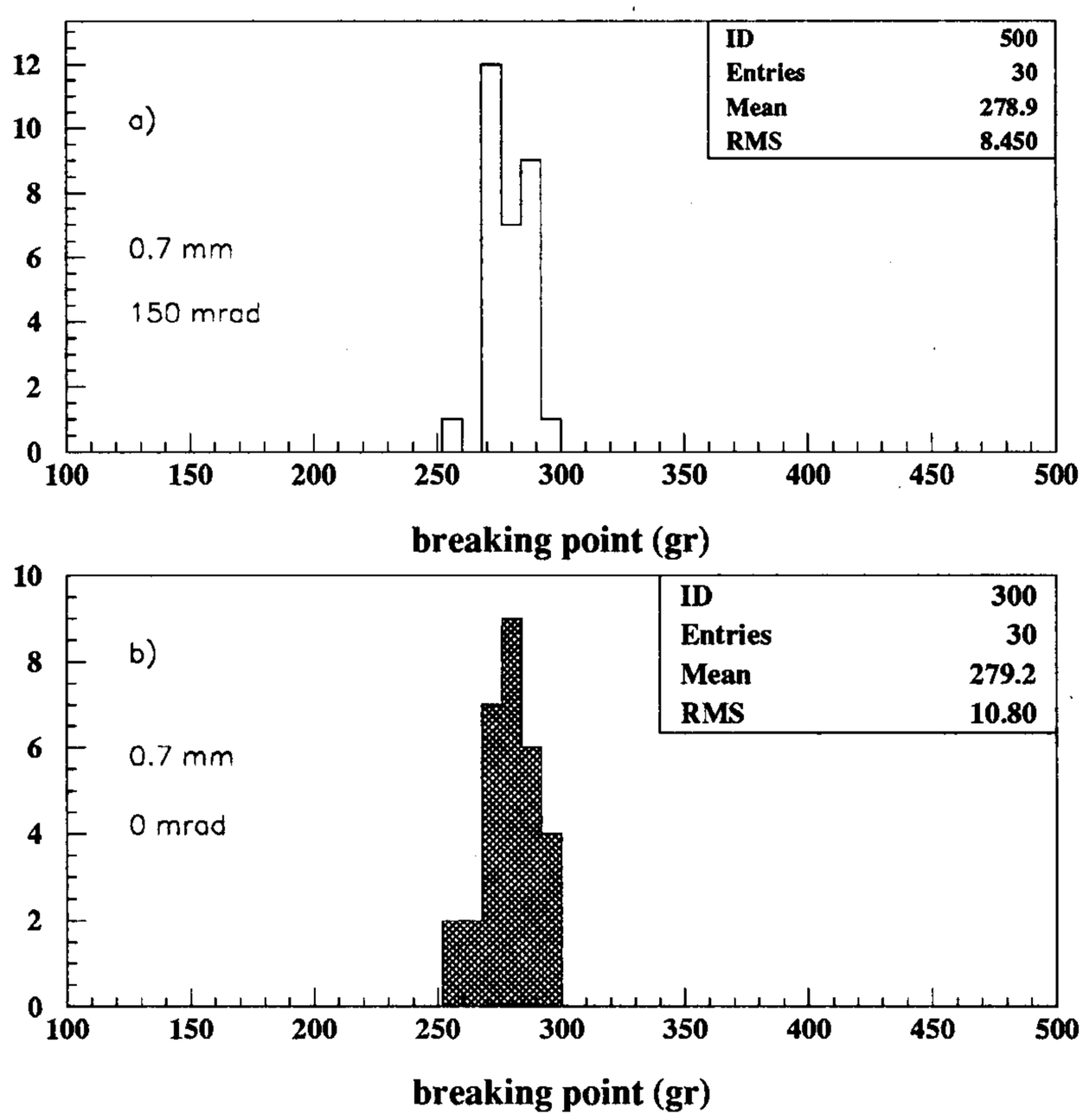

Fig. 4.4. Aluminum wire breaking point distribution for a) a stereo angle of 150 mrad and b) the axial wire configuration.

angles ranging between 50-120 mrad, tensional stress tests (both for aluminum and tungsten wires) with an angle of 150 mrad (between wire and feed-through axis) have been performed. These measurements have been done only for a crimping size of 0.7 mm, the value at which the best results in the axial configuration have been obtained. The fig. 4.4a, where the breaking point distribution obtained for the aluminum wire is reported, shows that no worsening, with respect to the axial configuration (fig. 4.4b) is found. The results obtained for the tungsten wire are shown in fig. 4.5a and fig. 4.5b, for the stereo and axial configuration respectively. Also in this case no appreciable differences are observed.

In order to study the long-term behaviour of the tungsten and aluminum wires and the stability of the wire/feed-through coupling, 8 aluminum wires and 2 tungsten wires (1500 mm long) were suspended with the proper feed-throughs and 100 gr and 69 gr weights respectively. Two Cu-Be (100 μm diameter) wires have been used as reference to monitor possibile global movements of the entire set-up (wires as well as measurement equipment). For a period of about six months the wire length (by means of a theodolite) and the local temperature have been monitored about every day. Each measurement has been corrected for the temperature changes and then normalized with respect to the first measurement. In addition, any change simultaneously observed on all the wires has been corrected on the aluminum wires just by subtracting the Cu-Be wire displacement.

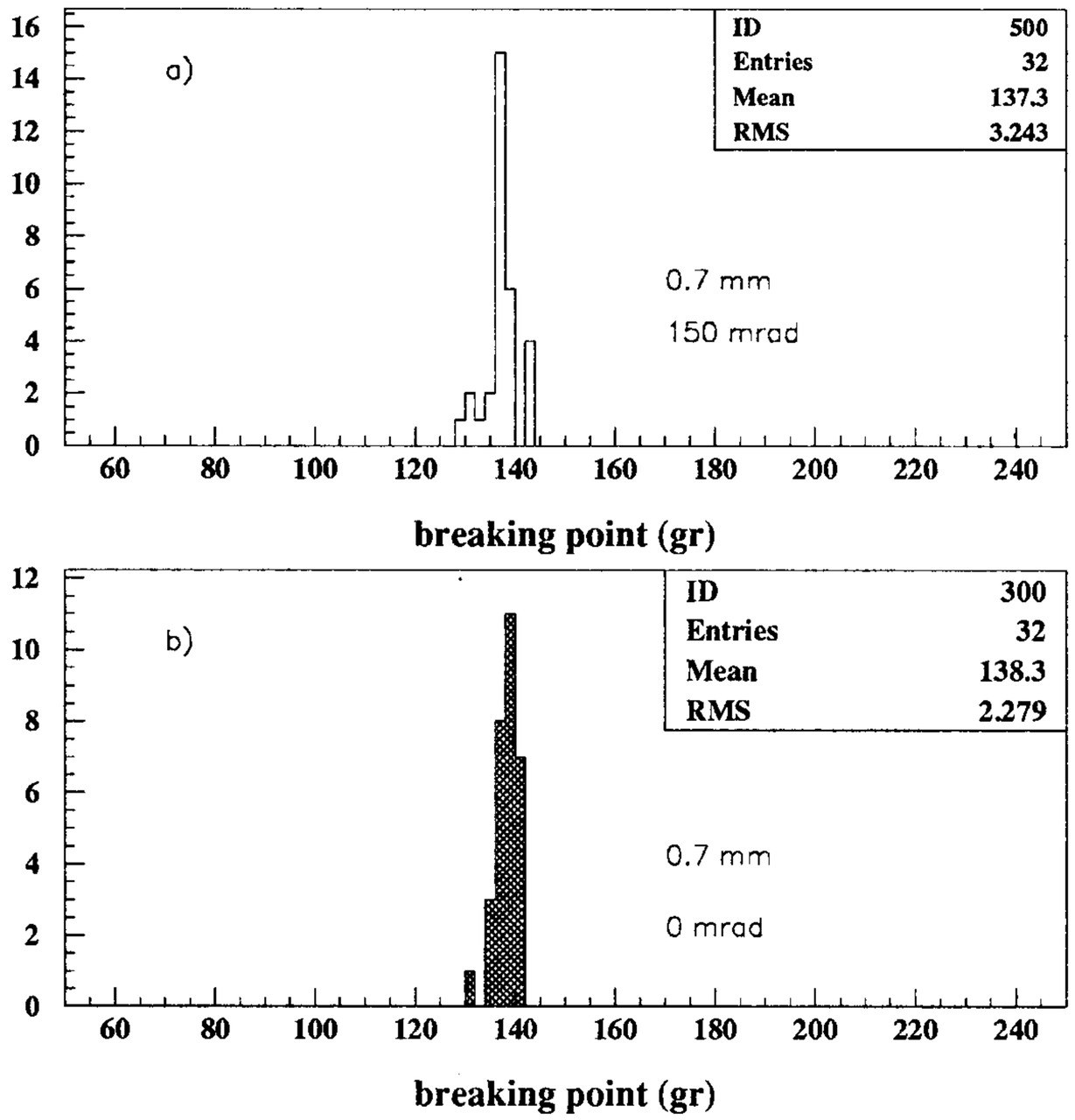

Fig. 4.5. Tungsten wire breaking point distribution for a) a stereo angle of 150 mrad and b) the axial wire configuration.

In fig. 4.6 the average normalized elongation of the aluminum wires is reported as a function of the time. After a first phase, characterized by a relatively fast increase of the wire length ($\sim$ 0.4 mm/200 hours), a region of a linear length increase of the order of 0.1 mm/month is reached. The result is in good agreement with data given in literature for similar aluminum alloys at a constant tension of 100 gr and a temperature of 20 °C. In fig. 4.7 the average long-term behaviour of tungsten wires is reported. Wire length changes are in this case pratically negligible ($\leq \pm 0.1$ mm).

4.2 Stringing strategy and tools

The need to string a large number of wires ($\sim$50,000) in one year requires a detailed study of a stringing strategy and the construction of specific stringing tools. Drift chambers similar to the KLOE chamber were recently built and strung prevalently in a manual way.[5,11] They were strung both vertically and horizontally, depending on the used stringing method.

We choose to string our chamber horizontally (fig. 4.8). In our stringing scheme two operators are needed, one for each end-plate, to pass the wire through the end-plate holes, to insert the wires into the feed-throughs, to stretch the wire and crimp the feed-through; maybe a third one would provide the wire to both of them moving between the end-plates.

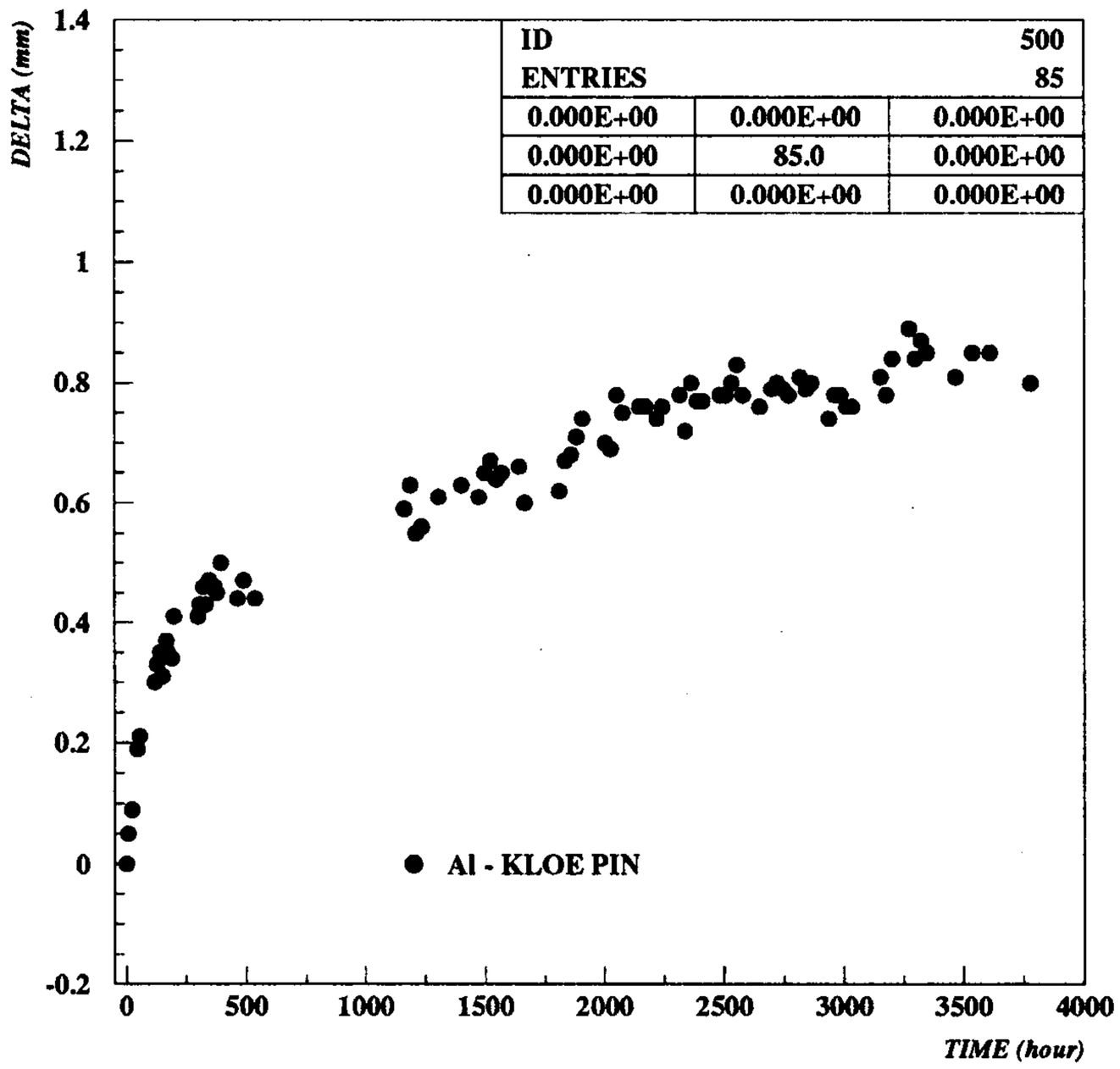

Fig. 4.6. Aluminum wire creeping (at a constant tension of 100 gr) as a function of the time.

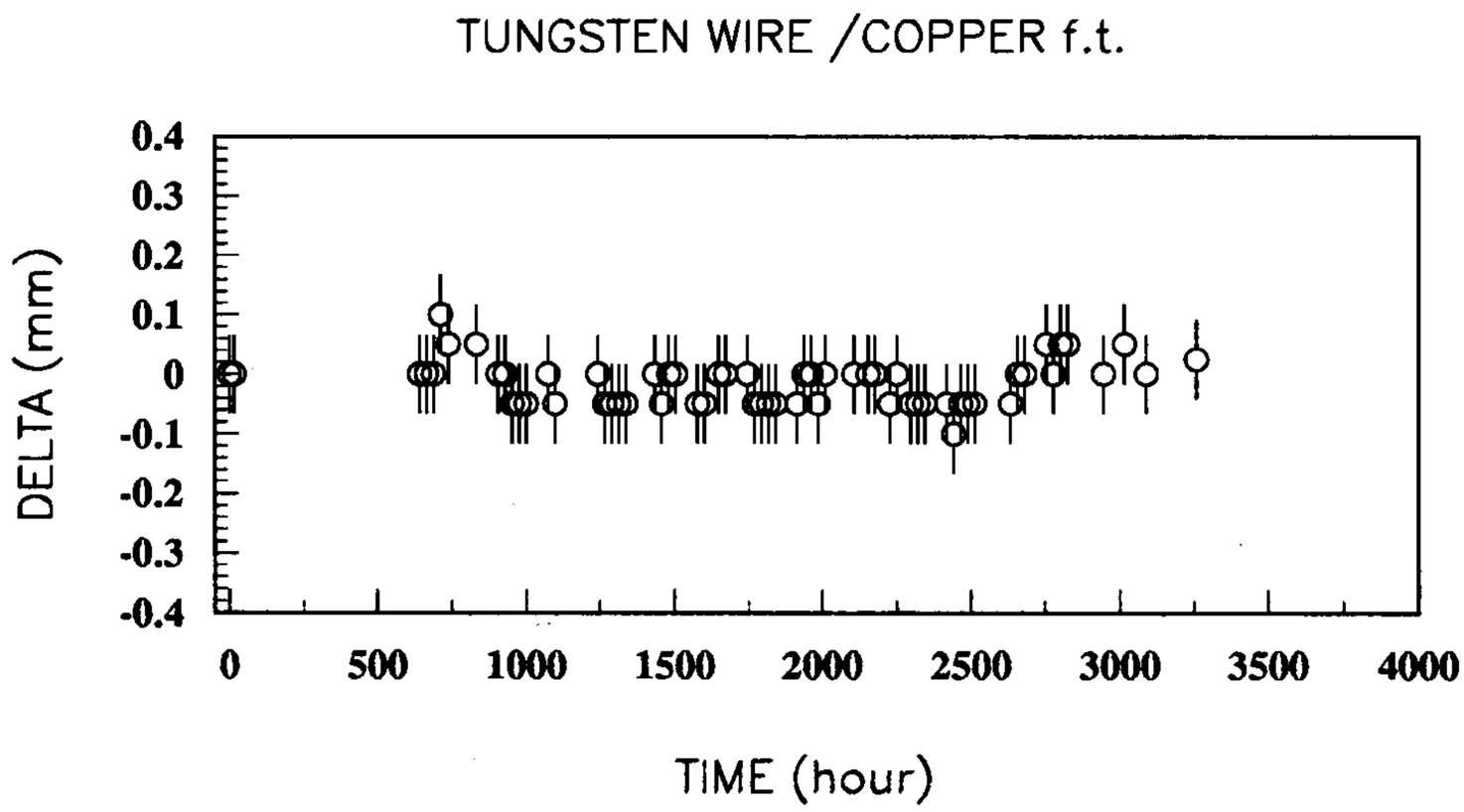

Fig. 4.7. Long-term behaviour of the tungsten wire/Cu feed-through coupling.

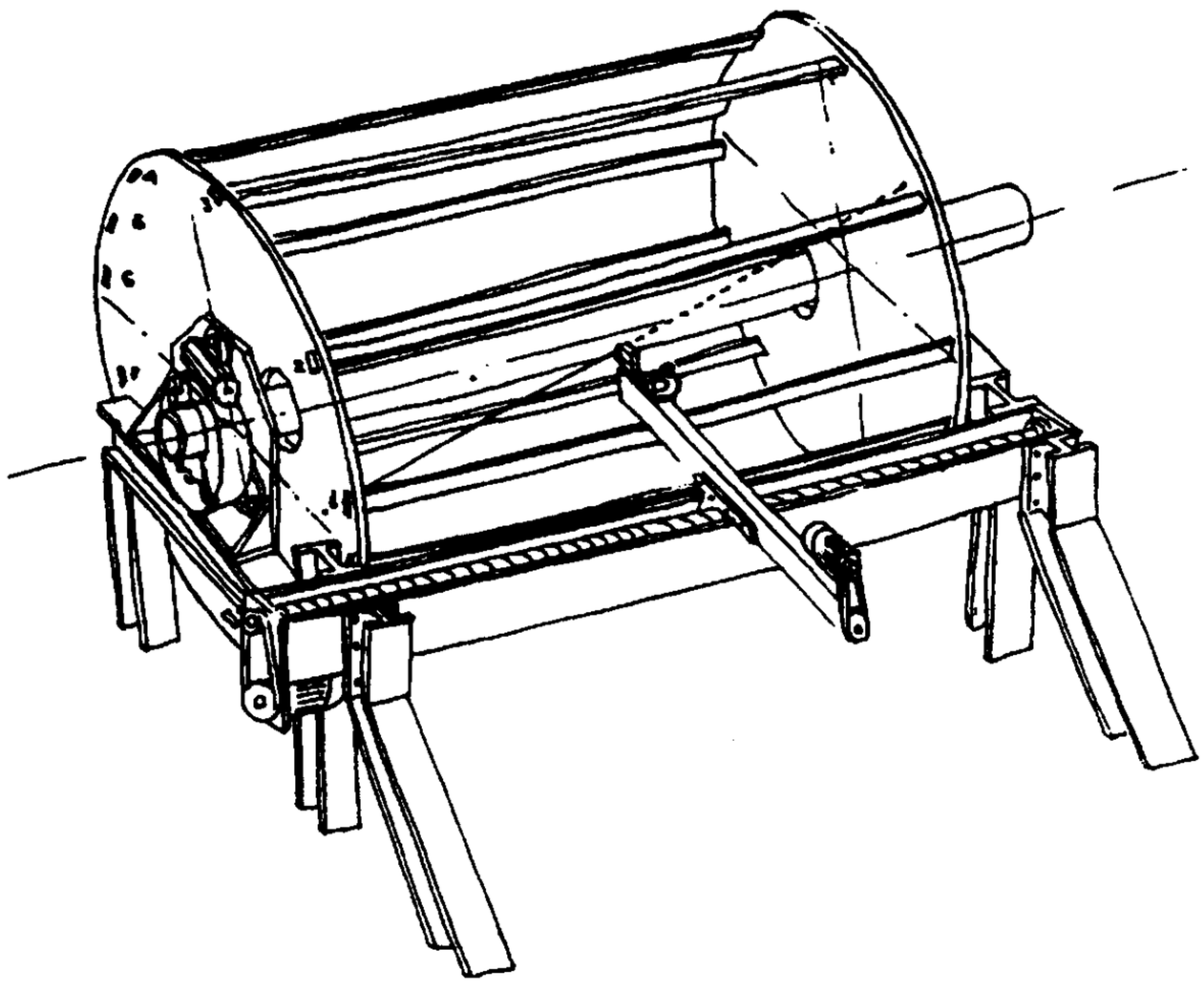

Fig. 4.8. Sketch of the drift chamber structure and the r-z stringing set-up.

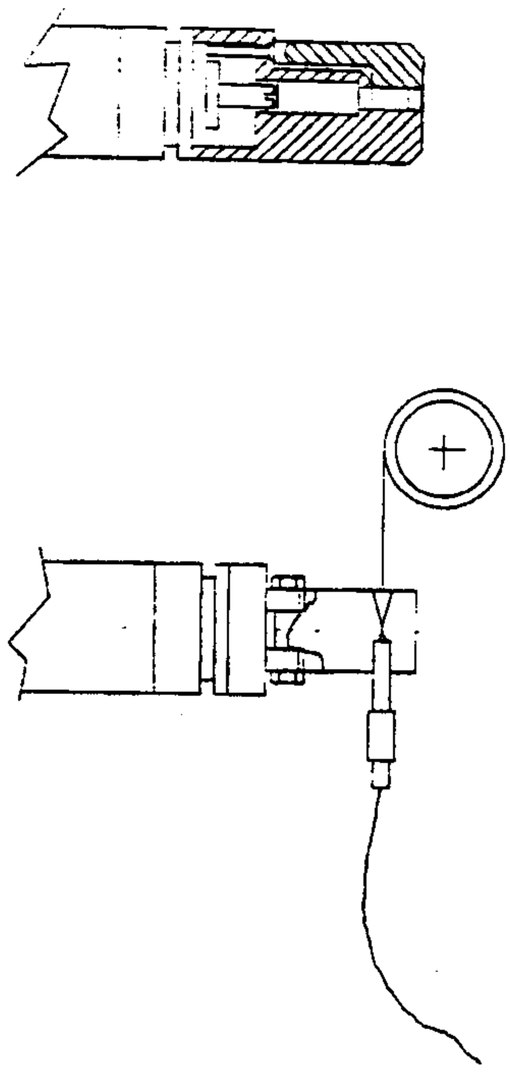

Fig. 4.9. Design of the motorized wire/feed-through insertion tool.

These operations can be helped by specific tools (see chapter 8). The crimping tool has been described in the previous section. For the insertion of the wire into the pin a prototype of a motorized tool has been designed and succesfully tested (fig. 4.9).

The wire transportation from one side to the other could be performed by a wire-transport tool (see chapter 8) or by a robot with at least two main movements (r-z). The latter option makes the operations inside the chamber cleaner but does not reduce the stringing time. On the other hand the presence of fixed bars (from 12 to 24), needed to support the chamber end-plates, affects the complexity of the stringing robot. A simple prototype of a robotized arm allowing the wire transportation and insertion into the end-plate holes is now under construction at the Frascati Laboratory. The two main movements and those of the special tools for the wire handling are obtained by means of step-in-motors (encoders ensure the needed precision and the repeatibilty of each movements). Since all the wires of the KLOE chamber are at a stereo angle, the movement of the robotized arm along the z-axis should be coupled to a rotation, around the same axis, of the chamber structure. For this movement a commercially available solution will be considered.

Experience on the prototype 1 (see chapter 8) shows that wires can be strung in a time of the order of two minutes each. Assuming that it will be possibile to have two diametrically opposite wiring stations and two five hours shifts (8 to 12 people per day + 1 supervisor) we should be able to complete the wiring of the KLOE chamber in about 30 weeks.

5. GAS SYSTEM AND MONITORING

5.1 Gas system

The KLOE tracking chamber will operate with a helium based gas mixture provided by a closed gas system. With the required gas flux of about 30 ℓ/min through the chamber, needed to flush the chamber volume of gas (40 m^3) by the gas system once per day, a closed system is not only more cost efficient than a single pass system, it also offers the possibility of optimal gas conditioning and purifying over a long period of time. A closed system, however, has to meet highest requirements of gas tightness and purity to avoid the accumulation of impurities.

All connections throughout the system are made with VCR connectors to meet the conditions for ultra clean systems. Stainless steal tubes of 12 mm and 6 mm diameter, which have been electropolished and specially cleaned are used for different parts of the gas system according to the required gas flux. All devices of the gas system like valves, flow meters and flow controllers, pumps and analysis instruments do not contain material like plastics or lubricants, that could cause impurities by outgassing. For the same reason a metal bellows pump, which does not contain any lubricant, is used to circulate the gas, and metal bellows valves, manually and pneumatically controlled, are used throughout the system.

The gas system will already be used for the Prototype I and for further studies of electron drift properties with a test chamber, which later will serve as a monitor chamber for the KLOE gas system. These studies will be carried out before the installation of the final system at LNF. To allow changes and further additions the system was designed in a modular way. All parts are assembled on aluminium plates, which fit into standard 19" racks.

The 'gas mixing' part (see fig. 5.1) can be connected to bottles containing up to 3 different gases. Very exact amounts of gas can be taken from the bottles using gas flow controllers (from MKS Instruments) remotely controlled by computer. Small gas fluxes (up to 200 cm^3/min) and large ones (up to 200 ℓ/min) can be taken from two separate lines to allow high accuracy for all required gas flows during the operation of the gas system.

The connection to the tracking chamber is made in the 'chamber supply' part (see fig. 5.2), where the gas flow through the detector, the pressure difference between gas entrance and exit and the absolute pressure at the detector exit are monitored. Under normal operational conditions the gas enters from the purification section, flows through the chamber and is afterwards pumped back to the analysis and purification section. The metal bellows pump works at constant power which is achieved by a gas flow controller which reduces the gas flow to the desired value. During the start-up procedure helium will enter from the mixing section and be vented to an exhaust line. Additional amounts of gas, e.g. to replace possible gas losses in the chamber, can also be added during operation. The exact number, position and size of gas inlets and outlets of the KLOE tracking chamber has still to be specified.

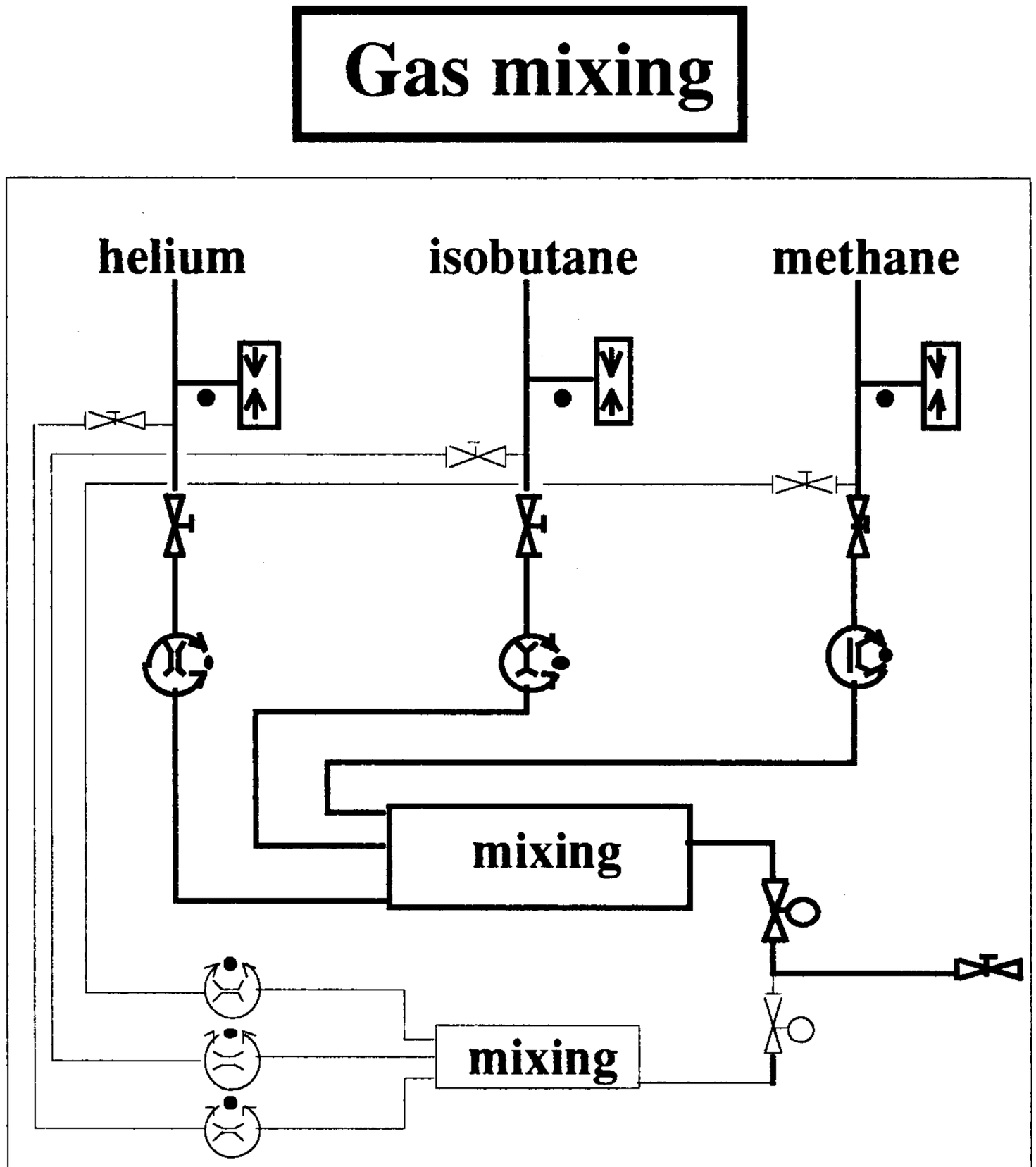

Fig. 5.1. Schematic drawing of the gas mixing module. Exact amounts of gas are taken from the pressure bottles using gas flow controllers.

In the 'analysis and purification' (see fig. 5.3) section the gas coming from the tracking chamber can be passed to a purification system, which was built by Messer Griesheim according to our specifications and consists of water (hydrosorb), oxygen (oxysorb) and specific hydrocarbon (molecular sieves) absorbing filters. Afterwards parts of the gas enter the different analysis instruments which are also assembled on separate modules, so that further instruments, e.g. the connection to a gas chromatograph with mass spectrometer, can be added, if additional parameters must be measured.

The electron drift velocity and the gas amplification are measured continuously with a small monitor chamber, which consists of several equally spaced brass electrodes, each with a hole of 2 cm diameter in the middle, through which electrons drift towards a small proportional counter. The 10 wires of this counter (10 μm diameter, 1 mm spacing) are read out with fast preamplifiers connected to TDCs and ADCs for the drift velocity and gas amplification measurements respectively.

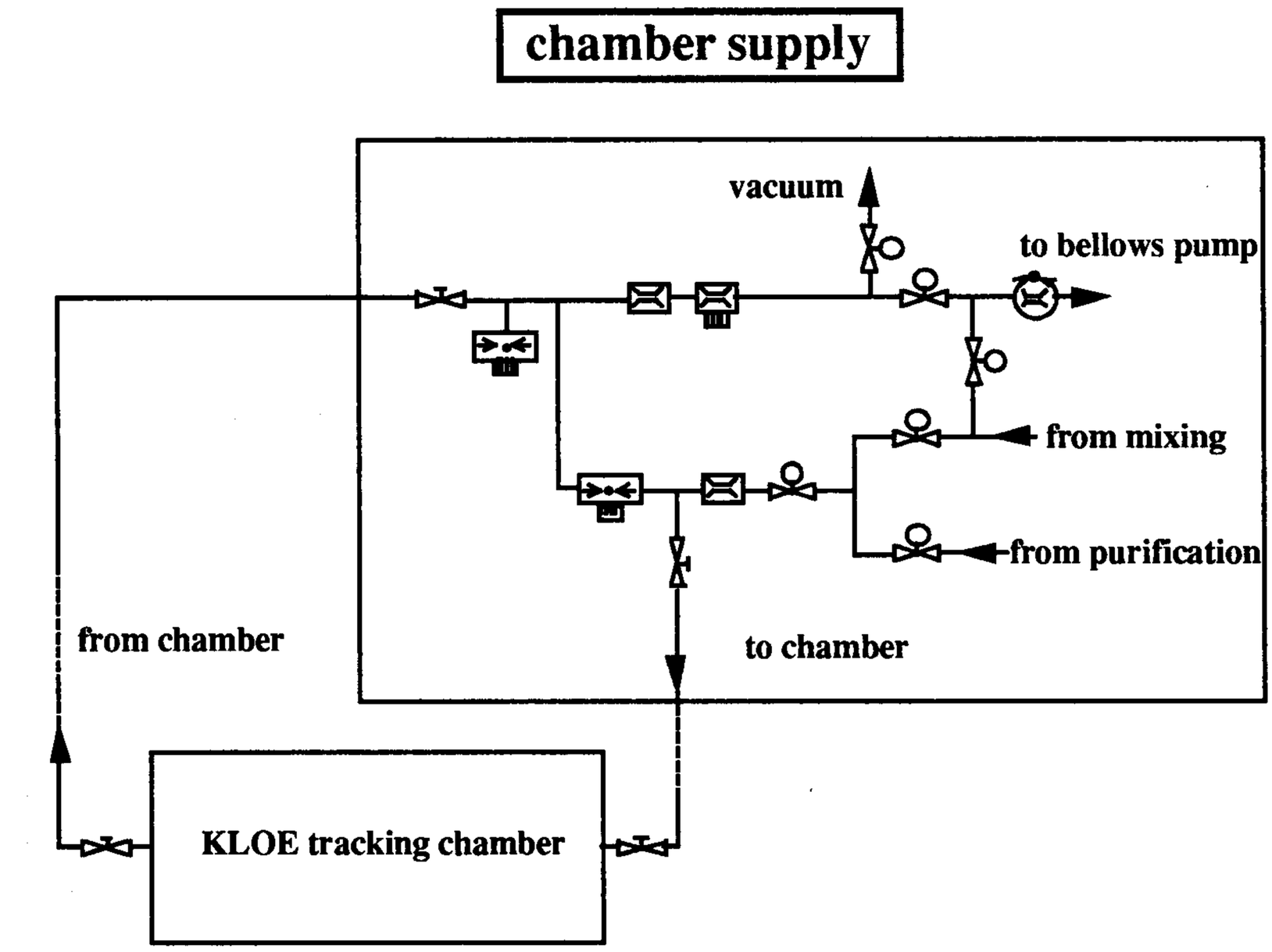

Fig. 5.2. Schematic drawing of the chamber supply module. The gas continuously circulates through the tracking chamber.

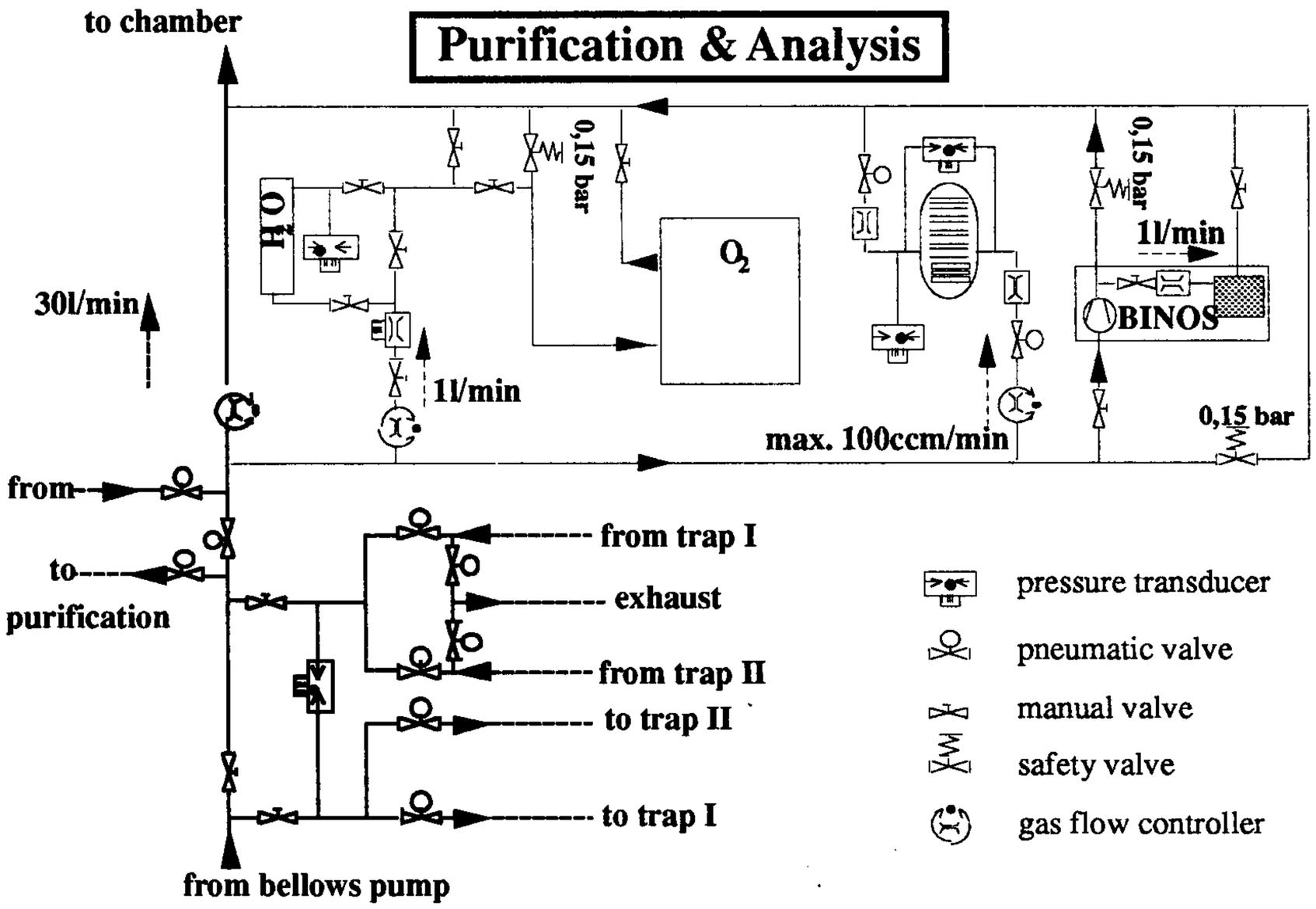

Fig. 5.3. Schematic drawings of the purification and analysis module. The gas continuously circulates through the various analysis and purification devices, driven by a metal bellows pump.

The gas inside the monitor chamber is ionised by means of an ultraviolet (266 nm) laser beam, provided by a Nd:YAG laser operated in a quadrupled frequency mode. To increase the accuracy of the drift velocity measurement to a few permille the laser beam is moved along the electrodes and a drift time measurement is made in every gap between electrodes.

The drift velocity and gas amplification measurements provide not only information for the tracking chamber operation, but are themselves very sensitive indicators of the gas composition. To find the cause for a change of the gas composition it is then necessary to measure independently the most important gas components. The content of isobutane is determined with an accuracy of $\pm 0.4\%$ of the total content by an IR-photometer (Binos-1001) which measures the infrared absorption of the gas, and the oxygen content is analysed with an electrochemical cell (Panametrics) in the ppm range. The gas system provides the possibility of adding water to prevent polymerisation and to reduce aging of the chamber. The water vapour content of the gas will be determined by measuring the dew point with an accuracy of $\pm 2^o$ (by a dew point sensor of Panametrics). During the forthcoming tests the gas will also be analysed with a gas chromatograph coupled to a mass spectrometer as a detector From these investigations it will be learned whether a permanent chromatographic analysis will be necessary.

During the start-up procedure after an opening of the tracking chamber and exposure to air we flush in a first step 2-3 fillings of pure helium gas through the chamber and vent the gas to the exhaust line. Then the system is closed and all gas components except for helium are removed in liquid nitrogen cooling traps. Remnants of impurities are removed by the purification system. Finally the hydrocarbon gas component and all necessary additives (water or alcohol etc.) are added under permanent control of the different analysis devices until gas conditioning is finished and normal operation of the system can start. Normal operation requires permanent readout of the analysis devices and the monitor chamber, replacement of possible losses of gas by addition of appropriate amounts of helium and hydrocarbon and permanent purification and stabilisation of the content of additives.

The normal operation of the gas system will be controlled automatically. The pneumatic valves are controlled by a PC through magnetic valves in the pressure lines. The instruments which control and monitor the gas flow, measure the pressure and temperature are read out by a computer through GPIB and serial interfaces. The stages which move the mirrors directing the laser beam are computer controlled as well. The monitor chamber electronics is read out by a computer connected to a VME crate. The whole system will be operated by a computer program which collects all relevant data from the gas system and generates warnings and information messages for the KLOE operators. This information together with temperature measurements inside and outside the tracking chamber and data from the high voltage system will be passed to the DAQ system for correlation with the events at analysis time.

5.2 Monitor chamber

The KLOE drift chamber will be operated with a helium based gas mixture[1] of typically 80-90% helium and 20-10% hydrocarbons, preferentially isobutane or methane. These mixtures offer the possibility to measure charged particle momenta with good resolution down to low values ($\approx$30MeV/c) in spite of the high ionization potential, low primary ionization and large

single electron diffusion of helium. While for high momentum particles the momentum resolution is basically limited by the spatial resolution of the tracking device ,[14] for low momentum particles, as in the case of KLOE, the resolution is dominated by multiple scattering.[15] Multiple scattering is heavily reduced in helium, because of its large radiation length X_0 (5300 m). In addition helium has a low sensitivity to background X rays from synchrotron radiation due its low photon absorption cross section. Also due to the fact that safety and gas purity problems do not allow the usage of hydrogen which has even a larger radiation length, helium appears as the most promising candidate for tracking detectors to be operated in experiments at electron positron colliders at intermediate energies like DAΦNE.[12,13]

To find an optimum helium based gas mixture for KLOE, a series of investigations have been started.[16] More specifically, the aims are:

- to optimize an experimental set up which should serve later on as a monitor chamber for the KLOE drift chamber providing information on the stability of the gas mixture by measuring the drift velocity and the electron diffusion;
- to check gas mixtures performances with respect to operation stability, primary ionization statistics and electron diffusion;
- to perform new and to reproduce existing measurements of the drift velocity and to investigate in more detail the dependence of drift velocity and electron diffusion on variations of gas composition, electric field and possible impurities.

The measurements of the drift parameters are performed with an experimental setup called the 'monitor chamber' which is shown in the two schematic views in Fig. 5.4. The drift cell is an apparatus made of plexiglas with a size of (15×15×20) cm^3 in which an homogeneous electric field is produced by a stack of copper plates 1 cm apart. Drifting electrons are detected by a proportional counter after passing a hole of 1.7×0.3 cm^2. The hole provides a good separation between the field in the drift and in the detection (gain) region. The proportional counter consists of a gold plated tungsten wire of 25 μm diameter. The detection efficiency has been measured with a ^{90}Sr source and found to be above 90% and depending on the drift field for the gas mixtures investigated.

The gas flow through the cell has been monitored by a flow controller, which allows also a rapid change of the gas mixtures. The gas circulates continuously through the chamber. No gas purification procedures have been applied up to now.

The ionization in the cell is produced by two different UV lasers, by a XeCl laser operating at 308 nm and by a N_2 laser at 337 nm. Data have been taken also with a ^{90}Sr β source. The drift cell can be moved in two directions (parallel and transverse to the laser beam, denoted by x and y in Fig. 5.4) while the laser beam can be focused at different points along the z axis thanks to the periscope shown in Fig. 5.4. The drift distance is varied within 3.3 and 8.6 cm focusing the laser at different positions along the x direction. The excimer laser has a pulse width of 8 ns. The nitrogen laser has a pulse duration of 300 ps and operates at a maximum repetition rate of 20 Hz. A fraction of the laser light is reflected from a quartz beam splitter just in front of the drift cell and directed towards a phototube with 60 ps risetime. The signal from this phototube, suitably delayed, is used as a start signal for the drift time measurements.

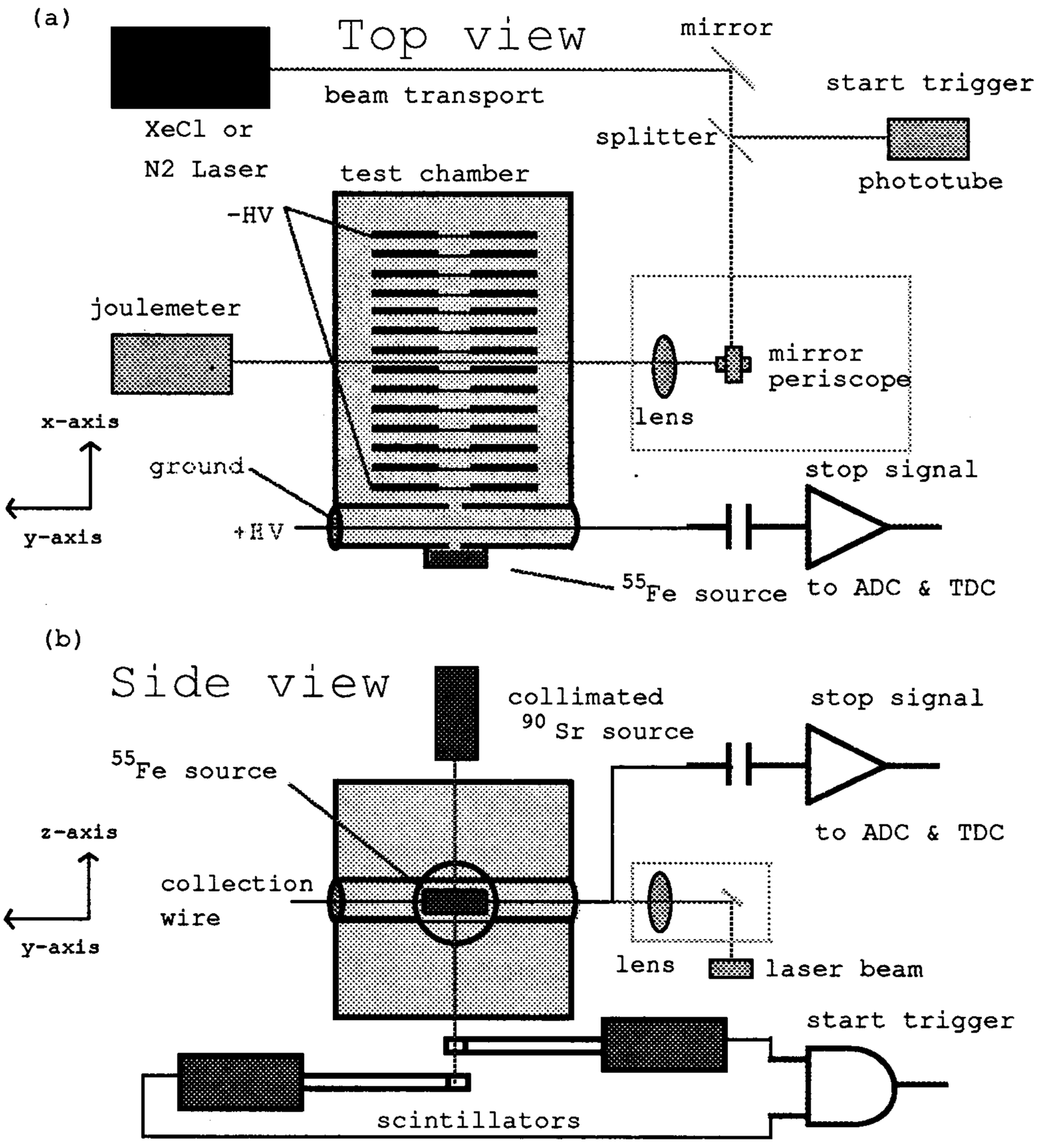

Fig. 5.4. Top (a) and side (b) views of the experimental setup.

The time interval between the delayed reference signal and the signal coming from the proportional counter is digitized and stored event by event. The distribution of these intervals is displayed on-line using the Labview acquisition package[17] and then analyzed off-line.

The ^{90}Sr source produces collimated electrons with a transverse cross section of 0.3 mm diameter. The electrons from the source move parallel to the z direction (as shown in Fig. 5.4) and enter the drift cell in the middle between two plates. They are detected by a pair of scintillation counters positioned below the chamber. A coincidence from the two scintillators provides the trigger for the measurement of the drift time.

From fits to the drift time spectra we obtain the peak value for each time distribution and from that the mean arrival time of the electrons for each drift path. Subsequently we compute the differences Δt between the various mean arrival times and the mean arrival time of electrons produced closest to the proportional counter and the differences $\Delta\ell$ between the corresponding drift paths and that one closest to the proportional counter. Finally the values of Δt as a

function of $\Delta\ell$ are fitted by a straight line in order to obtain the drift velocity w.

It should be emphasized that the computation of differences in space and time leads to a cancellation of possible error sources due to the uncertainties on the boundary effects, to the nonlinear effects in the gain of the preamplifier, to the time resolution of the detector and to the initial spread of the electron cloud, to the uncertainties in the absolute positions of the electrodes (the only error of $\Delta\ell$ arises from the less than perfect knowledge of the cell position), provided the electric field is homogeneous.

The results of the measurements of the drift velocity for three different mixtures of helium and isobutane obtained with the lasers are shown in Fig. 5.5. The full and the dashed lines in Fig. 5.5 represent Monte Carlo calculations[18] computed by solving the Boltzmann transport equation of the electron motion in an electric field. The errors indicated take into account uncertainties due to the drift cell displacements, uncertainties due to the time measurement and the fit of the time distribution, uncertainties on the electric field and finally systematic errors due to pressure changes during the experiment.

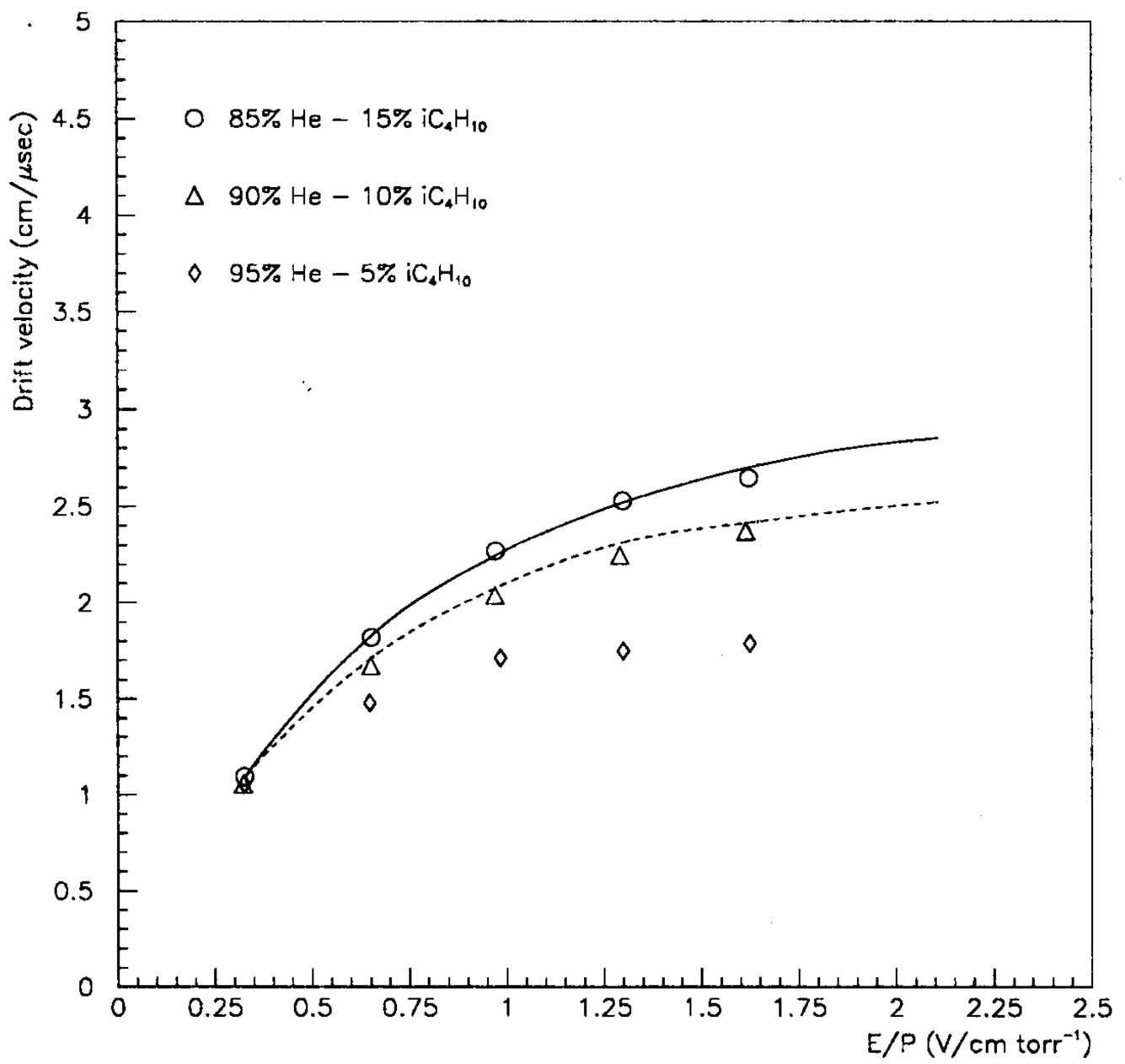

Fig. 5.5. Drift velocity at room temperature as a function of the reduced electric field in mixtures of helium with isobutane. The superimposed curves for two of these mixtures represent Monte Carlo calculations computed by solving the equation of motion of electrons in an electric field.

All molecular gases added to helium and the composition of the gas mixtures have been chosen in order to keep the radiation lengths as long as possible. All mixtures allow stable operating conditions of the proportional counter, have good gas amplification properties and consequently good electron detection efficiency, and correspond to high safety requirements.

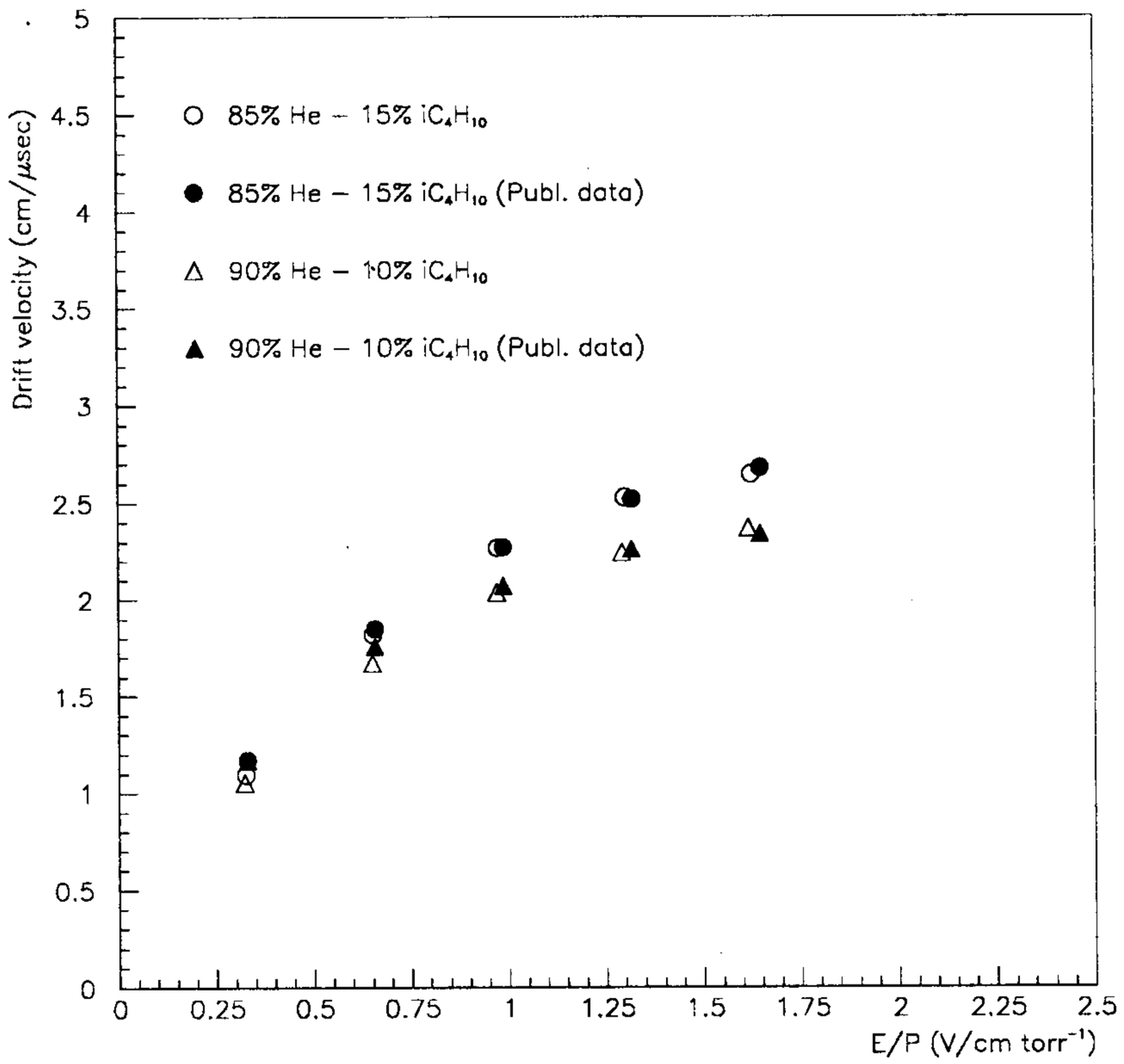

Fig. 5.6. Drift velocity in two mixtures of helium and isobutane as measured in the present experiment compared with published data.

A comparison with the present measurements data taken from the literature for two of these mixtures[19] is shown in Fig. 5.6. Our results agree both with Monte Carlo calculations and with published data. Work is in progress for the determination of the longitudinal and transverse diffusion coefficients. Also the accuracy of the measurements is going to be improved by reducing the error of the determination of the drift field which contributes at present with the largest uncertainties to the measurements shown.

6. FRONT-END ELECTRONICS AND HV SYSTEM

6.1 The preamplifier card

The function of preamplifier card, shown in fig. 6.1, is to provide fast, low noise amplification of the signals from sense wires.

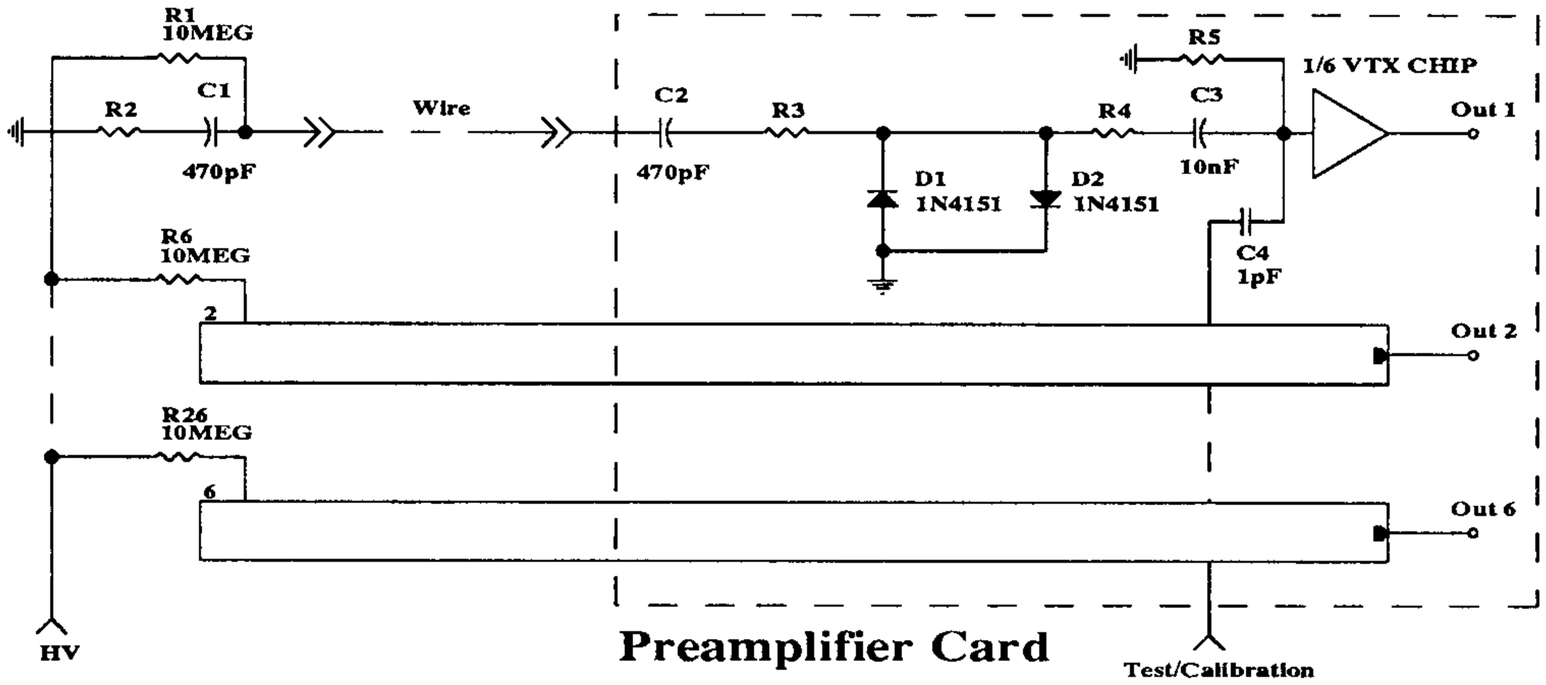

Fig. 6.1. Preamplifier card.

Investigation on different preamplifiers[20] showed that the VTX chip[21] is the best one thanks to his extremely low power dissipation, package mass and price/ch. Specification for this preamplifier are listed in table 6.1.

Gain	1.0mV/fc (50 Ω load)
Dynamic range	400 mV (3% linearity at the maximum output)
Crosstalk	< 0.5% between any two channels
Noise	860 electrons + 47e/pF (100 MHz bandwidth)
Output risetime	5 ns
Output falltime	16 ns
Input impedence	130 Ω
Output impedence	43 Ω
Power dissipation	10 mW/channel (1 mA output pulldown current)
Channels/chip	6

Tab. 6.1. Preamplifier specifications.

Sense wires are decoupled from the preamplifier circuit by a 470 pF 3 kV capacitor. Each preamplifier is protected against wire sparking by a diode pair and two current limiting resistors

chosen to provide a series termination for the sense wire when added to the input impedence of preamplifier. A calibration input is provided for calibration and test purposes.

6.2 The amplifier-discriminator card (A&D)

Signals from wire preamplifiers will be brought outside the KLOE detector by means miniature 50 ohm coaxial cables. Because expected signals from single cluster electrons have an amplitude of about 10 mV, they need to be amplified before discrimination. Furthermore, a splitted output analog signal must be provided.

Fig. 6.2 shows the block diagram of a single channel of the A&D circuit, details are given in fig. 6.3.

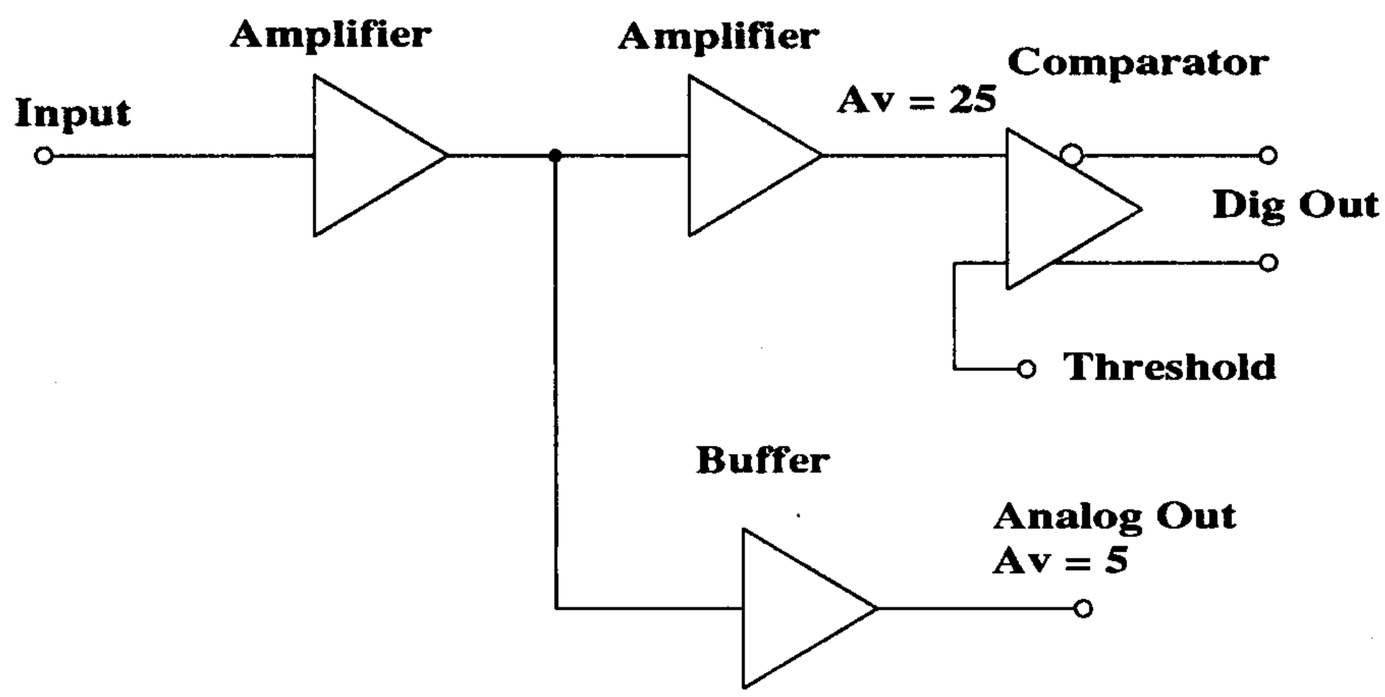

Fig. 6.2. Single channel A&D circuit block diagram.

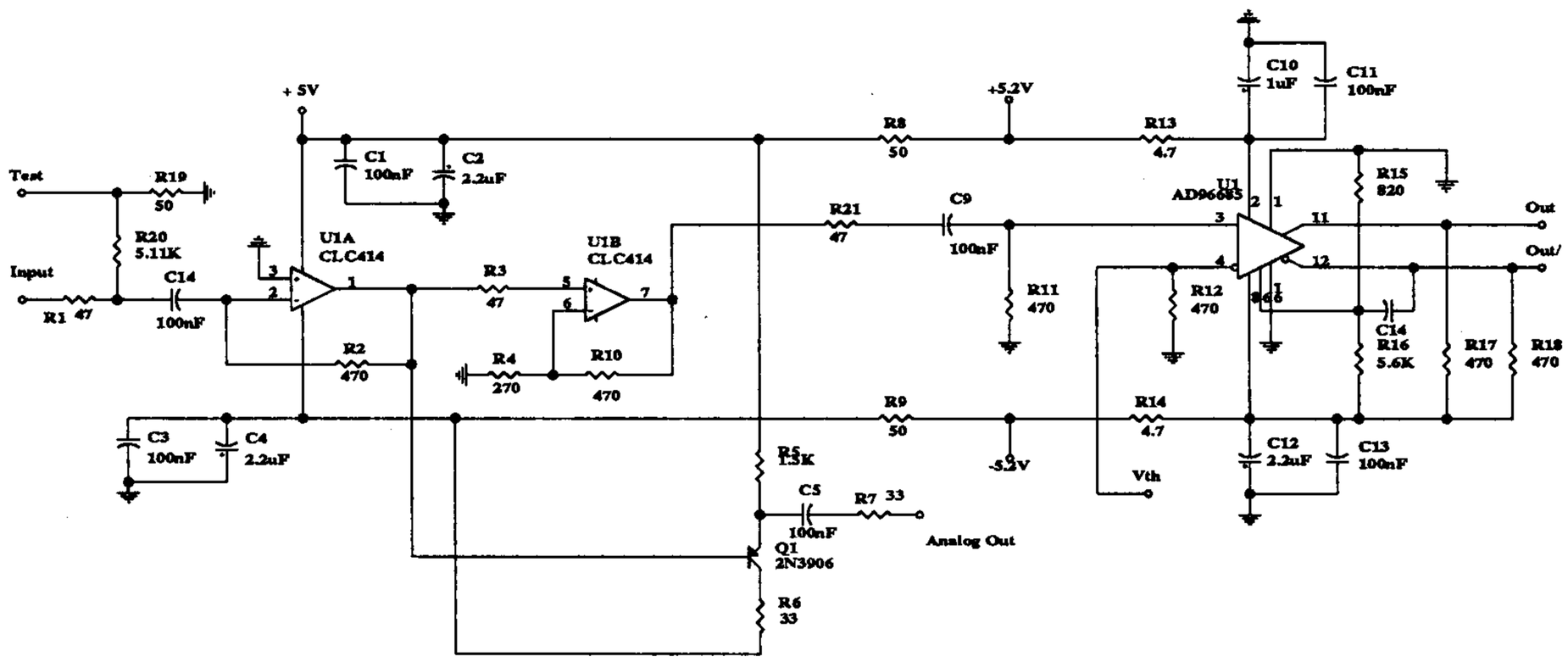

Fig. 6.3. A&D circuit diagram.

The first stage is X10 amplifier with low input impedence for trasmission line termination. Output signal drives both the analog output buffer and the comparator driving stage. The total voltage gain at the input of comparator is ~25. The comparator produces a differential ECL

pulse whose minimum width is fixed to 100 ns. The threshold is adjustable through a 10 to 1 voltage divider. An input is also provided for calibration/test purposes. Specification for the A&D circuit are given in table 6.2.

Analog output voltage gain	5
Voltage gain (comparator input)	~25
Output risetime	~5 ns
Dinamic range	~1.5V
Analog output	unipolar, 50 Ω
Digital out	differential ECL, ~110 Ω
Calibration Input	one per card

Tab. 6.2. A&D circuit specifications.

Forty-eight A&D channels should be packaged on a single VME 9U card togheter with ICs for the thresholds setting/sensing and logic for internal crate addressing decoding. Modularity for thresholds setting is 8.

6.3 The calibration-communication card

One card in each A&D crate allows communications with SLOW-CONTROL devices for threshold sensing/setting and calibration/test signals generation. Communications between SLOW-CONTROL processor and A&D crates exploit a RS232 serial link.

The calibration circuit allows us to apply the calibration signal to the preamplifier cards. A DAC controls the charge injected into the preamplifiers. A separate calibration pulse allows testing of the A&D cards.

6.4 High Voltage System

The proposed solution for high voltage sense wires power supply is shown in fig. 6.4. Requirements for HV channels are :

- programmable voltage setting (0 - 2.5 kV, 1V resolution, Master)
- programmable hardware trip (50 nA - 1 μA, Distributor)
- programmable ramp down (Master)
- programmable ramp up (Master)
- Voltage sensing (1 V resolution, Distributor)
- single channel on/off capability (Distributor)

Due to the circuit configuration these characteristics are shared between the master and the distribution cards as shown in fig. 6.3. Each HV channel supplies a group of sense wire connected by a daisy chain (we expect to use a modularity of 6/12 wires per HV channel).

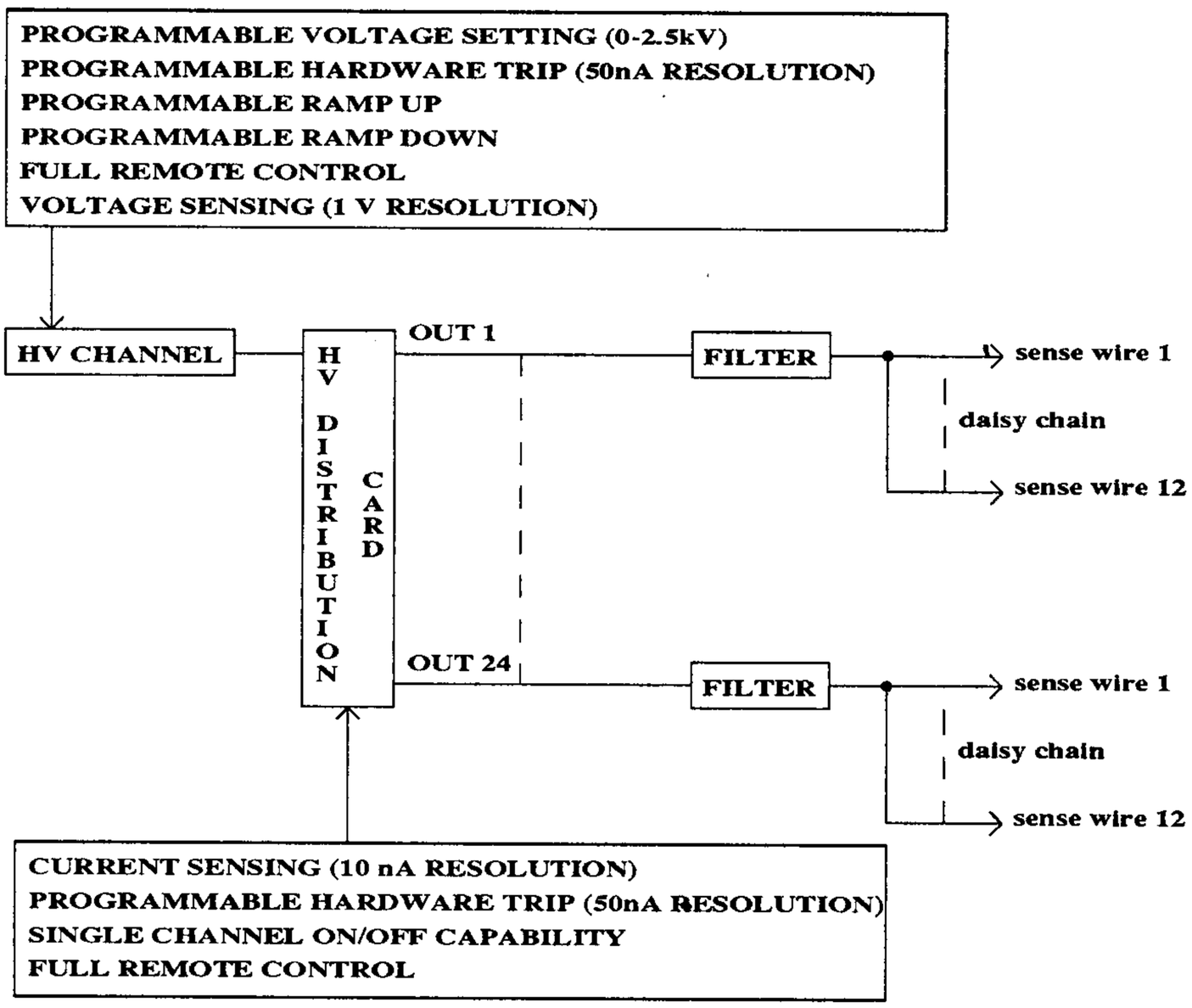

Fig. 6.4. High voltage sytem block diagram.

7. PSI TEST BEAM: STUDY OF PROTOTYPES 0.1 AND 0.2 OF THE KLOE DRIFT CHAMBER.

7.1 Prototypes 0.1 and 0.2

In order to assess the performances of the proposed drift structure for the KLOE tracking chamber and to evaluate the minimal number of field shaping wires for it, two prototypes have been built with cell size as small as one could foresee and with field to sense wires ratio of "3:1" and "2:1" (Fig. 7.1).

They will be denoted in the following as prototype 0.1 and 0.2 respectively for the "3:1" and "2:1" structure. In both prototypes a matrix of 5×5 cells is read out, but a bigger area of 49 cells in a 7×7 matrix is connected to the HV power supply, in order to correctly shape the electric field over the inner area of 25 cells. The wires employed are 20 μm W (sense wires) and 80 μm Al (field wires).

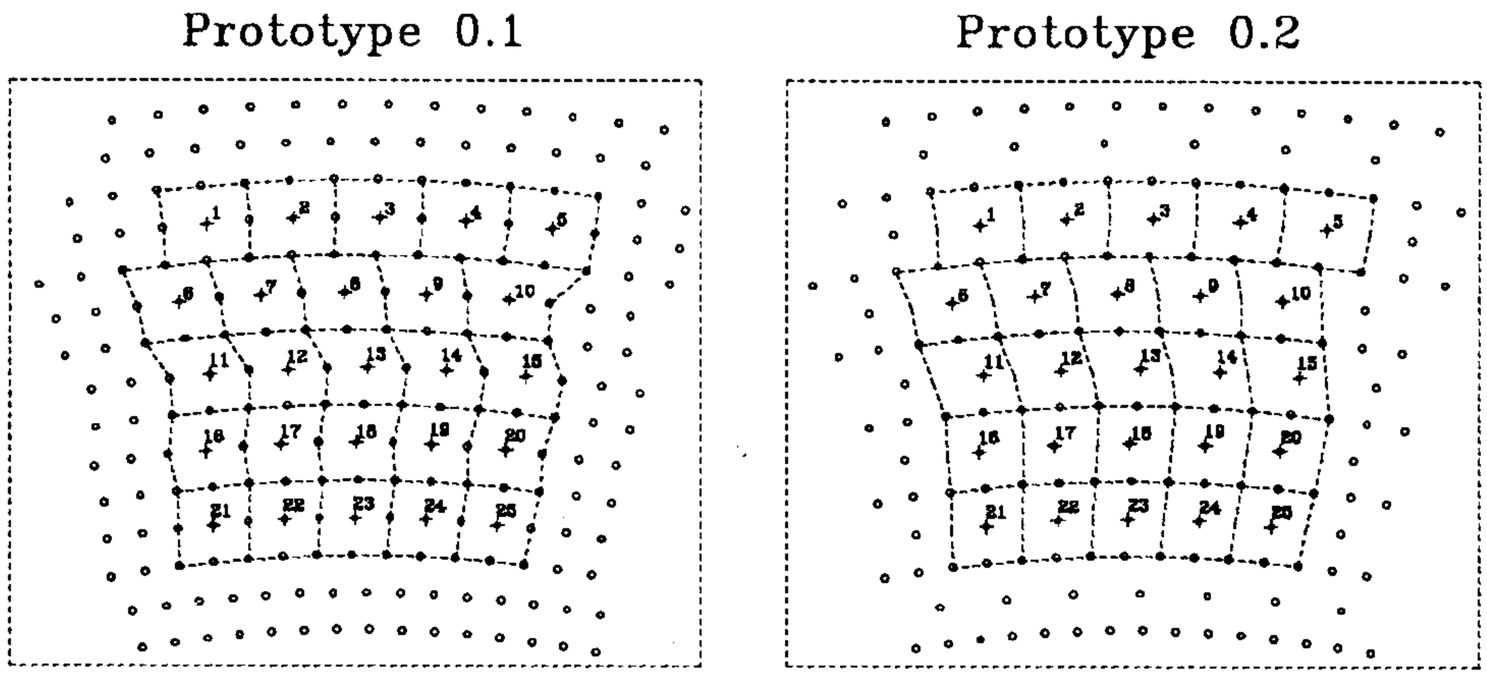

Fig. 7.1. Cells layout in the two prototypes.

Given the short length of the prototypes (50 cm) the wires were strung axially, and so one does not have any information on the properties of signal propagation in the "stereo" layers of the real chamber. This topic will have to be studied with the longer prototype being presently built in Lecce.

Another purpose of the test was to compare the performance of both cell structures to different gas mixtures: data have been taken with 90–10 He-iC_4H_{10}, as well as with 95–5 He-iC_4H_{10}, 60–40 He-CH_4, 80–20 He-$CO_2$and 60–40 Ar-iC_4H_{10}.

In the following section, a brief description will be given of the experimental setup. Then, the first results concerning efficiency and resolutions for both prototypes will be shortly presented. More details on these analyses are given in the Appendices 3–5.

7.2 The PSI setup

The two prototypes have been tested in a π beam with momenta P = 150–300 MeV/c obtained from the synchrotron of the Paul Scherrer Institut. A sketch of the experimental setup

is shown in Fig. 7.2: the prototypes were positioned (wires running vertically) on two revolving supports that enabled us to rotate them about their axis and study their response to different incident beam angles.

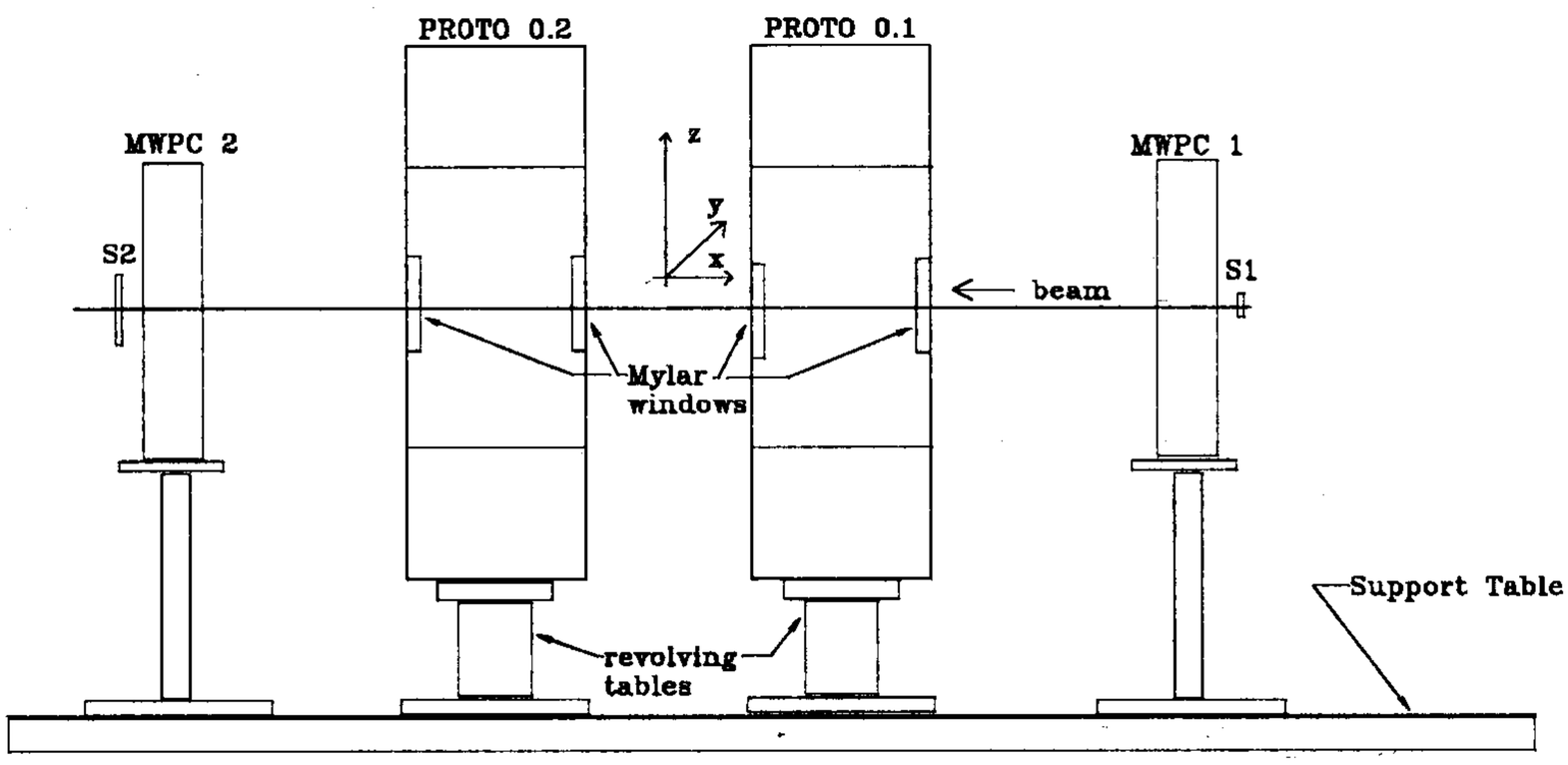

Fig. 7.2. Sketch of the experimental setup at PSI. The coordinate system used in the analysis is also shown.

The beam crossed the 4×4 cm^2 scintillator S1, then the first of two multiwire proportional chambers, MWPC1 and MWPC2, each one consisting of two orthogonal planes of 128 wires with a 1 mm pitch, and positioned immediately before and after the prototypes. A second 12×12 cm^2 scintillator S2 followed MWPC2. The two MWPCs gave two position measurements of the incident tracks, one for each of the two projection planes X,Y and X,Z as shown in Fig. 7.2, and hence a determination of the trajectories of beam particles in the prototypes.

The coincidence S1·S2 of the two scintillators formed the trigger. The signal from each sense wire (after amplification by a transresistance amplifier developed as a first prototype of the final front-end read out for the final chamber) was split and sent to an ADC for charge analysis and, after discrimination and a $\sim$ 60 ns cable delay, to the STOP of a TDC started by the trigger coincidence.

In Fig. 7.3 an event is shown as reconstructed by the offline; the solid line represents the external track obtained with the MWPCs, the others render the tracks fitted with the two prototypes individually, as well as the track obtained with a combined fit of the two.

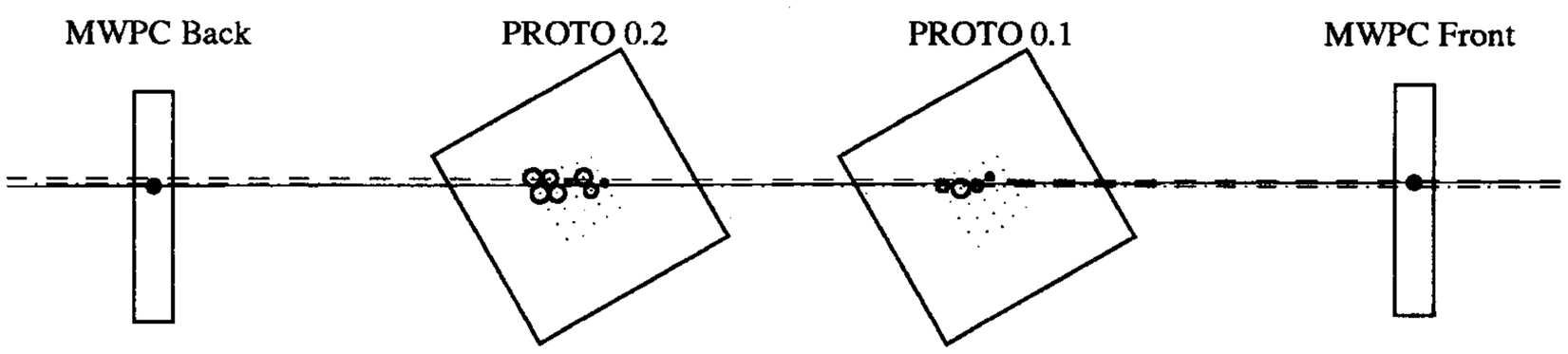

Fig. 7.3. Display of one event of a run taken at $\Phi = 30°$.

7.3 Measurements of efficiency

The single cell efficiency for pions having momentum P=250 MeV/c has been measured for both prototypes 0.1 and 0.2, at 0° and 90° incidence angles, using the gas mixture 90–10 He-iC_4H_{10}.

A "good track" is defined by the occurrence of a pattern of hit cells: three layers (the two most distant from each other, and one in between) are requested to have a TDC hit in the cell closest to the projection of the track as given by the MWPC's.

The efficiency for a given cell will then be given as the ratio of "good TDC hits" (*i.e.* TDC values below a certain cut) to the total number of events, being ideally equal to 1 when the track given by the MWPC's passes through the cell, 0 otherwise. Fig. 7.4 shows a typical efficiency profile across a cell. The fit assumes a constant "plateau" efficiency, smeared by a Gauss resolution function.

It must be pointed out that, while the apparent width of the cell depends on the upper cut used to define a "good TDC hit" (it increases when the cut is raised) the "plateau" efficiency does not depend on the above cut, but it does depend on HV settings (see Fig. 7.5). In this analysis, only the runs with the highest values of HV's (1.8 kV for Prototype 0.1, 1.95 kV for Prototype 0.2) have been used.

The average cell efficiency (fitted value of the plateau) is ~99.0% for both prototypes at 0° and 90°, as shown in Tab. 7.1.

	ε(%) "3:1" cells		ε(%) "2:1" cells	
cell #	0°	90°	0°	90°
13	99.1 ± 0.4	99.1 ± 0.3	99.1 ± 0.4	99.3 ± 0.3
14	98.2 ± 0.4	98.3 ± 0.3	98.7 ± 0.5	99.1 ± 0.3
07	99.6 ± 0.8	99.3 ± 0.5	98.3 ± 0.8	98.6 ± 0.6
08	98.5 ± 0.4	98.5 ± 0.3	98.9 ± 0.4	98.6 ± 0.7
18	98.9 ± 0.3	98.9 ± 0.3	98.6 ± 0.5	99.5 ± 0.3
19	99.5 ± 0.3	99.1 ± 0.3	99.0 ± 0.4	99.4 ± 0.3

TABLE 7.1. Efficiencies for "3:1" and "2:1" cell structures, at 0° and 90° incidence angles

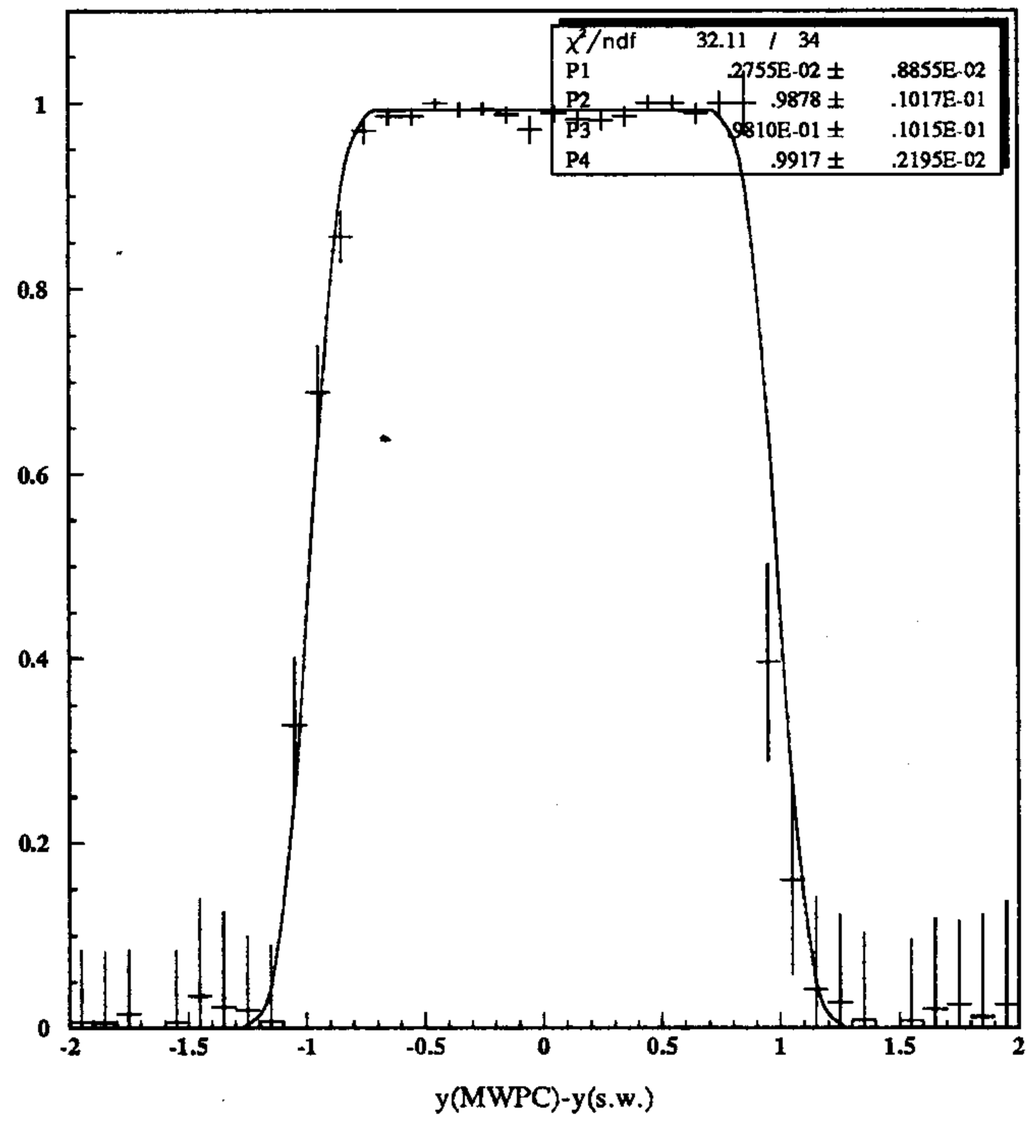

Fig. 7.4. Efficiency profile, Prototype 0.1.

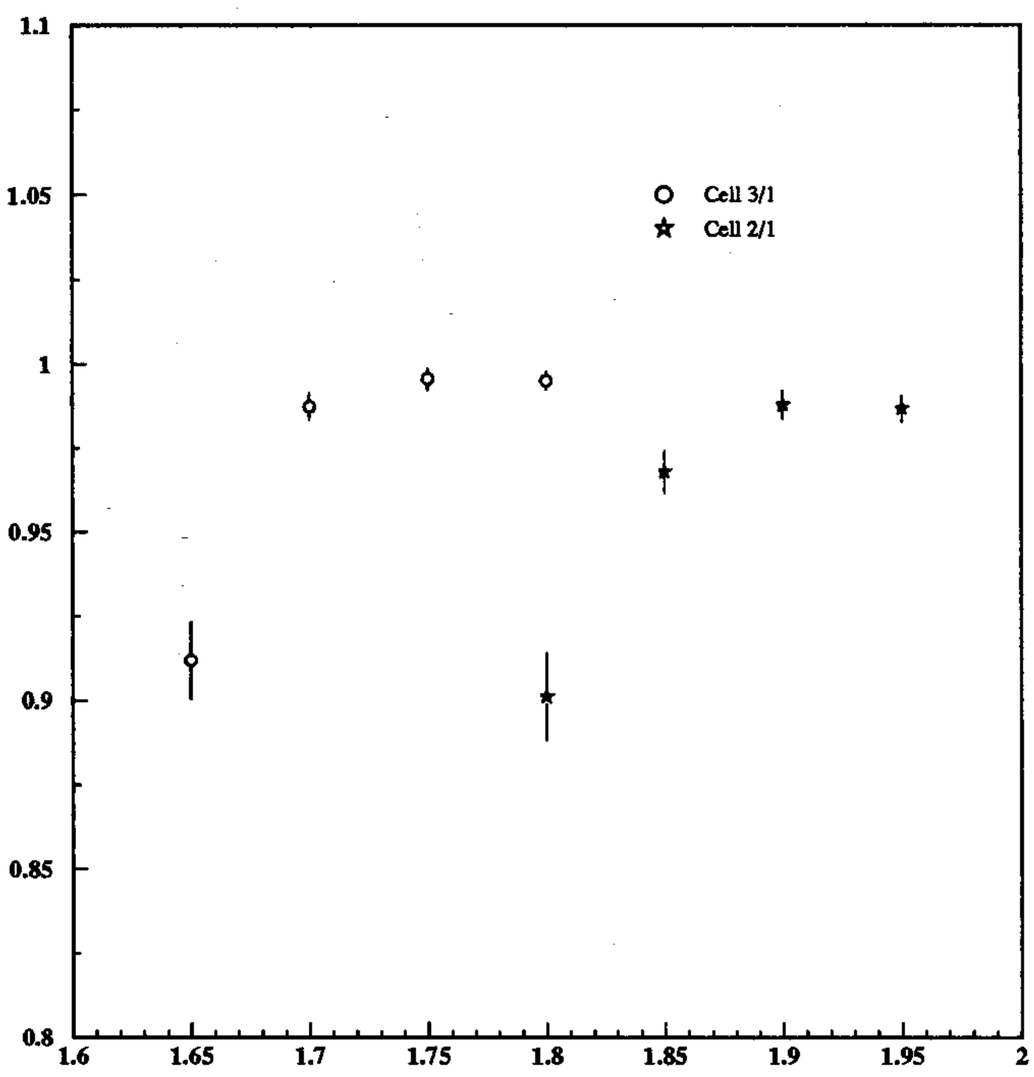

Fig. 7.5. HV Efficiency curves.

7.4 Measurements of local resolution

Measuring the local resolution, *i.e.* comparing spatial measurements in cells close to each other, and whose relative position is very accurately known from tolerances in mechanical construction, is advantageous: one automatically avoids any systematics due to misalignment in different parts of the setup, as well as the effect of multiple scattering of beam particles through the different materials of the detectors.

Looking at Fig. 7.6 it appears clear that a straight track passing through a prototype causes correlated times to be measured in cells "11", "13" and "15".

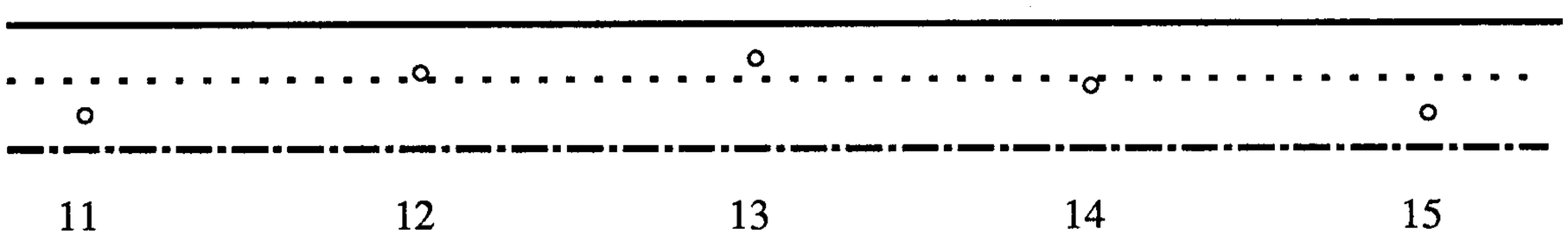

Fig. 7.6. Illustration of the stagger method. The little circles represent the wire positions in the central row of the prototypes. The lines stand for different track configurations. (see text)

These times are translated to a drift distance (inverting the fitted time-to-distance relation, see next section for more details) and the quantity

$$\Delta x_{\mathrm{stag}} = \frac{x(t_{11}) + x(t_{15})}{2} - x(t_{13})$$

is plotted against $x(t_{13})$ in Fig. 7.7.

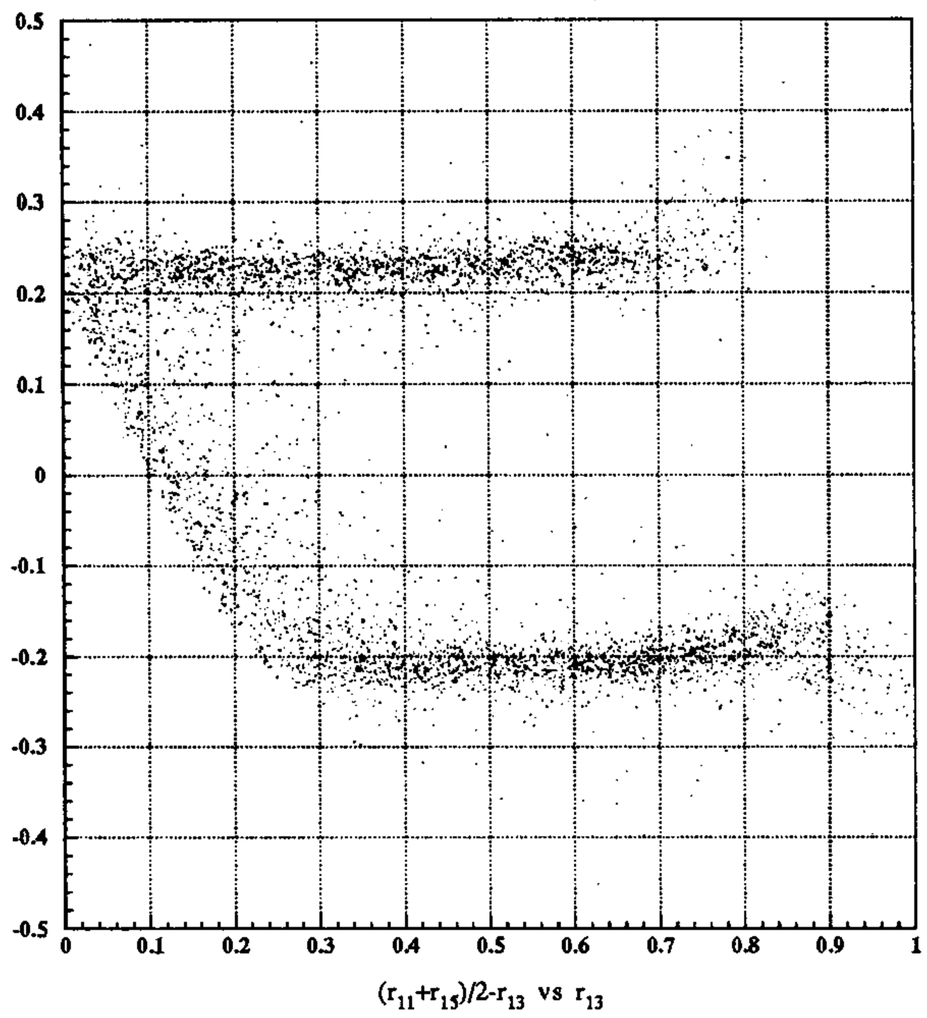

Fig. 7.7. Scatter-plot of the stagger vs. r_{13} The scales are in cm.

The plot splits into three clear branches, according to the three ways in which the track can pass with respect to the sense wires: above "13", below "11" and "15", or in between, and the distance between the straight branches is twice the stagger between the mean of cells "11" and "15" and cell "13". Examples of Gaussian fits to 500 μm slices of these branches are shown in Fig. 7.8. The half-distance between the peaks is 2.15 mm, to be compared with the nominal 2.20 mm. The space scale is therefore correctly reconstructed.

The thickness of each band is the convolution of the spatial resolution of the 3 cells. Slicing the upper branch of Fig. 7.8 one obtains Fig. 7.9, from which an average resolution $\sigma \leq$ 200 μm (over most of the cell area) can be estimated.

In Appendix A5 several examples are shown of local resolution curves for different values of high voltage, angle and beam momentum. In all configurations the mixture 90–10 He-iC_4H_{10} gives results within design specifications.

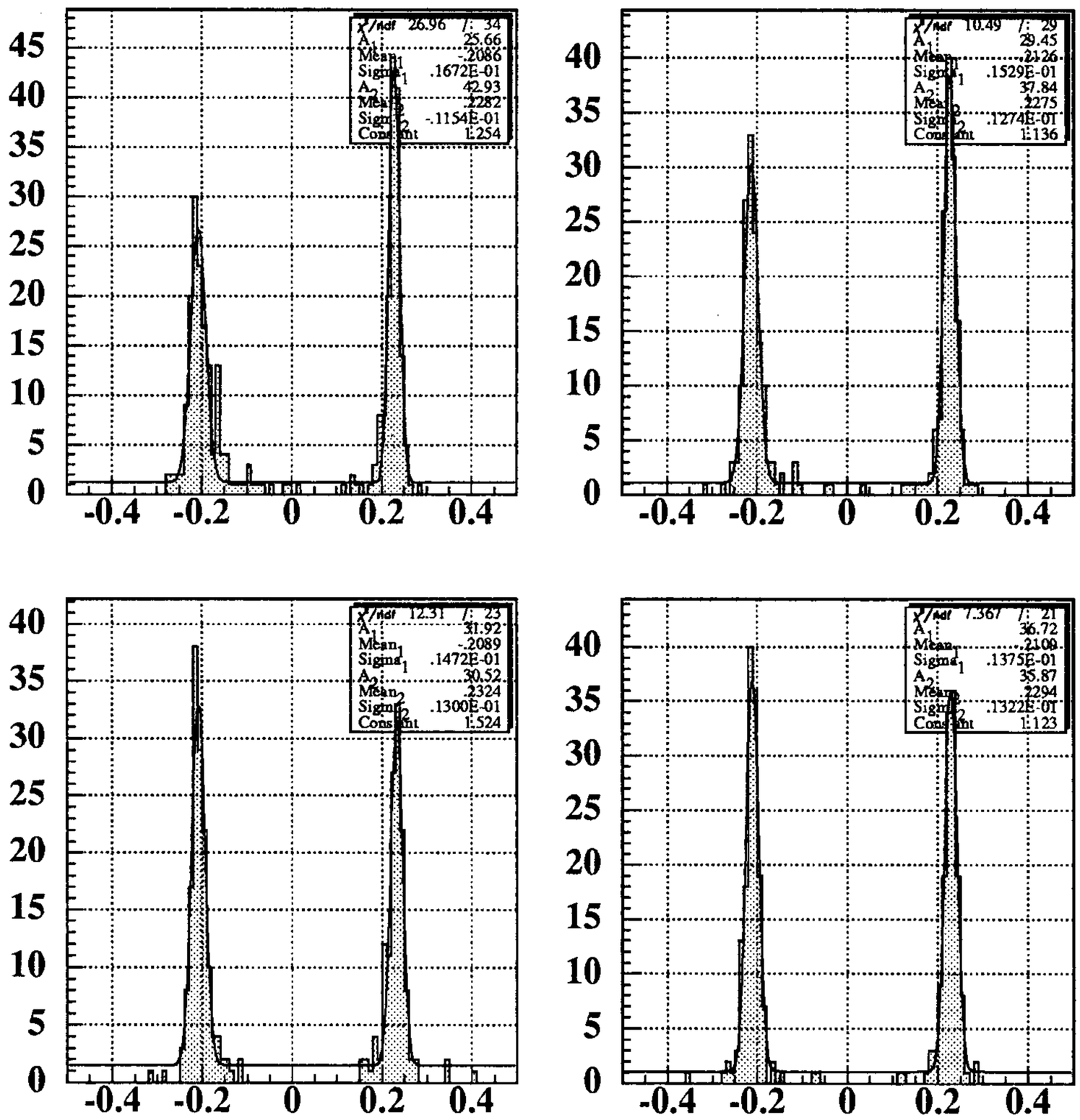

Fig. 7.8. Gaussian fits to slices ($r_{13} = (4 \div 6)$ mm) of the previous figure. Horizontal scales are in cm.

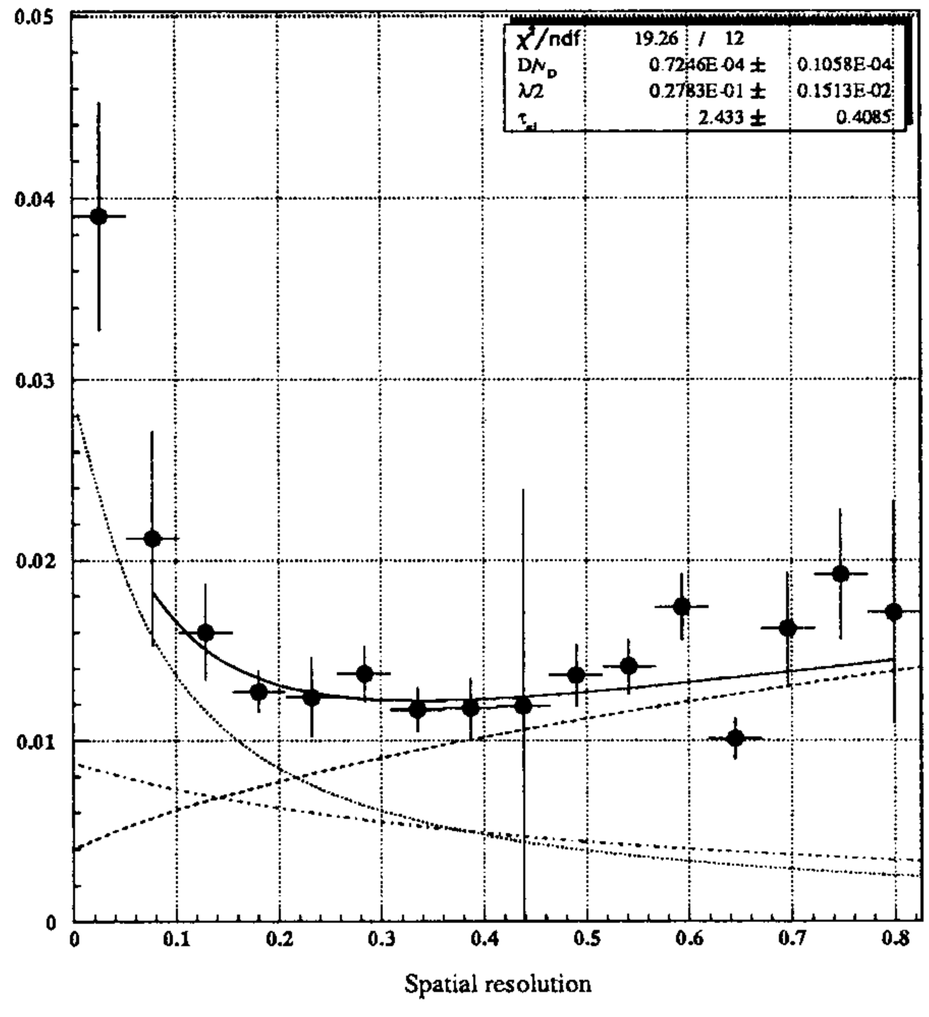

Fig. 7.9. Fit to the resolution curve for Prototype 0.1. HV_1=1800 V, $\phi_1 = 0°$, $p_{beam} = 150$ MeV/c. The scales are in cm.

7.5 Measurements of global resolution

To measure the resolution in Prototypes 0.1 and 0.2, after having found, with the help of the MWPCs, the cells crossed by the particle, one needs first to translate from time measurements to a distance from the sense wire of the crossed cell, and then to fit a straight line. The fit residuals give an estimate of the resolution.

Time-to-Distance Fit. As a starting point one has to measure the time-to-distance relation for a given gas mixture and electric field in the cells, *i.e.* the relation between t_d, the measured time of arrival of the ionization signal on the wires and R_d, the position where the ionization was produced. In our setup, R_d was given by the track measured with the MWPCs, and t_d directly by the TDC's.

In Fig. 7.10 the t_d Vs R_d correlation is shown for a cell of the two prototypes for ϕ=0° and 90°. The sign of R_d has been determined according to whether the tracks passed above ($Y_{trk} \geq Y_{wire}$, $R_d \geq 0$) or below the wire ($Y_{trk} \leq Y_{wire}$, $R_d \leq 0$). From the 0° plots one can clearly see the effect of the missing field wire on the cell structure of Prototype 0.2, namely the lengthening of the drift time of the "2:1" with respect to the "3:1" cell, which is due to the lower electric field. They also show that at 90° incidence angle the "2:1" cell is very similar to the "3:1", and that the latter appears the same at either 0° or 90° as expected.

To perform the fit, one starts from the average correlation, shown superimposed to the scatter plot before (Fig. 7.11b) and after (Fig. 7.11c) applying the cuts shown in Fig. 7.11a aimed at removing some of the background noise; Fig. 7.11d shows the comparison of the two profiles. The function used to fit the profile is:

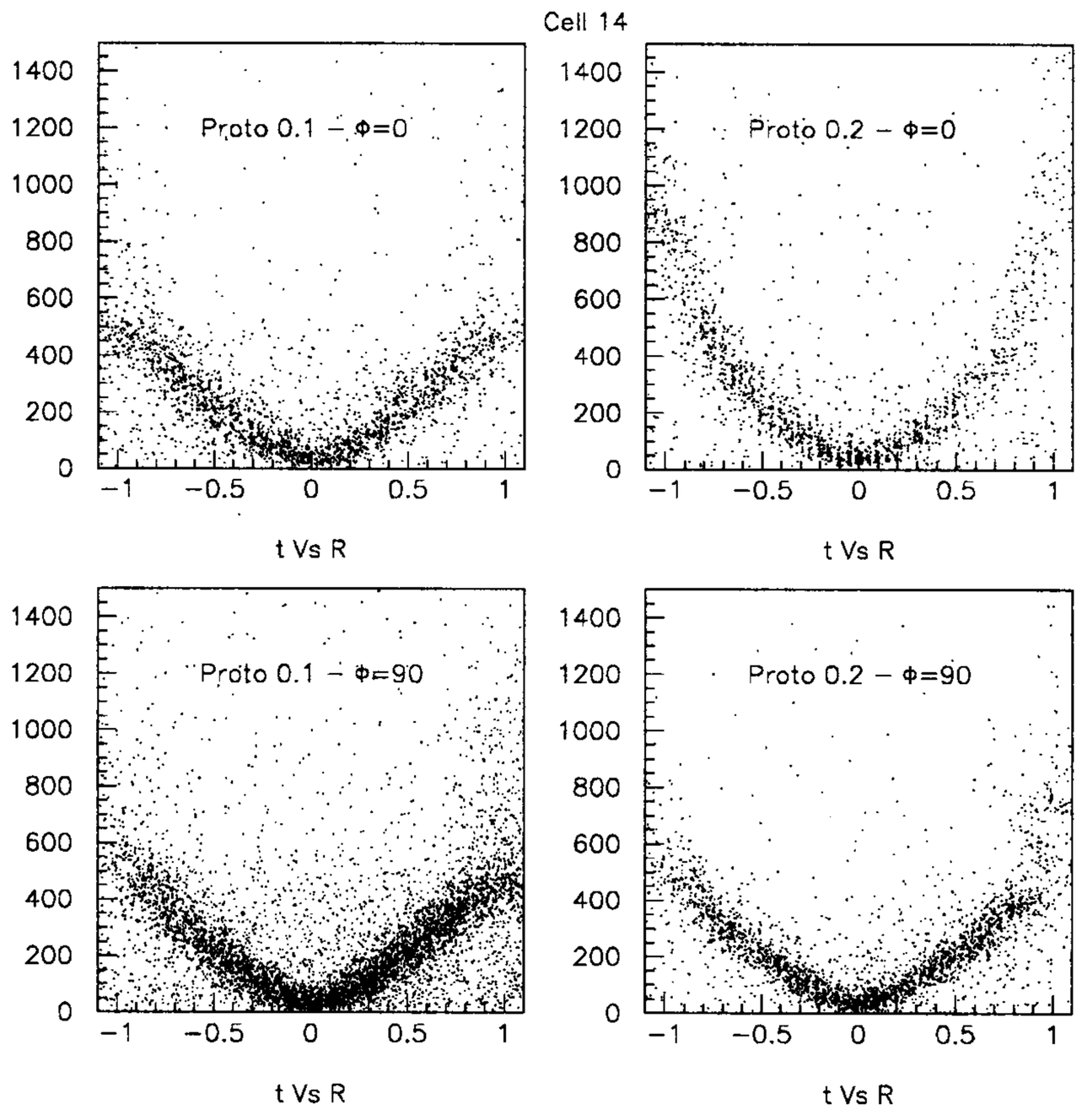

Fig. 7.10. Plots showing the time-to-distance correlation.

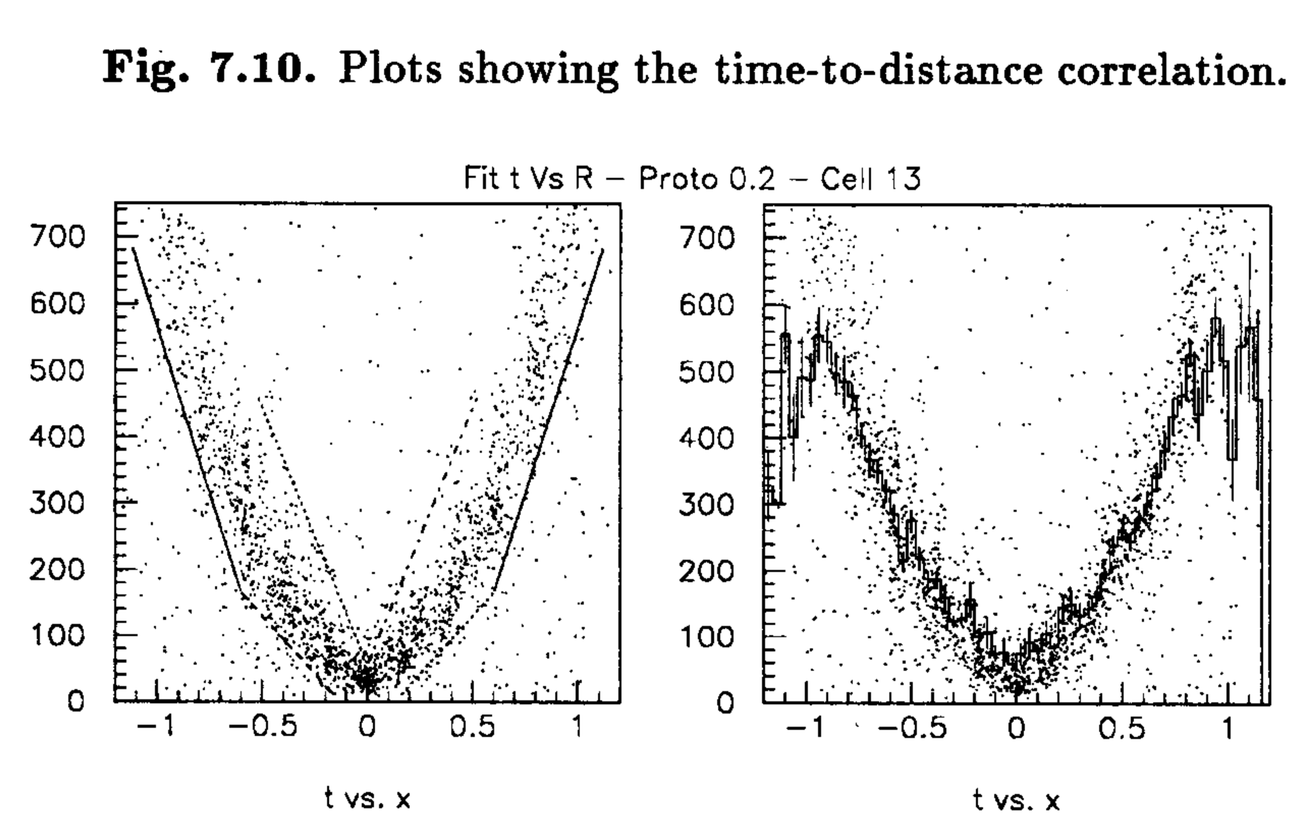

Fig. 7.11. Fit of the time-to-distance correlation plots (see text).

$$t_d = AR_d^2 + B|R_d| + t_0$$

Inverting this function one gets the drift distance for any measured t_d.

Resolution Vs Drift Distance. Since the time measurements can only be translated in radial distances from the wires and not to single points in space x_i, y_i, the fit is done by looking for straight lines which are best-tangent to all circles centered at the positions of the hit wires, and with radii proportional to the drift times via the time-to-distance relation. In Fig. 7.12 and Fig. 7.13 the plots of the residuals of the fit as a function of R_d for the two prototypes are shown. The residuals plotted for each given cell are calculated from fits which include the cell itself, and are therefore an optimistic estimate of the real resolution. For the cell of the figure, taking ~ 160 μm as an average value for the standard deviation, and applying known relations between the standard deviation and the real resolution, this number would translate into a resolution of ~ 190 μm.

The curves correspond to several track incidence angles, and the appropriate time-to-distance relation has been used for each one; the resolution is the same at all angles and for a number of different cells in both prototypes.

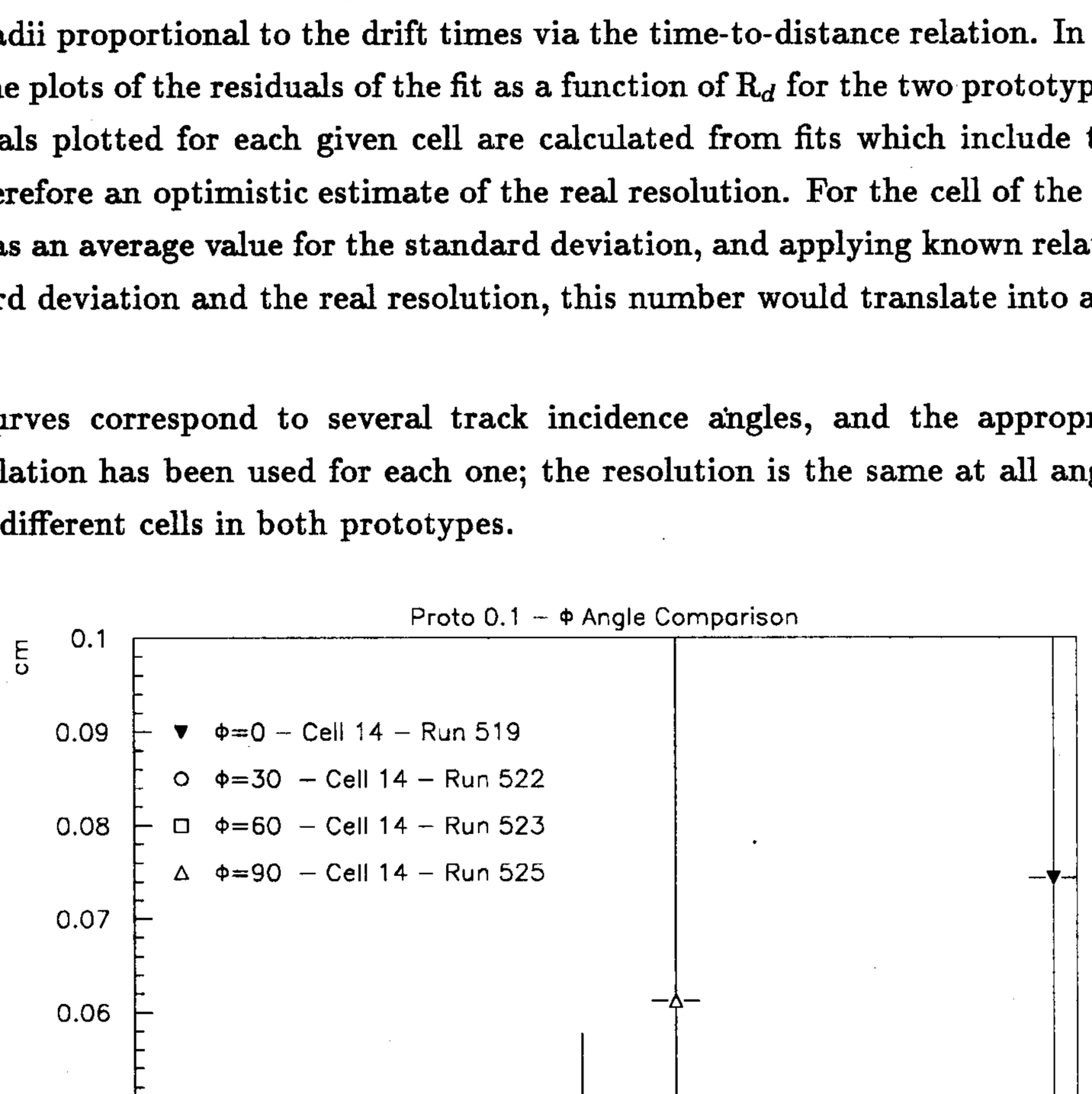

Fig. 7.12. Fit residual as a function of R_d for different Φ angles in Prototype 0.1.

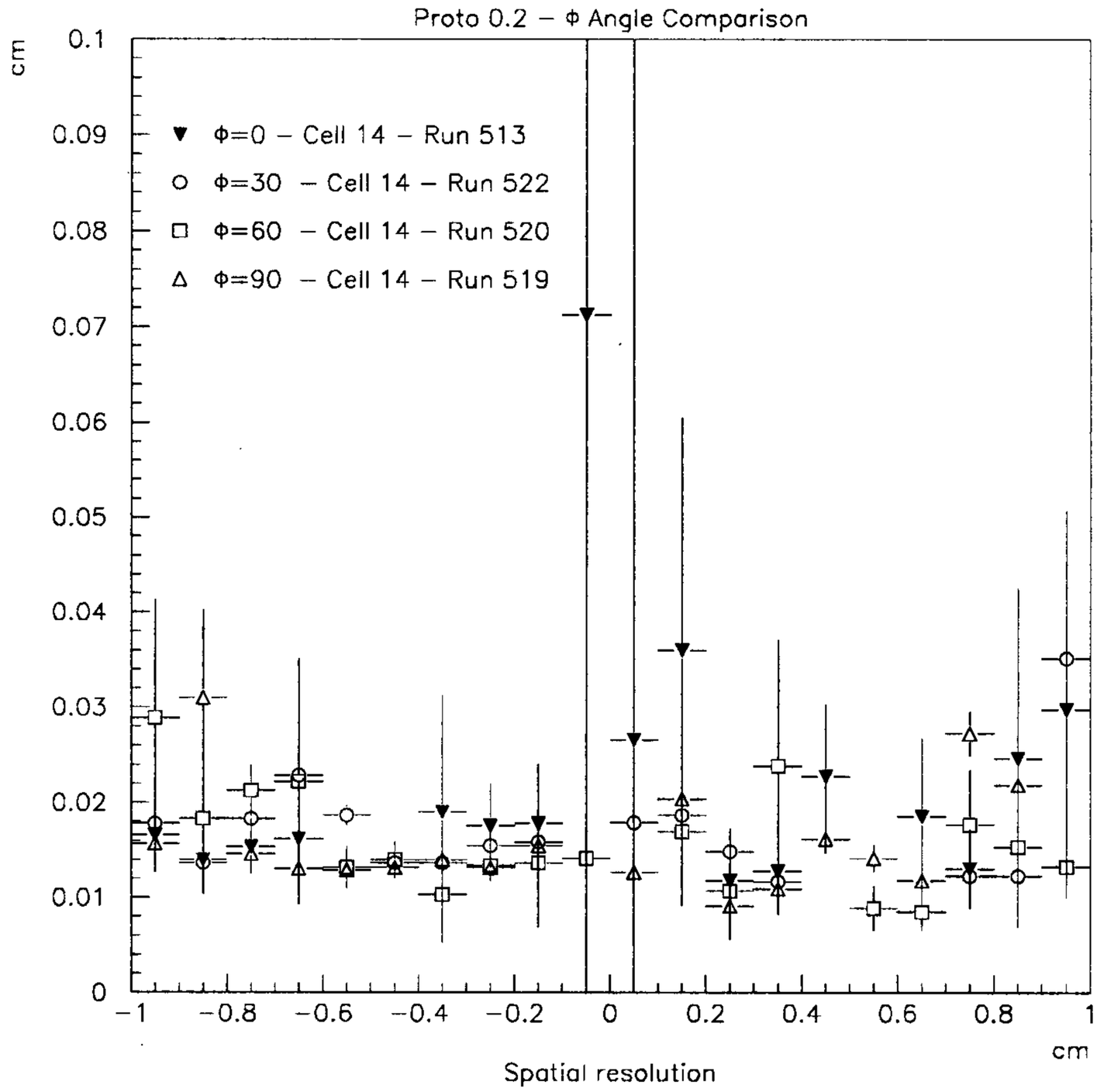

Fig. 7.13. Fit residual as a function of R_d for different Φ angles in Prototype 0.2.

7.6 Conclusions

At the level of "raw" efficiencies, no significant difference is found between the behavior of the cells with the "3:1" and the "2:1" structure.

The analyses of both local and global resolution have shown that the design goal $\sigma \leq 200\ \mu$m can be achieved in both cell configurations, "3:1" and "2:1".

A comparison of runs taken at different beam incidence angles has shown little dependence of the resolution on such angle in either prototype.

Within the present measurement errors, we observe no significant difference in the characteristics of the two cell types in any of the situations analyzed, as long as one takes care to correct for cell anisotropy, which of course is more pronounced for the "2:1" cell type than for the "3:1" one.

During the fall of 1994 the same series of tests will be repeated with a new setup in a magnetic field, to gain more insight about a situation, closer to the actual experiment, in which the electric field lines are more distorted in the outer cell regions.

8. PROTOTYPE I

8.1 Motivation

The reasons which justify the construction of a full scale prototype of the KLOE drift chamber are manifold. The prototype provides a realization of a detector close to the final design. In particular it contains a large gas volume, has the peculiar geometrical and wire structure and will allow tests of the materials and the mechanical tools anticipated for the final KLOE chamber. It will help to solve problems of the compatibility of different materials used in the construction; of finalizing the techniques to string, stress and crimp the wires; of optimizing the high voltage distribution system and the front end electronics; of checking mechanical and electrostatic stability of the chamber; of monitoring the stability of the gas mixture and possible gas contaminations as a function of time; of computing efficiency maps of the cell, time to distance relations, space resolution and the efficiencies to reconstruct tracks.

8.2 Prototype geometry

Prototype I has been designed to represent a cylindrical sector of the final KLOE drift chamber.

The prototype consists of two conical end plates made of almost isotropically laminated layers of prepreg T300-type carbon fiber fabric, 6.2 mm thick and plated with a 37 μm copper foil on both sides; two cylindrical sectors of 3 mm thick aluminium, reinforced along the perimeter with glued aluminium bars of a cross section of 20×30 mm^2; two lateral flat surfaces of 3 mm thick aluminium; a reticular aluminium frame of a size of 50×50 mm^2 on which both endplates and the closing surfaces are applied. An overall view of Prototype I is shown in Fig.8.1.

The most relevant geometrical parameters of the prototype are:

- the inner radius of 25 cm;
- the outer radius of 109 cm;
- the half aperture of the conical end plates of 80°;
- the full length at the inner radius of 290 cm.

The prototype consists of three sections which have different layer structures. The total number of layers is 30. The inner section is made of 10 layers with a cell size of $(1.5\times\pi/2)$ cm^2 and a drop at the centre of the prototype of 1 cm. The intermediate section consists of another 10 layers with a cell size of $(3\times\pi)$ cm^2 and has the same drop like the first one. The outer 10 layers differ only by the drop value at the centre chosen to be 2 cm. This solution has been adopted to simulate at a smaller radius the stereo angle configuration of the outer layers of the final KLOE chamber.

The second and the third section are separated by two layers of guard wires with an intermediate drop value of 1.5 cm and stereo angles of opposite signs. These wires ensure good gain uniformity in the cells near the boundary between the two regions with different drops. The same task is performed by two other layers of guard wires, both positioned at the inner and the outer closing surfaces of the prototype.

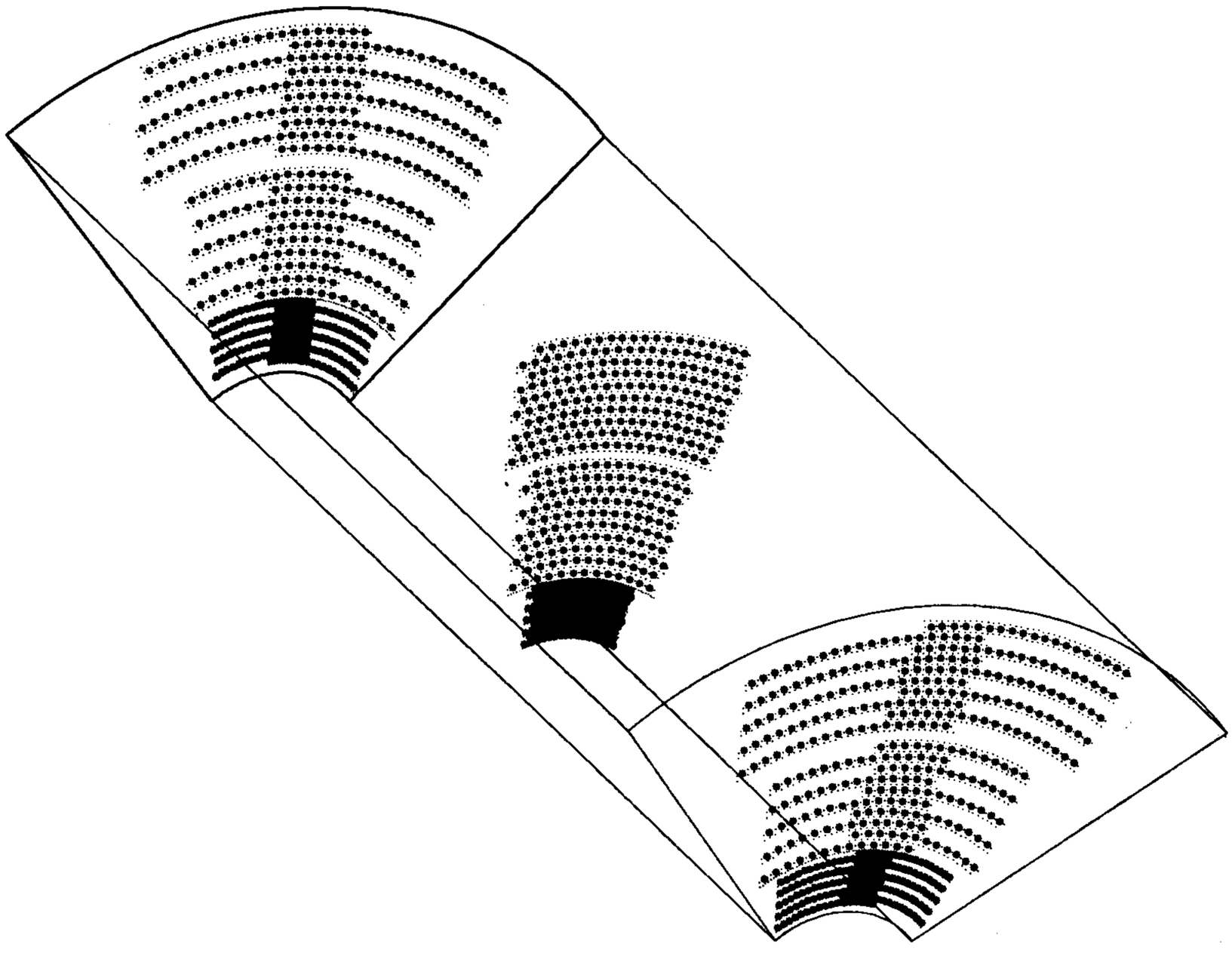

Fig. 8.1. View of Prototype I showing the position of the wires at the two endplates and at the center.

Since all the layers have stereo angles of alternating signs, the whole cylindrical sector cannot be filled uniformly with cells; this is possible only for a well defined region in the middle of the sector. A cross section in a plane perpendicular to the chamber axis shows that there are on the average 6 cells for all layers close to the endplates and 17 cells for all layers at the centre of the prototype. The total number of cells is 497 and the total number of sense, field and guard wires is ≈ 2300.

Survey measurements have been performed with a theodolite before starting wiring, in order to obtain the actual geometrical parameters[22] of the prototype. These parameters could be different from the nominal ones due to possible deformations of the mechanical structure, poor positioning of parts of the structure during the construction, the assembling operations or during drilling the holes of the endplates.

8.3 Stringing technique used for prototype I

The wiring of the prototipe I is accomplished inside a clean room (class 10000) to provide the necessary protection against dust. The temperature of the clean room is regulated within $\pm 3°C$. Temperature variations of this order affect the uniformity of the mechanical tension on the wires (Fig. 8.2).

The stringing procedure is carried out by a crew of three operators (called A, B, C). Operators B and C work stationary at the two endplates, while operator A provides the wire to both of them moving between the two endplates. The stringing has been done in the following subsequent steps:

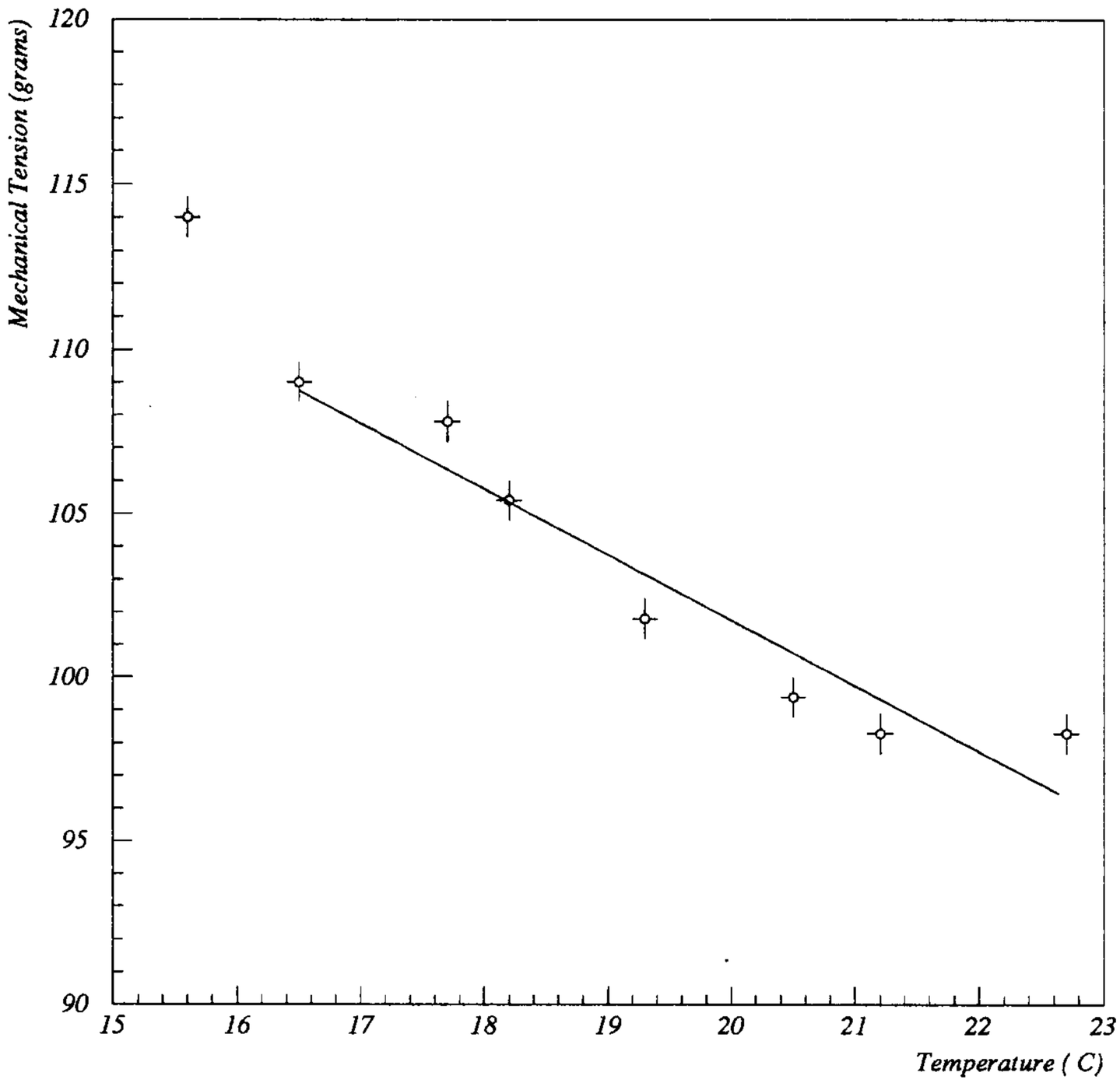

Fig. 8.2. Variation of the mechanical tension on an Al wire as a function of temperature.

1 The wires are unrolled by operator A with the help of an electromechanical system (see wire trasport tool).

2 The wire is inserted into the hole of one endplate (let us call it endplate I) by operator A (see wire insertion in the endplate tool).

3 Operator B at endplate I inserts the wire into the pin, then inserts the pin into the endplate hole and crimps the pin (see pin insertion and crimping tools).

4 During step 3 operator A cuts the wire at endplate II and inserts the wire into the endplate for operator C.

5 Operator C takes the wire from operator A, inserts it into the pin, then inserts the pin into the endplate hole and, after tensioning the wire (see aligning and tensioning tool), crimps the pin.

6 During operation 5 the operator A starts again with step 1 and the cycle is repeated.

The time needed for a complete cycle is about 2' for the Al wires and 2'-2'30" for the W wires. These are conservative times for an experienced crew. To summarize briefly, the main tasks of the operators are:

Operator A:

Management of the unrolling of the wire;

Handing over of the wire to operator B;

Cutting the wire and handing over of the wire to operator C.

Operator B:

Accepting the wire from operator A;

Insertion of the wire into the pin;

Insertion of the pin into the endplate hole;

Crimping of the pin.

Operator C:

Accepting the wire from operator A;

Insertion of the wire into the pin;

Insertion of the pin into the endplate hole;

Straining of the wire;

Crimping of the pin.

The most time consuming and tedious work is done by operator C who has to strain the wire. Operator B has some free time which he uses to change the pressure of the pneumatic crimping tool and to record the temperature.

During the wiring operation the necessary tools here described have been used:

Wire transport

An electromechanical cart on rails has been used which transports the wire from one endplate to the other. The unrolling of the wire is done extremely smoothly without any jolting. In the process the wires is passed through a slit made of a soft, lint-free material in order to remove possible dirt deposited on the surface of the wire. The commands for reversing the motion of the cart are located at both ends.

Wire insertion in end plate

A crochet hook has been used to ease the insertion of the wire into the endplate hole. This tool is necessary for the insertion of the tungsten wires because of their small diameter (25 μm), and for the insertion of all wires into the holes out of the confortable reach of operator A.

Wire insertion in feedthrough

No special tools have been used to ease the insertion of the wire into the pin. After getting more and more experienced, this procedure became a routine operation and did not require special attention.

Pin insertion

Given the tight tolerances of both the pin diameter and the hole on the endplates, the insertion

of the pin into the endplate has been done with the help of a specific tool, sketched in Fig. 8.3.

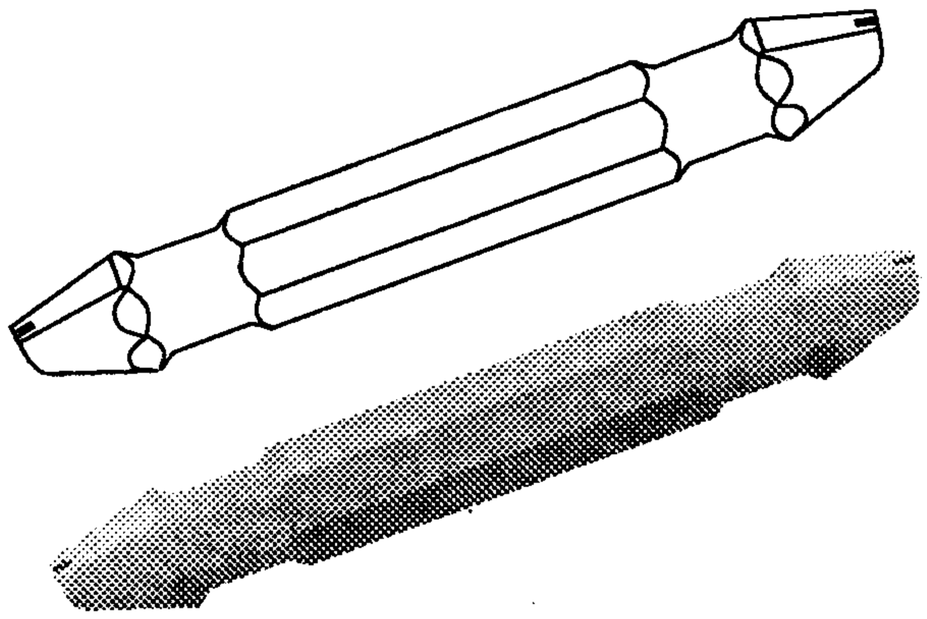

Fig. 8.3. Tool for the insertion of the feedthrough in the endplate.

Aligning and tensioning

The straining system consists of a laser fixed to a pulley. The laser light is aligned with the grooving of the pulley. To be sure that straining is applied in the direction of the pin it is sufficient to translate the system (in x and y directions) such that the the pin and the pulley are aligned by the laser beam.

Crimping

The crimping of the pin has been achieved with the pneumatic tool, shown in Fig. 8.4. The optimum working pressure of this tool has been chosen according to the curve in Fig. 8.5. Operator B and operator C have used identical tools. For the future, given the angle of the pin and the normal to the endplate, we propose a symmetric tool which would make crimping significantly easier.

Tension measurement

We have developed a computer-controlled system[23] for wire tension measurement. This is accomplished by passing a sinusoidal current through the wire, which is, for a short segment (10-15 cm) at its middle, placed in a magnetic field perpendicular to the wire and generated by small permanent horseshoe magnets. The Lorentz force acting on the wire produces a mechanical oscillation which induces an emf across the wire. The system changes the frequency of the current in the wire and measures the amplitude of the emf. Resonances are observed at the frequencies of the wire given by $f_n = (n/L)\sqrt{T}/\mu$ where T is the tension, μ is the mass per unit length, L the length of the wire and n the mode of oscillation (n odd only). The error on the measured tension is of the order of one percent. We are studying the possibility to place a suitable magnet outside the chamber near one end of the wire to allow for the monitoring of wire tension at any time and the possibility of observing change in wire tension due to deformation of the chamber structure.

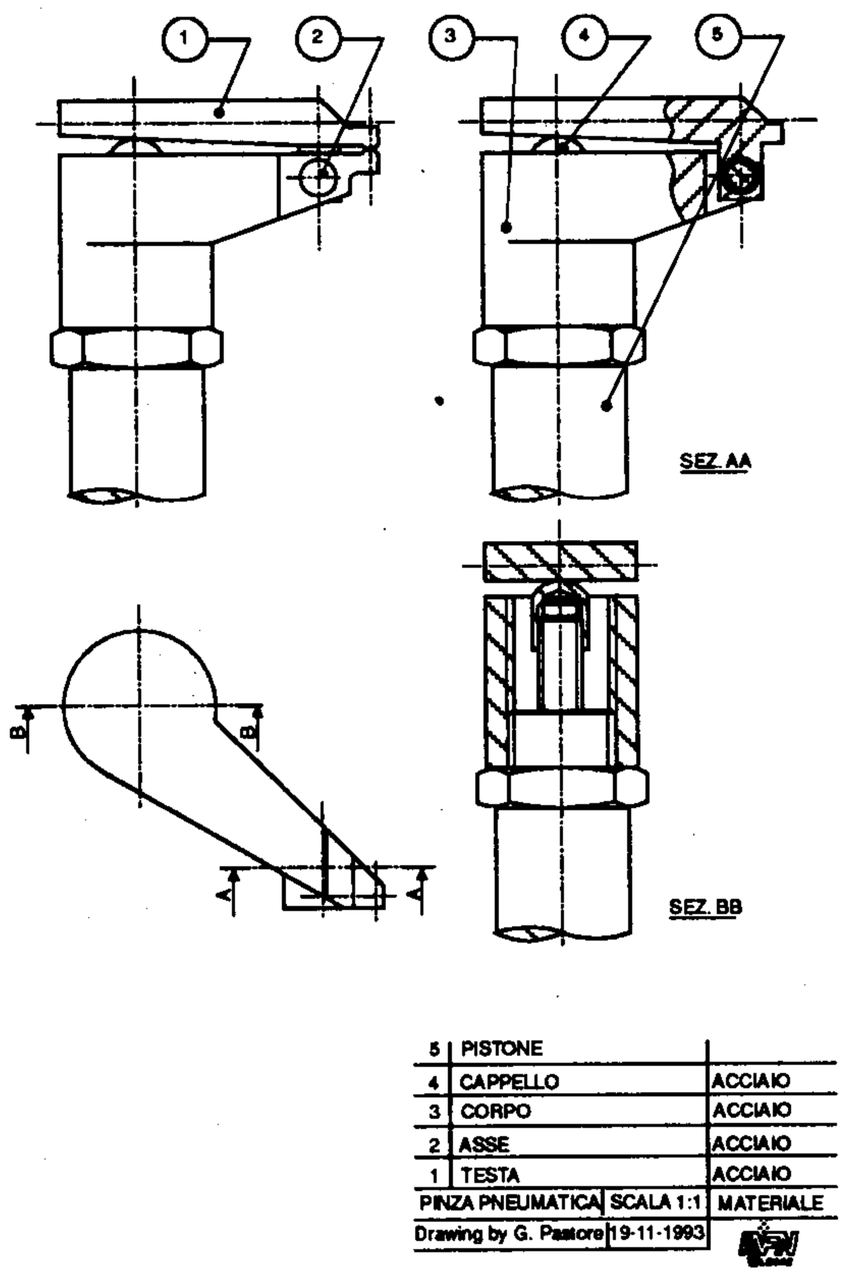

Fig. 8.4. Mechanical drawing of the pneumatic tool used for crimping.

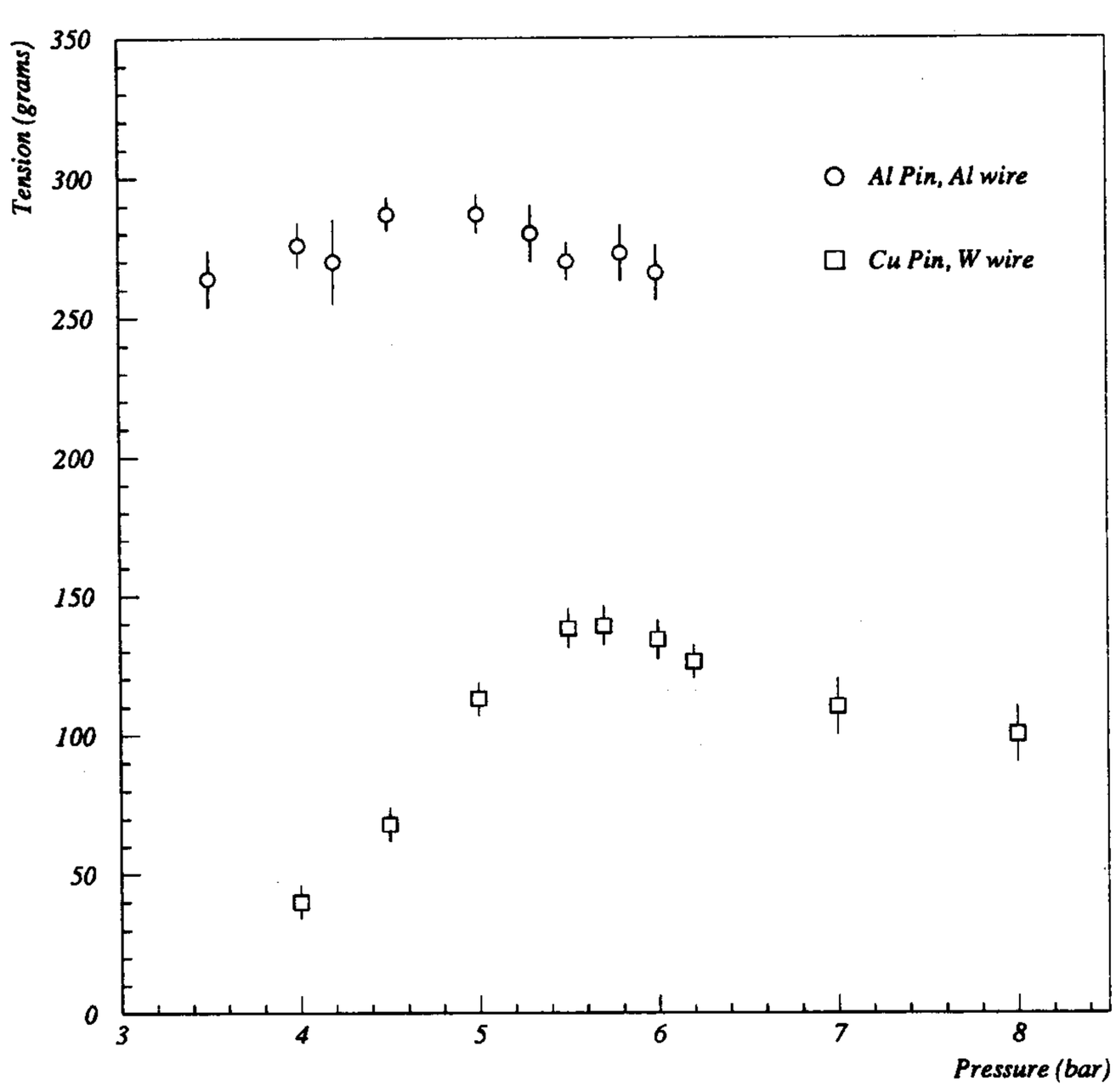

Fig. 8.5. Pressure required by the pneumatic crimping tool for a correct fastening of the wires inside the feedthrough ($\approx$ 0.7 mm size of the crimp). For values below 4.5 bar (Al wire) and 5.5 bar (W wire) the wire slips out of the feedthrough; for values above these the wire breaks far from the crimping zone.

After stringing a layer of wires, we measured the mechanical tension with the device just described. Our experience indicates that, after the first two layers of wires, when the insertion of the pins in the endplates revealed to be critical (the pin insertion tool had not been developed yet) very few wires had to be restrung because their measured value of tension was in the tails of the distribution outside the predetermined values ($\pm 5\%$ of the set value, Fig. 8.6). These values are, however, compatible with the tolerances of the measuring device and with the effects of the temperature gradient inside the clean room.

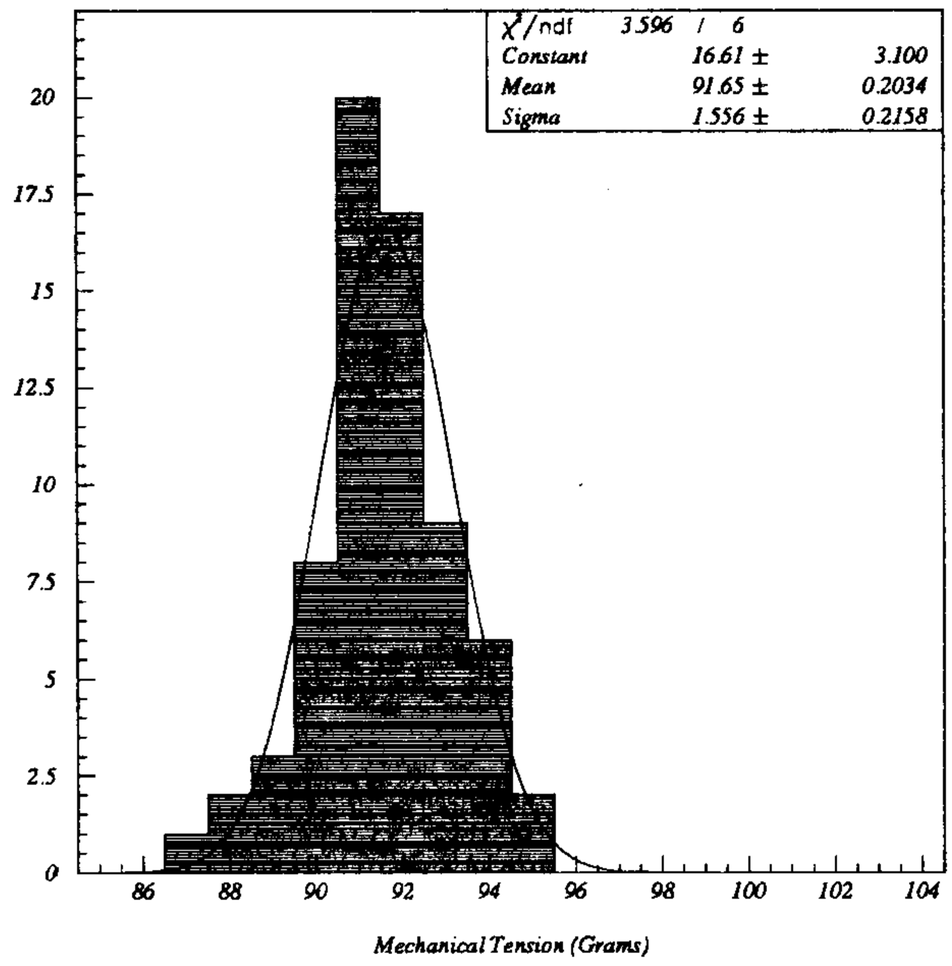

Fig. 8.6. Distribution of the mechanical tension on a set of Al wires. The spread is $\approx 2\%$ and is compatible with the measurement error.

8.4 Planned measurements with the Prototype I at PSI

Test measurements with Prototype I will be carried out at PSI during this summer to study systematically its performance and response to particles (electrons, pions, muons) of the same momenta as they will have in the KLOE experiment.

The main aims of these investigations are to determine:

- the dependence of the space time relation of the cells on the azimuthal angle and on the z-coordinate at which a track crosses the cell;
- the variation in the space time relation along z, revealing the well defined periodicity of the electrostatic configuration in this direction, which has been described above;
- the track finding and reconstruction efficiencies as a function of the azimuthal and polar angles and of the z-coordinate of the tracks.

Some of these investigations will be repeated for different particle momenta and gas mixtures.

For the scanning of the prototype in three dimensions the orientation of the prototype axis relative to the beam axis has to be changed accordingly, which will be done by a motion

controlled table. The table allows translations in the vertical and the horizontal directions and rotations around the chamber and a vertical axis.

9. MONTECARLO STUDY OF DRIFT CHAMBER PERFORMANCE

9.1 Introduction

The main purpose of this study is to analyze the Main Drift Chamber's (D.C.) performance considering different design options, in particular:

- cell size : 2x2 or 3x3 or mixed design

- ratio of field/sense wires : 3:1 or 2:1

The chamber performances to be compared are:

- resolution on single track parameters : P_T , ϕ, θ

- spatial resolution on K_L or $K_S \to \pi^+\pi^-$ decay vertex

- geometrical losses

- track fit and vertex fit losses

- $K_{\mu 3}$ rejection

This study has been performed on various samples of K_L or $K_S \to \pi^+\pi^-$ or $K_{\mu 3}$ events.

The report is divided in 4 sections :

- simulation of the detailed (stereo wires) geometry of the chamber in the MonteCarlo.

- study (using the CERN Garfield package and results from test beam data) of the time to space relations. Preliminary results of chamber resolution with realistic time to space relations are presented.

- results of the track fit and vertex fit.

- $K_{\mu 3}$ rejection.

Since we have not yet fully developed all the necessary algorithms some simplifying assumptions were made in this work :

- the cell efficiency was assumed to be 100 % and we neglected problems from pattern recognition, dead channels, noise in the chamber etc. Moreover the results reported in the last two sections have been obtained using a same linear time-to-space relationship for every drift cell.

- the ionization loss dE/dx of the charged tracks was not taken into account in simulation and fit, neither was the magnetic field inhomogeneity. These effects will add complexity to the algorithms but should not spoil the chamber resolution.

- in the reconstruction of a track there is no attempt to recognize the decay kink of a charged pion : we assume to be able to identify such a kink if the pion track has a minimal length before decay.

9.2 Drift chamber simulation

The standard simulation of the whole KLOE[24] detector is done by the MonteCarlo program Geanfi[25] . However the present version of Geanfi does not have detailed simulation of the wires of the D.C.. Therefore a standalone dedicated program has been developed which takes into account all the details of the stereo geometry as well as the wire thickness and material relevant to the multiple scattering. This code works in the frame of the Geant[26] package and has been written so as to be easily insertable in the standard Geanfi MonteCarlo.

The standard Geant simulation of a number of wires ranging between 5×10^4 and 10^5 is very CPU expensive. Therefore an hybrid solution was chosen that uses both the general package resources and some new dedicated routines written to speed up the code. So the code is a Geant standard code where the Drift Chamber is represented by a "policon" volume filled with the appropriate gas mixture of He-Isobutane. The particles are generated and stored in the Geant bank and tracked traditionally until the track enters the D.C. volume. At this point the dedicated package takes control and propagates the particle inside the chamber. All these new routines use and communicate with the standard Geant data structure (material banks, kinematics bank, etc..) through the usual Geant common block. Also the output information (hit plane, hit wire, drift time etc..) is written out in the format of a Geant hit bank. As soon as the particle leaves the chamber the control is given back to the general package.

The wire geometry is generated by a dedicated routine that considers the chamber made up of layers of stereo wires lying on hyperboloids with constant drop at the z=0 section. Since the layer drop is constant for all layers the stereo angles vary along the layer radius. Two layers of axial guard wires are placed one before the innermost cell layer and one after the outermost cell layer.

The main features of the chamber : dimensions, number of sense wire planes, 3:1 or 2:1 field/sense wire ratio, cell size, stereo waist drop, diameters of the wires, proportion of isobutane-helium mixture, magnetic field, as well as some simulation internal parameters (track step, multiple scattering step,etc) can be modified via data cards. Also implemented is the possibility to have a number of planes with half cell size in the inner region of the D.C. (the so called *mixed geometry*). The present version does not have yet particle energy loss by ionization and uses a constant axial magnetic field. A non homogenous magnetic field can be easily treated by using the corresponding field map in the Geant tracking routine.

A dedicated routine finds the distance of closest approach between the track helix and the nearest sense wire; this distance is converted to a drift time by using the proper time-to-space relationship and a measurement error variable with the drift distance is applied (see also below). However in the present study - if not otherwise mentioned - a linear time-to-space conversion has been used, also a constant measurement error of 200 μm is assumed.

The flow diagram in Fig. 9.1 shows the code layout and summarizes the main duties of the code.

Tracking

In the code the track steps along its trajectory by a step with fixed projection on the $r\phi$ plane. In the step choice care must be taken not to miss a cell when it is crossed near the edge.

To test the choice of different step lengths we used a sample of $K_L \rightarrow \pi^+\pi^-$ events. In table 9.1 is shown the average number of hits per track, for tracks that have a path inside the chamber shorter than 20 meters (2×2 cm^2; 3 : 1 cell geometry) together with the corresponding CPU time per event on a VAX station 4000-90 . A 3 mm transverse step was used.

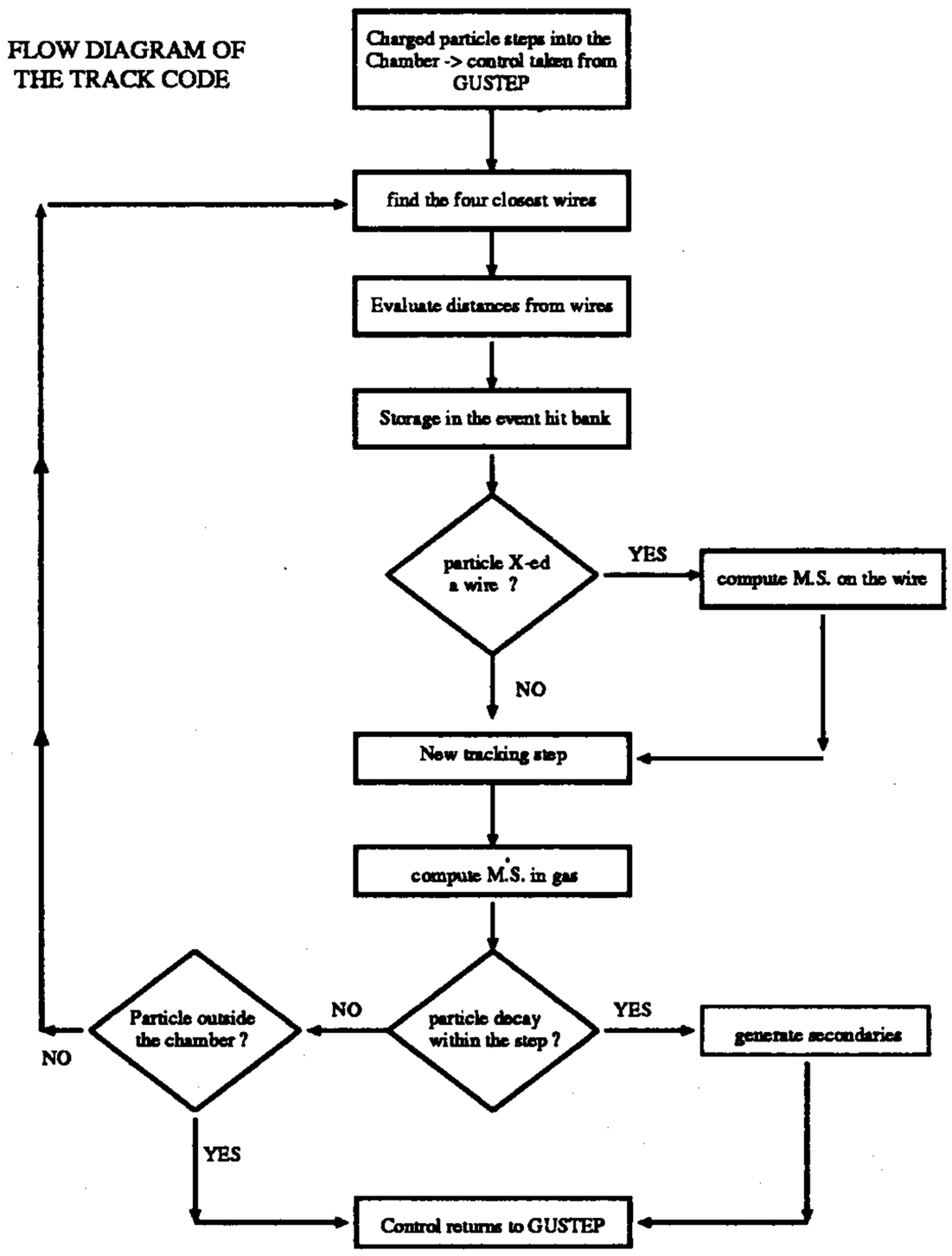

Fig. 9.1. Flow diagram of the dedicated routine of the tracking code

$step_t(mm)$	CPU/event (s)	$< N_{hit} >$/track
7	0.18	93 $\pm$1
5	0.21	95 $\pm$1
3	0.27	97 $\pm$1
1	0.46	101 $\pm$1
0.3	1.06	100 $\pm$1

Table 9.1. Average of hits/track and CPU time for different $step_t$ (2×2 cm^2 cell).

In Fig. 9.2 is shown the M.C. tracking efficiency as a function of the drift distance from the sense wire of the cell for different values of the transverse step size relative to an assumed 100% efficiency for a 300 μm transverse step sample.

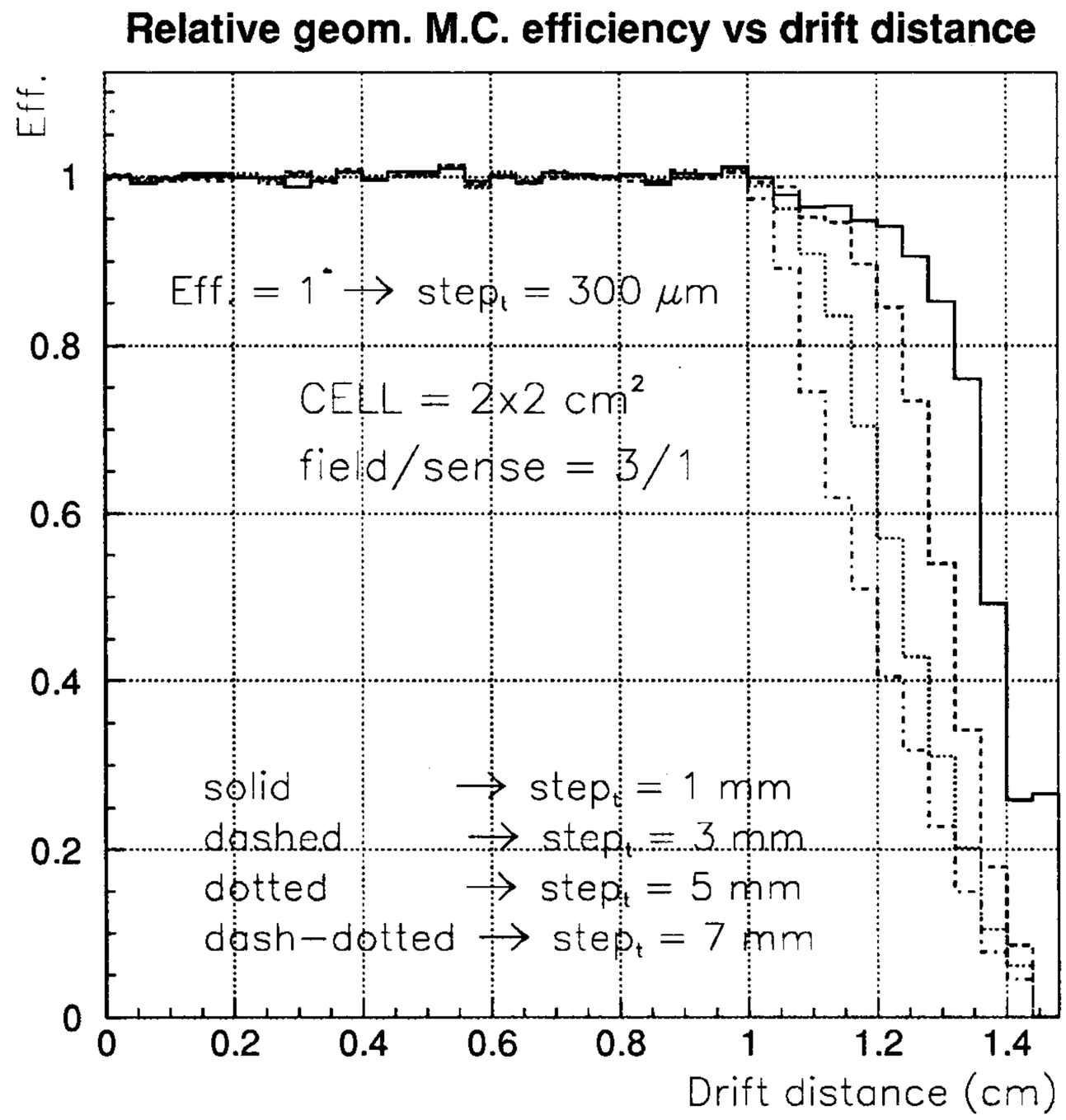

Fig. 9.2. Relative M.C. tracking efficiency vs the drift distance

As expected the only differences are in the regions of long drift distances (longer than the distance between the wires), due to tracks crossing the cell near the edge. We note that such long drift distances imply that the corresponding hits have large probability to be rejected because of low efficiency or bad resolution reasons in any case.

Wire crossings

The very large number of wires in the drift chamber implies a non negligible probability of wire crossing by the track; this is estimated with proper accuracy by using double precision code. In Fig. 9.3 is shown the distribution of the number of wires crossed per track, for K_L or $K_S \to \pi^+\pi^-$ events, for four typical geometries of the drift chamber under study : 2×2 cm^2 and 3×3 cm^2 cells, both with 3:1 and 2:1 ratio of field vs sense wires. The diameters of the wires were assumed to be 25 μm (tungsten sense wires) and 80 μm (aluminium field wires).

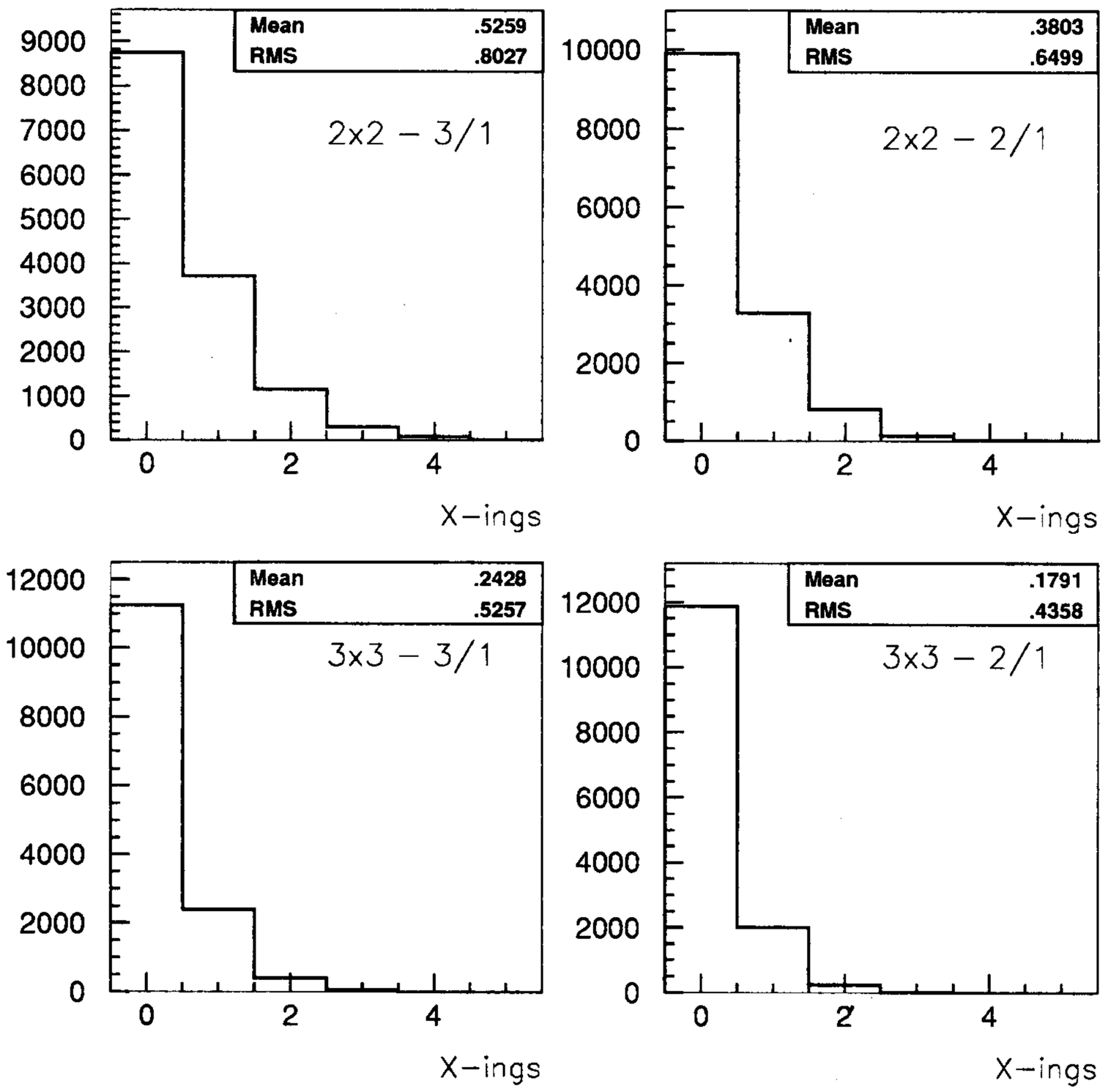

Fig. 9.3. Distribution of the number of wires crossed per track, for track with path in the detector shorter than 2 m. The four D.C. geometries are shown

The corresponding chamber "transparency" , given by the percentage of track that cross no wires at all, is shown in the table 9.2 .

type of cell	% of track with no X-ing	$< X - ing >$/track
$2 \times 2cm^2$; 3:1	62	0.53
$2 \times 2cm^2$; 2:1	70	0.38
$3 \times 3cm^2$; 3:1	79	0.24
$3 \times 3cm^3$; 2:1	85	0.18

Table 9.2. % of tracks with 0 wire X-ing and average wire X-ing/track

Multiple scattering : wires and gas mixture

The multiple scattering (m.s.) suffered by the track is one of the limiting factors of the

momentum resolution of the D.C. The sources of m.s. are the gas mixture itself and the wires crossed along the path. The relative contribution of these two sources are nearly comparable but the scattering induced by the gas is continuously distributed along the track while that due to the wires is concentrated in single, localized events. When a wire crossing is detected the code shifts the Geant pointer to the material bank from gas mixture to the wire material (Al or W). Then m.s. is computed by the usual Geant routine taking into account the finite wire cross section and at the end the pointer is shifted back to the gas mixture.

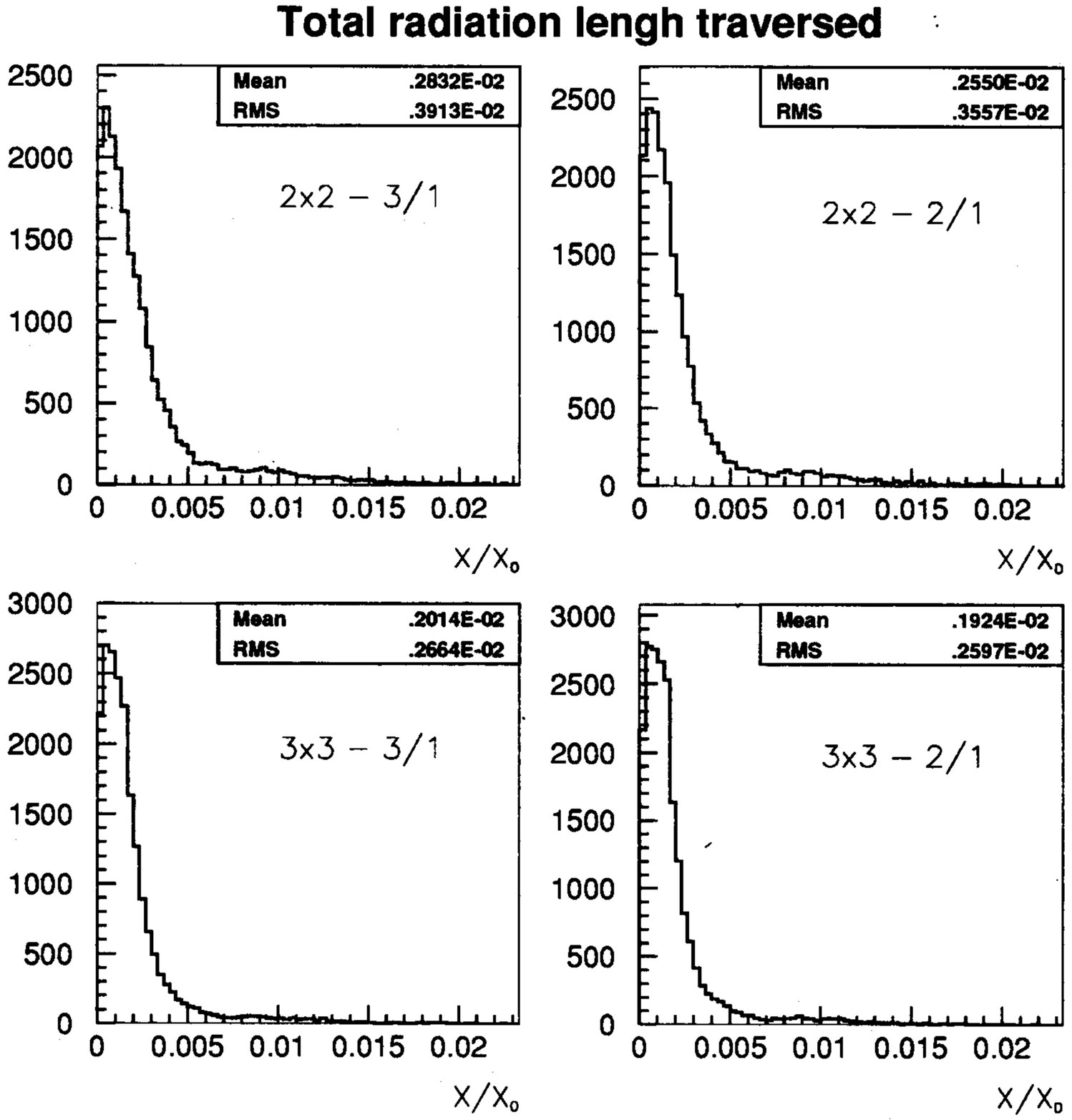

Fig. 9.4. Total radiation length traversed (wire + gas) per track.

In Fig. 9.4 is shown the comparison between the fraction of radiation length travelled per track for the usual D.C. geometries. The distribution of the scattering angle in space due to the crossing of a 25 μm W or 80 μm Al wires is shown in fig. 9.5.

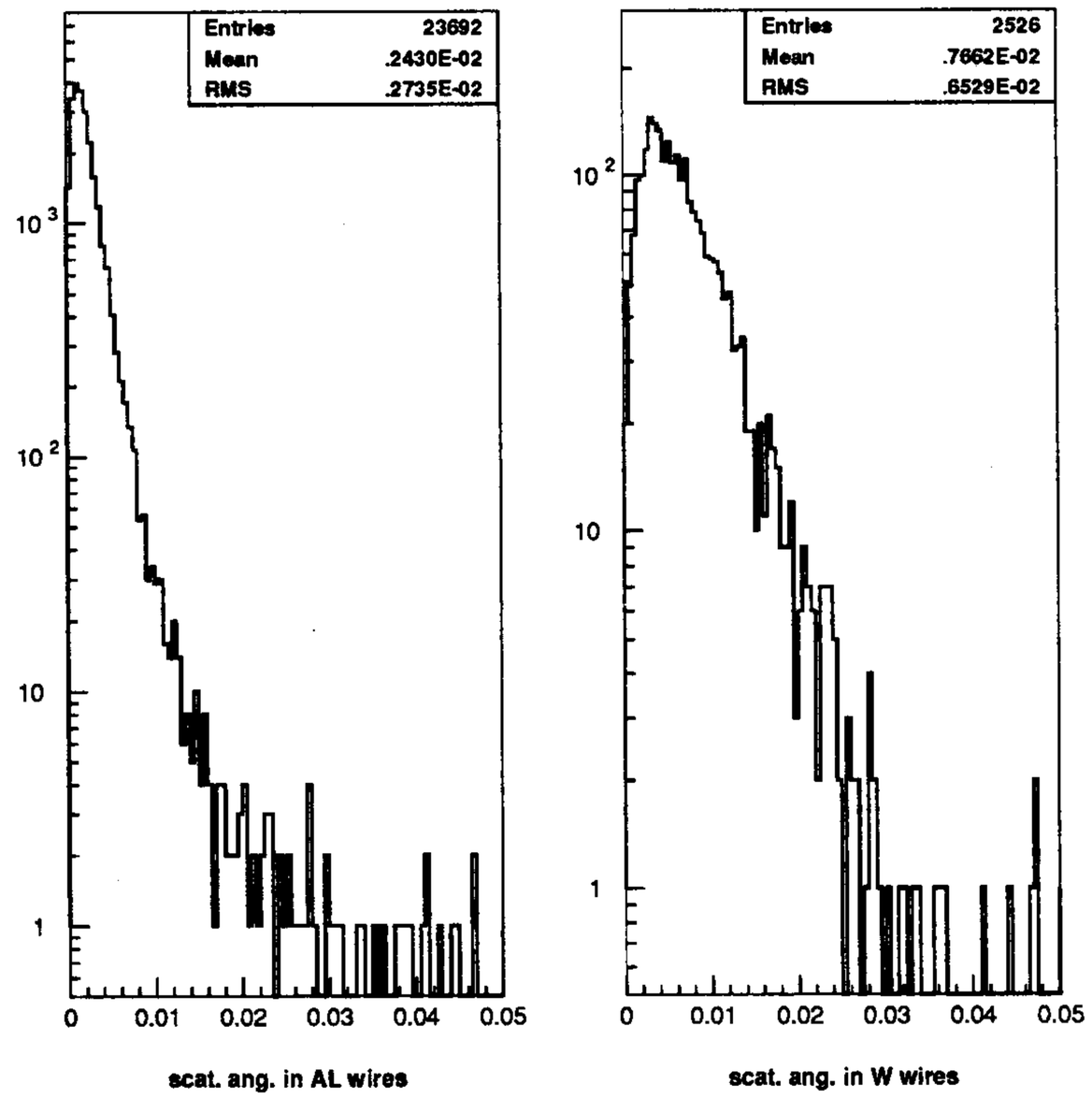

Fig. 9.5. Distribution of the angle in space due to the scattering on the W 20 μm and Al 80 μm wires.

9.3 Cell response parametrization

Cells geometry

Because of the stereo stringing of all wires, the shape of the cells changes along the z axis with a periodicity

$$\Delta z = \frac{\Delta a/2}{|sin(\Theta_s^i - \Theta_s^{i+1})|}$$

where Δa is the cell half size, and the index i runs over the layers of wires.

In the chosen geometry the sense wires have opposite sign (near equal) stereo angle respect the top (bottom) field wire layer of the cell; therefore a different periodicity follows between the upper part ($\Delta z = 5cm$) and the lower part of the cells ($\Delta z \simeq 2L_z$, L_z being the longitudinal dimension of the chamber). Due to the particular geometry inside the chamber, the shape of the cells is a distorted square: the extent to which the square shape of the cell is distorted is a function of the azimuthal direction ϕ, the radius r and the z coordinate of each cell. The cells may be classified according to their shape (in x-y view) using the β_1 and β_2 angles as defined in Fig. 9.6 .

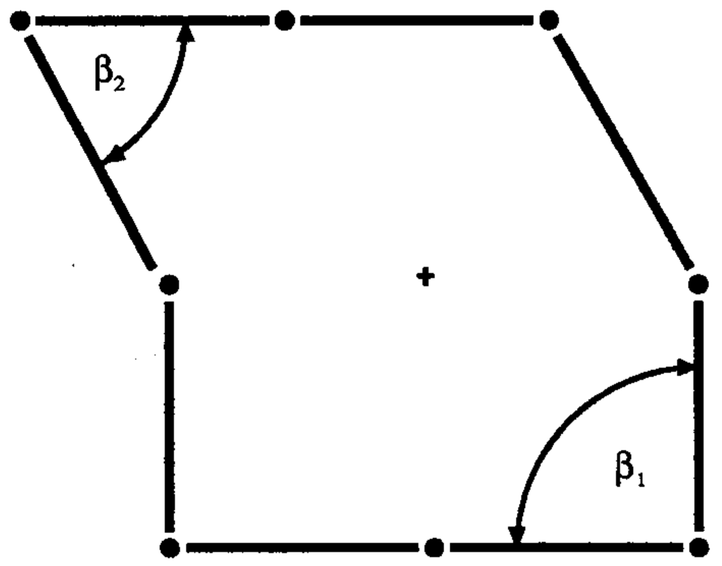

Fig. 9.6. β_1 e β_2 angle

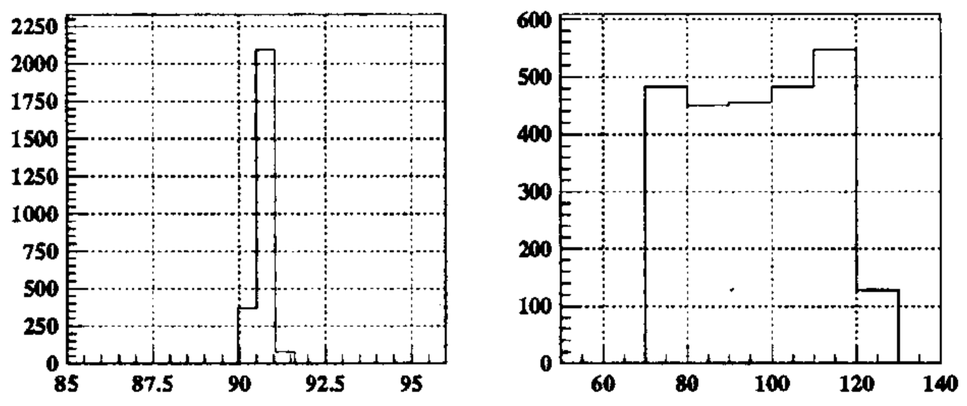

Fig. 9.7. β_1 and β_2 angles distribution (2x2 design).

Figure Fig. 9.7 shows the β_1 and β_2 distributions for cells at plane $z = 0$. Because of the different periodicities between the upper ($\Delta z \simeq 5\ cm$) and the lower part of the cells ($\Delta z \simeq 2L_z$), it follows that the distribution of the β_2 angle does not change with z, while the distribution of the β_1 angle ranges between 86^o and 96^o.

Cell response parametrization

To parametrize the cell response the GARFIELD[27] program developed at the CERN laboratories has been used.

The program needs the following inputs :

- sense and field wire positions
- electrical voltages applied to the wires
- the gas mixture parameters (drift velocity, diffusion coefficient as a function of the electric field, the number of clusters produced by minimun ionizing particles)
- the external magnetic field of the KLOE solenoid.

Then the program follows the drift trajectory of each cluster produced in the cell and returns the (x,y) coordinates of the cluster production point, the drift time, and the drift time corrected because of the diffusion.

The parameters of the gas mixture given as input to GARFIELD have been obtained from the analysis of the data collected at PSI with the two small prototypes 0.1 and 0.2[28] and of the data collected at the cosmic ray setup with prototype 0.[29]

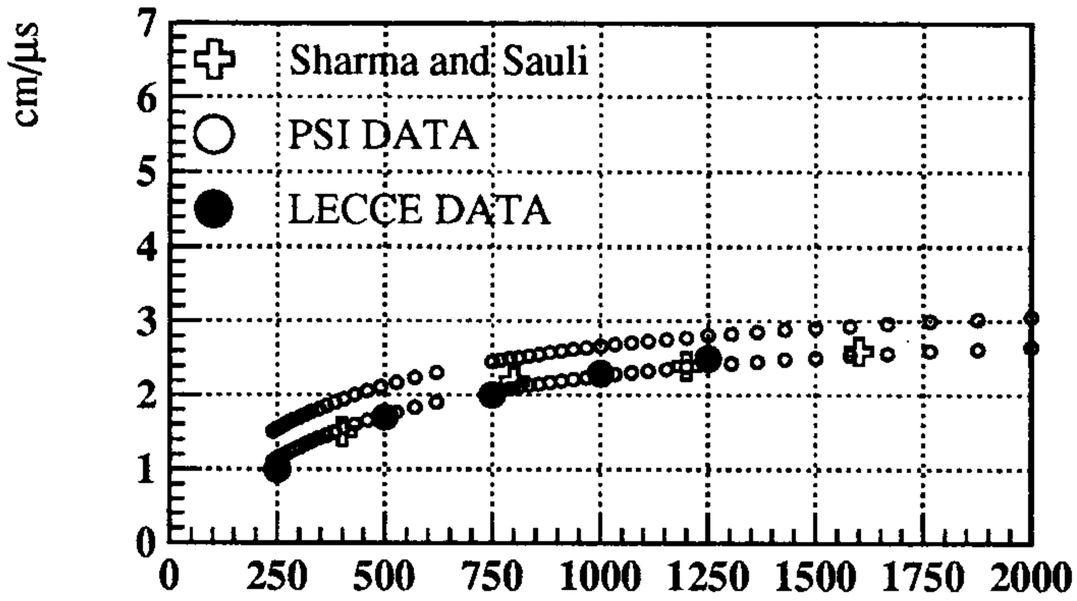

Fig. 9.8. Drift velocity as a function of the electric field
(the width of the band is $\pm 1\sigma$)

In particular the drift velocity v_d as a function of the electric field can be derived from the measured space-time relations. Figure 9.8 shows the v_d behaviour as function of E, it has been obtained from the analysis of the data collected by the prototype 0.1, with the gas mixture $90\%He - 10\%iC_4H_{10}$ without magnetic field . In the figure the measured valued of v_d are compared with the values computed by Sharma and Sauli[18] and with those measured in Lecce[30]

The analysis of the test beam data allows us to separate the different contributions to the cell spatial resolution due to:

- longitudinal diffusion of the electrons
- the ionization statistics of the primary clusters
- the instrumental resolution of the drift time measurement.

The diffusion contribution to the resolution σ_{diff} is given by

$$\sigma_{diff} = \sqrt{\frac{2Dr}{v_d}} = \sqrt{2Kr}$$

In the cell region where the diffusion is important, the electric field variation is sufficiently small to assume that $D/v_d \simeq const. = K$, where D is the diffusion coefficient. K is a parameter to be fitted and the analysis of the data collected by the prototype 0, with the gas mixture $90\%He - 10\%iC_4H_{10}$ gives $K = 7 \times 10^{-5}\ cm$, which implies a diffusion contribution of $\simeq 120\ \mu m$ at 1 cm of drift distance. This number is comparable with the evaluation result given by Sharma and Sauli of about 160 μm.

The contribution to the resolution due to the ionization statistics is given by the variance of the difference Δb between the path b of the closer released electron and the distance of minimun approach between the track and the wire: $b - \sqrt{b^2 - x^2}$, where x is the point along the track where it has been released the cluster closer to the wire. The x distribution is exponential $f(x) = 1/\lambda e^{-x/\lambda}$, and 2λ is the average distance between two primary ionization acts. λ is also a parameter to be fitted, and the data analysis yields $\lambda \simeq 380\ \mu m$.

Garfield simulation results

The measured gas mixture parameters were input to GARFIELD to simulate the crossing of the tracks through cells 2×2 *cm* with $\mathcal{R}_{fs}$= 3:1 and $\mathcal{R}_{fs}$= 2:1 and cells 3×3 *cm* with $\mathcal{R}_{fs}$= 3:1. For each cell design several cells of different shape were simulated. The magnetic field of the KLOE solenoid was assumed to be 6 Kgauss. Figure 9.9 shows the result of the simulation of the crossing of about 15000 tracks through cells 2×2 *cm* with $\mathcal{R}_{fs}$=3:1 and $\beta_1 \simeq \beta_2 \simeq 90^o$. The black points that fill the figure represent the starting points of all those clusters that are collected by the sense wire of the cell; so to give the map of the effective sensitive area of the cell.

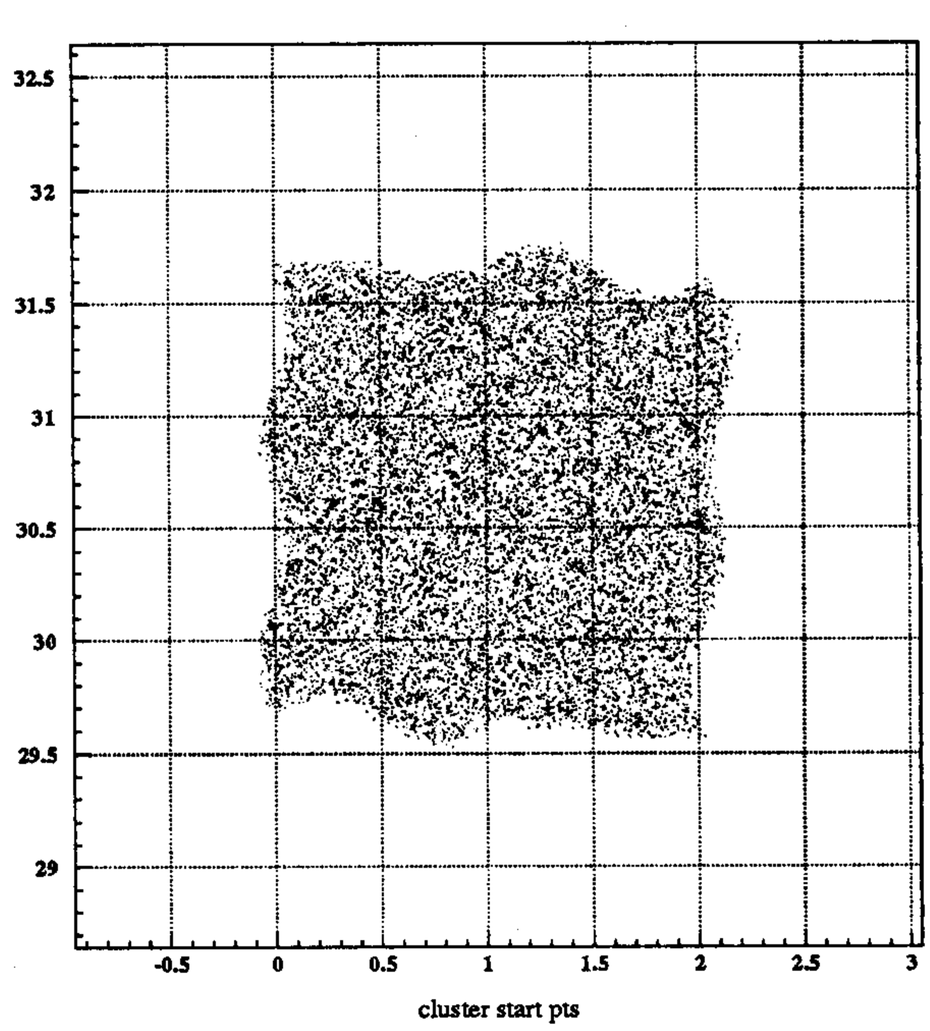

Fig. 9.9. Clusters start points (2x2, 3:1 design).

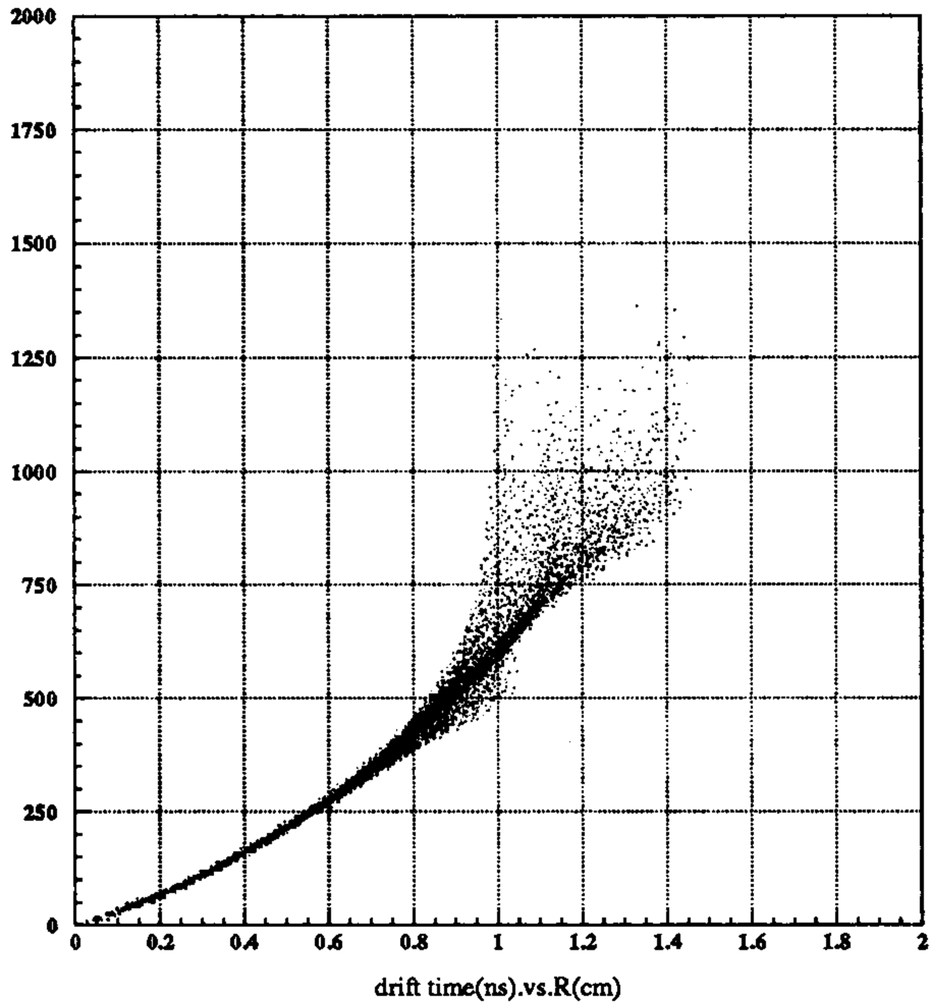

Fig. 9.10. Space time relation: cell 2×2 *cm* with $\mathcal{R}_{fs}$= 3:1

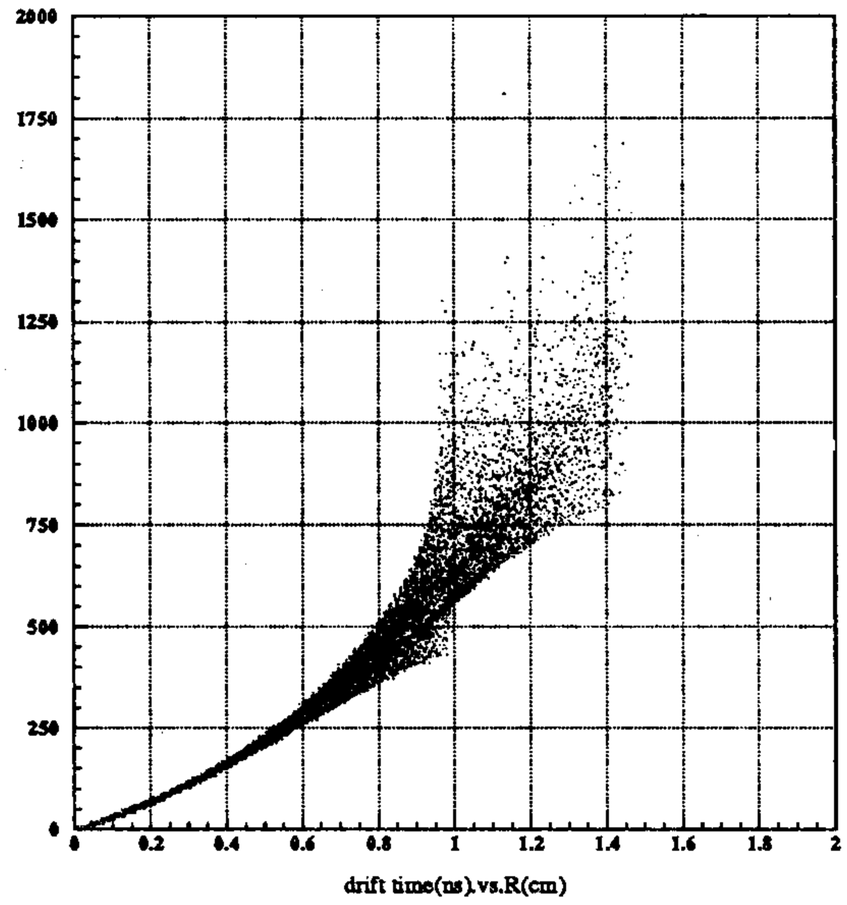

Fig. 9.11. Space time relation: cell 2×2 *cm* with $\mathcal{R}_{fs}$= 2:1

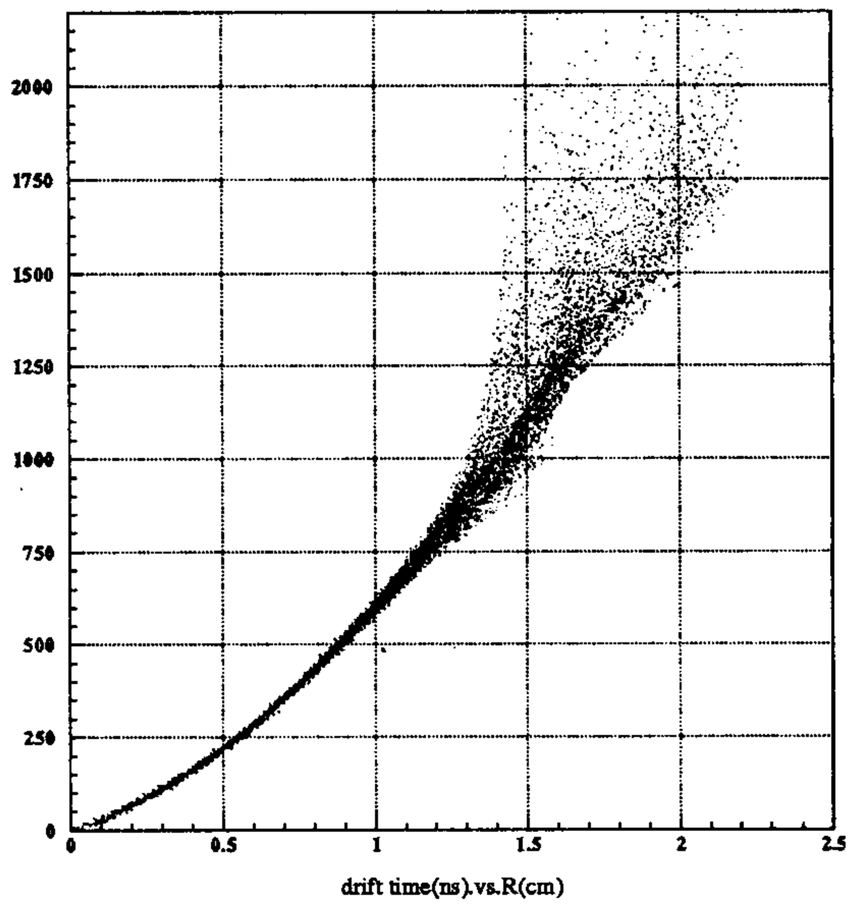

Fig. 9.12. Space time relation: cell 3×3 cm with $\mathcal{R}_{fs}$= 3:1

Figures 9.10, 9.11 and 9.12 show the space-time relations for 3 different cell designs. The figures make clear that to parametrize the cell response over the greatest possible extent of the collecting area, it is necessary to correct for the ϕ dependence of the space-time relations in the region of large impact parameters where the effects due to the distorted electric field and to the magnetic field are more important.

To this scope the cell was divided in 36 $\phi - sections$, each one 10^o wide and in each one the Garfield results were fitted to a polynomial time to space relationship using the third order Chebychev polynomials :

$$t_d = U_1 + U_2(2a-1) + U_3(8a^2 - 8a + 1) + U_4(32a^3 - 48a^2 + 18a - 1)$$

with $0 \leq a \leq 1$, $a = \frac{r}{r_{limit}}$ and r_{limit} is the radius at which the R.M.S. of the reconstructed clusters starting points becomes greater than 500 μm . The parameter r_{limit} defines a sort of effective cell radius within which the fit procedure is able to produce a good parametrization of the space-time relations. r_{limit} varies around a mean value $\simeq$ 80% of the maximum drift distance $\simeq \Delta a\sqrt{2}$ where Δa is half cell size: the shape of the effective cell is close to a square and its area is about 90% of the geometric area of the cell.

Studying the accuracy of the parametrization versus the angles β_1 and β_2 one finds that only six different parametrizations are enough to describe all possible cell shapes. The choice is to keep β_1 fixed $\simeq$ 90 degrees and use six different values of β_2 (from 70 to 120 degrees): in fact with this approximation the standard deviations worsen only by a few per cent. The accuracy of the parametrization for the 3 different cell designs is shown in table 9.3 . The results are shown both for the whole cell (effective) size or only the central region $0.2 \leq r \leq 50\%(\Delta a\sqrt{2})$ cm, and both with or without the diffusion effect.

				$0.2 \leq r \leq 50\%(\Delta a\sqrt{2})$ cm	
size	$\mathcal{R}_{fs}$	$\sigma_{fit}(\mu m)$	$\sigma_{diff}(\mu m)$	$\sigma_{fit}(\mu m)$	$\sigma_{diff}(\mu m)$
2×2	3:1	35.4 ± 0.5	84.9 ± 0.7	21.2 ± 0.2	65.0 ± 0.6
2×2	2:1	46.6 ± 0.7	86.6 ± 0.8	26.1 ± 0.4	65.3 ± 0.7
3×3	3:1	58.3 ± 0.7	108.2 ± 0.9	39.5 ± 0.5	85.4 ± 0.8

Table 9.3. Resolution as a function of cell designs

Implementation in the Montecarlo program

New routines have been added to the standard MonteCarlo code Geanfi to implement the parametrization of the cell response. One routine gets the shape (that is the β_2 angle) of the crossed cell from the position in space of the track segment. Another routine computes the drift time from the distance of minimum approach of the track respect to the sense wire. Here a correction must be made for the finite ionization statistics of the primary clusters. Because of this effect the distance of minimum approach is systematically less then the drift distance covered by the first cluster that reaches the sense wire; the correction is more important closer to the wire. After this correction the program adds the contribution due to the diffusion, and finally, given the shape of the cell (β_2), it assigns the correspondent cell response parametrization to calculate the drift time. At the moment the parameters are stored in one DATA BLOCK as 5 matrices : U1(6,36), U2(6,36), U3(6,36), U4(6,36) and rl(6,36) (6 is the number of different β_2 angles and 36 is the number of $\phi - sections$). Finally, the routine adds the contribution to the resolution due to the instrumental resolution of the drift time measure: $\sigma_e \simeq 5\ ns$. Figure 9.13 shows the predicted spatial resolution : the full curve represents a fit with $K = 0.67 \times 10^{-4}\ cm$, $\lambda = (0.377 \pm 0.002) \times 10^{-1}\ cm$ and $\sigma_e = (5.1 \pm 0.4)\ ns$, with $\chi^2/NDOF \simeq 1.8$.

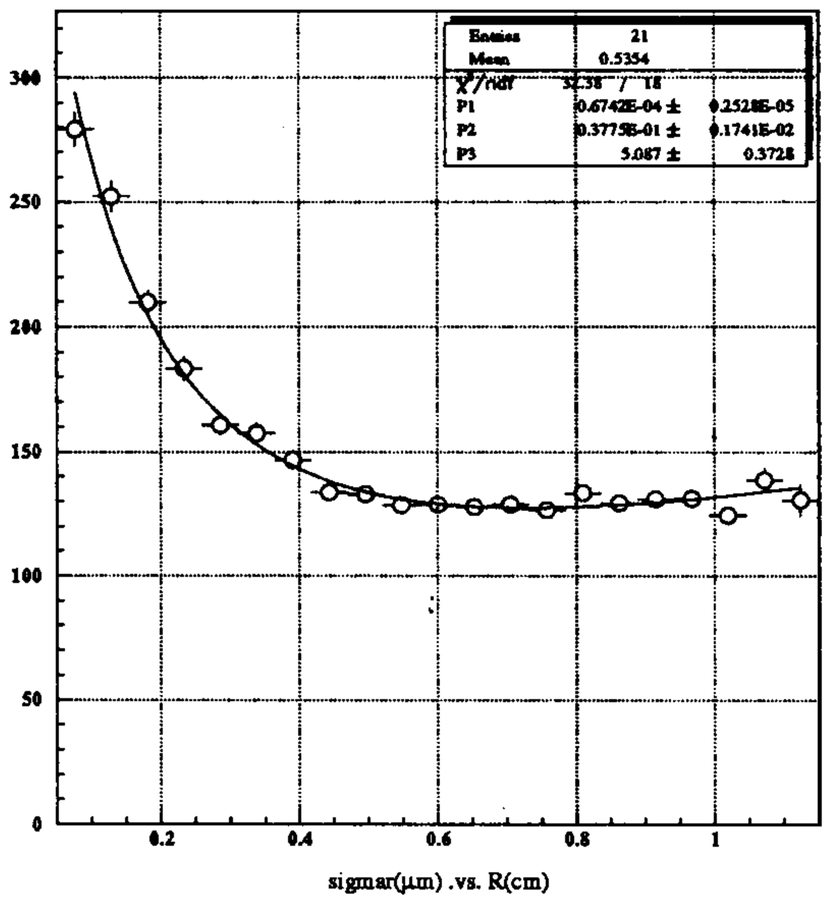

Fig. 9.13. Resolution curve predicted by Garfield

Implementation in the reconstruction program

The detailed time-space relations cannot be used when beginning the pattern recognition because at this stage the space reconstruction of the track is still lacking. Therefore to start the pattern recognition a properly averaged time-space relation is used, where the drift distance is function of the drift time only (and not also of ϕ). The accuracy of the average time to space relations are $\simeq$ 210 μm (2 $\times$ 2 cm, $\mathcal{R}_{fs}$=3:1 design), $\simeq$ 300 μm (2 $\times$ 2 cm,$\mathcal{R}_{fs}$=2:1 design) and $\simeq$ 230 μm (3 $\times$ 3 cm,$\mathcal{R}_{fs}$=3:1 design). Afterwards at the stage of the track fit the detailed time-space relations are used. These have been implemented for three cell designs : (2$\times$2 cm,$\mathcal{R}_{fs}$=2:1),(2$\times$2 cm,$\mathcal{R}_{fs}$=3:1) and (3$\times$3 cm,$\mathcal{R}_{fs}$=3:1). During the iteration procedure, points along the track that are outside the effective area of the cell are reconstructed using the averaged time-space relation and the corresponding σ. Only at the last iteration the points outside the effective area are rejected. The percentage of the rejected points for all the analysed cell designs is about 10%, as expected since the ratio between the effective and the full cell area is about 90%.

The Montecarlo program was used to generate and then fully reconstruct three samples of events $K_L \rightarrow \pi^+\pi^-$, each for the three different cell designs. In tables 9.4 , 9.5 and 9.6 are compared the resolutions on track fit parameters and on $K_L$decay vertices, obtained with average and with detailed time space relations. The results show the importance of using the detailed time to space relation: it improves the resolution up to a factor one and a half, especially for the cells (2 $\times$ 2 cm,$\mathcal{R}_{fs}$=2:1) which have an open electric field configuration, and for the cells (3 $\times$ 3 cm,$\mathcal{R}_{fs}$=3:1).

	Raw Time→ space	Time→ space relations
$(P_T^{fit} - P_T)/P_T$	$(0.38 \pm 0.02) \times 10^{-2}$	$(0.39 \pm 0.02) \times 10^{-2}$
$\phi_{fit} - \phi$	$4.3 \pm 0.2\, mrad$	$3.9 \pm 0.2\, mrad$
$\phi_{(vertex-fit)} - \phi$	$1.9 \pm 0.1\, mrad$	$1.9 \pm 0.1\, mrad$
$cot(\theta)_{fit} - cot(\theta)$	$(3.6 \pm 0.2) \times 10^{-2}$	$(3.3 \pm 0.1) \times 10^{-2}$
$X_{vertex}^{fit} - X_{vertex}$	$498 \pm 43\, \mu m$	$420 \pm 35\, \mu m$
$Y_{vertex}^{fit} - Y_{vertex}$	$452 \pm 31\, \mu m$	$416 \pm 32\, \mu m$
$Z_{vertex}^{fit} - Z_{vertex}$	$0.14 \pm 0.01\, cm$	$0.10 \pm 0.01\, cm$

Table 9.4. Cells 2 × 2 cm with $\mathcal{R}_{fs}$= 3:1

	Raw Time→ space	Time→ space relations
$(P_T^{fit} - P_T)/P_T$	$(0.41 \pm 0.02) \times 10^{-2}$	$(0.36 \pm 0.02) \times 10^{-2}$
$\phi_{fit} - \phi$	$4.3 \pm 0.3\, mrad$	$3.2 \pm 0.2\, mrad$
$\phi_{(vertex-fit)} - \phi$	$2.4 \pm 0.1\, mrad$	$1.8 \pm 0.1\, mrad$
$cot(\theta)_{fit} - cot(\theta)$	$(4.2 \pm 0.3) \times 10^{-2}$	$(3.6 \pm 0.1) \times 10^{-2}$
$X_{vertex}^{fit} - X_{vertex}$	$596 \pm 63\, \mu m$	$399 \pm 32\, \mu m$
$Y_{vertex}^{fit} - Y_{vertex}$	$712 \pm 62\, \mu m$	$508 \pm 59\, \mu m$
$Z_{vertex}^{fit} - Z_{vertex}$	$0.23 \pm 0.02\, cm$	$0.12 \pm 0.01\, cm$

Table 9.5. Cells 2 × 2 cm with $\mathcal{R}_{fs}$= 2:1

	Raw Time→ space	Time→ space relations
$(P_T^{fit} - P_T)/P_T$	$(0.38 \pm 0.02) \times 10^{-2}$	$(0.33 \pm 0.02) \times 10^{-2}$
$\phi_{fit} - \phi$	$4.3 \pm 0.2\, mrad$	$2.7 \pm 0.1\, mrad$
$\phi_{(vertex-fit)} - \phi$	$2.2 \pm 0.1\, mrad$	$1.8 \pm 0.1\, mrad$
$cot(\theta)_{fit} - cot(\theta)$	$(4.2 \pm 0.2) \times 10^{-2}$	$(3.4 \pm 0.1) \times 10^{-2}$
$X_{vertex}^{fit} - X_{vertex}$	$606 \pm 41\, \mu m$	$437 \pm 90\, \mu m$
$Y_{vertex}^{fit} - Y_{vertex}$	$506 \pm 49\, \mu m$	$376 \pm 26\, \mu m$
$Z_{vertex}^{fit} - Z_{vertex}$	$0.19 \pm 0.01\, cm$	$0.12 \pm 0.01\, cm$

Table 9.6. Cells 3 × 3 cm with $\mathcal{R}_{fs}$= 3:1

Charged track reconstruction and initial assumptions

The current version of the charged track reconstruction program[31] is based on the ARGUS track fit algorithm[32]

The input for this program is a set of wires positions and drift distances from track to wires for each track. The information actually measured in a drift chamber are drift times which are transformed to drift distances by means of time–space relations. Practically all results presented in this note were obtained using perfect time–space relations (preliminary results using realistic time to space relations are reported in the previous section). In other words, we assumed that we know the drift distance anywhere inside cells, with a constant accuracy of $\sigma_{r,\phi}$=200 μm. Another important assumption was that, before starting the track fitting, the pattern recognition has succeeded in:

- grouping the measurements assigned to particular track candidates,
- ordering the measurements for each track according to increasing path length from the found starting point, and
- resolving the left–right ambiguities at each wire.

The pattern recognition is assumed to be perfect, i.e. it is 100% efficient in achieving its goals (preliminary results on realistic pattern recognition are reported further below).

The ARGUS track fit algorithm is a least–squares fit which finds a set of track parameters by minimizing χ^2-function, based on drift distances to hit wires. The parameter set used in the ARGUS track fit algorithm to describe particle trajectory is the following:

k – curvature of the helix (inverse of its bending radius);

d_0 – distance between the origin and the reference point (the reference point was chosen to be the point of closest approach to the first hit wire), measured in $x-y$-plane;

ϕ_0 – azimuthal angle of the track tangent at the reference point;

z_0 – z-coordinate of the reference point;

$\cot\theta$ – cotangent of the angle the track makes with respect to the z-axis.

From this parameter set one can see that the minimal number of measurements (or hit wires) for track to be reconstructable in space is 6. These 6 hits cannot lie on the same cell layer: in fact a z measurement requires that the track crosses two consecutive layers with opposite stereo angles. Two z measurements are necessary to determine $\cot\theta$ and z_0; therefore in general 3 layers (or only 2 in particular cases) are required. The tracks which do not satisfy these two requirements are called hereafter as short tracks. The 6 hits cutoff produces an event loss of about 1 - 2.5 % depending on the chamber design (see below).

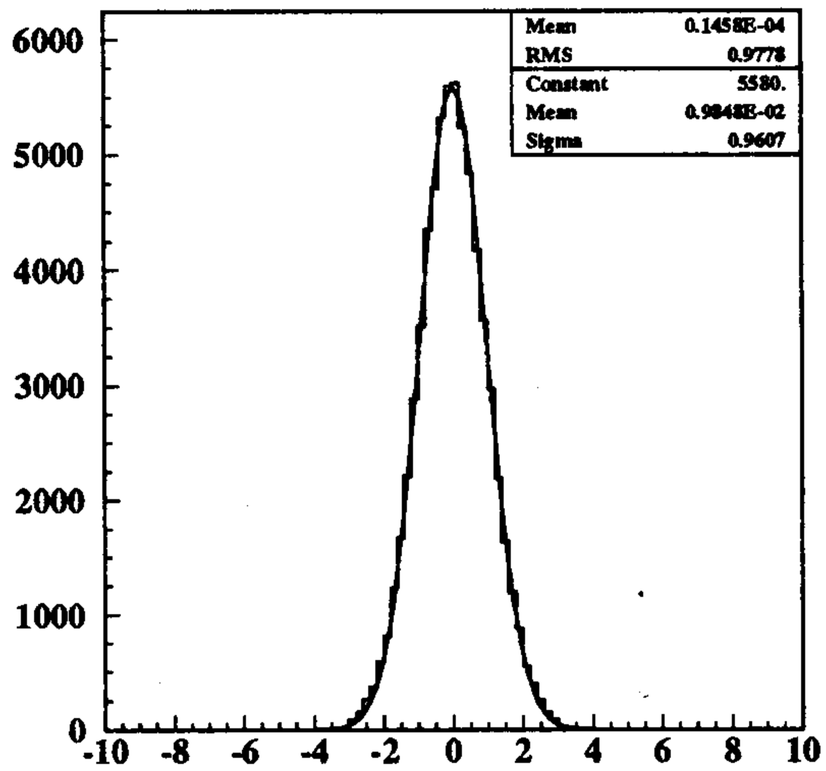

Fig. 9.14. Residuals in the units of drift distance error. Curve is a result of gaussian fit.

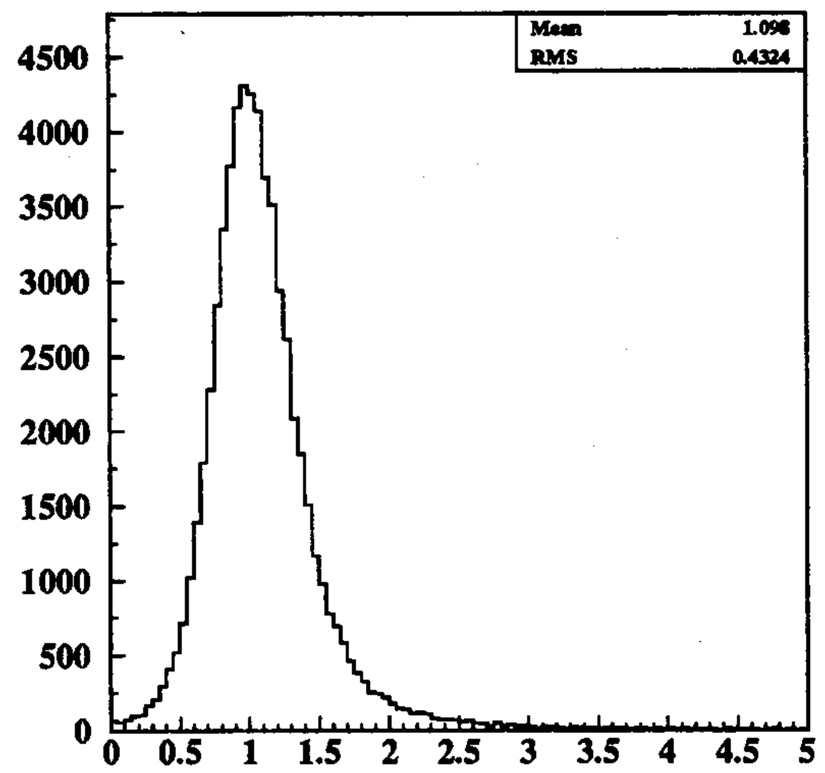

Fig. 9.15. $\chi^2/\mathrm{N}_{d.f.}$

The track fit algorithm is quite suitable for our purposes; the event losses due to algorithm failures (mainly due to tracks with few hits) amount to about 0.3%. As an example, figures 9.14 and 9.15 show distributions of the track fit residuals and $\chi^2/\mathrm{N}_{d.f.}$ of the π from $K_L \to \pi^+\pi^-$ decays for one of the chamber designs. As one can see from this figure the track fit residuals are essentially gaussian distributed and the $\chi^2/\mathrm{N}_{d.f.}$ distribution is correctly centered at 1.

The reconstruction efficiency depends also on the choice of the fiducial volume (f.v.). The optimization of the boundaries of the fiducial volume for $K_L \to \pi^+\pi^-$ events had already been studied[31] for some chamber designs. In general we choice the upper radius of f.v. to be 175 cm and the lower one to begin after the 6 innermost cell layers. The z boundaries of the f.v. are taken to be at 50 cm distance from the chamber endcaps. The dependence of the reconstruction

efficiency on the inner boundary of the fiducial volume has also been studied and is shown below.

Another important point is how to treat $\pi \rightarrow \mu$ decays. μ's from such decays will deteriorate the parameters of the helix if their hits are treated as those of the pion's. The reconstruction efficiencies and experimental resolutions have been studied in two cases of the $\pi \rightarrow \mu$ decay kinks treatments. In one case we assume that we cannot recognize these kinks and we used π's and μ's hits together as pion's hits. It is the most pessimistic estimate. In the second case we assumed that we can recognize 100% $\pi \rightarrow \mu$ decay kinks for the pions which have more 8 hits before decaying. This case is quite realistic and it relies on estimates of some algorithms which have 98% efficiency of $\pi \rightarrow \mu$ kink recognitions for pions from K_L decays.

Track fit, effect of multiple scattering on wires

In the track fit up to 127 points or a maximum track length of 150 cm are input to the fitting routine. Two "mixed" chamber designs with base cells of size 2cm (2×2) and 3cm (3×3) were studied in two cases of $\mathcal{R}_{fs}$ (2:1 and 3:1). The field wires are supposed to be 80 μm in diameter of aluminum and the sense wires - 25 μm in diameter of tungsten. The gas is a mixture of 90% He and 10% iso-C_4H_{10}. We quote in table 9.7 the resolutions (σ of gaussian fit) for P_T, ϕ and cotθ.

Chamber design	2×2	3×3
$(P_T^{fit}\text{-}P_T)/P_T$, (%)	0.39 ± 0.02	0.35 ± 0.02
$\phi^{fit} - \phi$, (mrad)	1.78 ± 0.01	1.67 ± 0.01
$(\cot\theta)^{fit} - \cot\theta, (\times 10^{-3})$	3.60 ± 0.02	3.70 ± 0.02
$M_{\pi\pi}^{fit}$- $M_{\pi\pi}$,(MeV)	1.17 ± 0.01	1.10 ± 0.01

Table 9.7. Experimental resolutions of 2×2 and 3×3 "mixed" designs with $\mathcal{R}_{fs}$=3:1

Figures 9.16 and 9.17 show the behaviour of the P_T and $M_{\pi\pi}$ resolutions obtained keeping fixed the measurement error and increasing the material inside the chamber (vacuum, gas only, gas + wires 2:1, gas + wires 3:1).

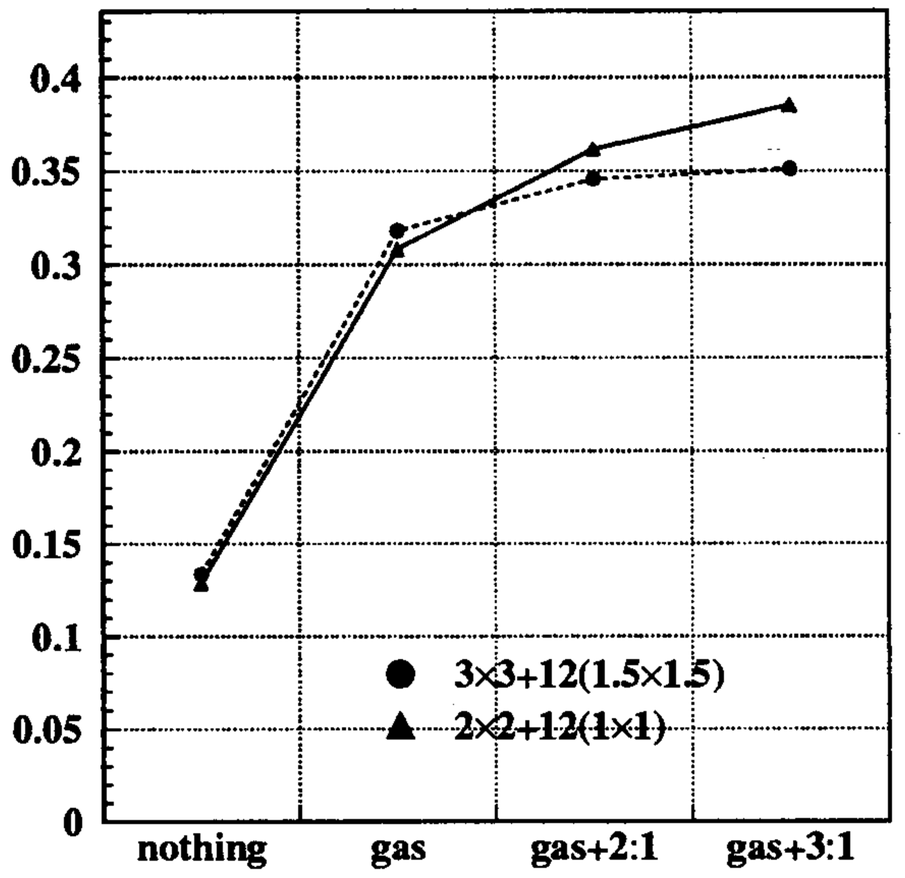

Fig. 9.16. σ of $(P_T^{fit} - P_T)/P_T$, (%)

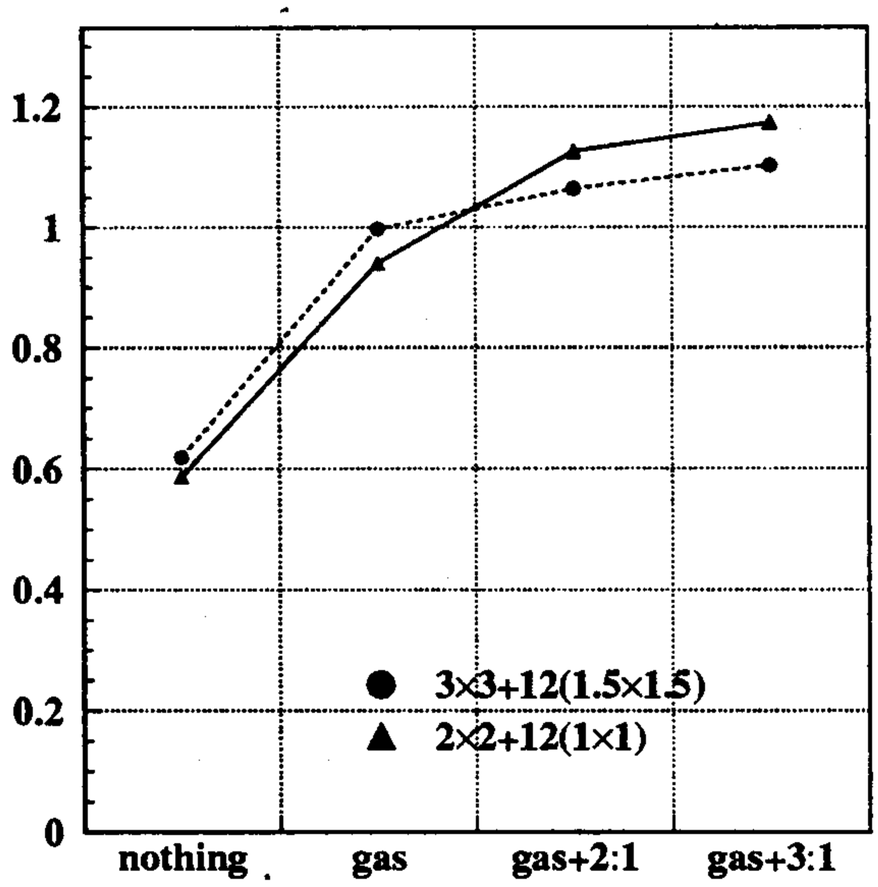

Fig. 9.17. σ of $M_{\pi\pi}^{fit} - M_{\pi\pi}$, (MeV)

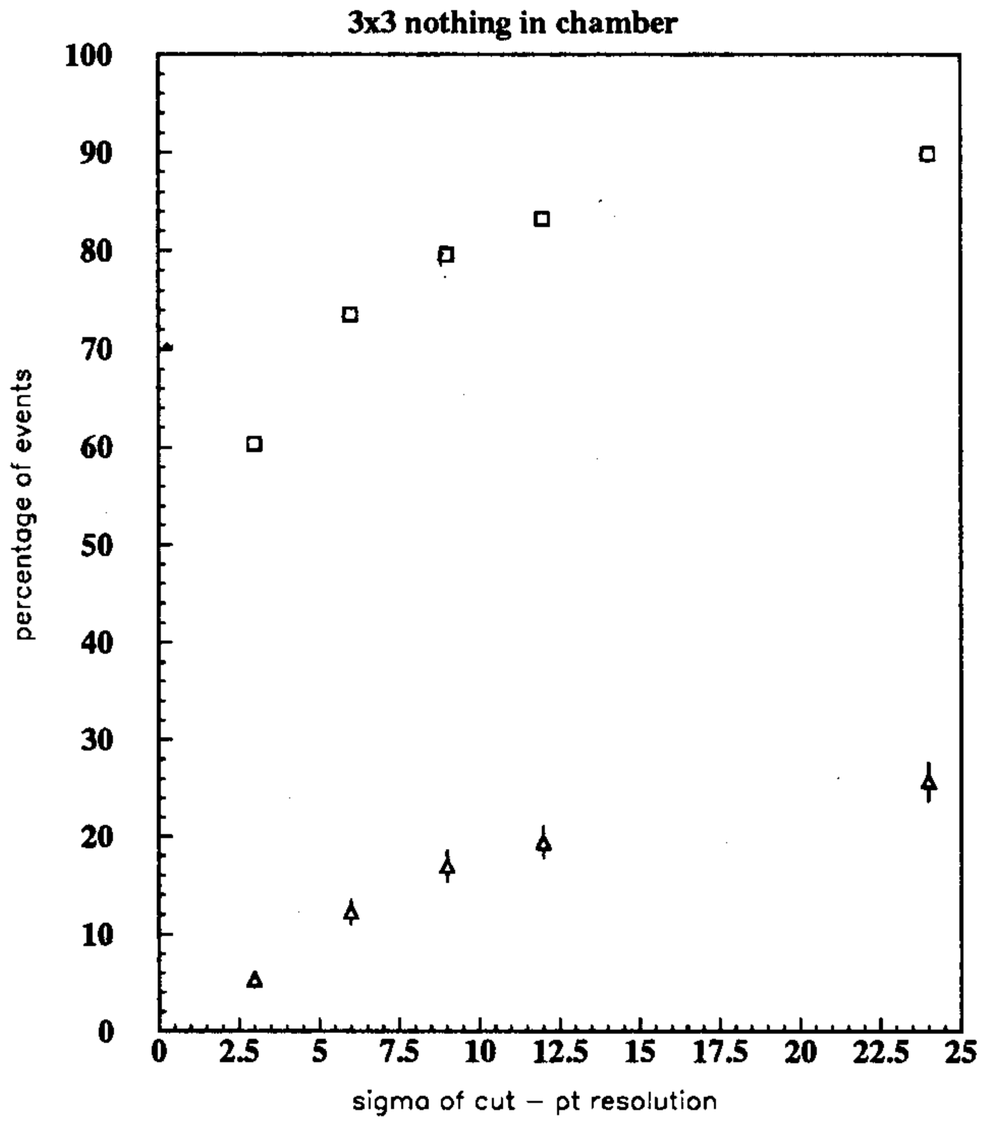

Fig. 9.18. $(P_T^{fit} - P_T)/P_T$, (%). Curve is a result of gaussian fit

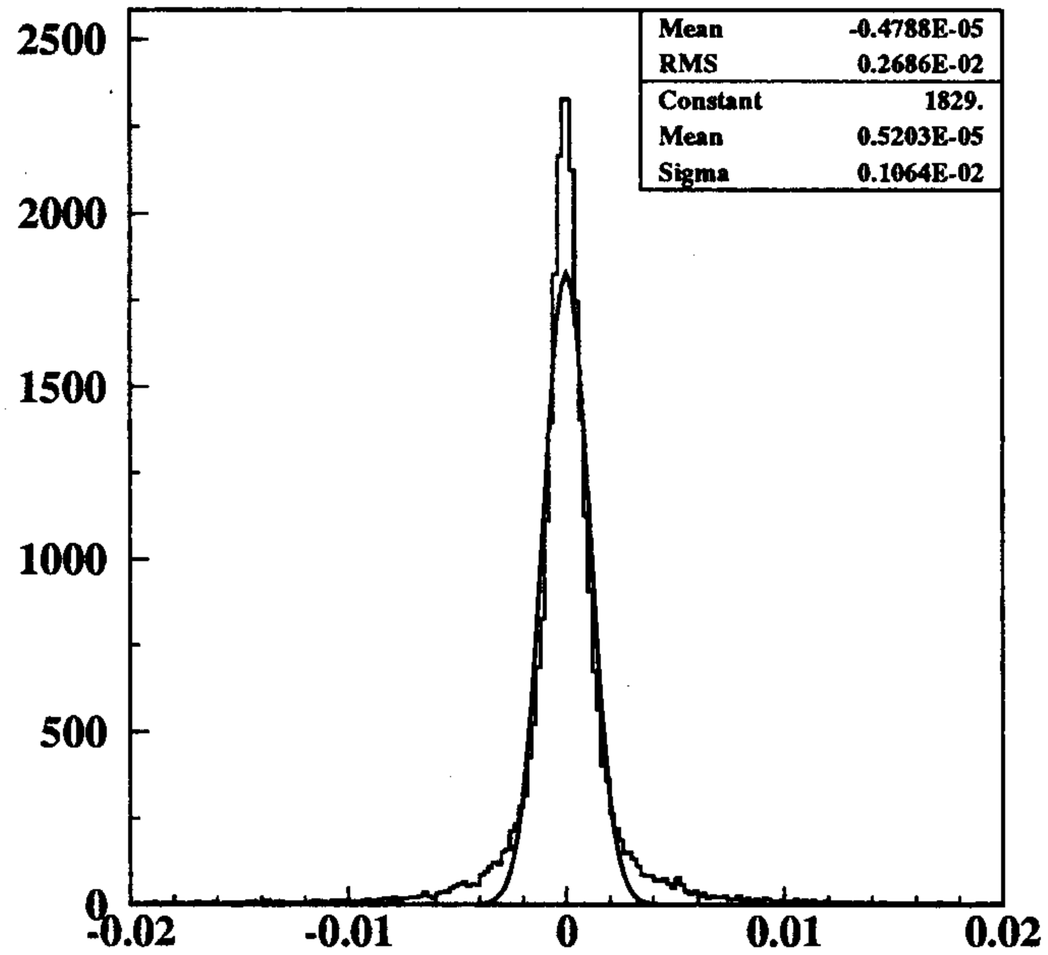

Fig. 9.19. $M_{\pi\pi}^{fit} - M_{\pi\pi}$, (MeV). Curve is a result of gaussian fit

The results show the relative importance of the measurement error alone respect to the effect of the multiple scattering due to the gas. On the other hand the addition of the wires seems not to degrade too much the experimental resolutions. In the most sensitive case with respect to this effect, the $\mathcal{R}_{fs}$=3 the 2×2 design has the resolutions worsened, at maximum, by 10% more than 3×3 one.

Fig. 9.18 and 9.19 show the P_T and $M_{\pi\pi}$ distributions for 3×3 "mixed" design with $\mathcal{R}_{fs}$=3:1. These distributions do not exhibit perfect gaussian behaviour and show some tails essentially because we are adding up tracks of different length from all K_L decays. For instance, for 2×2 design with $\mathcal{R}_{fs}$=3:1 only 73.7% of tracks appear to be within simultaneous 3σ limit of P_T, ϕ and cotθ. A closer look at the tracks outside the 3σ limits lead to the conclusion that there are two main contributions to these tails: first are the tracks moving almost parallel to the z-axis ($|\cos\theta| > 0.8$), fig 9.20(b), *i.e.* the tracks with very small P_T and very large curvature. Secondly, short tracks with $|\cos\theta| < 0.8$ which originate near the fiducial volume boundary, fig 9.21(b), and whose momentum vector points outwards of this volume, fig 9.22(b). Angle ψ on the fig 9.22 is the angle between radius vector and particle momentum in $x-y$-plane.

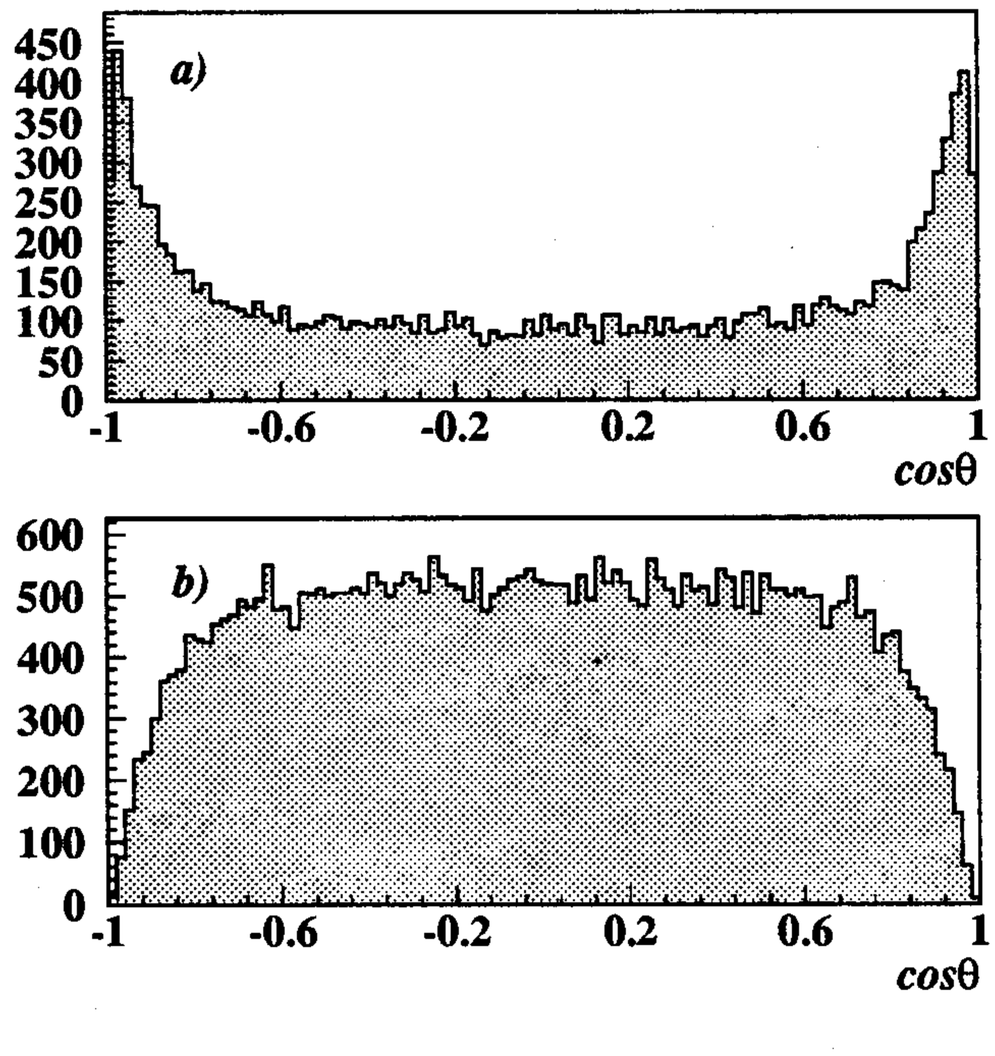

Fig. 9.20. cosθ -distribution of events a) outside and b) inside common 3σ limit of P_T, ϕ and cotθ

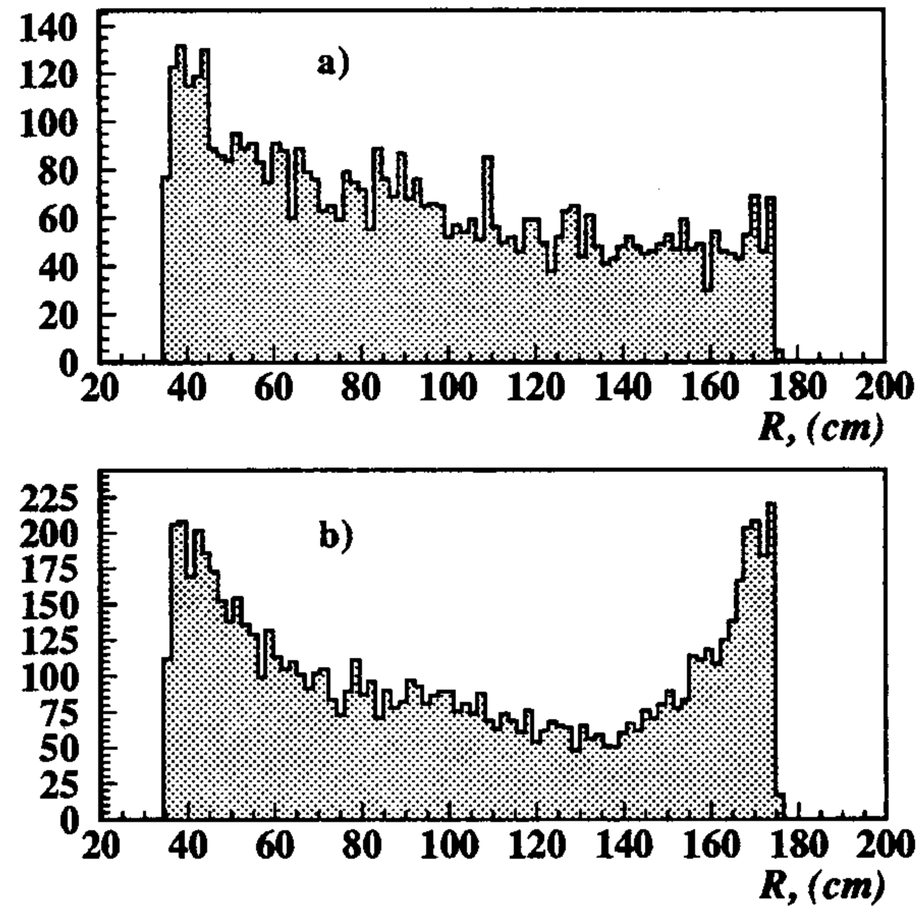

Fig. 9.21. Distribution of the radius of the K_L^0 decay points for events outside common 3σ limit of P_T, ϕ and $\cot\theta$. (a) $|\cos\theta| > 0.8$, b) $|\cos\theta| < 0.8$)

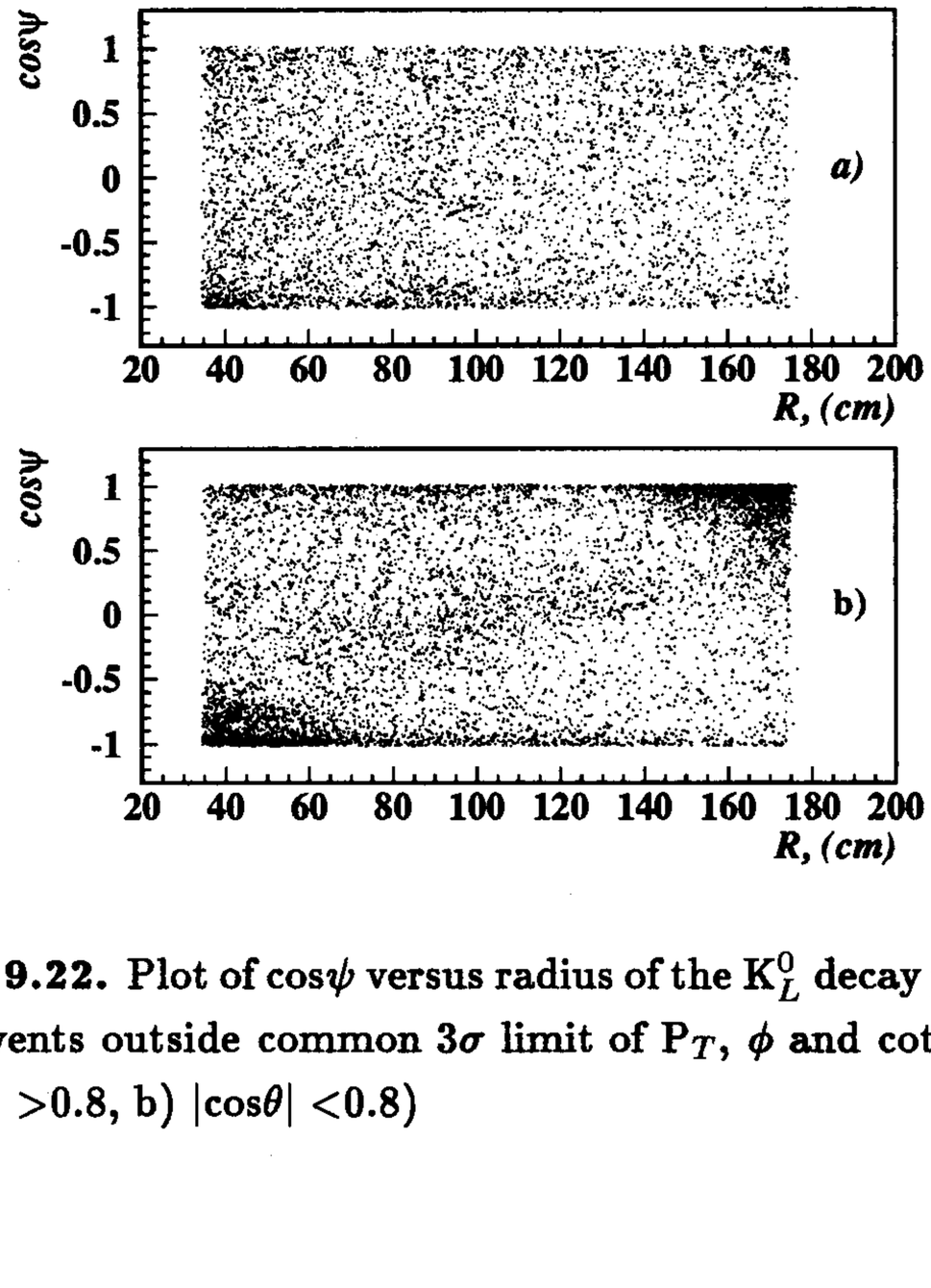

Fig. 9.22. Plot of $\cos\psi$ versus radius of the K_L^0 decay points for events outside common 3σ limit of P_T, ϕ and $\cot\theta$. (a) $|\cos\theta| > 0.8$, b) $|\cos\theta| < 0.8$)

From fig 9.21 and 9.22 one can see that moving the inner and upper boundaries of the fiducial volume so as to shrink it can decrease the number of events in the tails. These tails are quite important for they give the most troubles for $K_{\mu 3}$ rejection. In principle it is possible to reduce the tails by 10% by moving the inner boundary of the f.v. up to 55 cm, but at the cost of losing about some 20% of events inside f.v.

Vertex fit

The charged track reconstruction program has a part for vertex reconstruction. This part is based on the usual algorithm of propagation of the error matrix. Study of the efficiency of this algorithm have been done for two simple 2×2 and 3×3 chamber designs with $\mathcal{R}_{fs}$=3:1. Two separate sample of events were analysed: all tracks and only events with pions which do not undergo $\pi \rightarrow \mu$ decay (along the path used in track fit) . This second sample has reconstruction efficiencies a little bit better than the one with kink recognition as described above. Tables 9.8 and 9.9 show the achieved spatial resolution on the reconstructed vertex and the event losses encountered in vertex fitting.

	All tracks	Tracks without decay along track fit path
X^{fit}_{vertex} - X_{vertex},(mm)	0.39 ± 0.01	0.36 ± 0.01
Z^{fit}_{vertex} - Z_{vertex},(mm)	1.29 ± 0.02	1.21 ± 0.02
1-$\varepsilon_{vertex\ fit}$, (%)	12.57 ± 0.22	3.45 ± 0.12
There is no vertex, (%)	3.64 ± 0.11	1.37 ± 0.08
Bad guess (out of chamber, or Δz to large), (%)	0.79 ± 0.05	0.13 ± 0.02
Circles don't touch or intersect, (%)	2.10 ± 0.09	1.02 ± 0.07
One of two tracks rejected before fit	0.57 ± 0.04	0.15 ± 0.03
Fit did not converge, (%)	0.13 ± 0.02	0.04 ± 0.01
Others, (%)	0.05 ± 0.01	0.03 ± 0.01
Vertex with bad resolution, (%)	8.93 ± 0.18	2.08 ± 0.09
Removed "bad" track during fit, (%)	2.90 ± 0.10	1.62 ± 0.08
Fit converged but one of two tracks is "bad", (%)	6.00 ± 0.15	0.42 ± 0.04
Fit converged but errors are to large, (%)	0.03 ± 0.01	0.04 ± 0.01

Table 9.8. Vertex fit resolution and losses for 2×2 design with $\mathcal{R}_{fs}$=3:1

Vertex reconstruction efficiencies are unacceptably low for the case of absence of any kink recognition. Comparison of the inefficiencies for the event samples with and without kinks shows how important it is to recognize the decay kink and to cut the π track before it decays.

Event losses may be classified into two categories :

1) events in which the algorithm of vertex fit fails.

2) events with bad quality vertex fit. Bad quality means that χ^2 of the fit is too large (more

precisely one of the two tracks tends to be rejected during the execution of the algorithm). The spatial resolution of the vertex in the case of bad quality fit degrades by more than 10 times in comparison with the normal fit. Usually events with this bad vertex fit have one of the tracks badly reconstructed. The accuracy of the reconstruction of the bad track is about 10 times worse than that of the good ones in the event. The main contributions to the events with bad quality vertex fit are made by events where at least one of the two π's decays into muon along the path which is used in the track fit.

	All tracks	Tracks without decay along track fit path
X^{fit}_{vertex} - X_{vertex},(mm)	0.41 ± 0.02	0.39 ± 0.02
Z^{fit}_{vertex} - Z_{vertex},(mm)	1.41 ± 0.02	1.35 ± 0.02
1-$\varepsilon_{vertex\ fit}$, (%)	11.30 ± 0.22	3.00 ± 0.12
There is no vertex, (%)	3.44 ± 0.12	1.26 ± 0.08
Bad guess (out of chamber, or Δz to large), (%)	0.69 ± 0.05	0.10 ± 0.02
Circles don't touch or intersect, (%)	1.95 ± 0.09	0.89 ± 0.06
One of two tracks rejected before fit	0.67 ± 0.05	0.24 ± 0.03
Fit did not converge, (%)	0.10 ± 0.02	0.02 ± 0.01
Others, (%)	0.03 ± 0.01	0.01 ± 0.01
Vertex with bad resolution, (%)	7.86 ± 0.18	1.74 ± 0.09
Removed "bad" track during fit, (%)	2.64 ± 0.13	1.41 ± 0.08
Fit converged but one of two tracks is "bad", (%)	5.20 ± 0.14	0.30 ± 0.03
Fit converged but errors are to large, (%)	0.02 ± 0.01	0.03 ± 0.01

Table 9.9. Vertex fit resolution and losses for 3×3 design with $\mathcal{R}_{fs}$=3:1

The question of acceptability of the bad quality vertex fit has two aspects. The most important of them is how much this deterioration of the experimental resolutions will affect the $K_{\mu 3}$ rejection. This will be discussed separately. The second aspect is the problem of correctly counting the number of $K_L \to \pi^+\pi^-$ decays in the fiducial volume. To estimate the effect of the experimental resolutions on the counting events inside fiducial volume the numbers of the lost and extra-counted events were found. The difference between these two numbers gives us the error of events counting. Such estimates have been done with a sample of 40000 $K_L \to \pi^+\pi^-$ events with and without π-tracks decaying along the track fit path, separately. The results for 2×2 design with $\mathcal{R}_{fs}$=3:1 are shown in the table 9.10.

$\mathcal{R}_{fs}$=3:1, all tracks				
Losses-Extracounts / Number of vtx. fitted (%)	All tracks		Tracks without decay along track fit path	
Cell size, (mm)	2×2	3×3	2×2	3×3
Good vertex fit, (%)	0.01 ± 0.03	0.00 ± 0.03	0.00 ± 0.01	0.02 ± 0.02
Bad quality vertex fit, (%)	0.15 ± 0.36	0.17 ± 0.46	1.46 ± 0.92	1.35 ± 1.13
Total vertex fit, (%)	0.00 ± 0.04	0.02 ± 0.04	0.03 ± 0.03	0.04 ± 0.03

Table 9.10. Error of counting events inside fiducial volume

The counting errors are larger in the case of bad quality vertex fit; however in the limits of the available statistics there is no clear evidence of any systematic counting unbalance in each case.

This problem has been looked into also from a different point of view by studying the decay $K^+ \rightarrow \pi^+\pi^0$. In this case one may reconstruct the K^+ decay vertex inside the chamber in two independent ways. First by reconstructing the charged vertex of the K^+ and π^+ tracks; secondly by finding along the reconstructed K^+ helix the point that best matches with the measured photons Tof's. In doing the K^+ reconstruction particular care must be given to the energy loss in the beam pipe and in the inner wall of the chamber (the K^+ range at these energies is only $\sim$0.5 g/cm^2).[33] A full simulation and reconstruction[33] of this process shows that the vertices reconstructed with the two methods agree within a precision of $\sim$9 mm in R and 4.2 mm in z.

Reconstruction efficiencies

Overall reconstruction efficiencies (i.e. including f.v. losses, track fit losses and vertex fit losses) of the "mixed" chamber designs have been studied. In "mixed" design the 6 innermost cell layers are replaced by 12 layers of cells of half size (1x1 or 1.5x1.5 cm^2). This allows us to move down the inner boundary of the fiducial volume and to recover some of the event losses due to the fiducial volume cut without any losses of the reconstruction efficiency.

Results on evaluations of the reconstruction efficiency of the "mixed" 2×2 and 3×3 chamber designs for $\mathcal{R}_{fs}$=3:1 are shown in the table 9.11. The numbers of events inside fiducial volume in this table are normalized to the number of K_L decays inside the drift chamber. Normalization of these numbers to the total number of K_L produced reduces them to 29.8% and 28.9%, for 2×2 and 3×3 chamber designs respectively. As one can see from these results recognition of the $\pi \rightarrow \mu$ decays reduces the overall reconstruction inefficiencies by a factor of 2, roughly. Another observation is that the bad quality vertex fit gives very large contributions to the overall inefficiency. Comparison of the two last rows of the table demonstrates this. In case of kink recognition the differences between overall inefficiencies of the 2x2 and 3x3 designs are approximately equal to the geometrical losses of the tracks.

	All tracks		100% kink recognition for π longer than 8 hits	
Cell size, (cm)	2×2	3×3	2×2	3×3
Low radius of f.v. (cm)	32	35	32	35
Number of events in f.v., (%)	78.5	76.1	78.5	76.1
$1\text{-}\varepsilon^2_{track\ fit}$	1.24 ± 0.05	2.50 ± 0.06	1.56 ± 0.07	2.88 ± 0.10
Short tracks	0.92 ± 0.05	2.14 ± 0.06	1.27 ± 0.06	2.55 ± 0.09
Reconstruction fails	0.32 ± 0.03	0.36 ± 0.02	0.29 ± 0.03	0.33 ± 0.03
$1\text{-}\varepsilon^2_{track\ fit} \times \varepsilon_{vertex\ fit}$	13.51 ± 0.19	13.80 ± 0.16	6.01 ± 0.14	7.60 ± 0.16
bad quality vertex fit accepted	4.77 ± 0.11	6.08 ± 0.10	3.08 ± 0.10	4.63 ± 0.12

Table 9.11. Reconstruction efficiencies for mixed chamber designs (case of $\mathcal{R}_{fs}$=3:1)

The reconstruction efficiencies are not very much affected by varying the $\mathcal{R}_{fs}$. The efficiencies in two cases of $\mathcal{R}_{fs}$ are consistent within 2σ.

As one can see from table 9.11 the main contribution to the track fit inefficiency is made by the short tracks. These tracks[31] make a small angle with respect to z-axis, or originate near z-boundary of the fiducial volume and have momenta directed outwards of the chamber. Another source of inefficiency is the failures of the algorithm. But again most of the tracks making the algorithm fail are close to be classified as short tracks. These tracks pass the cuts on number of hits and crossed layers but have hits barely more than 6. The track fit algorithm can discard some hits considered by it as bad ones, so to leave the track with less than 6 hits and hence reject it.

Figures 9.23, 9.24 and 9.25 show the effect of the varying the inner boundary of the fiducial volume on reconstruction efficiencies on track fit, vertex fit and vertex fit with bad quality vertex accepted respectively ($\mathcal{R}_{fs}$=3:1, $\pi \rightarrow \mu$ decay kinks are supposed to be recognised as it was described above). These plots justify our previous choose of the fiducial volume inner boundary (32 cm for 2×2 and 35 cm for 3×3 designs). The right axis of these plots shows the accuracy to which one has to know the corresponding inefficiency to keep the contribution due to this inefficiency to $\sim \Delta\mathcal{R}/\mathcal{R} \sim 3\times10^{-4}$.

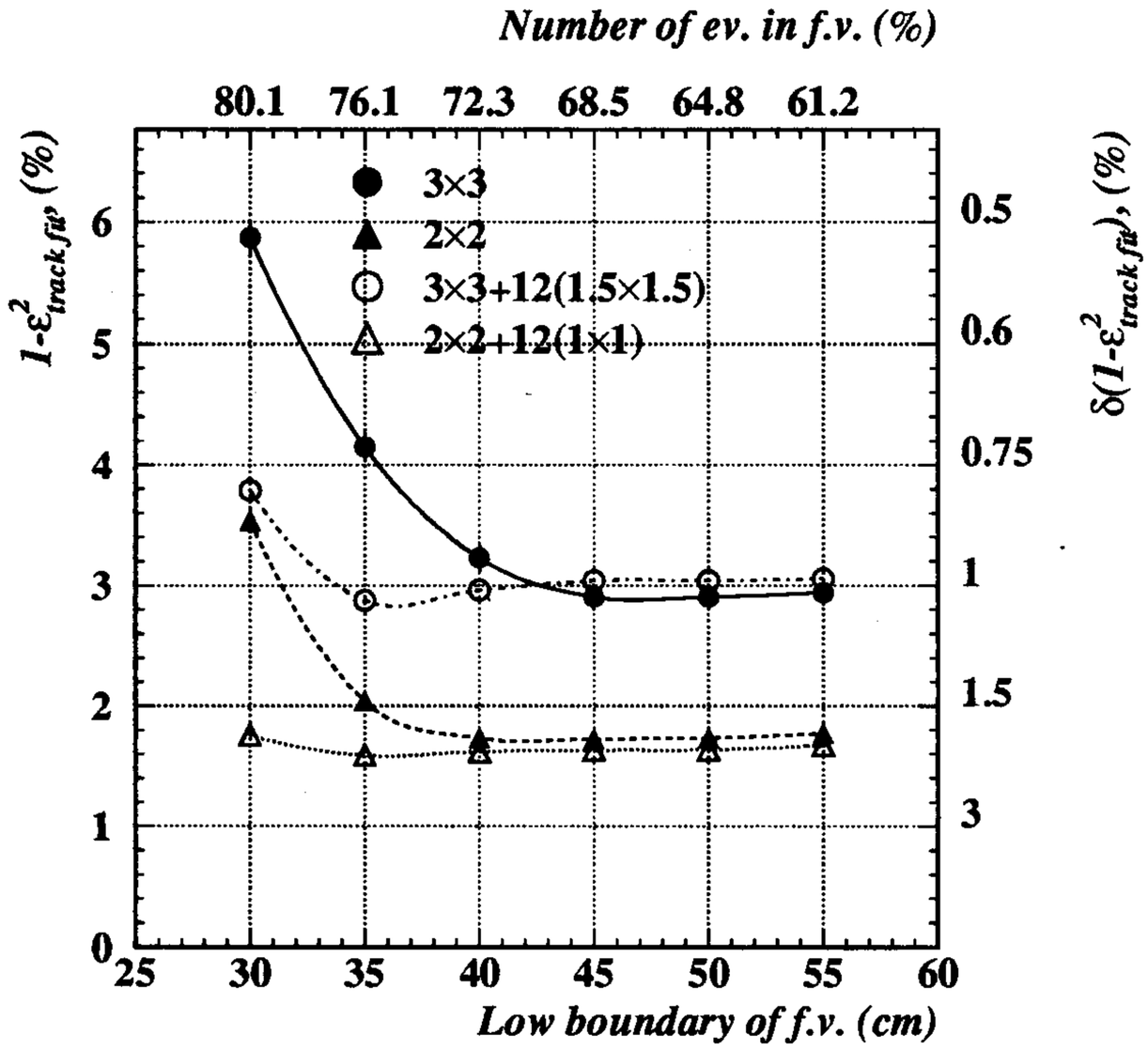

Fig. 9.23. $1-\varepsilon^2_{track\ fit}$

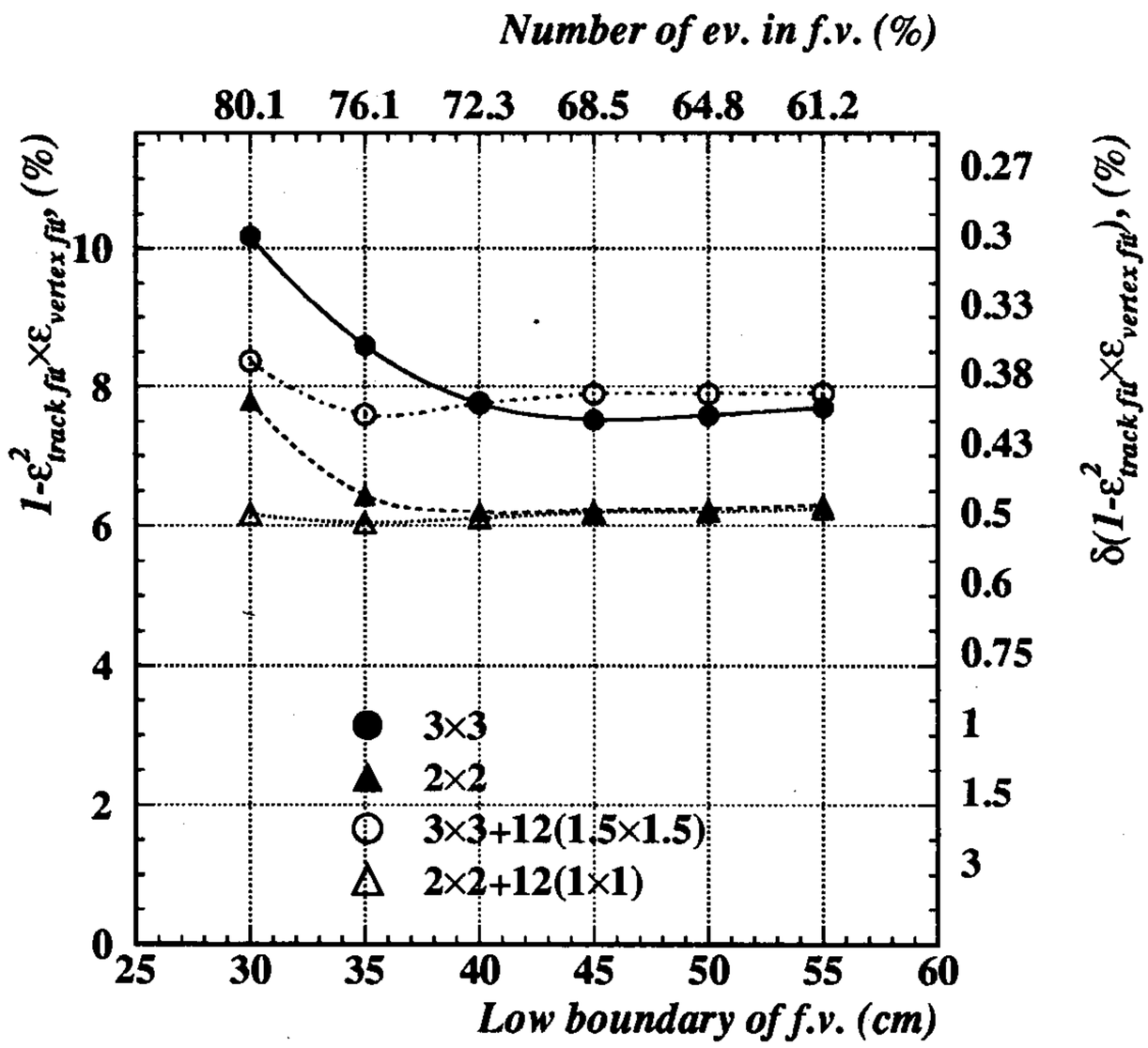

Fig. 9.24. $1-\varepsilon^2_{track\ fit} \times \varepsilon_{vertex\ fit}$

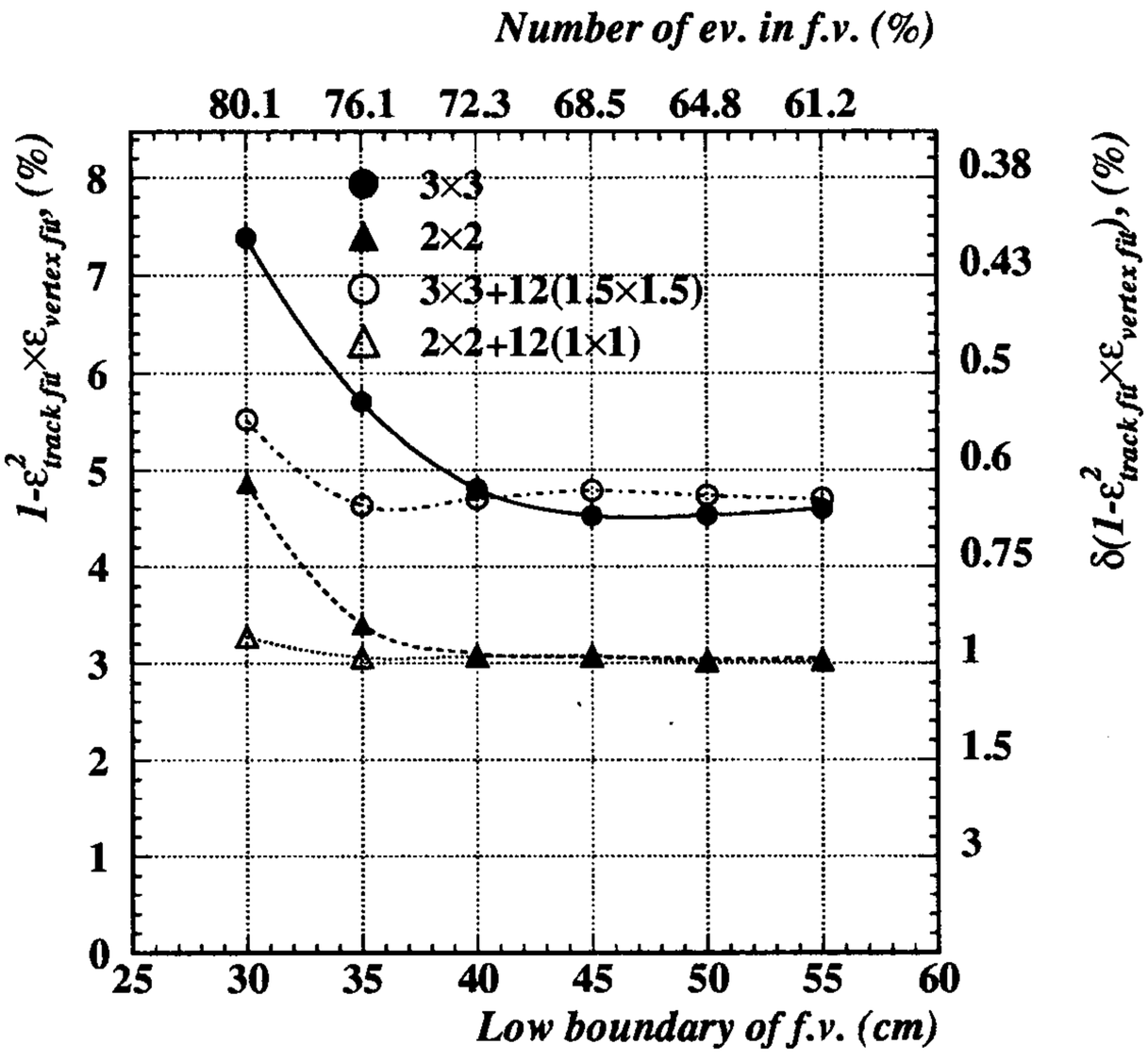

Fig. 9.25. $1\text{-}\varepsilon^2_{track\ fit} \times \varepsilon_{vertex\ fit}$ (bad quality fit accepted)

The mixed design can also give some improvement of the reconstruction of $K_S \to \pi^+\pi^-$ decays. "Simple" and "mixed" designs of the 2×2 and 3×3 chambers were studied. The standard GEANFI simulation program were used to get a sample of the $K_S \to \pi^+\pi^-$ decays. This program describes the materials in the chamber volume as a homogeneous mixture of gas and wires materials. The results of this study are shown in the table 9.12. As one can see from this table, the track reconstruction inefficiency is completely dominated by pure geometrical losses of the tracks, named in the table as "short tracks". These losses are much bigger than those in the case of $K_L \to \pi^+\pi^-$ decays (table 9.11) , because of the topology of the events. K_S's from interaction region decay practically always outside the chamber therefore their secondaries may not enter at all in the chamber, which starts from radius of 25 cm. In K_L case we select decays only in chamber, thereby excluding such losses completely.

Chamber design	"simple"		"mixed"	
Cell size, (cm)	2×2	3×3	2×2	3×3
1-ε^2_{track} (%)	7.48 ± 0.28	8.14 ± 0.30	6.59 ± 0.27	6.81 ± 0.30
Short tracks	7.12 ± 0.28	7.77 ± 0.29	6.18 ± 0.26	6.48 ± 0.26
Reconstruction fails	0.36 ± 0.06	0.37 ± 0.06	0.41 ± 0.06	0.33 ± 0.06
$(P_T^{\rm fit} - P_T)/P_T$, (%)	0.58	0.59	0.59	0.59
$\phi^{\rm fit} - \phi$, (mrad)	15.8	15.5	15.6	15.5
$(\cot\theta)^{\rm fit} - \cot\theta, (\times 10^{-3})$	13.2	13.2	13.2	13.4
$M^{\rm fit}_{\pi\pi} - M_{\pi\pi}$,(MeV)	0.95	0.96	0.95	0.96
$X^{\rm fit}_{\rm vertex} - X_{\rm vertex}$,(mm)	6.84	6.82	6.77	6.78
$Z^{\rm fit}_{\rm vertex} - Z_{\rm vertex}$,(mm)	5.32	5.61	5.63	5.54

Table 9.12. Reconstruction efficiencies and experimental resolutions for $K_S \to \pi^+\pi^-$ decays

Pattern recognition

The pattern recognition package for the drift chamber with only stereo wires has been written and checked in a single track regime. This package is based on the ARGUS pattern recognition algorithm for axial wires.[32] Our algorithm considers each stereo view as an axial view and performs pattern recognition for each view independently. This simplified description of the stereo view can be done only locally. Indeed in a small volume wires of each stereo view are almost parallel. On the other hand the ARGUS pattern recognition algorithm for axial wires is also local. It is an algorithm of extending circular segment, which for two last hit wires of the segment tries to find the third one in nearest cells of few next layers. This justifies our application of the algorithm. After one view pattern recognitions have been done, their results are combined together and track candidates in space are built. After that the raw track fit starts to find starting values for the helix parameters to be used in the track fit.

The efficiency of this program to assign hits to the track candidate is of the order of 90% and the efficiency of solving right-left ambiguities is about 97% for pions from K_L-decays. These performances of the algorithm do not depend very much on cell size, so they do not differ remarkably for 3×3 and 2x2 design. Fig 9.26shows distribution of the drift distances for right and wrong solutions of right-left ambiguities for the 2×2 chamber design. As expected the algorithm is less efficient for hits with small values of the drift distances. But even at drift distances shorter than 1 mm the algorithm is still 80% efficient for ambiguity solving (fig 9.27). The program estimates the starting values of the track curvature with accuracy of ~11% and the $\cot\theta$ with accuracy of ~18%.

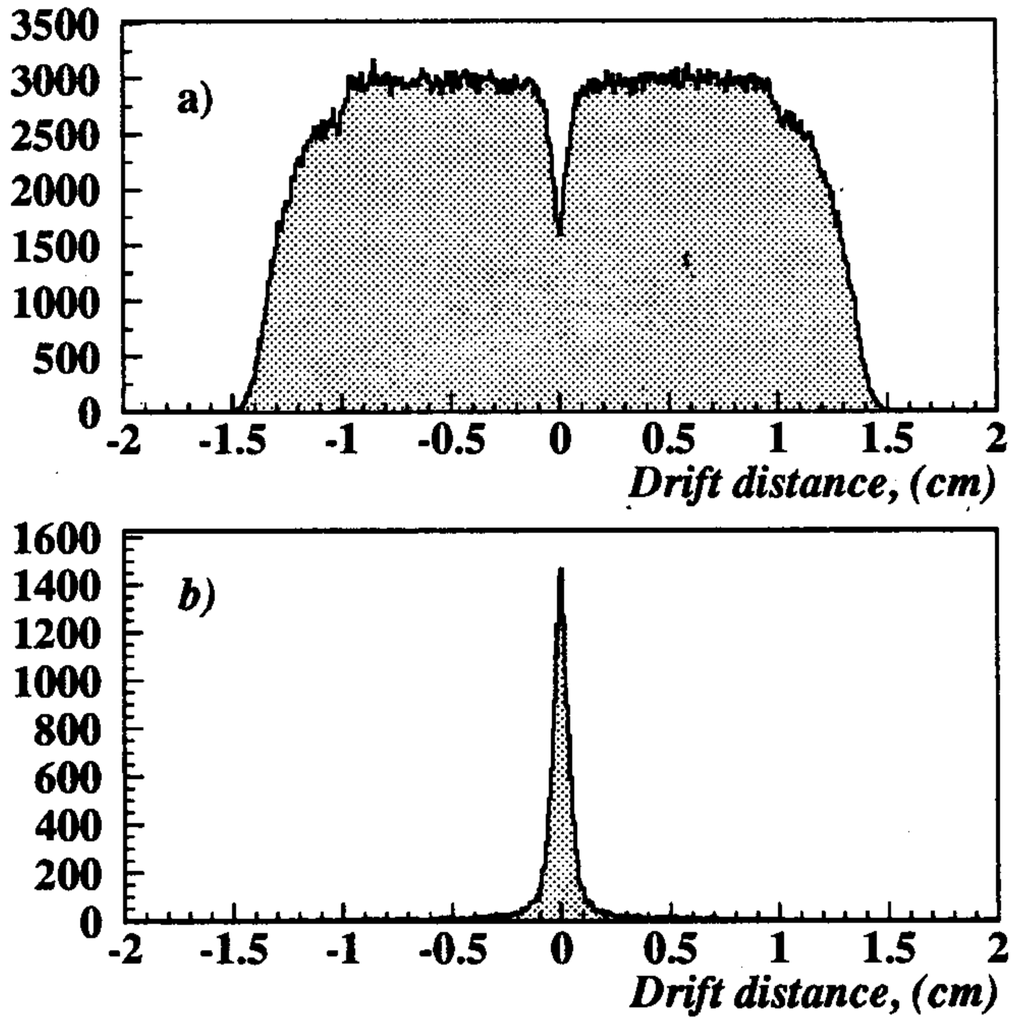

Fig. 9.26. Drift distance distributions for the cases of a) – right and b) – wrong solving right-left ambiguity

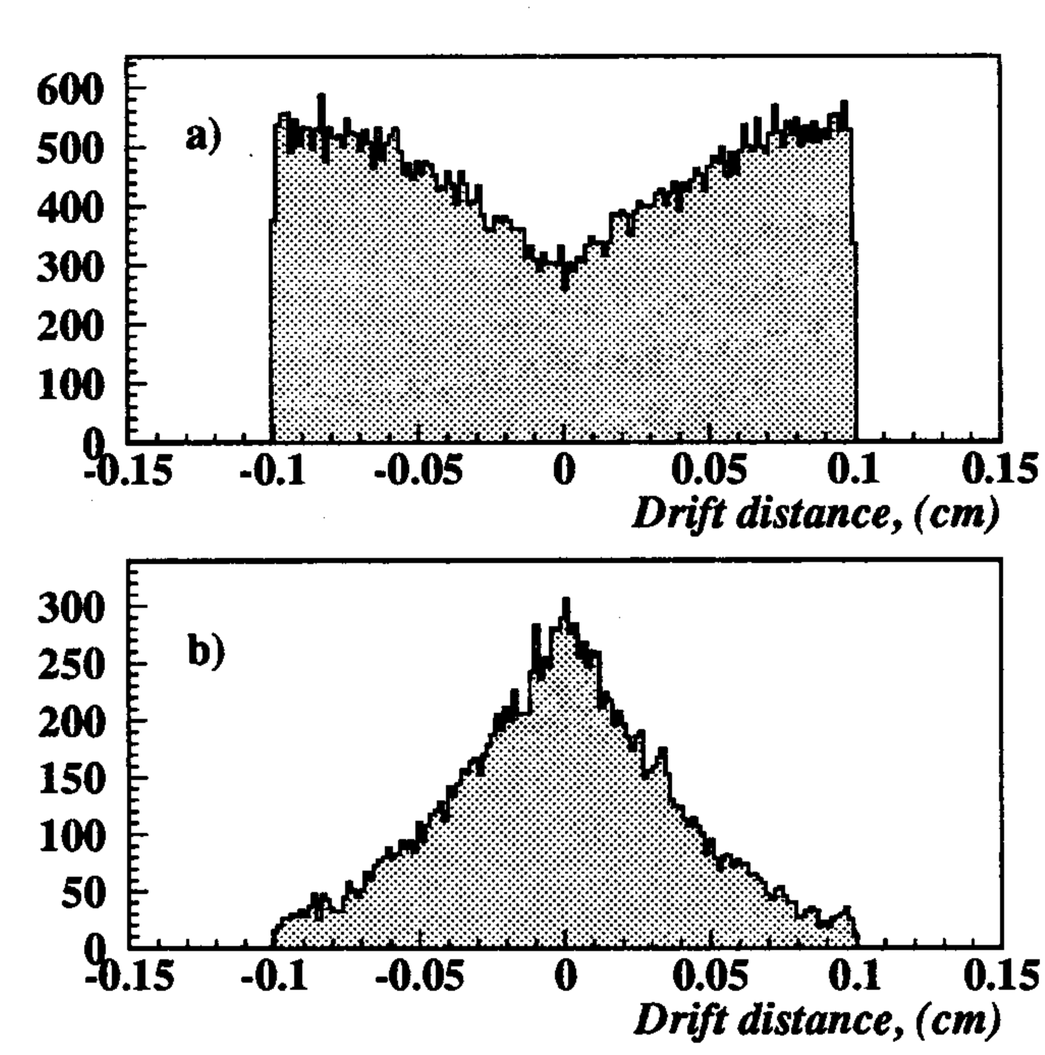

Fig. 9.27. Drift distance distributions for the cases of a) – right and b) – wrong solving right-left ambiguity. (Small drift distances)

Since the pattern recognition requires at least 4 hits in each view to form a track candidate, the whole algorithm can deal with only tracks of 8 or more hits. The shorter tracks can be treated in subsequent stages of the whole track reconstruction procedure with looser cuts and taking into account the information obtained at previous reconstruction stages.

Experimental resolutions for half stereo angle chamber

A comparison of the chamber resolutions with full stereo angle (1 cm stereo waist) and with half stereo angle (0.25 cm stereo waist) has been done (2×2 design with multiple scattering on wires being switched off). The results are shown in the table 9.13.

Stereo drop, (cm)	0.25	1
$(P_T^{fit}\text{-}P_T)/P_T$, (%)	0.29	0.29
$\phi^{fit} - \phi$, (mrad)	1.43	1.42
$(\cot\theta)^{fit} - \cot\theta, (\times 10^{-3})$	4.04	2.69
$M_{\pi\pi}^{fit}$- $M_{\pi\pi}$,(MeV)	0.95	0.82
X_{vertex}^{fit} - X_{vertex},(mm)	0.31	0.32
Z_{vertex}^{fit} - Z_{vertex},(mm)	1.95	1.10

Table 9.13. Experimental resolutions of the chamber of half stereo angle

As expected the value of the stereo angle does not affect the resolutions of the fit variables connected to the $x - y$-plane measurements (P_T, ϕ, x and y position of the vertex). These resolutions are equal within errors for full and half angle designs. The most sensitive to the value of the stereo angle are the variables $\cot\theta$ and z position of the vertex which become 50% and 70% worse for the half angle design. Also the two pions effective mass degrades by 20% with half stereo angle.

9.5 $K_{\mu 3}$ REJECTION

Introduction

In order to measure to a 10^{-4} precision level the CP violating parameter $\Re(\epsilon'/\epsilon)$, the error in counting CP violating $K_L \to \pi^+\pi^-$ events must be less than 6×10^{-4}. The main source of background is the $K_{\mu 3}$ decay. To achieve the required accuracy it implies a $K_{\mu 3}$ rejection factor of $\simeq 4.5 \times 10^4$.[34]

A critical benchmark for the chamber design is therefore its ability to discriminate the $K_L \to \pi^+\pi^-$signal from the $K_{\mu 3}$ background. A powerful way, as described in the following, is based on kinematical cuts which require the best resolution on single track parameters, the best accuracy on the K_L decay vertex and the ϕ decay vertex positions, these latter are needed to define the K_L line of flight. It must be added that a global constrained fit, which we have yet to incorporate, can also improve the discrimination power of the present analysis. Moreover, it is not clear that we have found the optimum discriminating function. We are at present trying to

build the correct test function, using the "H" or covariance matrix. "Neural network" techniques can be also used to build the elements of the "H"–matrix.

It must also be emphasized that in addition to, and independent of the chamber discrimination, we have available time-of-flight and energy deposition profile in the calorimeter to aid in π/μ discrimination. These further factors HAVE NOT been included in the present section.

Event simulation

Events were generated for different "mixed" chamber designs (cell size 3×3 cm^2 or 2×2 cm^2 and $\mathcal{R}_{fs}$= 3:1 or 2:1) . Also, to isolate the effects of multiple scattering, events were generated with no wires in the chamber, also with no gas, for both the 3×3 and 2×2 designs. For each chamber design 5.4×10^6 $K_{\mu 3}$ and 4.0×10^4 $\pi\pi$ events were generated. The events were generated with the simulation program previously described. In particular with respect to a previous study[35] the features that are relevant to this study are the insertion of the wires and the subsequent multiple scattering of particles off them. Also included was the smearing of the interaction point, $\sigma_x = .2$ cm, $\sigma_y = 20$ μm, and $\sigma_z = 5$ mm, beam energy spread, $\sigma_E = 700$ KeV, radiative corrections to the beam energy, and the half-crossing angle of the beams, $\theta_{cross} = 15$ mrad. The gas mixture was 90% helium and 10% isobutane.

To save computer time and disk space a preliminary selection cut on the $K_{\mu 3}$ events was made. The neutrino energy from the $K_{\mu 3}$ decay was required to be less than 35 MeV. The justification of this cut can be seen from the spectrum of the reconstructed missing energy for $K_{\mu 3}$ events shown below.

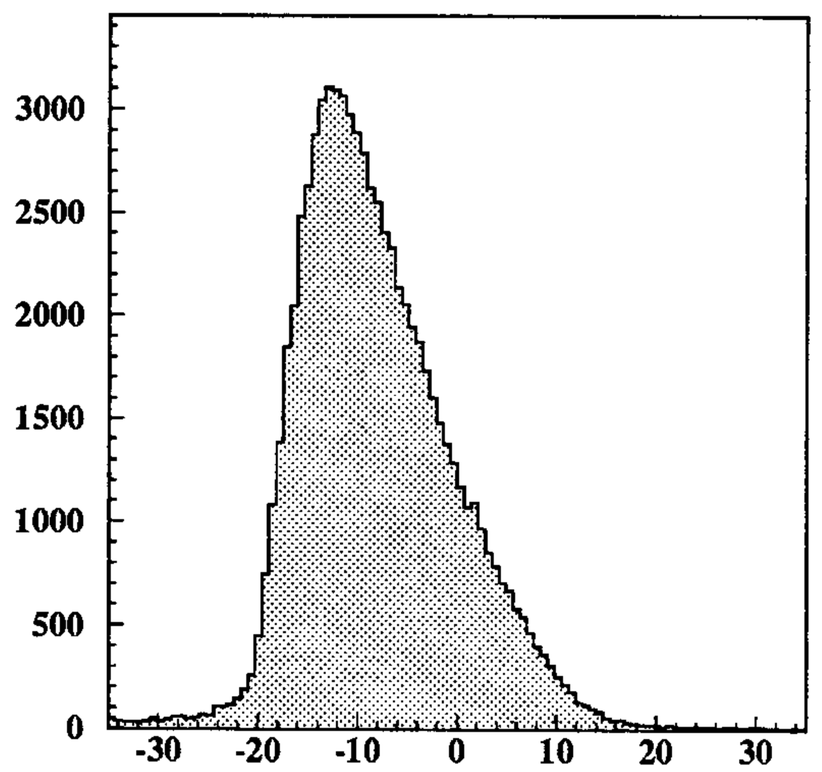

Fig. 9.28. Reconstructed missing energy for $K_{\mu 3}$ events in MeV:
$E_{miss}=E_1 + E_2 - E_{K_L}$ (3×3 cell,$\mathcal{R}_{fs}$=3:1)

The events were reconstructed[36] assuming, as described in the previous chapter, exact kink recognition of pion decay for pion tracks which decay after 8 hits.

The kinematical variables

The variables used to discriminate between signal and background are the same as those used in a previous study.[35] The physical properties of the decays $K_L \to \pi^+\pi^-$ are energy

conservation, the two pion invariant mass equal to that of the K_L, and collinearity between the K_L decay path and the total momentum vector of the two pions. The relevant equations are:

$$\Delta E_{tot} = E_1 + E_2 - E_{K_L}(\theta, \phi) = 0$$
$$\Delta M_{inv} = \sqrt{2}\left(M_\pi^2 + E_1 E_2 - \vec{p}_1 \cdot \vec{p}_2\right)^{\frac{1}{2}} - M_{K_L} = 0$$
$$\Delta\phi = \phi_{\vec{p}_{tot}} - \phi_{\vec{l}_K} = 0$$
$$\Delta cot\theta = \cot\theta_{\vec{p}_{tot}} - \cot\theta_{\vec{l}_K} = 0$$

where $\vec{l}_K$ is the vector from the origin to the K_L reconstructed vertex. Due to the crossing angle between the beams the Φ is not created at rest and has a momentum $\simeq$ 15 MeV in the x-direction. As a result the energy of the K_L depends on the angle with respect to momentum of the Φ. The quantity $E_{K_L}(\theta, \phi)$ is calculated using the position of the reconstructed K_L vertex. The difference between the true and calculated value of the K_L energy is shown in fig. 9.29.

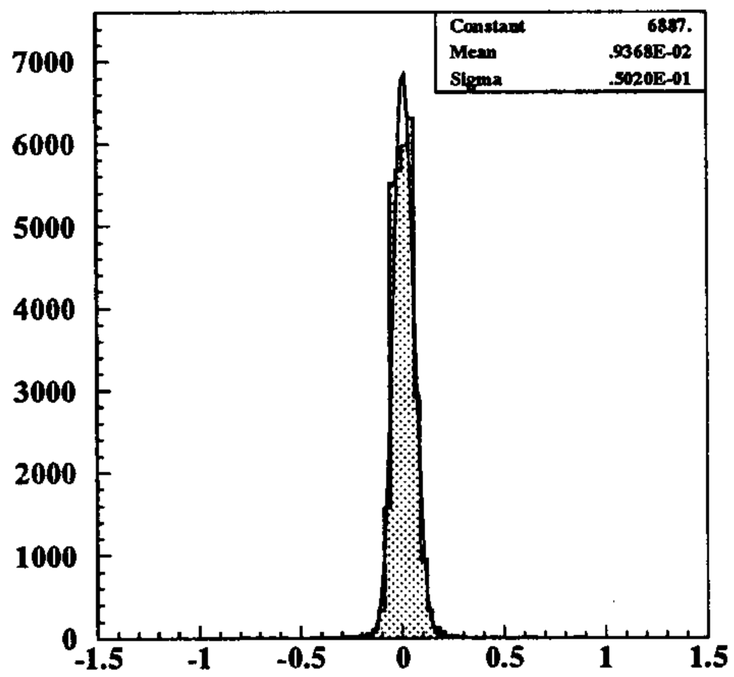

Fig. 9.29. True E_{K_L} - $E_{K_L}(\theta, \phi)$ in MeV for $K_L \to \pi^+\pi^-$. (3×3 $\mathcal{R}_{fs}$=3:1 data).

To discriminate the $K_{\mu 3}$ background we build from the kinematical variables a χ^2-like variable as follows :

$$x_1 = \Delta E_{tot} - \Delta M_{inv}$$
$$x_2 = \Delta E_{tot} + \Delta M_{inv}$$
$$x_3 = \Delta\phi$$
$$x_4 = \Delta cot\theta$$

$$\chi^2 = \sum_{i=1}^{4} \frac{x_i^2}{\sigma_i^2}$$

The variable x_1 and x_2 were constructed so as to eliminate most of the correlation existing between ΔE_{tot} and ΔM_{inv}. The σ_i are obtained from a gaussian fit to the corresponding distributions for the $K_L \to \pi^+\pi^-$ signal.

The rejection factor

The distributions of the x_i variables which enter in the χ^2 definition are shown in fig. 9.30. for the case of a 3×3 $\mathcal{R}_{fs}$=3:1 chamber design. Typical distributions of the χ^2 are shown in fig. 9.31, for the $K_L \to \pi^+\pi^-$ events and for the $K_{\mu 3}$ ones.

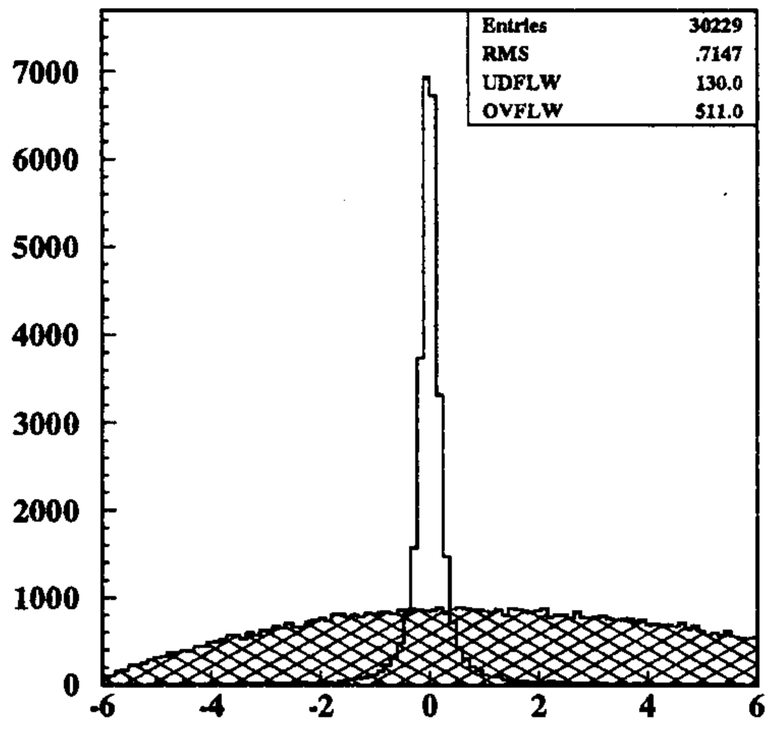

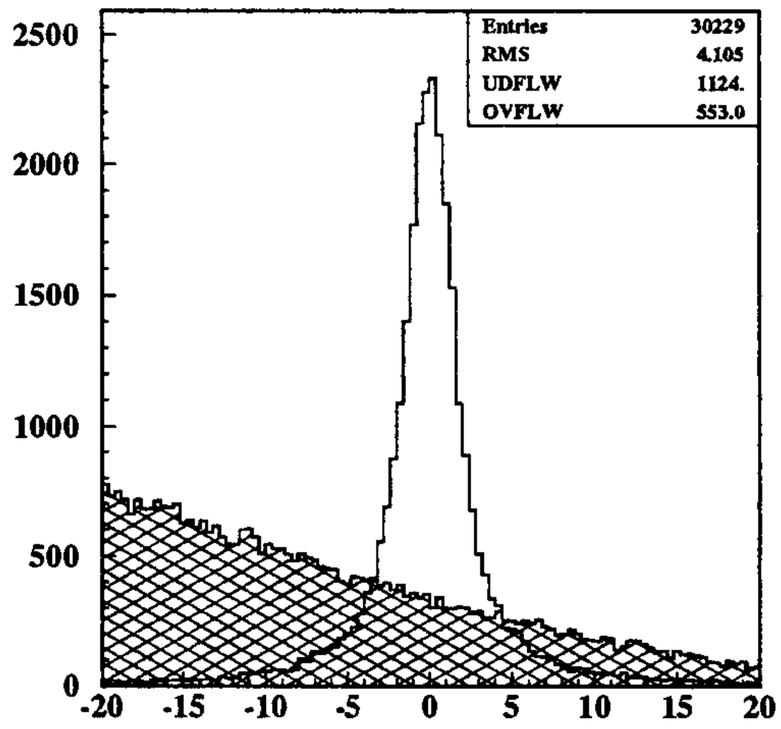

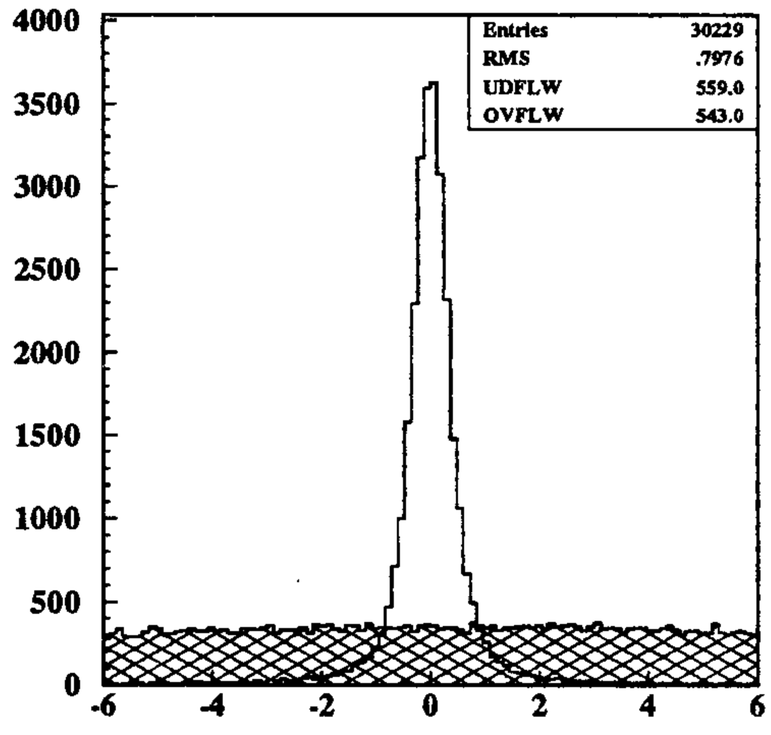

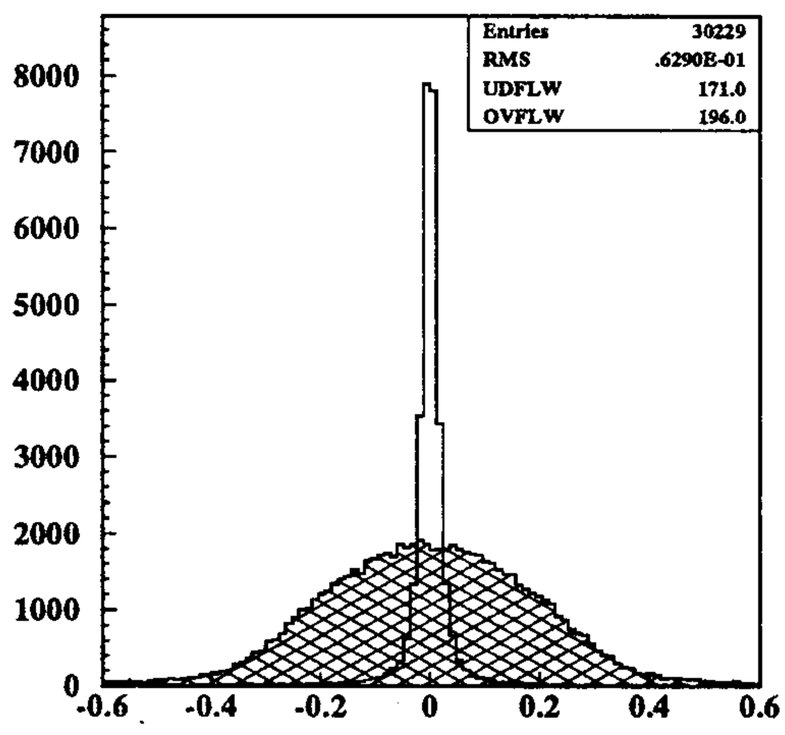

Fig. 9.30. The distribution of the kinematical variables used in the construction of χ^2. The unshaded part is for $K_L \to \pi^+\pi^-$ and the shaded part is for $K_{\mu 3}$.

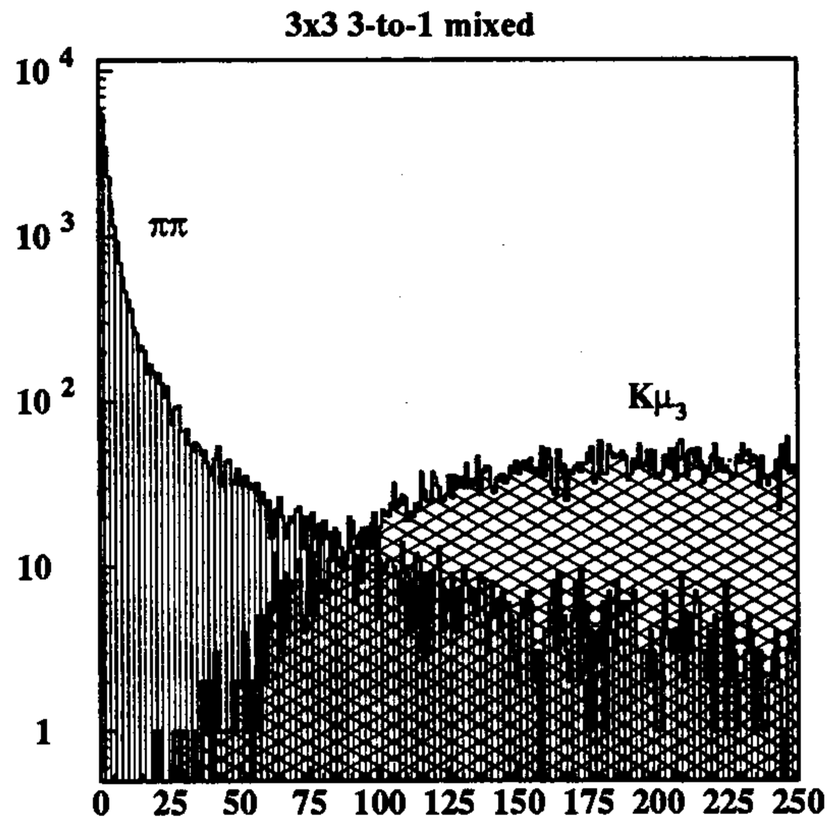

Fig. 9.31. The χ^2 distributions of $K_L \to \pi^+\pi^-$ and $K_{\mu 3}$ (3×3 $\mathcal{R}_{fs}$=3:1 design).

By selecting only events having the χ^2 value below a given cut we may reject a very large fraction of the $K_{\mu 3}$ background. When doing this we lose a fraction of the signal because of the tail of good events with large χ^2. We have studied this loss and we have found that it is mainly due to :

- early pions decay kinks which happen before the 8 hits cut

- short tracks

- tracks nearly parallel to the z-axis

Short tracks can be reduced by choosing a smaller fiducial volume and those near parallel to the z-axis by putting a cut on cosθ. No optimization with respect to these cuts (which lead to a smaller acceptance for the $K_L \to \pi^+\pi^-$ signal) has yet been done at this stage of the analysis; in the following we have used :

- R_{min} 25 $\to$ 60 cm and R_{max} 175 $\to$ 140 cm

- abs(cosθ) $\leq$ 0.8

Moreover to show the effect of the early decays we have analysed a case with the pions undergoing such decays being excluded from the sample. The corresponding results are shown in table 9.14 where are quoted the $K_L \to \pi^+\pi^-$ reconstruction efficiency, the fiducial volume acceptance (normalized to 100 for the standard choice) and the fraction of signal events $\epsilon(K_L \to \pi^+\pi^-)$ which survive a χ^2 cut chosen to obtain a $K_{\mu 3}$ rejection factor (RJ) equal respectively to 10^5 or 10^4.

The table shows that both cuts are effective: the cosθ cut seems somewhat more effective (*i.e.* the same rejection factor is achieved with a higher f.v. acceptance). The case with both cuts applied, yields a substantial improvement of the $K_L \to \pi^+\pi^-$ efficiency at a price of a factor $\sim$2 in counting rate (note that the statistical error on the double ratio is affected to a smaller extent since the $K_L \to \pi^+\pi^-$ channel has a branching ratio about twice respect to the $K_L \to \pi^0\pi^0$ one).

Table 9.14 $\epsilon(K_L \rightarrow \pi^+\pi^-)$ (in %) for different cuts. $\epsilon(K_L \rightarrow \pi^+\pi^-)$ is 100 % when no χ^2 cut is applied.

reconstruction efficiency (%)	small f.v.	cosθ cut	π decays $<$ 8 hits	f.v. accept	$\epsilon(K_L \rightarrow \pi^+\pi^-)$ (RJ=10^5)	(RJ=10^4)
95.5	N	N	Y	100.0	88.5	91.0
95.2	Y	N	Y	57.8	92.5	94.0
97.5	N	Y	Y	72.6	89.8	91.8
97.3	Y	Y	Y	42.2	94.2	95.0
97.4	Y	Y	N	40.7	97.3	98.0

In figure 9.32 the $K_{\mu 3}$ rejection factor is plotted versus $\epsilon(K_L \rightarrow \pi^+\pi^-)$ for different cuts. Note how the slope of the curves becomes steeper when we select better quality tracks and that the early decay kinks account for ~3 % of the large χ^2 tail.

All these results have been obtained for the 3x3, 3:1 mixed design. The other cell designs differ mainly in the reconstruction efficiency (as discussed in the previous chapter), and are quite comparable in $K_{\mu 3}$ rejection. In this analysis we have assumed a spatial resolution on the interaction point of $\sigma_z = 0.5$ cm (this is the value achieved when tagging K_L decays with the charged K_S decay).

As stated in the introduction of this section, we expect to improve upon these results by developing further our present algorithms, to achieve :

- more efficient decay kink recognition.
- optimization of the fiducial volume and track/vertex quality requirements.
- more powerful discriminating functions

9.6 Summary

We may try to summarize the main results of this study as follows.

1) Concerning the wire ratio field/sense the increase of material of the 3:1 configuration respect the 2:1 one seems to have little effect in worsening the resolutions and has no appreciable effect on reconstruction efficiencies and $K_{\mu 3}$ rejection.

2) The main difference between the two considered cell sizes 3x3 or 2x2 resides in the overall reconstruction losses : ~4.6 % for the big one and ~3.1 % for the smaller one (cf table 4.5). The $K_{\mu 3}$ rejection capability is otherwise practically the same.

3) The "mixed" design helps to maximize the useful fiducial volume , while event losses and the $K_{\mu 3}$ rejection are almost unchanged. It improves slightly (~1%) the reconstruction efficiency for $K_S \rightarrow \pi^+\pi^-$ events.

4) We achieve a $K_{\mu 3}$ rejection factor of order 10^5 with $K_L \rightarrow \pi^+\pi^-$ efficiencies around 89 - 97 % by the kinematical analysis of the drift chamber data alone. This is when normalized to the number of reconstructed K_L decays. We separate the reconstruction efficiency from the

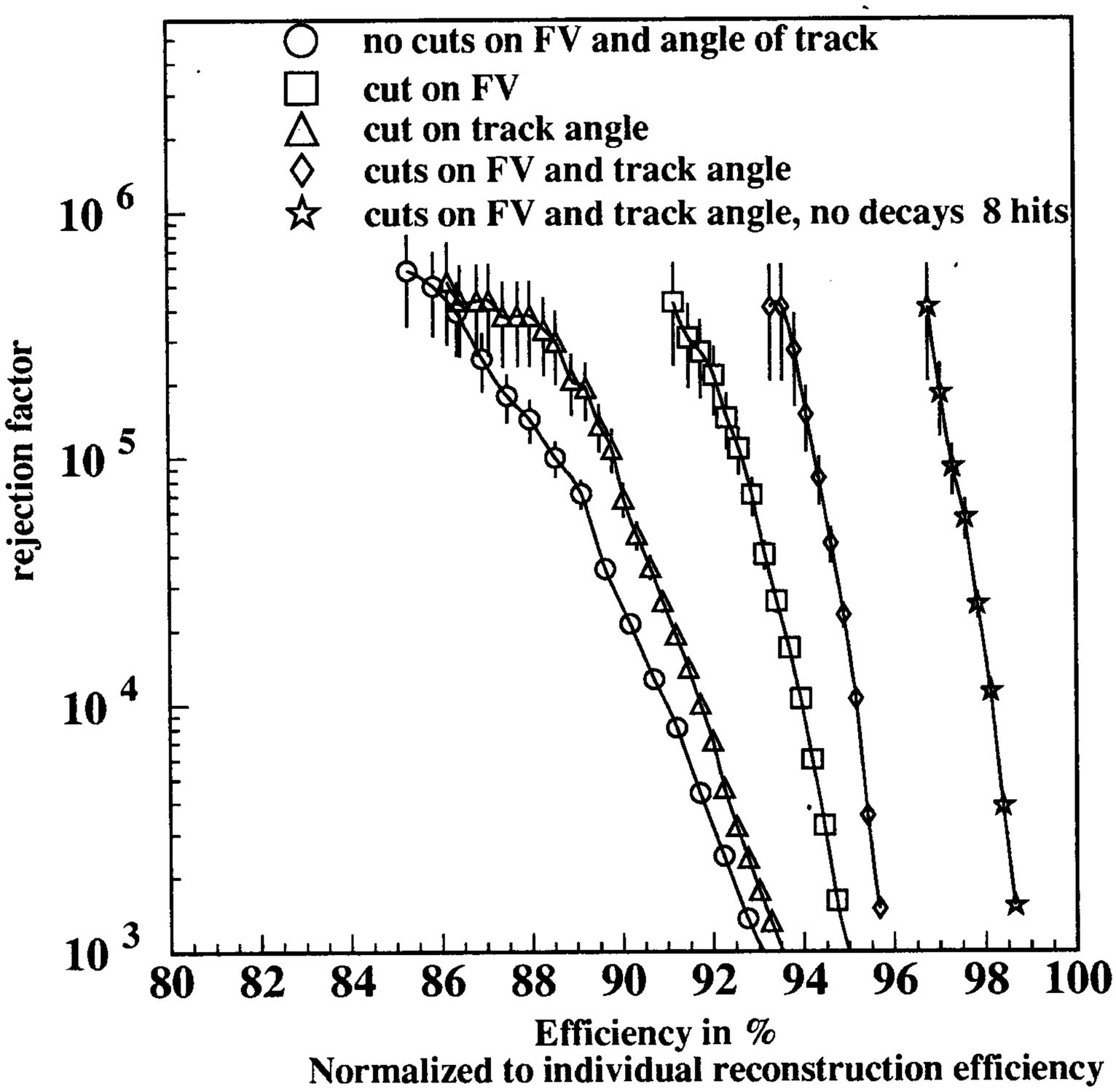

Fig. 9.32. $K_{\mu 3}$ rejection factor vs $K_L \to \pi^+\pi^-$ efficiency.

rejection efficiency because specific, dedicated, algorithms are being studied and constructed for each class of events.

5) We will have enough data to make a statistically accurate extrapolation of the $K_{\mu 3}$ background under the $K_L \to \pi^+\pi^-$ peak. To control the systematics we will need to evolve an accurate MonteCarlo to simulate the chamber behaviour. The data themselves will provide many control distributions (e.g. all those of the four x_i variables defined previously and others such as χ^2 of track fit, number of fitted hits/track, angular distributions, etc.) on which to tune the MonteCarlo parameters.

6) Other rejection factors will be provided by the calorimeter (time of flight and energy deposition profile to discriminate pions and muons).

10. SCHEDULE AND COSTS

10.1 CONSTRUCTION SCHEDULE

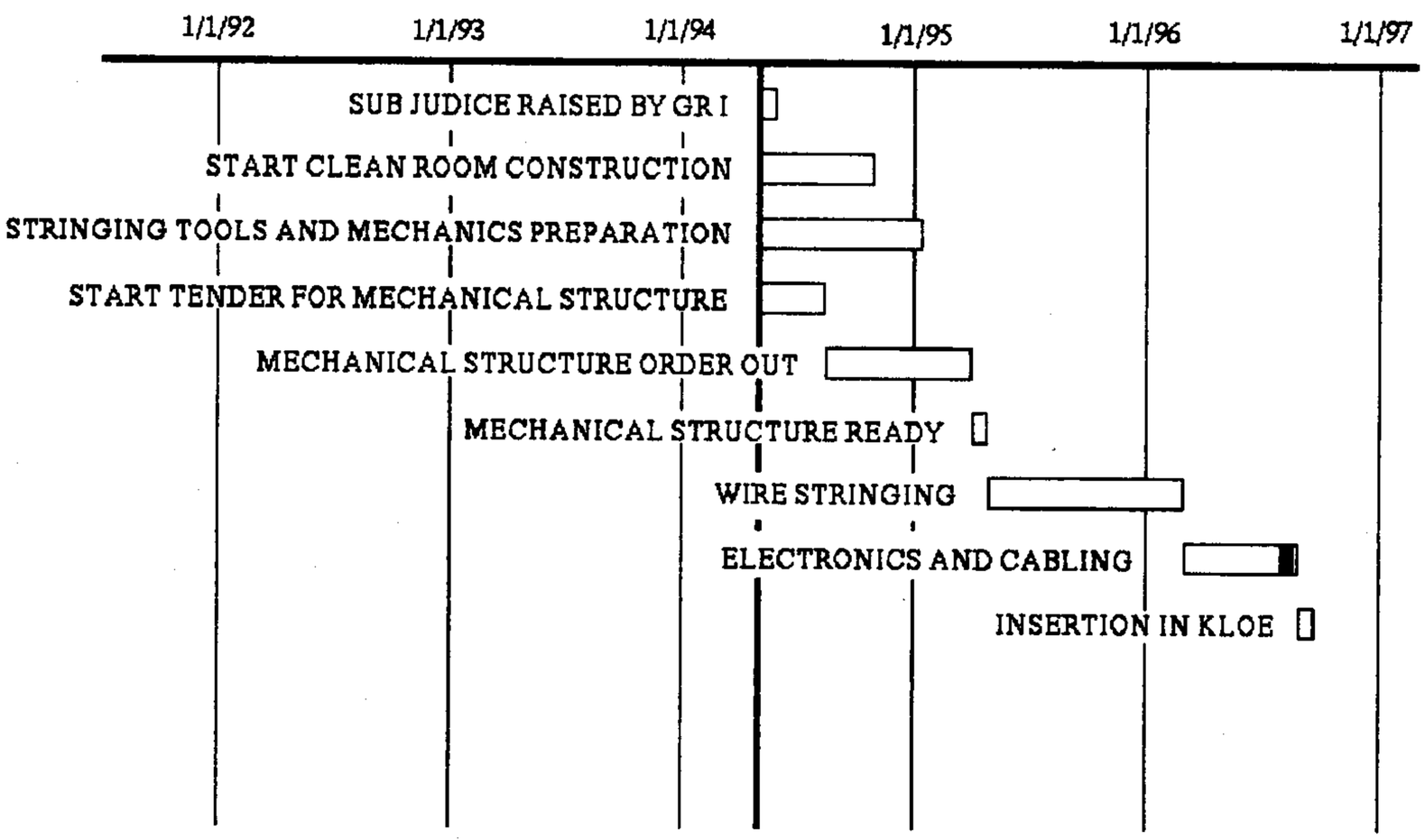

10.2 Costs

Item	Quantity	Unit cost	Total in kL
Mechanical Structure	1	1 500 000	1 500 000
Pins, feedthroughs	150 000	2	300 000
Al wire	200 km	1 500	300 000
W wire	60 km	300	18 000
Wire quality test station	1	10 000	10 000
Stringing frame	1	20 000	20 000
Crimping and stringing stations	5	30 000	150 000
Wire dispensing system	3	20 000	60 000
Robot	1	100 000	100 000
Gas system	1	250 000	250 000
Stringing manpower	8	50 000	400 000
Insertion and transportation tools	1	100 000	100 000
Preamplifiers	12 000	10	120 000
Cables + connectors	12 000	10	120 000
Amplifiers, shapers, discriminators	12 000	40	480 000
Crates	12	10 000	120 000
High Voltage System	500	200	100 000
TOTAL			**4 148 000**

ACKNOWLEDGEMENTS

We wish to acknowledge the fundamental contributions provided by the collaboration's technical staff, to all the construction and commissioning of the prototypes and of the related tools.

In particular, we thank U. Denni, M. A. Frani and E. Iacuessa for their skill and ingenuity in the design, construction and tests of the feedthroughs and of the wiring machine prototypes. We also thank P. Locchi and M. Carletti for the layout, assembly and test of the front-end electronics used in the prototypes; L. Iannotti, A. De Paolis, G. Ferretti, U. Martini, M. Meli of the LNF SPECAS group for having contributed to several steps of the construction and wiring of the prototypes. From the Lecce group, we wish to thank G. Fiore, R. Gerardi, L. Pastore and C. Pinto for their efforts in building the full length prototype sector and for the skill shown in solving many related problems. We want finally to thank K. Kaercher for the invaluable help provided to the group during the P.S.I. tests.

INFN - Laboratori Nazionali di Frascati
P.O.Box 13, I-00044 Frascati (Italy)

KLOE Note No. 98
March 1994

APPENDIX A1.

Cell response parametrization

Patrizia de Simone

A1.1 Introduction

The realistic description of the cell response is an important problem to solve for the KLOE experiment; the main difference with respect to other collider experiments is that the charged tracks coming from the $K_L$at DAΦNE do not start from the interaction point but all over the volume of the drift chamber; the minimum opening angle is about 150°. This particular topology of the events causes a loss of correlation between cell positions and azimuthal emission angle of the detected tracks so that space to time relations has to be known for all wires impact parameter over the full azimuth.

In the next sections I will describe the principal geometric characteristics of the wires inside the chamber, and the procedure adopted to parametrize the cell response. I will then discuss the implementation of the cell response in the Montecarlo and in the reconstruction codes, and finally I will report on the first results on the algorithm resolution.

A1.2 The cells geometry inside the KLOE Drift Chamber

Because of the uniform distribution of the $K_L$decay vertices, the KLOE Drift Chamber has to provide uniform efficiency and resolution for the reconstruction of the $K_L \to \pi^+\pi^-$decays all over the tracking volume. To achieve this result, square cells and non axial wires are chosen, because this configuration allows uniform and isotropic filling of the decay and detection volume.

The maximum radial drop Δr is defined as the distance between the center of one stereo wire projection onto one plane, $z = 0.$, and the wires ring where is the projected wire (see fig. A1.1). The stereo angles of the wires are chosen to give a costant Δr in all layers, thus maintaining the dimensions of the cells.

The stereo angle of the wires $\Theta_s$can be written as a function of the radius r of the layers of wires, as

$$\Theta_s = \mathrm{Arctg}(\frac{1}{Z/2}\sqrt{2r\Delta r + \Delta r^2})$$

where Z is the length of the wire. If the radial drop $\Delta r = 1$cm, the stereo angle ranges from $\simeq$ 51 mrad to $\simeq$ 112 mrad.

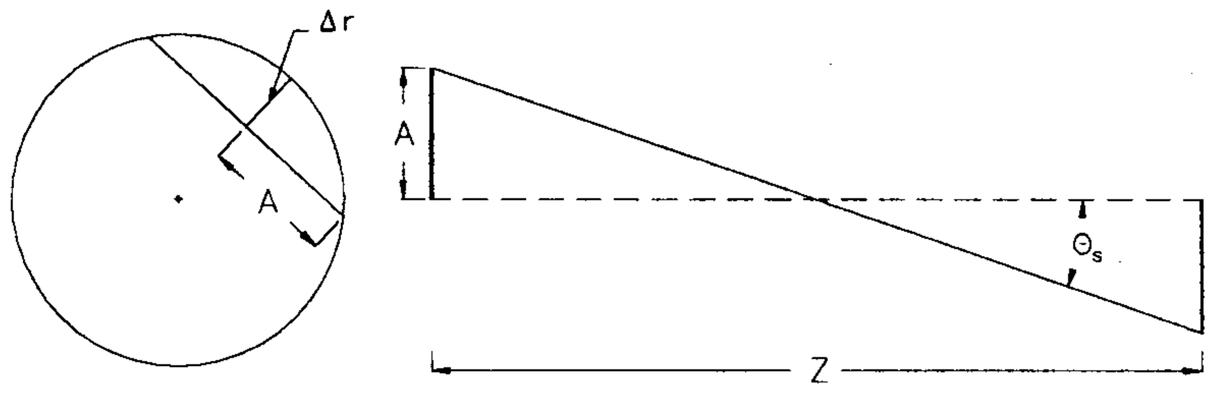

Fig. A1.1. Radial drop.

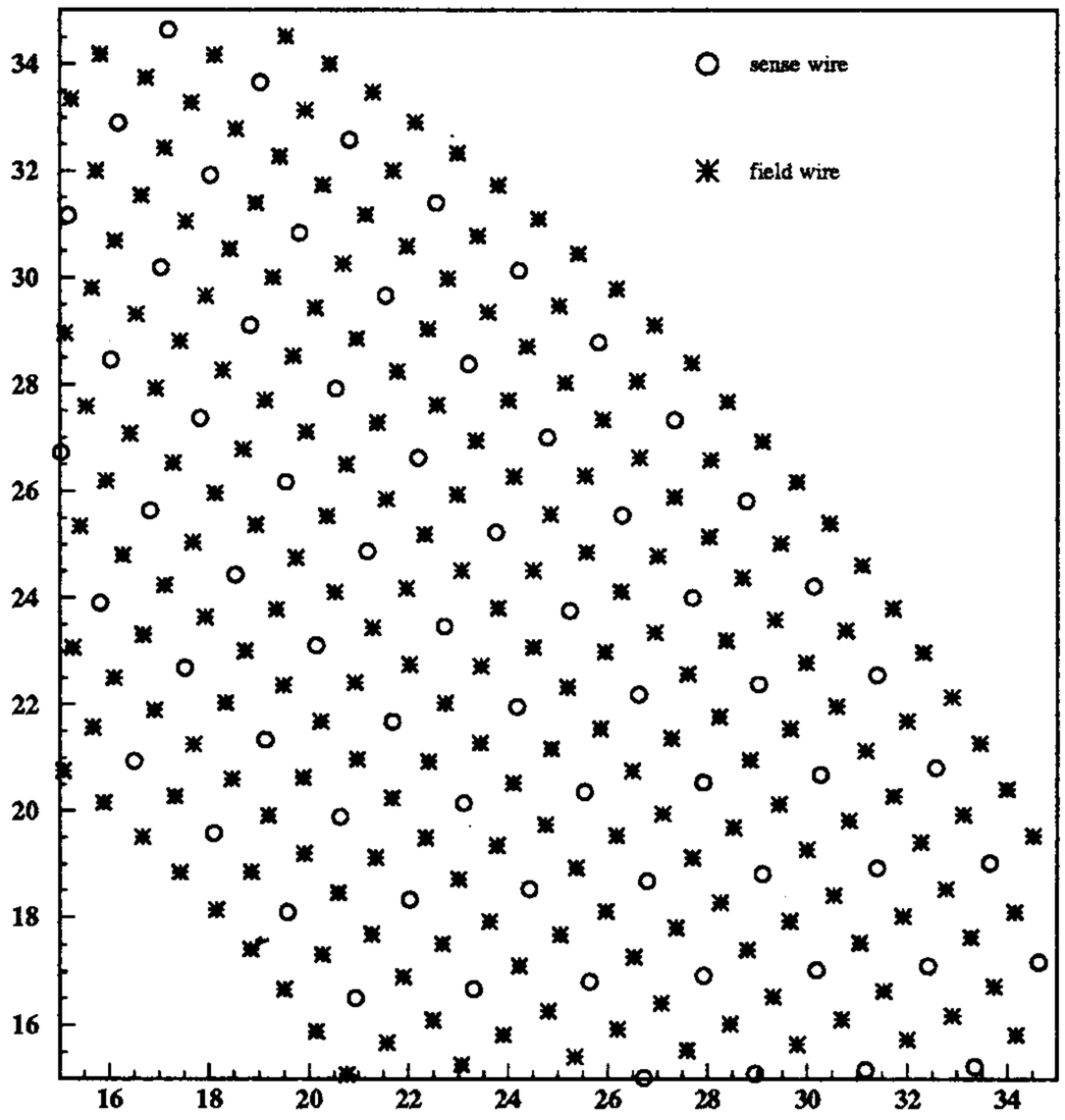

Fig. A1.2. Layout of the wires in one section of the KLOE drift chamber.

Because of the stereo stringing of all wires, the shape of the cells changes along the z axis with a periodicity

$$\Delta z = \frac{\Delta a/2}{|sin(\Theta_s^i - \Theta_s^{i+1})|}$$

where Δa is the cell half size, and the index i runs over the layers of wires. To measure the z coordinate of the tracks, the sense layers have $\Theta_s$angles opposite in sign layer by layer, so a different periodicity follows between the upper part ($\Delta z = 5$ cm) and the lower part of the cells ($\Delta z \simeq$ twice the longitudinal dimension of the chamber).

Due to the particular geometry inside the chamber, the shape of the cells is a distorted square: the extent to which the square shape of the cell is distorted is a function of the azimuthal direction ϕ, the radius r and the z coordinate of each cell. The figure A1.2 shows the layout of the wires in one section of the chamber. This geometry complicates the cell response; at first look it would seem necessary to provide so many cell response parametrizations as the number

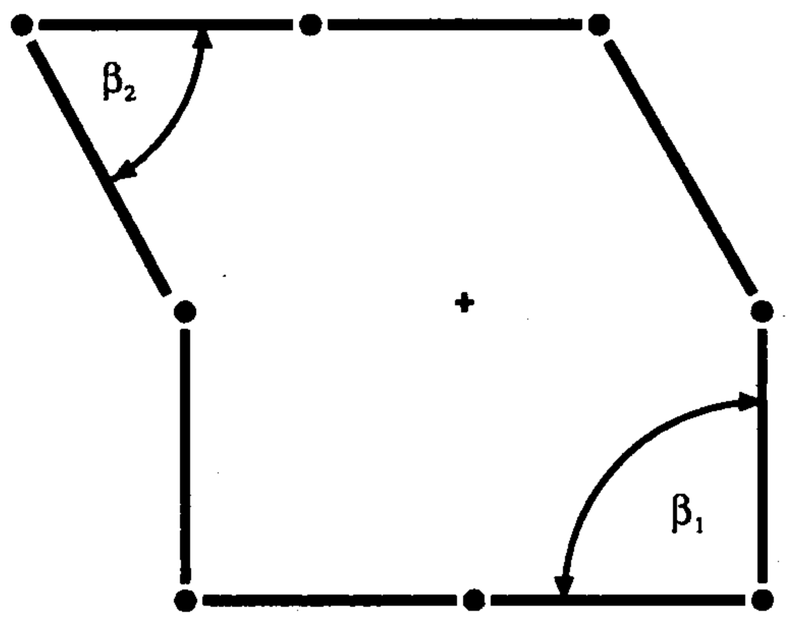

Fig. A1.3. β_1 e β_2 angle.

of cells with different shape.

A1.3 Cell selection

To get a sort of map of the wires disposition inside the chamber, I selected the cells on the basis of their shape and using the two angles β_1 and β_2 showed in figure A1.3.

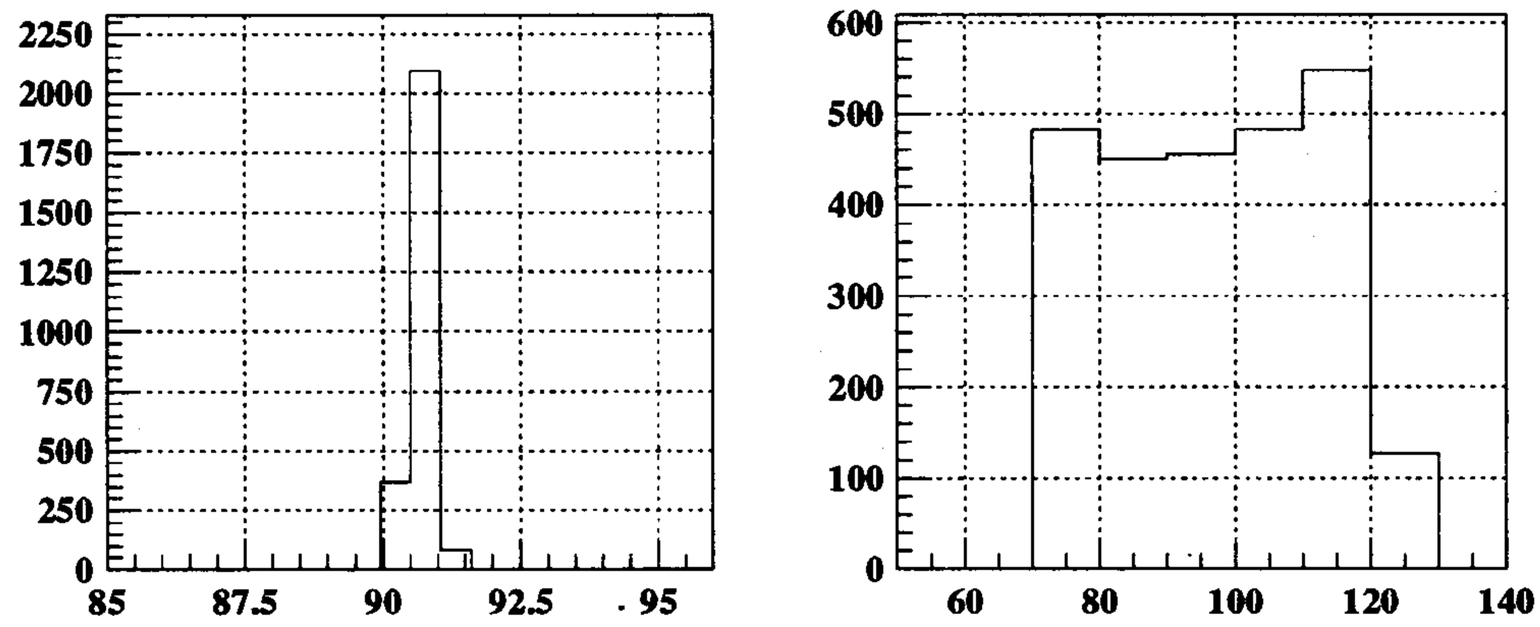

Fig. A1.4. β_1 and β_2 angles distribution.

Figure A1.4 shows the β_1 and β_2 distributions for cells at the plane $z = 0$. Given the periodicity of the upper part of the cell, that is ($\Delta z \simeq$5 cm), the distribution of the β_2 angle does not change with z. Instead, since the periodicity of the lower part of the cell is $\Delta z \simeq$ twice the longitudinal dimension of the chamber, it follows that the distribution of the β_1 angle spreads out with increasing z, up to a maximum of 86^o - 96^o.

A1.4 Cell response parametrization

In order to parametrize the cell response, I used the GARFIELD[37] program developed at the CERN laboratories.

Once that the sense and field wire positions are given as input to GARFIELD, together with the voltages, the gas mixture parameters (the drift velocity and the diffusion coefficient as

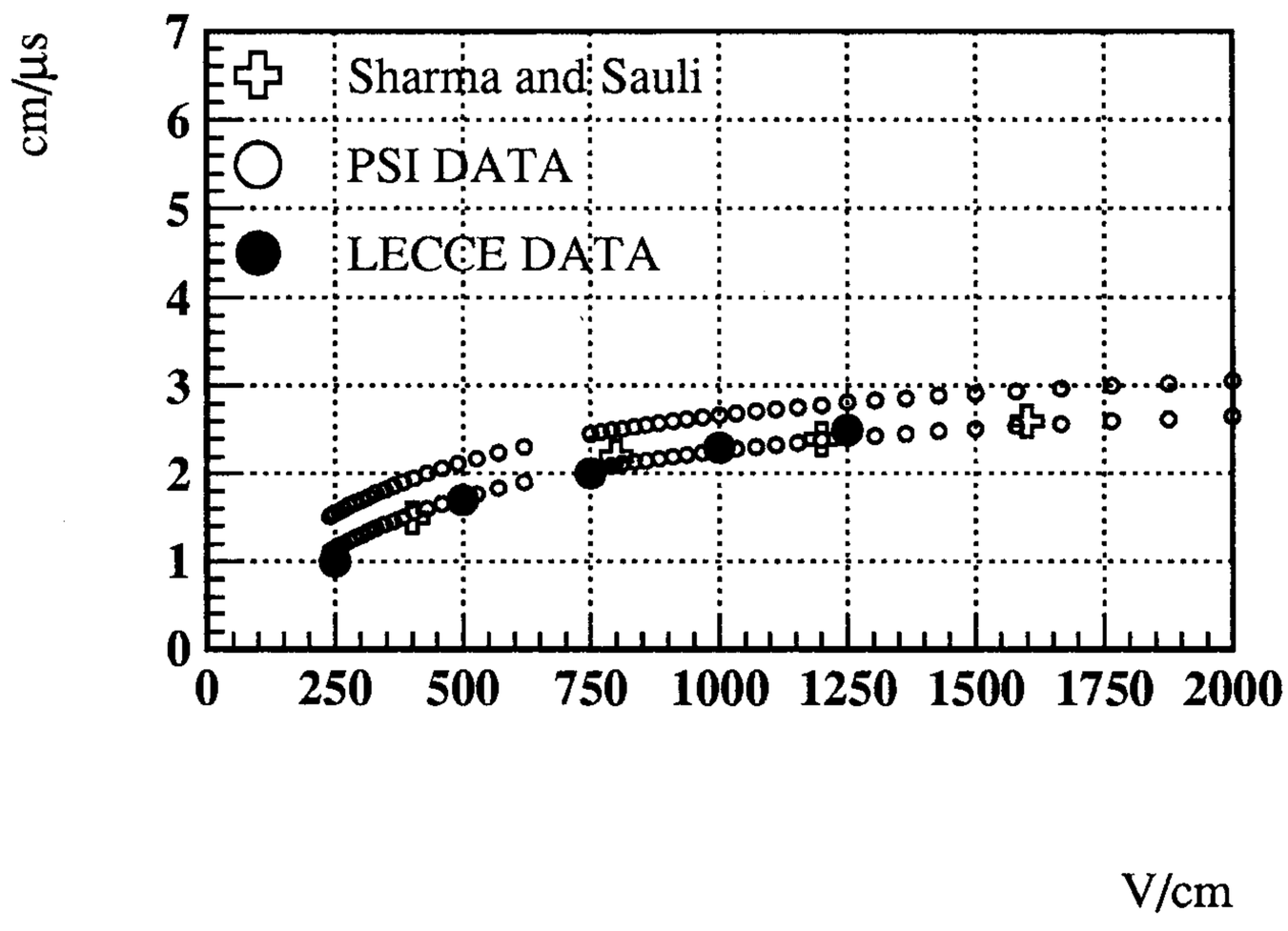

Fig. A1.5. Drift velocity as a function of the electric field (the width of the band is 1σ).

a function of the electric field, the number of cluster produced by minimum ionizing particles), and the applied magnetic field, it is possible to obtain one complete simulation of the drift of the clusters released by the tracks that cross the selected cell, and are collected by the sense wire. For each released cluster, the program computes the (x,y) coordinates of the cluster start point, the *geometric* drift time, and the *diffused* drift time.

The parameters of the gas mixture that I gave as input to GARFIELD have been obtained from the analysis of the data collected at PSI with the two small prototypes 0.1 and 0.2[38] and the data collected at cosmic ray setup with prototype 0[39] .

The table of the drift velocity v_d as a function of the electric field can be derived from the measured space-time relations; in figure A1.5, I show the v_d behaviour as function of E, it has been obtained from the analysis of the data collected by the prototype 0.1, with the gas mixture $90\%He - 10\%iC_4H_{10}$ without magnetic field (the width of the band is 1σ). The drift velocity experimental points are compared with the values computed by Sharma and Sauli[18] and with those measured in Lecce[40] .

The estimates of the diffusion and the number of produced clusters can be obtained from the experimental resolution curve; it is possible to separate the different resolution contributions due to:

- the instrumental resolution of the drift time measurement;
- the ionization statistics of the primary clusters;
- longitudinal diffusion of the electrons.

The diffusion contribution to the resolution is given by

$$\sigma_{diff} = \sqrt{\frac{2Dr}{v_d}} = \sqrt{2Kr}.$$

In the cell region where the diffusion is important, the electric field is restricted in a range where it can be safe to affirm that $D/v_d \simeq cost. = K$, where D is the diffusion coefficient. K is one fit parameter and the analysis of the data collected by the prototype 0, with the gas mixture $90\%He - 10\%iC_4H_{10}$ gives $K = 7 \times 10^{-5}$ cm, which implies a diffusive contribution of $\simeq 120\mu$m for each cm of drift. This number is comparable with the evaluation given by Sharma and Sauli of about 160 μm.

The contribution to the resolution due to the ionization statistics is given by the variance of the difference Δb between the path of the closer released electron and the distance of minimun approach between the track and the wire: $\Delta b = b - \sqrt{b^2 - x^2}$, where x is the point along the track where it has been released the cluster closer to the wire. The x distribution is exponential $f(x) = 1/\lambda e^{-x/\lambda}$, and 2λ is the average distance between two primary ionization acts. Also λ is one fit parameter, and the data analysis produces $\lambda \simeq 380\mu$m.

I used the measured gas mixture parameters as input to GARFIELD to simulate the crossing of the tracks through cells 2×2 cm with $\mathcal{R}_{fs}$= 3:1 and $\mathcal{R}_{fs}$= 2:1 and cells 3×3 cm with $\mathcal{R}_{fs}$= 3:1. For each cell category, I simulated the crossing of the tracks through several cells of different shape. I assumed the magnetic field of the KLOE solenoid to be 6 Kgauss.

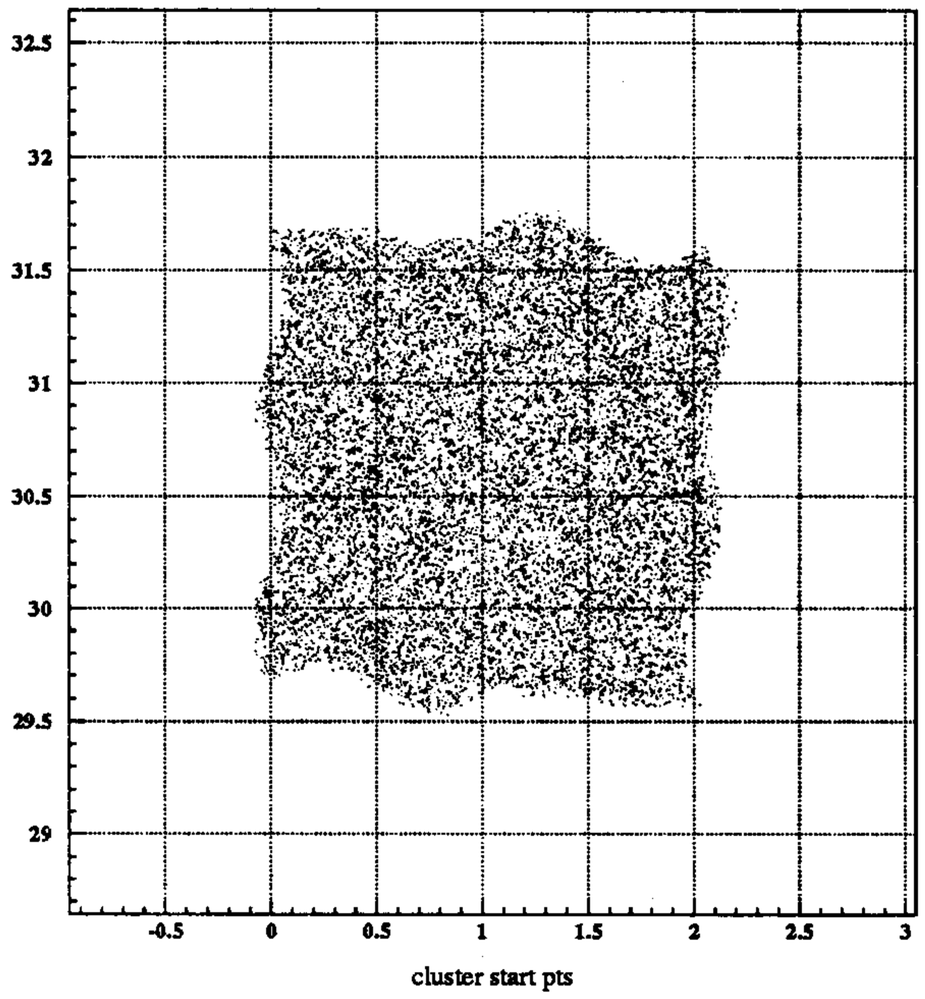

Fig. A1.6. Clusters start points.

In figure A1.6, I show the result of the simulation of the crossing of about 15000 tracks through cells 2×2 cm with $\mathcal{R}_{fs}$=3:1 and $\beta_1 \simeq \beta_2 \simeq 90^o$. The black points that fill the figure are the starting points of the clusters that are relased along the tracks and collected by the sense wire of the cell.

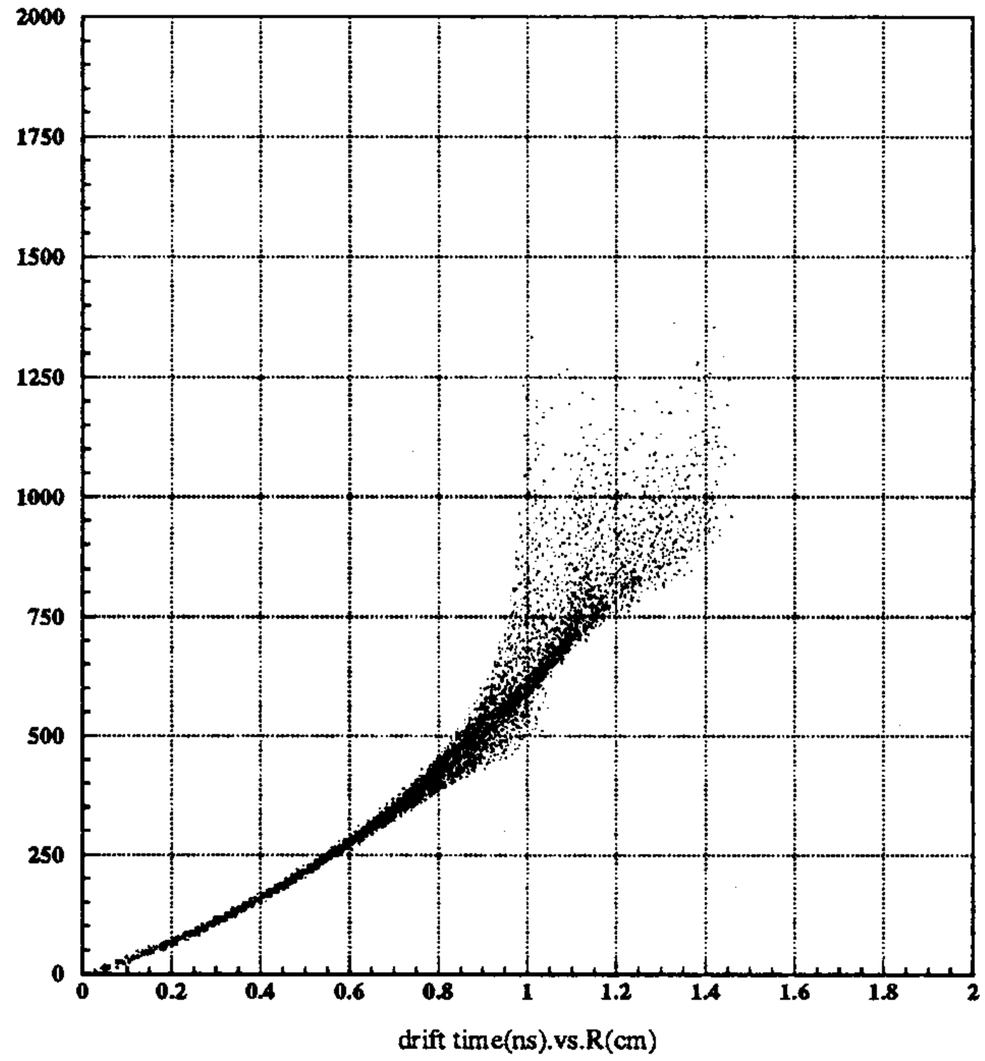

Fig. A1.7. Space time relation: cell $2 \times 2cm$ with $\mathcal{R}_{fs}$= 3:1.

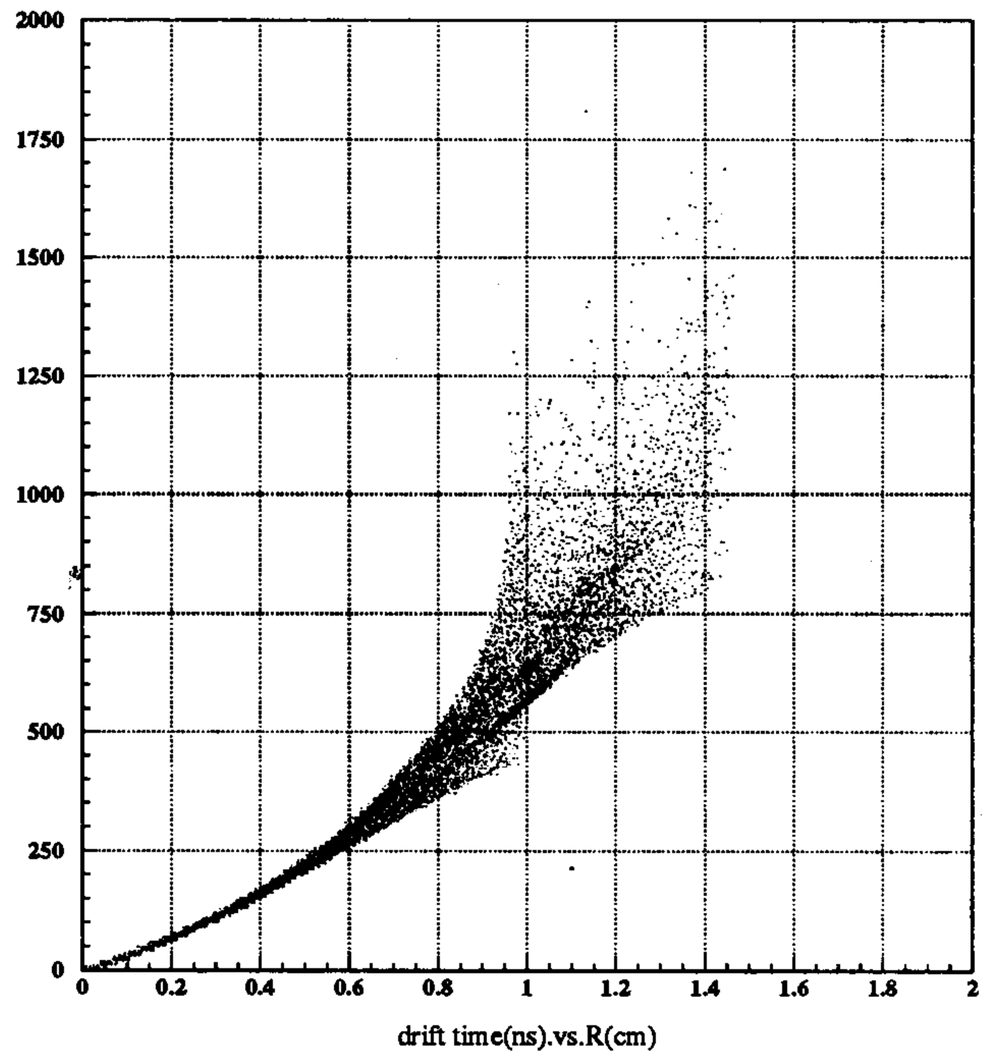

Fig. A1.8. Space time relation: cell $2 \times 2cm$ with $\mathcal{R}_{fs}$= 2:1.

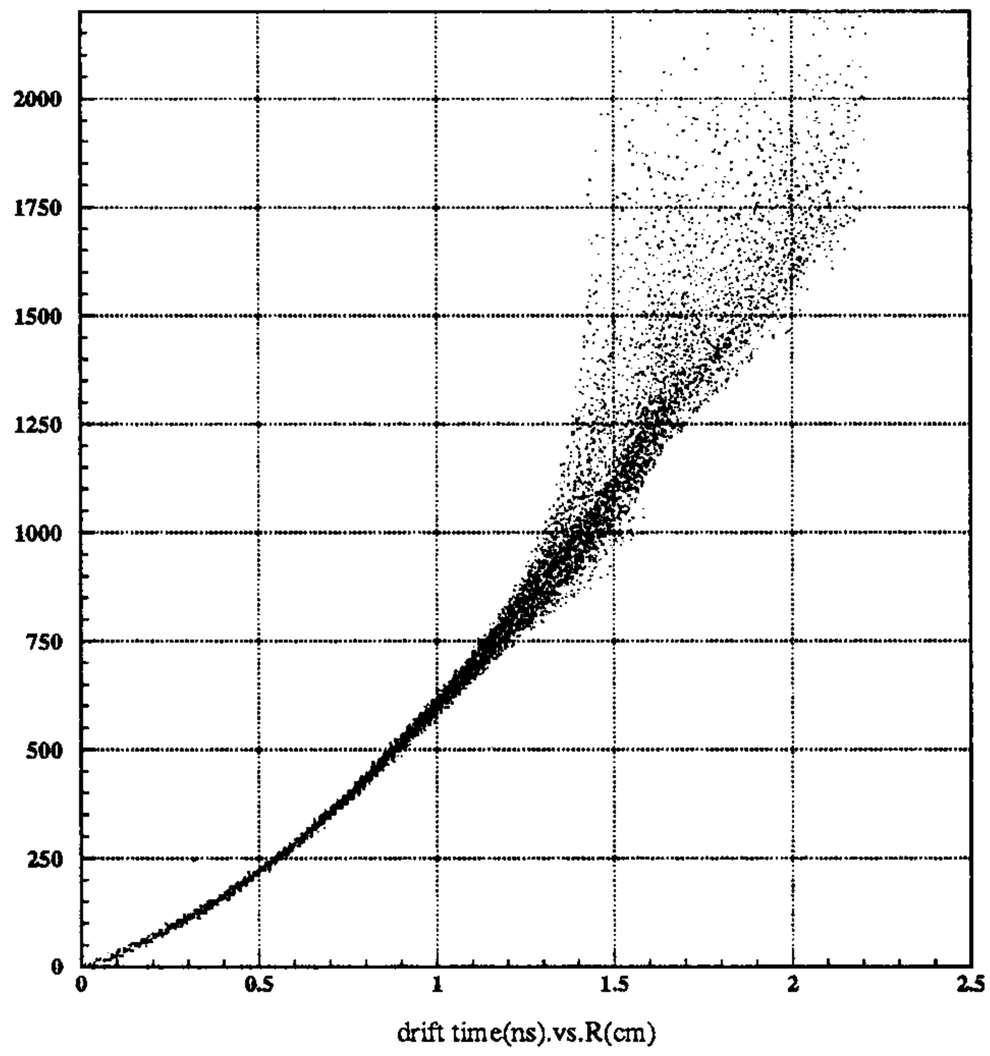

Fig. A1.9. Space time relation: cell $3 \times 3cm$ with $\mathcal{R}_{fs}$= 3:1.

In figures A1.7, A1.8 and A1.9, I show the space-time relations of the clusters collected by cells with different design. The figures make clear that to parametrize the cell response over the greatest possible extent of the collecting area, it is necessary to correct for ϕ the space-time relations at the big impact parameters (for cells 2×2 cm with $\mathcal{R}_{fs}$= 3:1 it is necessary to correct for ϕ at r $\geq$ 0.8 cm, while for cells 2×2 cm with $\mathcal{R}_{fs}$= 2:1 at r $\geq$ 0.6 cm, and for cells 3×3 cm with $\mathcal{R}_{fs}$= 3:1 at r $\geq$ 1.2 cm), where the effects due to the distorted electric field and to the magnetic field, are more important.

The procedure that I have adopted to correct the space-time relations for ϕ, divides the cell 'like a cake' in 36 $\phi - sections$, each one 10^o wide, and it computes the fit of 36 space-time relations, for the clusters coming from the different $\phi - sections$.

I have fitted the reconstructed curves of the 36 $\phi - sections$, with the third order modified Chebychev polynomials :

$$t_d = U_1 + U_2(2a-1) + U_3(8a^2 - 8a + 1) + U_4(32a^3 - 48a^2 + 18a - 1)$$

with

$$0 \leq a \leq 1$$

where

$$a = \frac{r}{r_{limit}}.$$

and r_{limit} is the radius at which the R.M.S. of the reconstructed clusters starting points becomes greater than 500 μm (see figure A1.10 that shows one example of the fits of the reconstructed

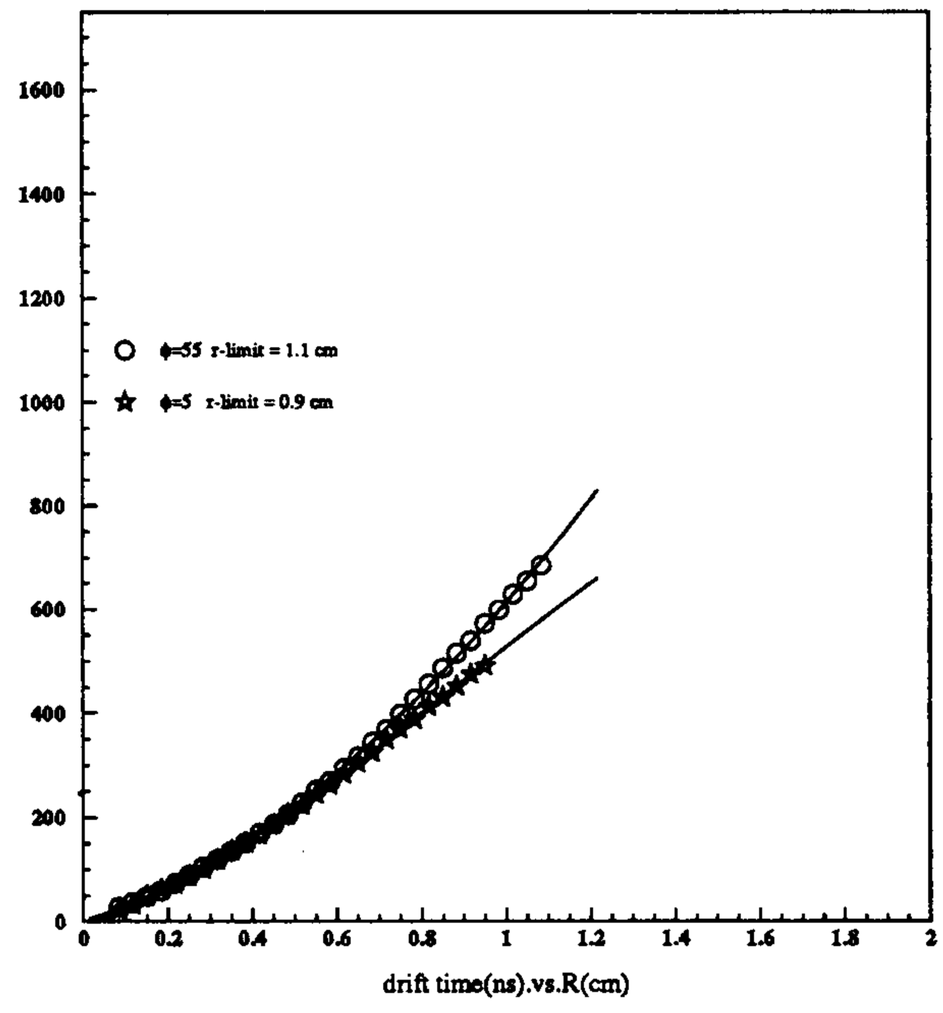

Fig. A1.10. Example of the space time relation fit.

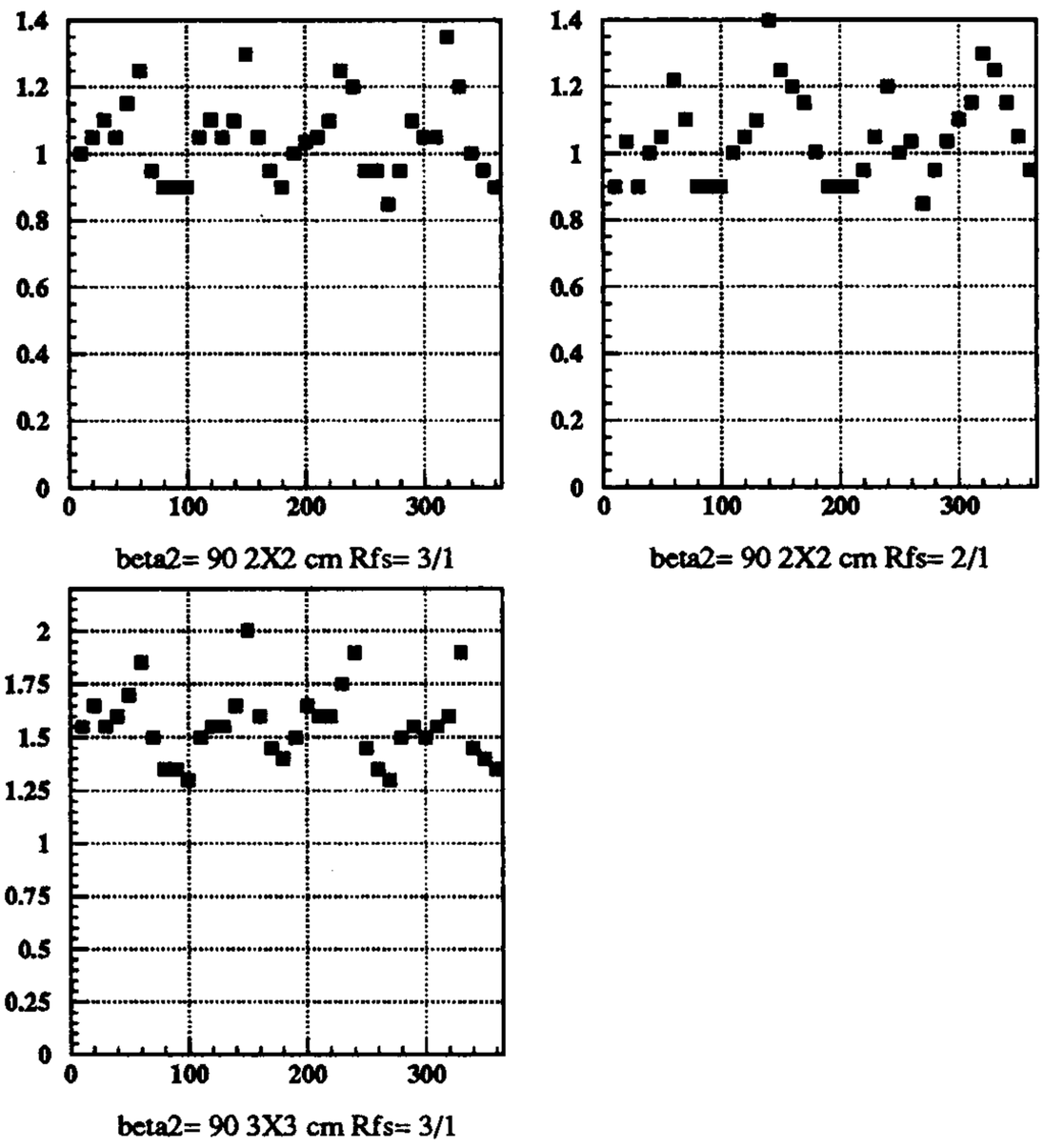

Fig. A1.11. r_{limit} as a function of the $\phi - sections$ for different cell designs.

curves of two ϕ – *sections*). With the parameter r_{limit} I define a sort of effective cell within which the fit procedure is able to produce a good parametrization of the space-time relations.

To give an idea of the dimensions of the effective cells, in figure A1.11 I show the behaviour of r_{limit} as a function of the ϕ – *sections*, for cells 2×2 cm with ratios $\mathcal{R}_{fs}$=3:1 and $\mathcal{R}_{fs}$= 2:1, and for cells 3×3 cm with ratio $\mathcal{R}_{fs}$= 3:1. The oscillations of r_{limit} are due to the shape of the cell: the shape of the effective cell is close to a square and its area is about 90% of the geometric area of the cell.

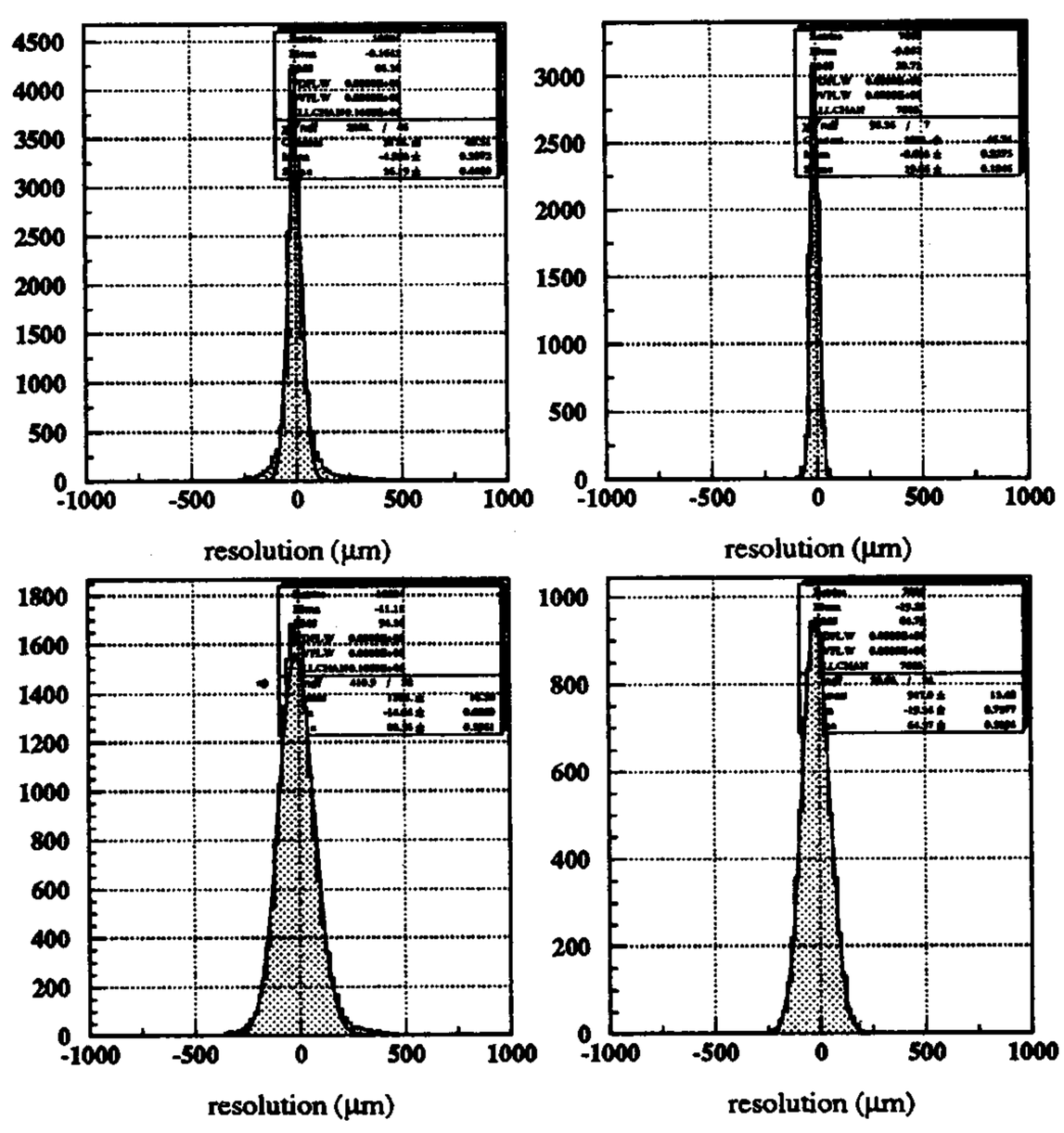

Fig. A1.12. Reconstruction resolutions of the cluster starting points in μm, due to the parametrization algorithm and to the diffusion.

Figure A1.12 shows one example of the resolutions to reconstruct the cluster points, they have been obtained using the described parametrizations for one cell with $\beta_1 \simeq \beta_2 \simeq 90^o$, 2×2 cm and $\mathcal{R}_{fs}$= 3:1. The first two distributions are due only to the parametrization algorithm, the gaussian fit of the first distribution gives one evaluation of the resolution for clusters collected over the complete effective area of the cell, while the second distribution gives the resolution for clusters with impact parameter within the range $(0.2 \leq r \leq 0.7)$ cm (this evaluation of σ is comparable with the experimental resolutions because in the quoted r range the effects due to the low statistics of clusters production in helium important at low r, and to the distortion of the electric and magnetic fields, are neglectable). The second two distributions show the resolutions after adding diffusion.

Observing how the resolution changes using the response parametrizations of one cell with angles β_1 and β_2, for cells with $86^o \leq \beta_1' \leq 96^o$ and $\beta_2' = \beta_2 \pm 5^o$, I have concluded that only

six different parametrizations are enough to describe the cell response over the entire chamber volume, in fact the standard deviations worsen only of a few per cent.

In tables A1.1, A1.2 and A1.3, I listed the resolutions obtained with the six selected parametrizations for cells 2 × 2 cm with ratios $\mathcal{R}_{fs}$= 3:1 and $\mathcal{R}_{fs}$= 2:1, and for cells 3 × 3 cm with ratios $\mathcal{R}_{fs}$= 3:1.

				$0.2 \leq r < 0.7$ cm	
size	$\mathcal{R}_{fs}$	$\sigma_{fit}(\mu m)$	$\sigma_{diff}(\mu m)$	$\sigma_{fit}(\mu m)$	$\sigma_{diff}(\mu m)$
$\approx 90^o$	70^o	35.4 ± 0.5	84.9 ± 0.7	21.2 ± 0.2	65.0 ± 0.6
	80^o	40.5 ± 0.6	85.3 ± 0.8	26.9 ± 0.4	69.2 ± 0.8
	90^o	36.2 ± 0.4	83.6 ± 0.6	19.6 ± 0.2	64.6 ± 0.5
	100^o	38.1 ± 0.5	84.1 ± 0.6	21.6 ± 0.2	65.3 ± 0.6
	110^o	45.6 ± 0.6	86.3 ± 0.9	29.3 ± 0.4	69.1 ± 0.8
	120^o	41.2 ± 0.6	85.9 ± 0.8	26.6 ± 0.4	68.6 ± 0.8

Table A1.1. Resolution as function of the cell shape - cells 2 × 2 cm with $\mathcal{R}_{fs}$= 3:1.

				$0.2 \leq r < 0.7$ cm	
size	$\mathcal{R}_{fs}$	$\sigma_{fit}(\mu m)$	$\sigma_{diff}(\mu m)$	$\sigma_{fit}(\mu m)$	$\sigma_{diff}(\mu m)$
$\approx 90^o$	70^o	46.6 ± 0.7	86.6 ± 0.8	26.1 ± 0.4	65.3 ± 0.7
	80^o	46.4 ± 0.7	86.8 ± 0.9	29.9 ± 0.4	68.8 ± 0.8
	90^o	43.1 ± 0.5	84.9 ± 0.6	25.3 ± 0.3	65.2 ± 0.6
	100^o	44.1 ± 0.5	82.9 ± 0.7	28.6 ± 0.3	67.2 ± 0.7
	110^o	47.1 ± 0.5	93.3 ± 0.8	28.0 ± 0.6	67.9 ± 0.9
	120^o	47.0 ± 0.7	89.7 ± 0.9	28.6 ± 0.3	69.6 ± 0.8

Table A1.2. Resolution as function of the cell shape - cells 2 × 2 cm with $\mathcal{R}_{fs}$= 2:1.

A1.5 Implementation of the cell response parametrization in the Montecarlo program

The Montecarlo code provides[41] for each fired sense wire the distance of minimum approach between the track and the wire; the aim of the implementation of the parametrization of cell response in the Montecarlo, is to translate this information into the drift time that corresponds to the measured value.

To begin, I wrote one routine,(SHAPE-CELL) that, given as input the coordinates of the tracks at the current point and the index of the fired sense wire, is able to recognize the shape

				$0.2 \leq r < 1.2$ cm	
size	$\mathcal{R}_{fs}$	$\sigma_{fit}(\mu m)$	$\sigma_{diff}(\mu m)$	$\sigma_{fit}(\mu m)$	$\sigma_{diff}(\mu m)$
$\approx 90^o$	70^o	58.3 ± 0.7	108.2 ± 0.9	39.5 ± 0.5	85.4 ± 0.8
	80^o	56.8 ± 0.7	108.2 ± 0.9	41.5 ± 0.4	84.6 ± 0.7
	90^o	55.8 ± 0.6	107.9 ± 0.9	40.7 ± 0.4	82.7 ± 0.7
	100^o	55.2 ± 0.7	103.5 ± 0.9	40.8 ± 0.4	84.5 ± 0.7
	110^o	51.3 ± 0.6	102.8 ± 0.9	39.2 ± 0.4	83.2 ± 0.7
	120^o	54.4 ± 0.6	104.8 ± 0.9	40.9 ± 0.4	84.6 ± 0.8

Table A1.3. Resolution as function of the cell shape - cells 3×3 cm with $\mathcal{R}_{fs}$= 3:1.

of the cell, in other words, the routine computes the angles β_2.

Then, the routine DRF-TIME computes the drift time. The distance of minimum approach given as input to the routine has to be corrected because of the effect due to the ionization statistics of primary clusters and to the longitudinal diffusion of the electrons.

Because of the low ionization statistics in helium, the distance of minimum approach is systematically less then the distance covered by the first cluster that reaches the sense wire; this effect is more important at small impact parameters. After this correction the program adds the contribution due to the diffusion, and finally, given the shape of the cell (β_2), it assigns the corrispondent cell response parametrization to calculate the drift time. At the moment the parameters are stored in one DATA BLOCK.

Finally, the routine adds the contribution to the resolution due to the instrumental resolution of the drift time measure: $\sigma_e \simeq 5\, ns$. Such number is a conservative estimate obtained from PSI data.

In figure A1.13, I show the simulated resolution curve: the parameters of the fit are respectively $K = 0.67 \times 10^{-4}$ cm, $\lambda = (0.377 \pm 0.002) \times 10^{-1}$ cm and $\sigma_e = (5.1 \pm 0.4)$ ns, with $\chi^2/NDOF \simeq 1.8$.

A1.6 Implementation of the cell response parametrization in the reconstruction program

As stressed before the cells response parametrization depend on the cell shape, the impact parameter and the azimuthal incidence angle, so, the detailed time-space relations cannot be used at the pattern recognition level because of the lack of space informations about the tracks. In the part of the track fit routine[42] which simulates the pattern recognition, an average time-space relation is used, it depends on the value of the drift time only and it has been obtained from the fit of the Montecarlo simulated scatter plot of the drift time versus the drift distance.

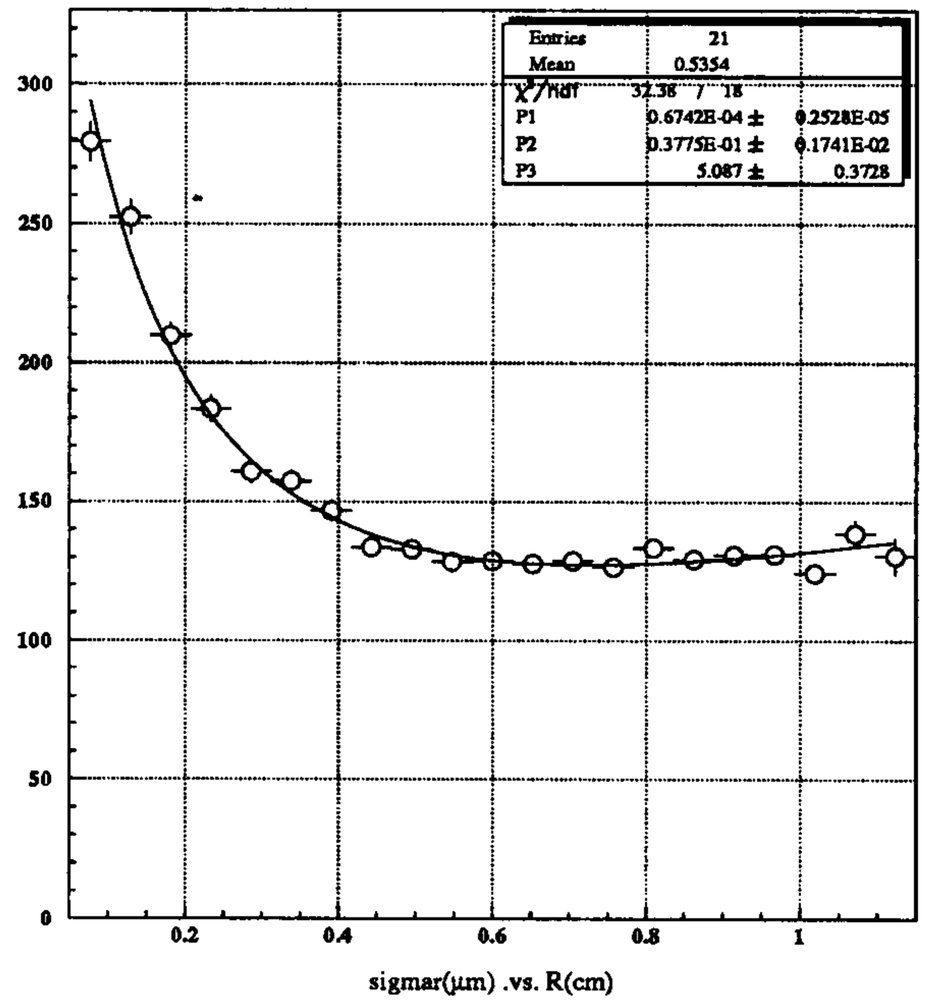

Fig. A1.13. Simulated resolution curve.

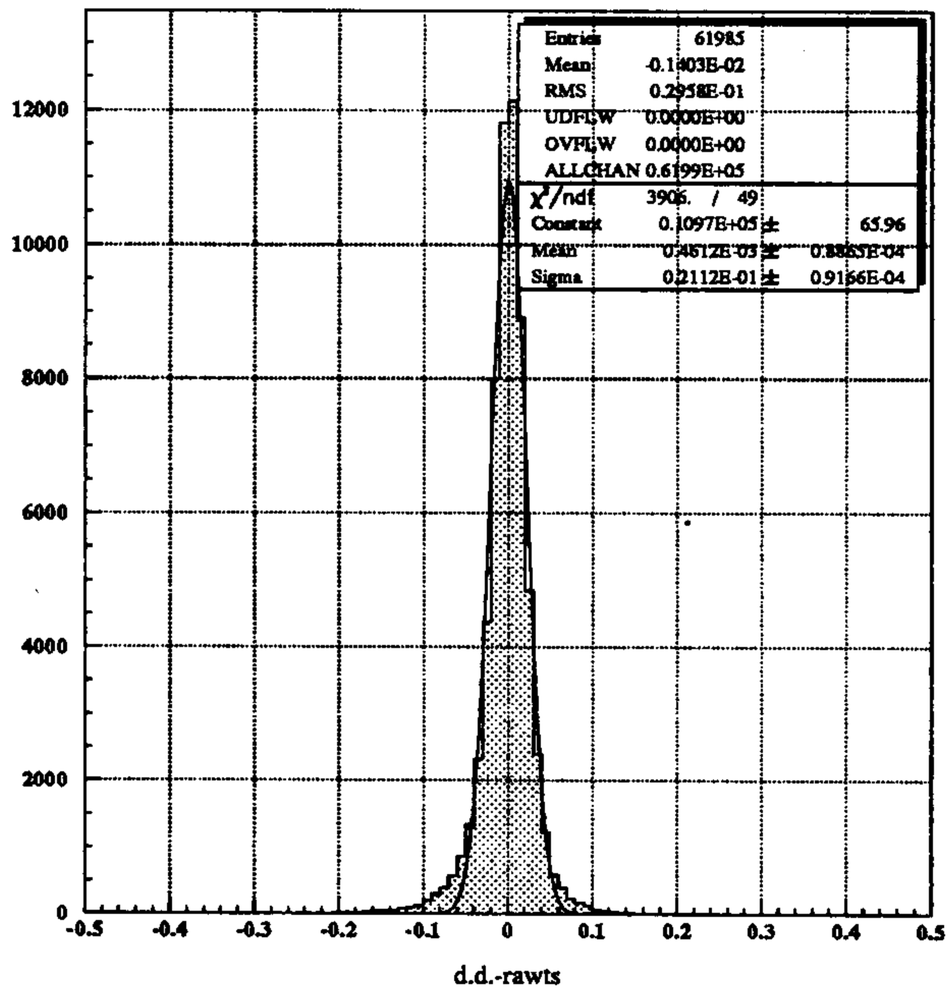

Fig. A1.14. Raw drift distance sigma : cell $2 \times 2cm$ with $\mathcal{R}_{fs}$= 3:1.

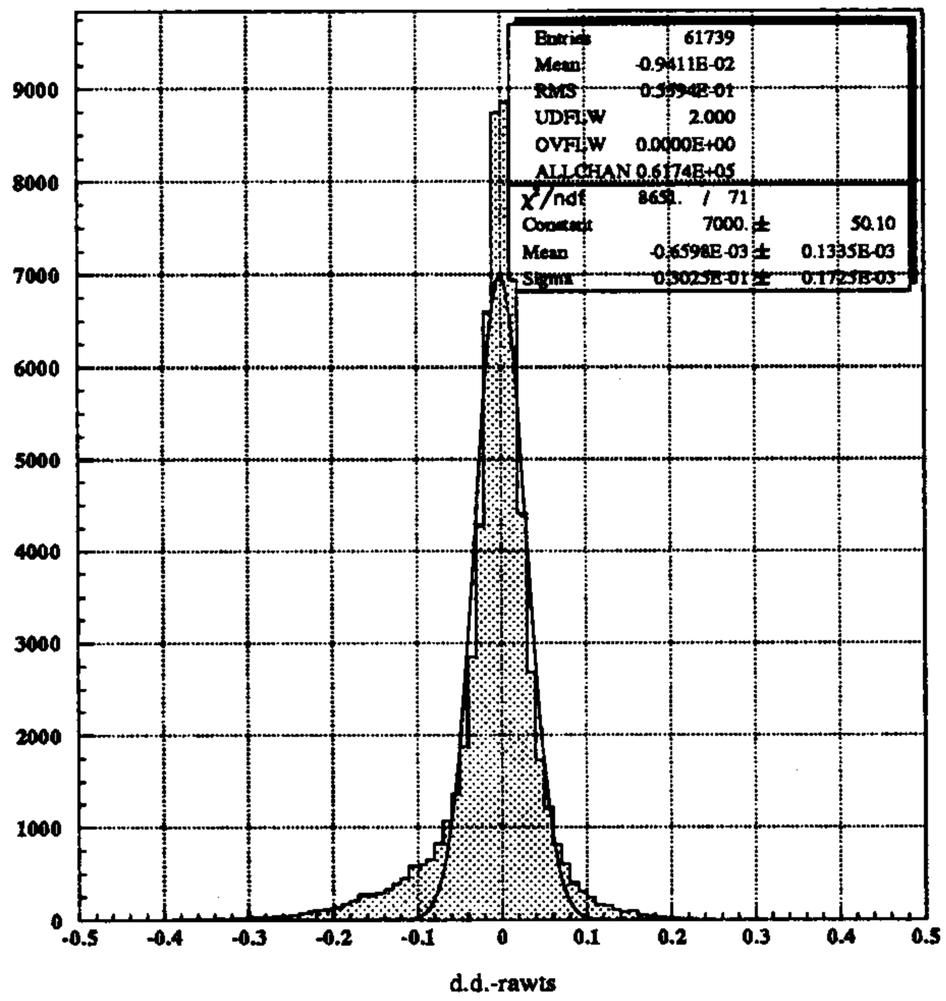

Fig. A1.15. Raw drift distance sigma : cell $2 \times 2cm$ with $\mathcal{R}_{fs}$= 2:1.

$K^0_L \to \pi^+\pi^-$ (84(2ϖ2)⊂ 37⊂ 50⊂ 80%) 08/[illegible]Z19.06

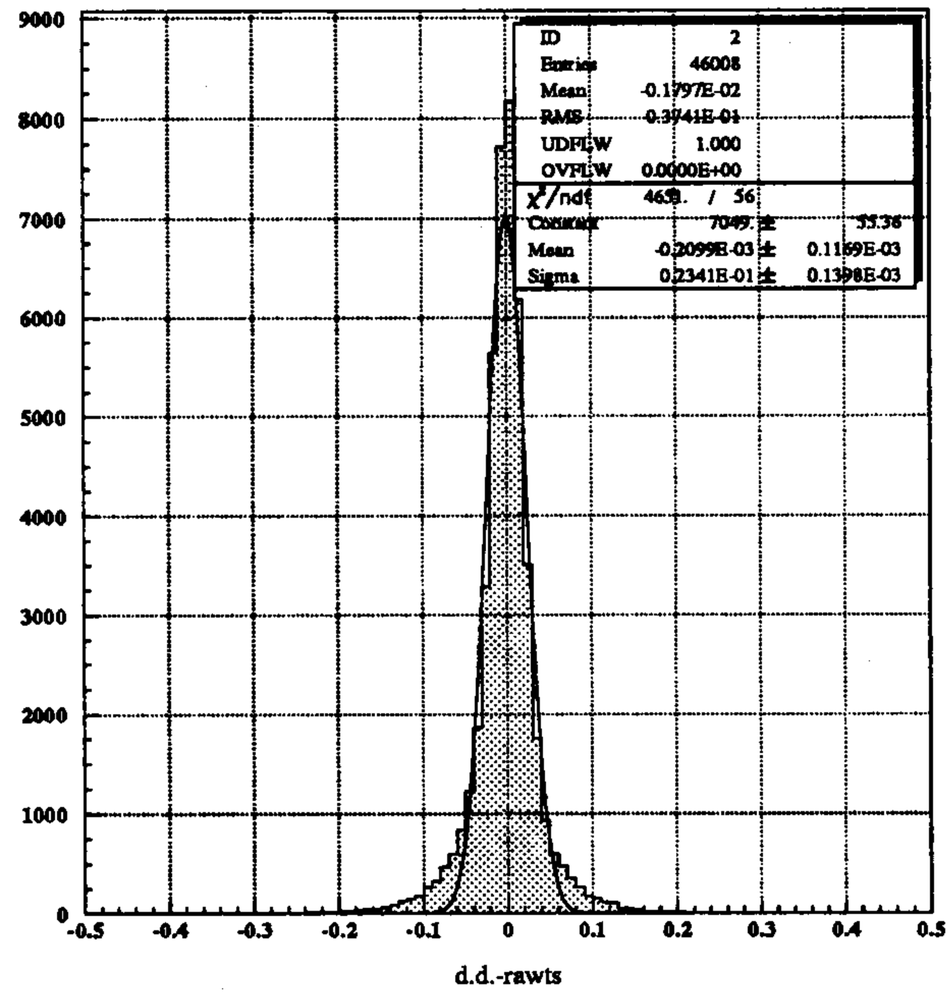

Fig. A1.16. Raw drift distance sigma : cell $3 \times 3cm$ with $\mathcal{R}_{fs}$= 3:1.

Figures A1.14, A1.15, and A1.16, show the σ of the reconstructed drift distances using only the averaged time-space relations.

The detailed time-space relations have been implemented in the iterative procedure of the track fit, for the 2 × 2 cm cells design with $\mathcal{R}_{fs}$= 3:1 and with $\mathcal{R}_{fs}$= 2:1, and for the 3 × 3 cm

cells design with $\mathcal{R}_{fs}$=3:1, with the aim to provide an accurate evaluation of the drift distance and of its uncertainty σ. To this purpose the routine (TSREL) that I added to the tracks reconstruction program, recognizes the shape of the cells crossed by the charged particles, and assigns the appropriate response parametrizations.

During the iterative procedure, the estimates of the points along the tracks that are outside the effective area of the cells are treated using the averaged time-space relation and the corresponding σ, only at the last iteration if the points are outside the effective area, they are rejected; the percentage of the rejected points for all the analysed cell designs is about 10%, as expected because of the ratio between the effective and the geometric cell area, that is about 90%.

I used the Montecarlo program to produce three samples of events $K_L \rightarrow \pi^+\pi^-$, each sample for each of the three different cell design.

In tables A1.4, A1.5 and A1.6, I compare the resolutions of some track fitted parameters (the azimuthal angle ϕ, and the cotangent of the polar angle θ) and the fitted coordinates of the $K_L$decay vertices, obtained with a raw time space relation, with those obtained using the detailed time space relations. It is striking the improvement in resolution with a detailed parametrization of the cells response, particularly for the cells 2 × 2 cm with $\mathcal{R}_{fs}$= 2:1 which have an open electric field configuration, and for the cells 3 × 3 cm with $\mathcal{R}_{fs}$= 3:1.

	Raw Time→ space	Time→ space relations
$(P_T^{fit} - P_T)/P_T$	$(0.38 \pm 0.02) \times 10^{-2}$	$(0.39 \pm 0.02) \times 10^{-2}$
$\phi_{fit} - \phi$	$4.3 \pm 0.2\, mrad$	$3.9 \pm 0.2\, mrad$
$\phi_{(vertex-fit)} - \phi$	$1.9 \pm 0.1\, mrad$	$1.9 \pm 0.1\, mrad$
$cot(\theta)_{fit} - cot(\theta)$	$(3.6 \pm 0.2) \times 10^{-2}$	$(3.3 \pm 0.1) \times 10^{-2}$
$X_{vertex}^{fit} - X_{vertex}$	$498 \pm 43\, \mu m$	$420 \pm 35\, \mu m$
$Y_{vertex}^{fit} - Y_{vertex}$	$452 \pm 31\, \mu m$	$416 \pm 32\, \mu m$
$Z_{vertex}^{fit} - Z_{vertex}$	$0.14 \pm 0.01\, cm$	$0.10 \pm 0.01\, cm$

Table A1.4. Cells 2 × 2 cm with $\mathcal{R}_{fs}$= 3:1.

	Raw Time→ space	Time→ space relations
$(P_T^{fit} - P_T)/P_T$	$(0.41 \pm 0.02) \times 10^{-2}$	$(0.36 \pm 0.02) \times 10^{-2}$
$\phi_{fit} - \phi$	$4.3 \pm 0.3\, mrad$	$3.2 \pm 0.2\, mrad$
$\phi_{(vertex-fit)} - \phi$	$2.4 \pm 0.1\, mrad$	$1.8 \pm 0.1\, mrad$
$cot(\theta)_{fit} - cot(\theta)$	$(4.2 \pm 0.3) \times 10^{-2}$	$(3.6 \pm 0.1) \times 10^{-2}$
$X_{vertex}^{fit} - X_{vertex}$	$596 \pm 63\, \mu m$	$399 \pm 32\, \mu m$
$Y_{vertex}^{fit} - Y_{vertex}$	$712 \pm 62\, \mu m$	$508 \pm 59\, \mu m$
$Z_{vertex}^{fit} - Z_{vertex}$	$0.23 \pm 0.02\, cm$	$0.12 \pm 0.01\, cm$

Table A1.5. Cells 2×2 cm with $\mathcal{R}_{fs}$= 2:1.

	Raw Time→ space	Time→ space relations
$(P_T^{fit} - P_T)/P_T$	$(0.38 \pm 0.02) \times 10^{-2}$	$(0.33 \pm 0.02) \times 10^{-2}$
$\phi_{fit} - \phi$	$4.3 \pm 0.2\, mrad$	$2.7 \pm 0.1\, mrad$
$\phi_{(vertex-fit)} - \phi$	$2.2 \pm 0.1\, mrad$	$1.8 \pm 0.1\, mrad$
$cot(\theta)_{fit} - cot(\theta)$	$(4.2 \pm 0.2) \times 10^{-2}$	$(3.4 \pm 0.1) \times 10^{-2}$
$X_{vertex}^{fit} - X_{vertex}$	$606 \pm 41\, \mu m$	$437 \pm 90\, \mu m$
$Y_{vertex}^{fit} - Y_{vertex}$	$506 \pm 49\, \mu m$	$376 \pm 26\, \mu m$
$Z_{vertex}^{fit} - Z_{vertex}$	$0.19 \pm 0.01\, cm$	$0.12 \pm 0.06\, cm$

Table A1.6. Cells 3×3 cm with $\mathcal{R}_{fs}$= 3:1.

A1.7 Conclusions

The procedure to describe in a realistic way the cell response has been defined. The reconstruction program of the tracks is now able to recognize the shape of the cells crossed by the charged particles, and to assign to each cell the appropriate response parametrization.

The very first results about the reconstruction resolutions show the importance to have a good knowledge of the cell response.

INFN - Laboratori Nazionali di Frascati
P.O.Box 13, I-00044 Frascati (Italy)

KLOE Note No. 87
January, 1994

APPENDIX A2.

Measurement of the Young Modulus of a carbon fiber-epoxy sample

Stefano Moccia
Andrea Gaddi
Alvaro Ceccarelli

ABSTRACT

We present a method to obtain the Young Modulus from measurements of the deflections of a loaded square plate made of carbon fiber in an epoxy resin matrix.

This method is particularly suitable because this kind of material is non-isotropic, and its mechanical properties depend on several parameters, specially fiber-epoxy volume ratio, manufacturing procedures, orientation and number of fiber layers, so that the theoretical formulas cannot always give reliable results.

A2.1 THE KLOE DRIFT CHAMBER

Fig. A2.1 shows the mechanical structure of the KLOE drift chamber for track particles K decays. Efficient tracking requires a large number of wires, up to 100000, which are tensioned between the two endplates. The total axial load acting over each endplate is about 5000 kg. In order to string the wires to the required tension the maximum axial displacement of each endplate has to be lower than 3 mm. In addition the thickness of the plates must be as small as possible, in radiation length, in order to minimize the degradation of photons before they reach the electromagnetic calorimeter. Aluminum and carbon fiber-epoxy composite appears to satisfy these requirements, the latter seems being better economical and less dense.

A2.2 Composite carbon fiber-epoxy sample

Stesalit provided us a square sample to check its mechanical properties. The sample overall dimensions are shown in fig. A2.2.

It built piling up layers of preimpregnated layers of fibers and epoxy, each with different orientation. Every 1 mm consists of 4 layers each 0.25 mm thick rotated by 45 degrees one respect to the previous one. This procedure results in a quasi-isotropic mechanical behaviour to the final plate.

The two Young Moduli of the carbon fibers, whose commercial name is T300, are:

$$E_{long} = 11040 \text{ Kg/mm}^2$$

$$E_{trasv} = 730 \text{ Kg/mm}^2$$

The carbon fiber-epoxy volume ratio is 50%.

The Young Modulus of the sample material is to be expected to be:

$$E_{long} = E_{trasv} = 4300 \text{ Kg/mm}^2$$

which allows buiding end walls of the required stiffness.

From now on this value will be called *theoretical Young Modulus*, E_{theor}. On one side of the sample there is a 0.07 mm thick copper foil which is necessary for electrostatic reasons.

A2.3 Measuring procedure

The deformation of a loaded plate is given by the following expression:

$$\frac{\delta = P(1-\nu^2)}{Et^3 f_{b.c.},}$$

where:

δ = deformation along a direction normal to the plane of the plate

P = load acting on the plate

ν = Poisson coefficient (assumed to be 0.3)

E = Young Modulus of the plate material

t = plate thickness

$f_{b.c.}$ = function of the boundary conditions, i.e. where and how the plate is restrained.

This was the measuring procedure:

1 The plate was loaded on the center over a very small area. The plate was simply supported on two opposite sides.

2 Deflection was measured in several points of the plate, over a 5×5 cm^2 grid as shown in fig. A2.2.

3 With a finite element code, whose name is Ansys 4.4A, we computed the displacements of a plate with the same geometric dimensions as the sample, loaded in the same way and with a Young Modulus equal to E_{theor}.

4 From equation 1 and comparing the measured displacements with the computed ones in the same point of the grid, we obtained for each point a value of the Young Modulus from the following expression:

$$\frac{E_{theor} = \delta_{theor} E_{theor}}{\delta_{meas}}$$

5 The mean of the measure values is the mean effective Young Modulus of the material.

6 We repeated the steps 1, 2, 4, 5, increasing each time the load acting on the plate, until the mean measured Young Modulus did not change in a significant way increasing the load.

Step number 6 was necessary in order to control systematic errors, basically due to positioning errors of the measuring touch probe (with digital readout into a PC) which is manually positioned, by increasing the measured effect.

We repeated steps 1, 2, 4, 5, 6 on the plate rotated of 90 degrees in order to verify the material quasi-isotropic behaviour.

Due to the fact that the endplates will be drilled to allow the wires to be fixed, steps 1, 2, 4, 5, 6 have been repeated on the plate drilled with 3 mm diameter holes arranged according to a square grid of 1 cm sides.

This measurement gave the effective Young Modulus loss due to the holes.

A2.4 Supporting frame

To simulate as well as possible the ideal conditions (plate simply supported, concentrated load) which we had carried out with the finite element analysis, we used a supporting frame shown in fig. A2.33 It consists of two grinded ground bars with circular cross section which are rigidly connected by two beams. Between these beams there is a cross member with a hole in the center. The plate was layed down on the two grinded bars, so thst we got a simply supporting restraint on two opposite sides of the plate. The sample is loaded with a small cylindrical rod terminating with a sphere, shown in fig. A2.3, which slides in the hole until it touches the plate surface. The load is determined by weights on flange at the top of the rod.

A2.5 Measurements results

In fig. A2.4 we show the results of the measurements with the plate loaded by 11170 g. For points lying on the strips C and D of the grid on the plate. Units on the ordinate axis are given in mm. On the abscissa axis there are the labels of the poins where we measured the displacements. Both measured and computed deflections are given.

In fig. A2.5 and fig. A2.6 we give measurements for loads of 22 and 33 kg respectively. Measured and computed deflections are inconsistent for 11 kg but they become consistent at higher loads and we determined a mean measured Young Modulus equal to 4000 kg/mm^2, which is 7% less than E_{theor} derived from the assumed properties of the components.

Rotating the sample of 90 degrees does no change significantly the result.

Fig. A2.7 shows the measurements of the plate, after drilling, loaded with 33 kg and drilled according to the grid described formerly. In this picture are reported both experimental measurements with and without holes.

The mean measure Young Modulus is about 3600 kg/mm^2 which is 10% less than the Modulus of the plate before drilling.

A2.6 Conclusions

The plate has mechanical properties quite close to expectations. After the drilling of the holes, the Young Modulus decreases by 10% and becomes marginal for our requirements. The mechanical properties can of course be recovered by raising carbon fiber-epoxy volume ratio up to 60%.

Acknowledgements

We would like to thank Paolo Franzini for suggestions about the measuring procedure.

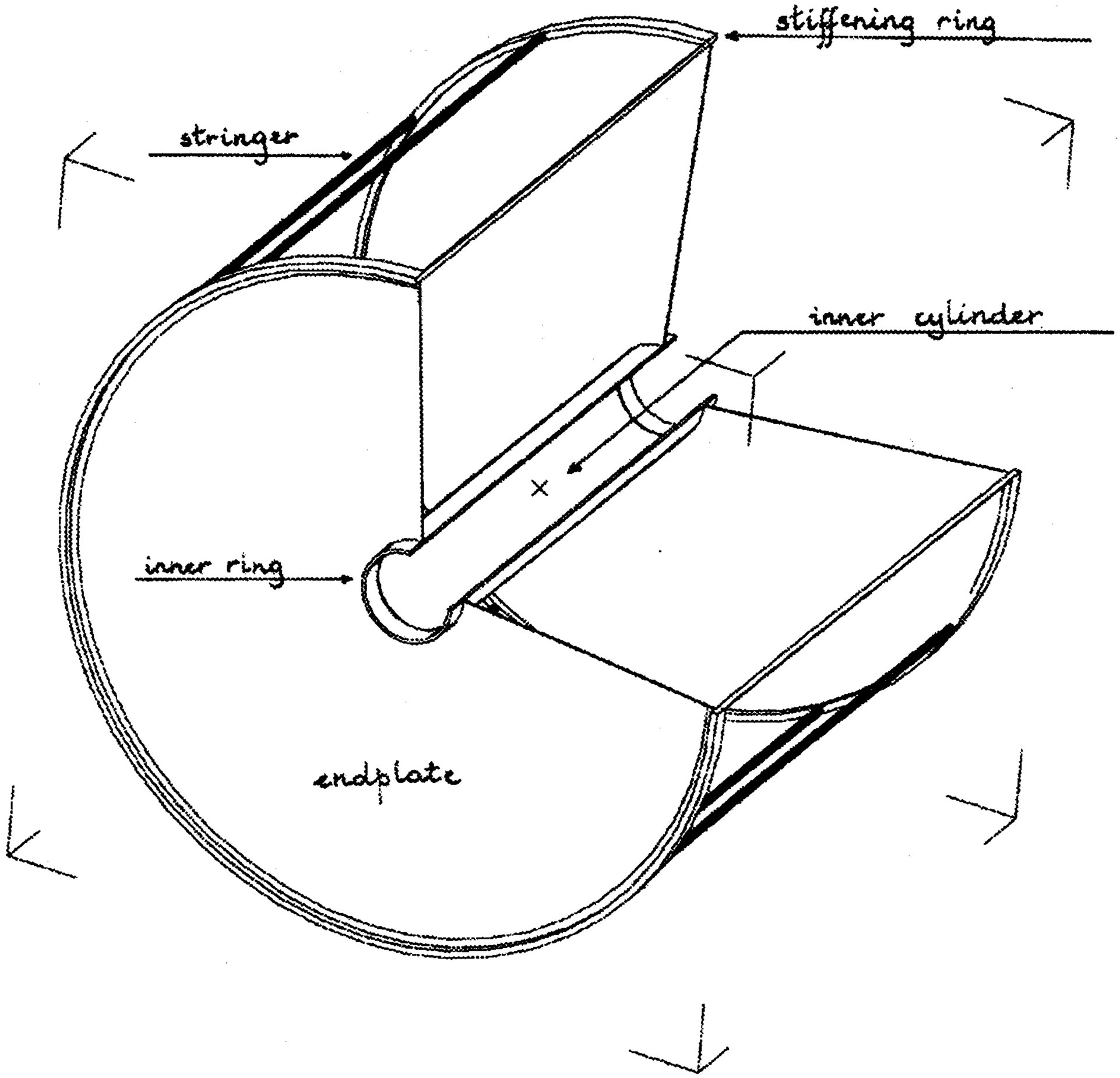

Fig. A2.1. Sketch of the mechanical structure of the KLOE drift chamber.

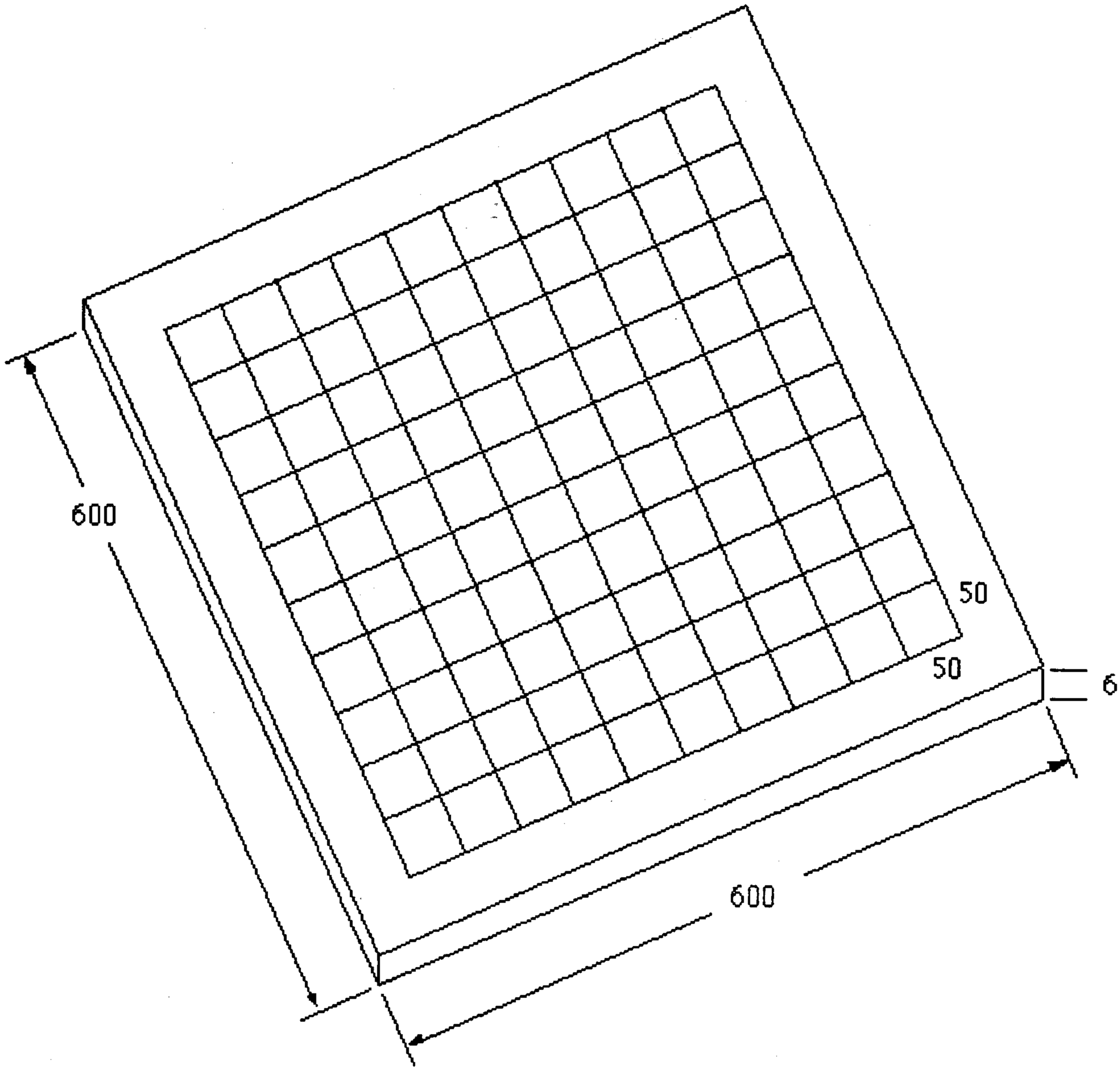

Fig. A2.2. Sample overall dimension.

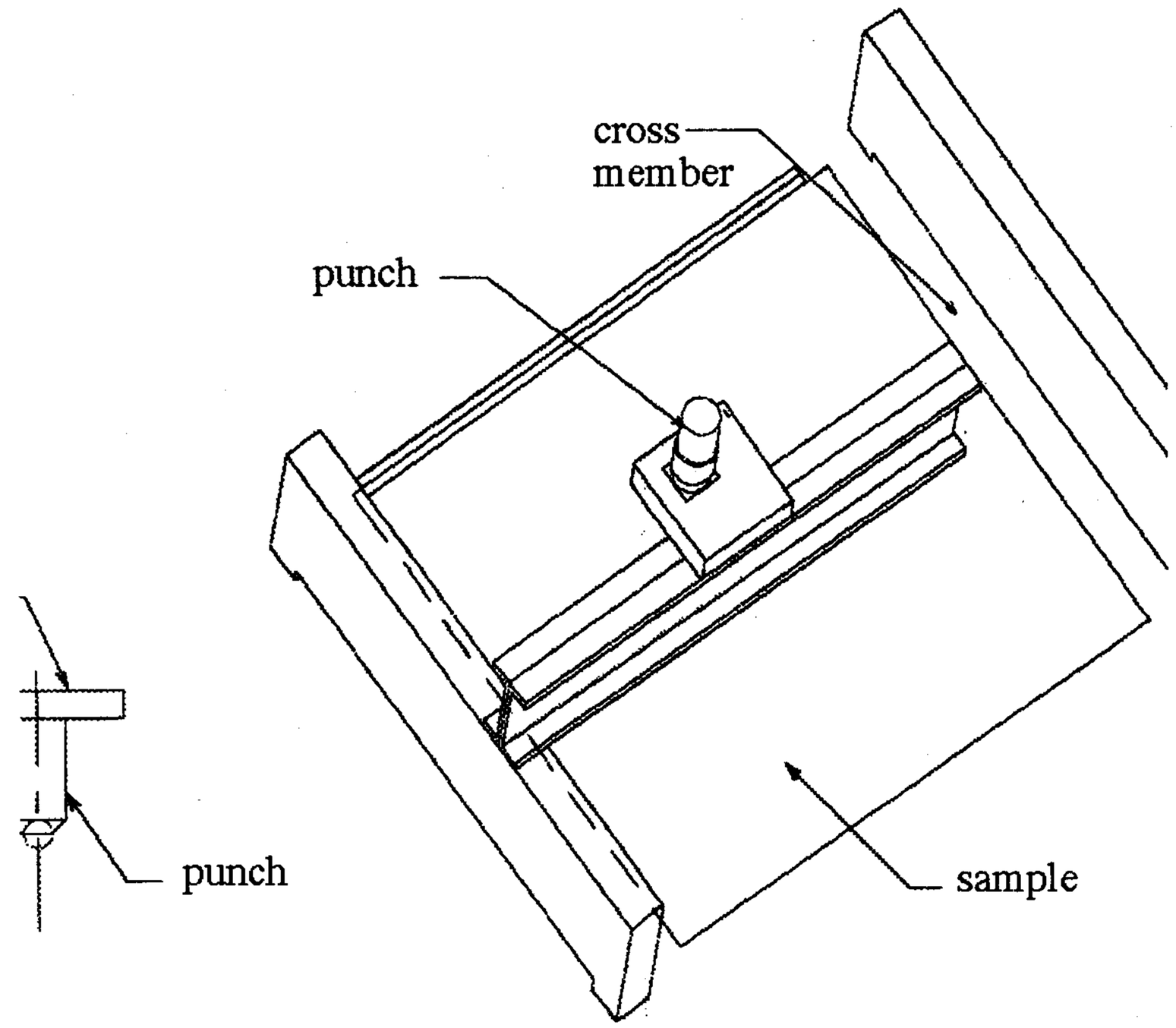

Fig. A2.3. Endplate sample testing tool.

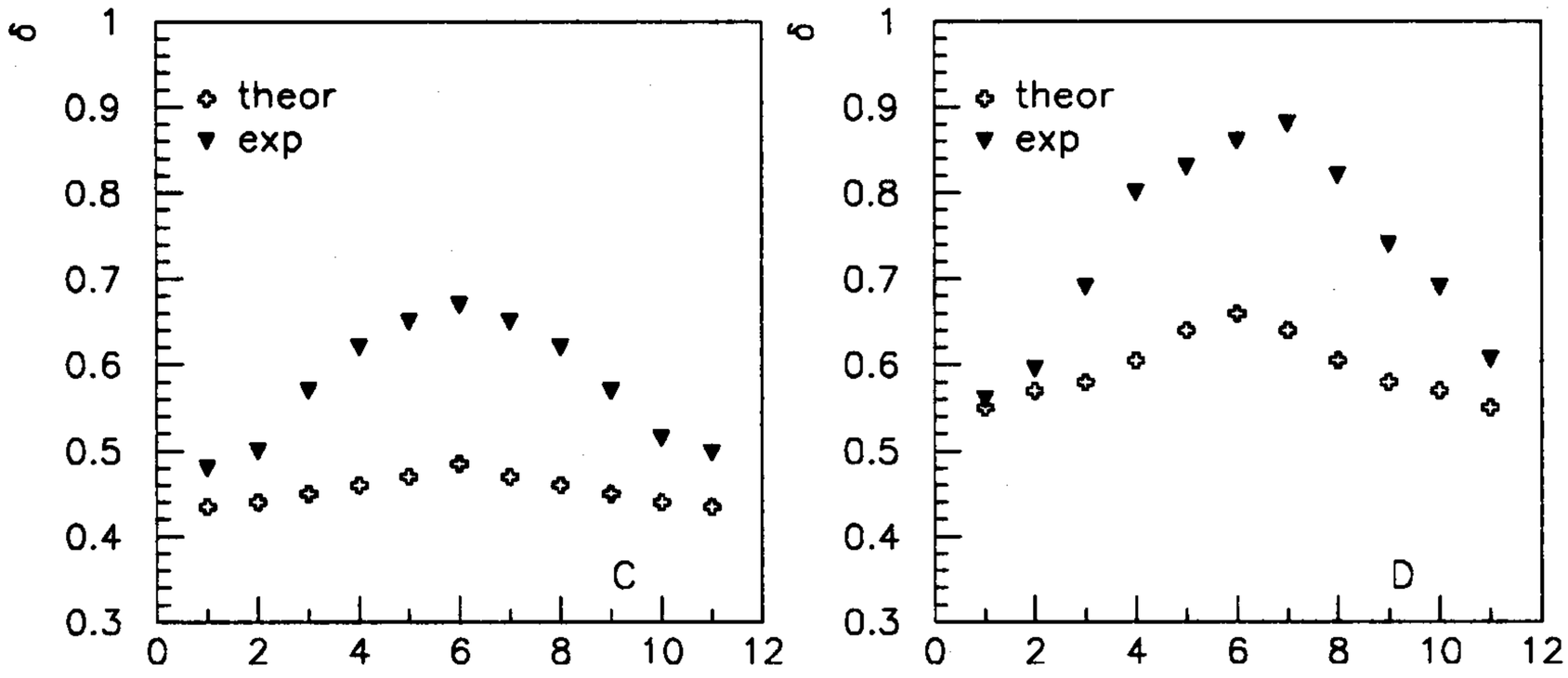

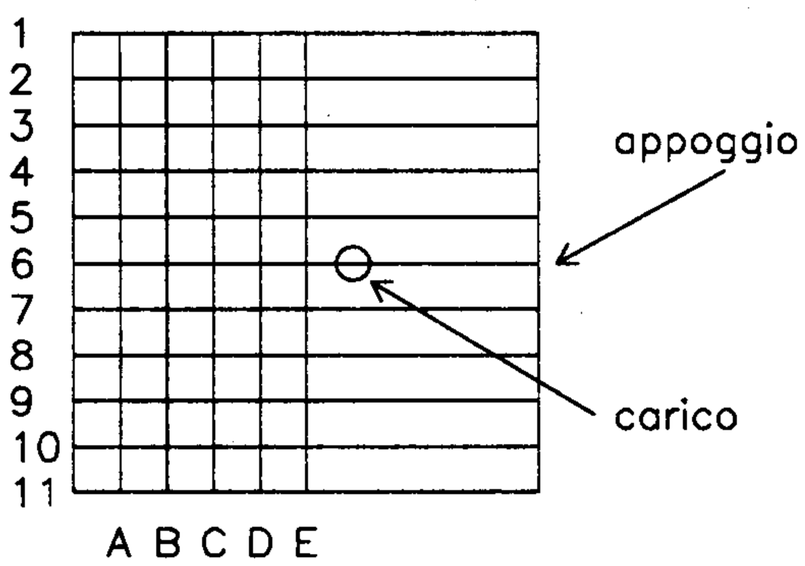

$E_{theor.} = 4300$ kg/mm^2

C) $E_{med.} = 3430$

$\sigma = 300$

D) $E_{med.} = 3643$

$\sigma = 345$

Fig. A2.4. Deflection of the plate loaded with 11 kg.

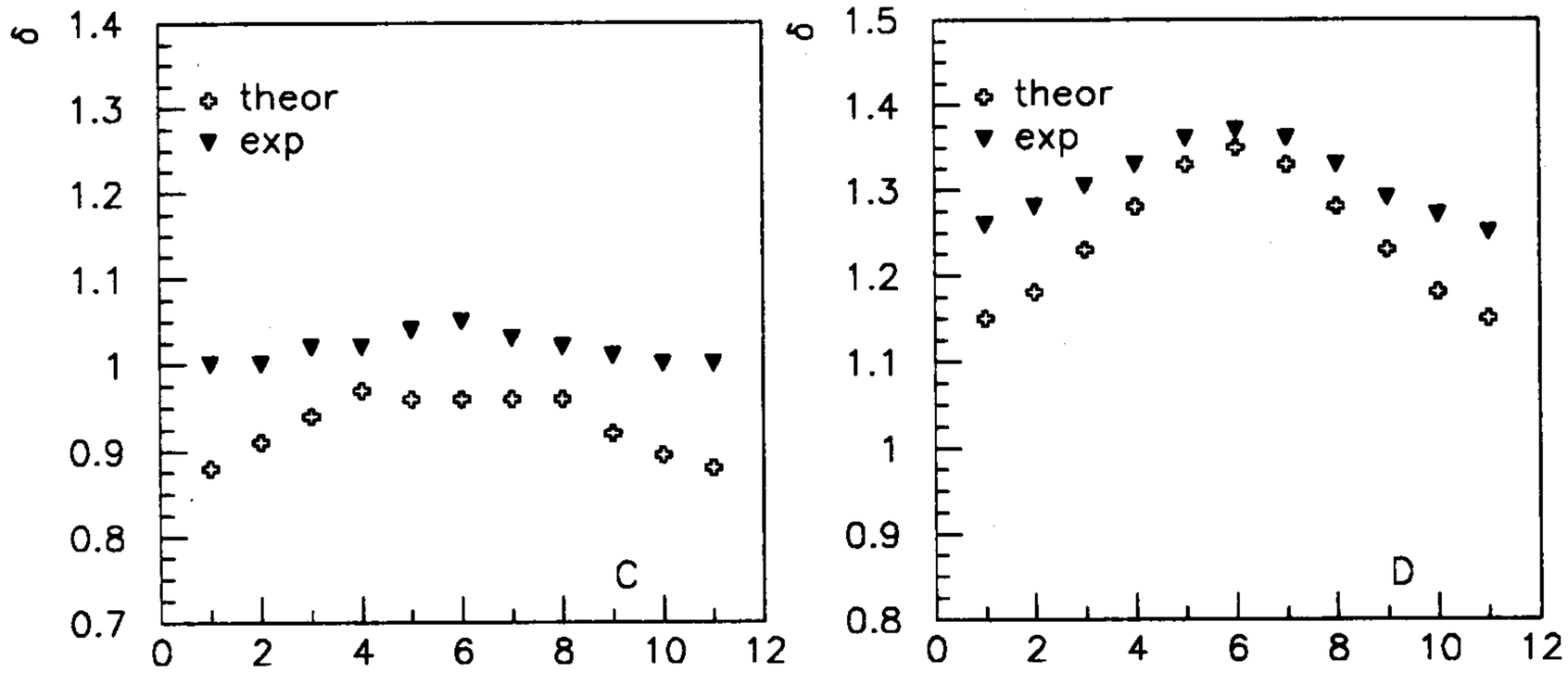

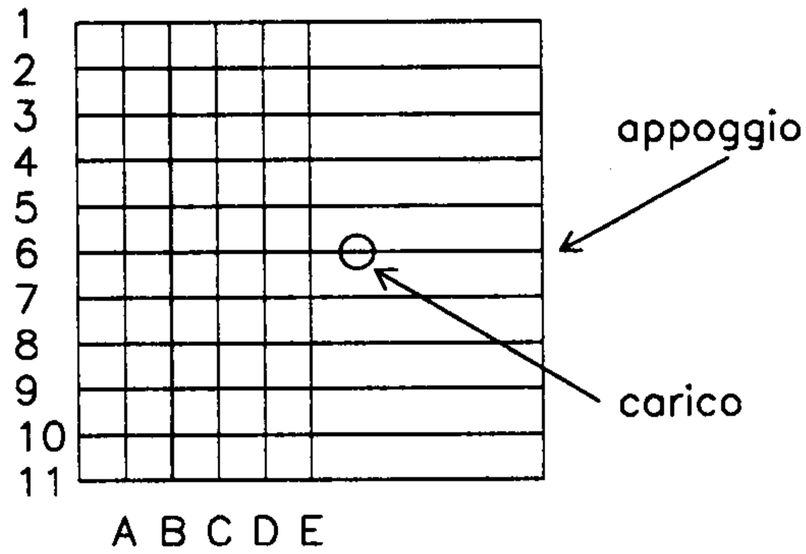

$E_{theor.} = 4300$ kg/mm²

C) $E_{med.} = 4000$

$\sigma = 125$

D) $E_{med.} = 4132$

$\sigma = 90$

Fig. A2.5. Deflection of the plate loaded with 22 kg.

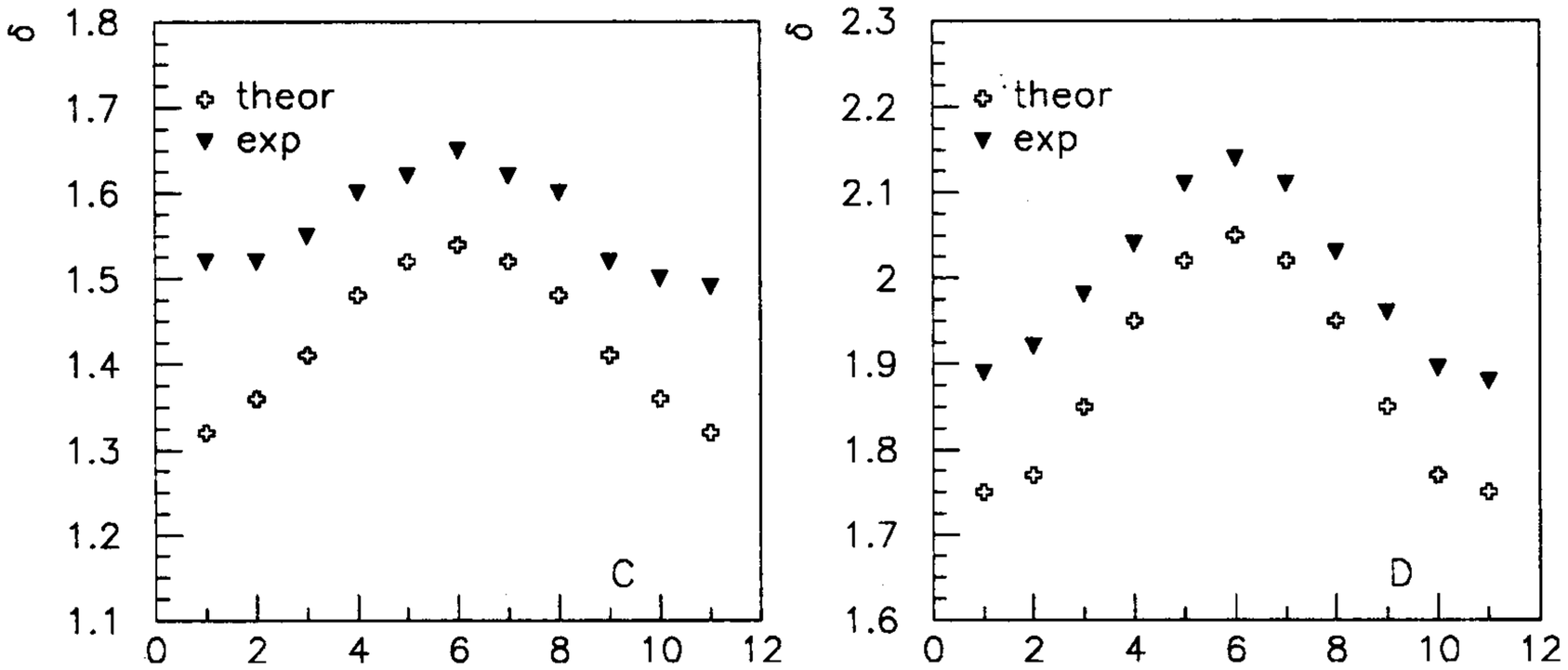

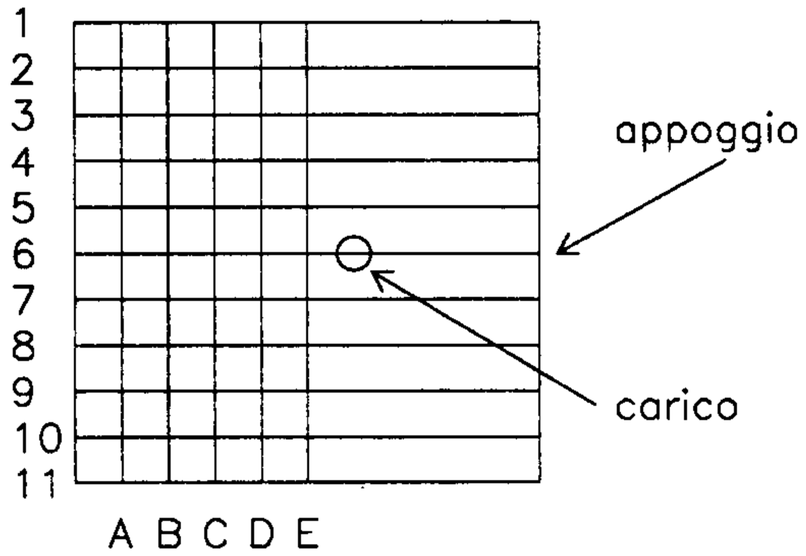

$E_{theor.} = 4300$ kg/mm^2

C) $E_{med.} = 3960$

$\sigma = 115$

D) $E_{med.} = 4040$

$\sigma = 90$

Fig. A2.6. Deflection of the plate loaded with 33 kg.

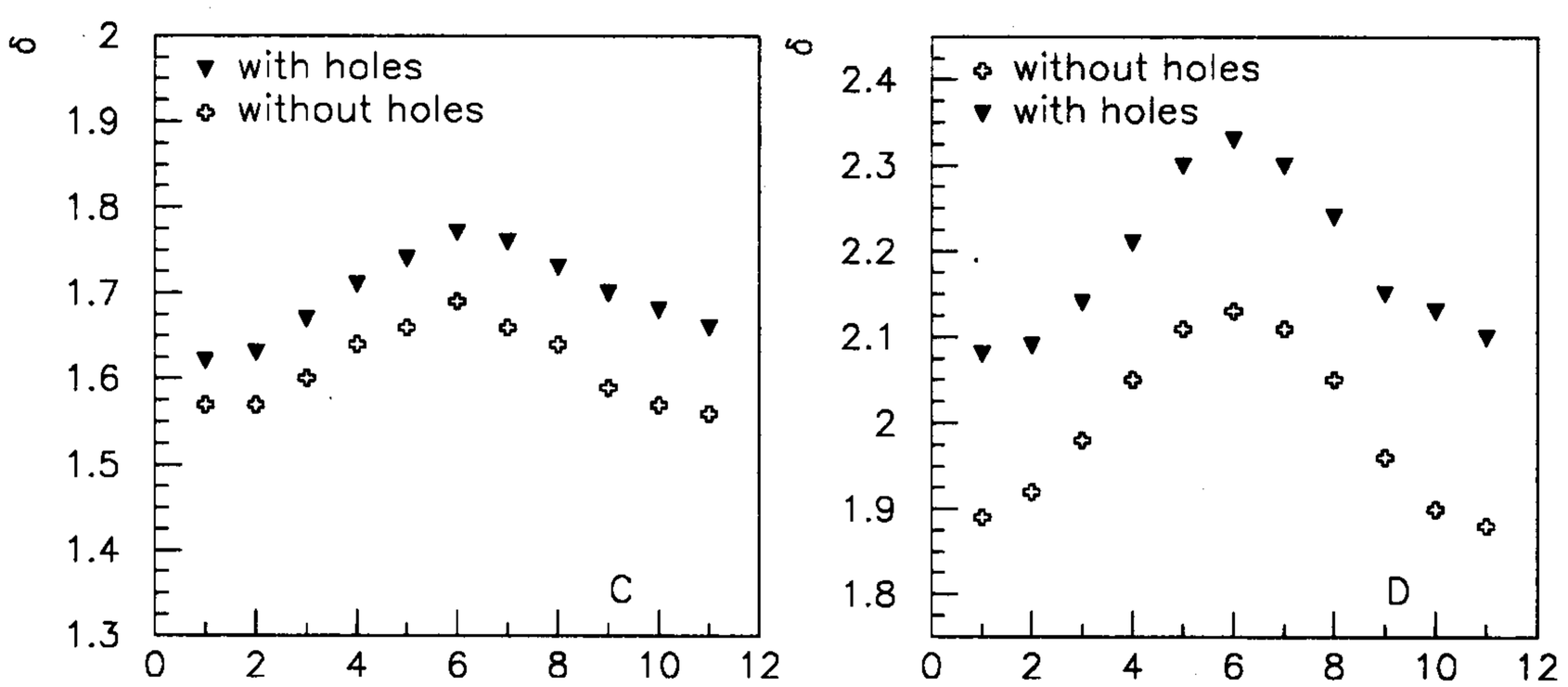

Fig. A2.7. Deflections of the plate after drilling.

INFN - Laboratori Nazionali di Frascati
P.O.Box 13, I-00044 Frascati (Italy)

KLOE Note No. 95
March 1994

APPENDIX A3.

PSI test beam: study of efficiencies of prototypes 0.1 and 0.2 of the KLOE drift chamber

Alessandro Calcaterra

The single cell efficiency for pions having momentum P=250 MeV/c has been measured for both prototypes 0.1 and 0.2, at 0° and 90° incidence angles, using the 90 – 10 He-iC_4H_{10} gas mixture, with two different methods: the first one uses only minimal information from the prototypes to select the events to be used; the second one does a full simultaneous fit of data in both prototypes, and a χ^2 cut helps to reject bad events.

In the first method a "good track" is defined by the occurrence of a simple pattern of hit cells: three layers (the two most distant from each other, and one in between) are requested to have a TDC hit in the cell closest to the projection of the track as given by the MWPC's. The hit is accepted only if below an upper cut, but this will not bias the efficiency, which will be calculated only for cells not belonging to the trigger layers.

Figures A3.1–4 show some characteristics of the remaining events. In particular, in Fig. A3.2 and Fig. A3.4 it can be seen that to almost every TDC hit corresponds an ADC beyond pedestal.

The efficiency for a given cell will then be given as the ratio of "good TDC hits" (*i.e.* TDC values below a certain cut) to the total number of events, being ideally equal to 1 when the track given by the MWPC's passes through the cell, 0 otherwise. Fig. A3.5 shows a typical efficiency profile across a cell. The fit assumes a constant "plateau" efficiency, smeared by a Gauss resolution function.

It must be pointed out:

- The fitted value of the resolution ($\sim$ 1 mm) is not only due to the intrinsic resolution of the MWPC's, coupled moreover to multiple scattering in the setup, but also to the fact that cell borders are not exactly square to begin with, and not electrostatically well defined, particularly so in prototype 0.2.
- The apparent width of the cell depends on the upper cut used to define a "good TDC hit", and in fact it increases when the cut is raised, saturating at approximately 600 ns for prototype 0.1 and 0.2 at 90° incidence angle and at 1000 ns for prototype 0.2 at 0°.

- The "plateau" efficiency does not depend on the TDC cut, but it does depend on HV settings (see Fig. A3.6). In this analysis, only the runs with the highest values of HV's (1.8 kV for prototype 0.1, 1.95 kV for prototype 0.2) have been used.
- A relatively high proportion of "good hits" is found out of the cell limits, even taking into account resolution effects. This is attributed to excess noise in the cells, as can be seen from Fig. A3.7, showing the difference between the impact parameter of the track as expected from the MWPC's, and from the TDC value through the space-time relation appropriate for that cell: a broad central accumulation, dominated by the MWPC resolution, and a flat background. The origin of this noise (also visible in every basic space-time correlation) is probably the test beam environment.

The average cell efficiency (plateau value) calculated in this way is of 99.0% for both prototypes at 0° and 90°, as shown in Tab. A3.1. Requesting consistency between the two impact parameter measurements (a cut at ± 0.4 cm on the distribution of Fig. A3.7) removes every hit outside the cell, while the efficiency inside the cell is reduced, uniformly for both prototypes and angles, to the 98% level.

Table A3.1. Efficiencies for 3/1 and 2/1 cell structures, at 0° and 90° incidence angles

	ε(%)–cell 3/1		ε(%)–cell 2/1	
cell #	0°	90°	0°	90°
13	99.1 ± 0.4	99.1 ± 0.3	99.1 ± 0.4	99.3 ± 0.3
14	98.2 ± 0.4	98.3 ± 0.3	98.7 ± 0.5	99.1 ± 0.3
07	99.6 ± 0.8	99.3 ± 0.5	98.3 ± 0.8	98.6 ± 0.6
08	98.5 ± 0.4	98.5 ± 0.3	98.9 ± 0.4	98.6 ± 0.7
18	98.9 ± 0.3	98.9 ± 0.3	98.6 ± 0.5	99.5 ± 0.3
19	99.5 ± 0.3	99.1 ± 0.3	99.0 ± 0.4	99.4 ± 0.3

The efficiency found with this method does not overestimate the true one, and can possibly underestimate it if the selection algorithm does not reject 100% of the bad triggers (doing a visual scan of 200 selected triggers, none of these seemed rejectable), but it represents just the efficiency for an ionization cluster to give a signal above discriminator threshold: it is not certain that every hit will be equally useful to the purpose of fitting the track with good accuracy.

A different sample of events for calculating efficiencies, though not an independent one, can be found requesting a satisfactory track fit through both prototypes, if care is taken to exclude the cell whose efficiency is being measured from both the fit as well as from any request on the number of hit cells prior to the fit. This method has the advantage over the previous one of a better resolution, but with some drawbacks:

- It introduces systematics into the efficiency denominators, *i.e.* into the distribution of

beam tracks across the cells: the request of a lower cut on the number of hit cells before attempting the fit, together with the close parallelism of beam tracks and the particular geometry of the cells tends to eliminate tracks passed in particular regions of the setup (see Fig. A3.8)

- Systematics introduced from the imperfect knowledge of the space-time relations also influences now the "good hits" when cutting on the consistency between the hit radius measured from the value of the TDC in one cell and the one predicted from the fit of all the others. Such a systematics was previously swamped by the overall $\sim$ 1 mm resolution of the MWPC's.

In Fig. A3.9 the efficiency profiles for two cells in prototype 1 and 2 are shown. The better resolution of the track fit with respect to the MWPC track is now apparent: the (fitted) shoulders now have a standard deviation of the order of 400–500 μm. The difference between expected and fitted value of the impact parameter (*i.e.* the fit residual) for the same 4 cells is shown in Fig. A3.10 : narrow central quasi-Gaussian distributions over broader and sometimes non-symmetric accumulations.

Imposing a consistency cut also in the case of a fit-driven selection of events, one can get more insight on the nature of the "broad" part of the residual: while a mild cut at $\pm$2 mm on the distributions of Fig. A3.10 lowers the plateau efficiency at the 97.5% level but has no or little effect on the shape of the efficiency profiles, cutting at $\pm$1 mm yields Fig. A3.11, showing that the broad part of the residual distribution is more correlated with the cell region closest to the wire, in which the fit of the space-time correlation is more problematic. As for the average values of the efficiency plateaus, including the central part of the cell, they tend to vary from cell to cell, reflecting systematics in the width, and possibly shape, of residuals in different cells, from a minimum of 90% to a maximum of 95%.

Two conclusion can be drawn at this point: the first is that, even though the efficiency for *finding* any hit is at the 99% level, the efficiency for getting a *useful* hit can be lower. The second is that in any case no significant difference is found between the behavior of the cells with 3/1 field/sense wire structure with respect to those of the 2/1 type.

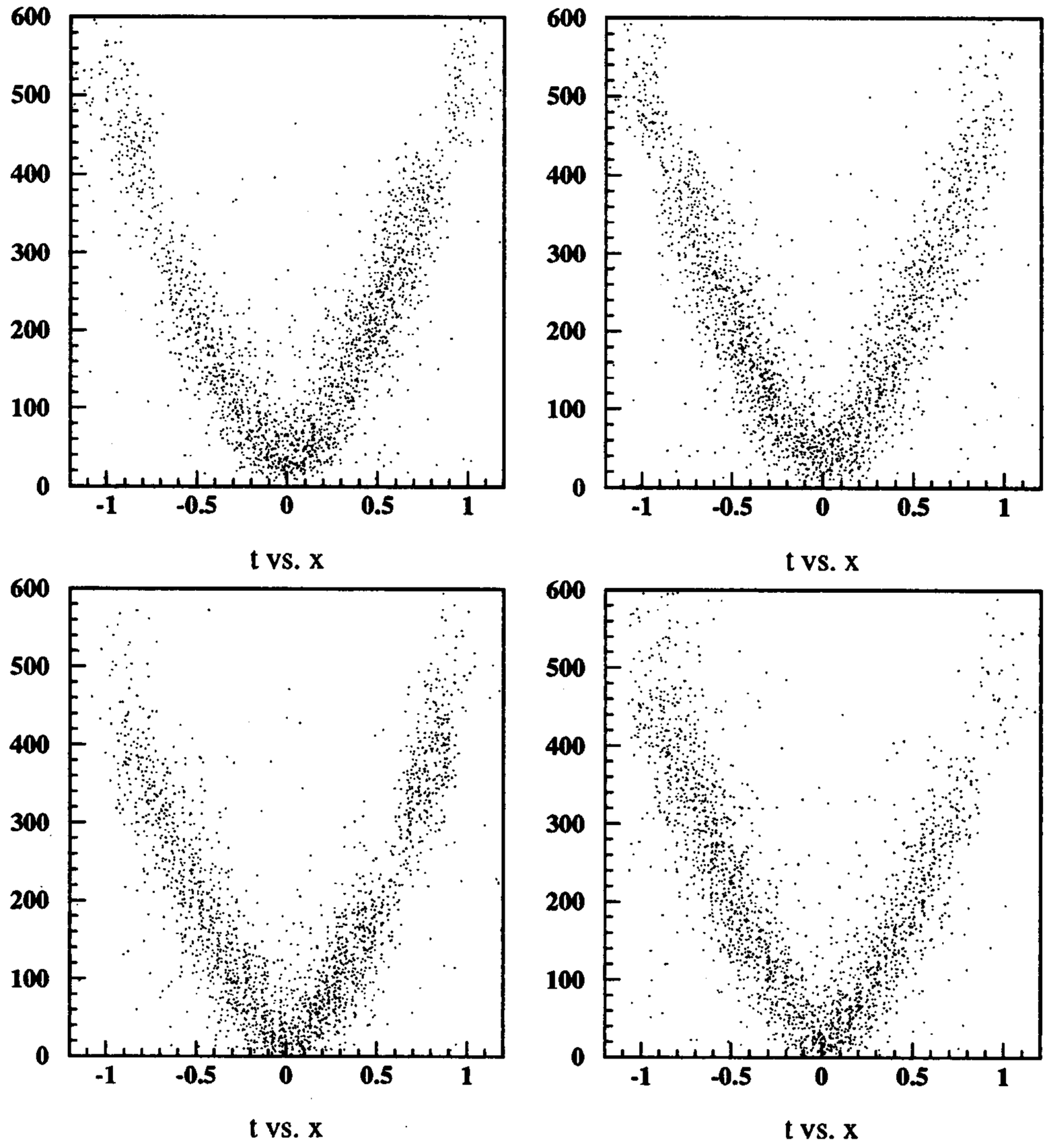

Fig. A3.1. Space-time correlations for cells 13,14,18,19, prot.0.1

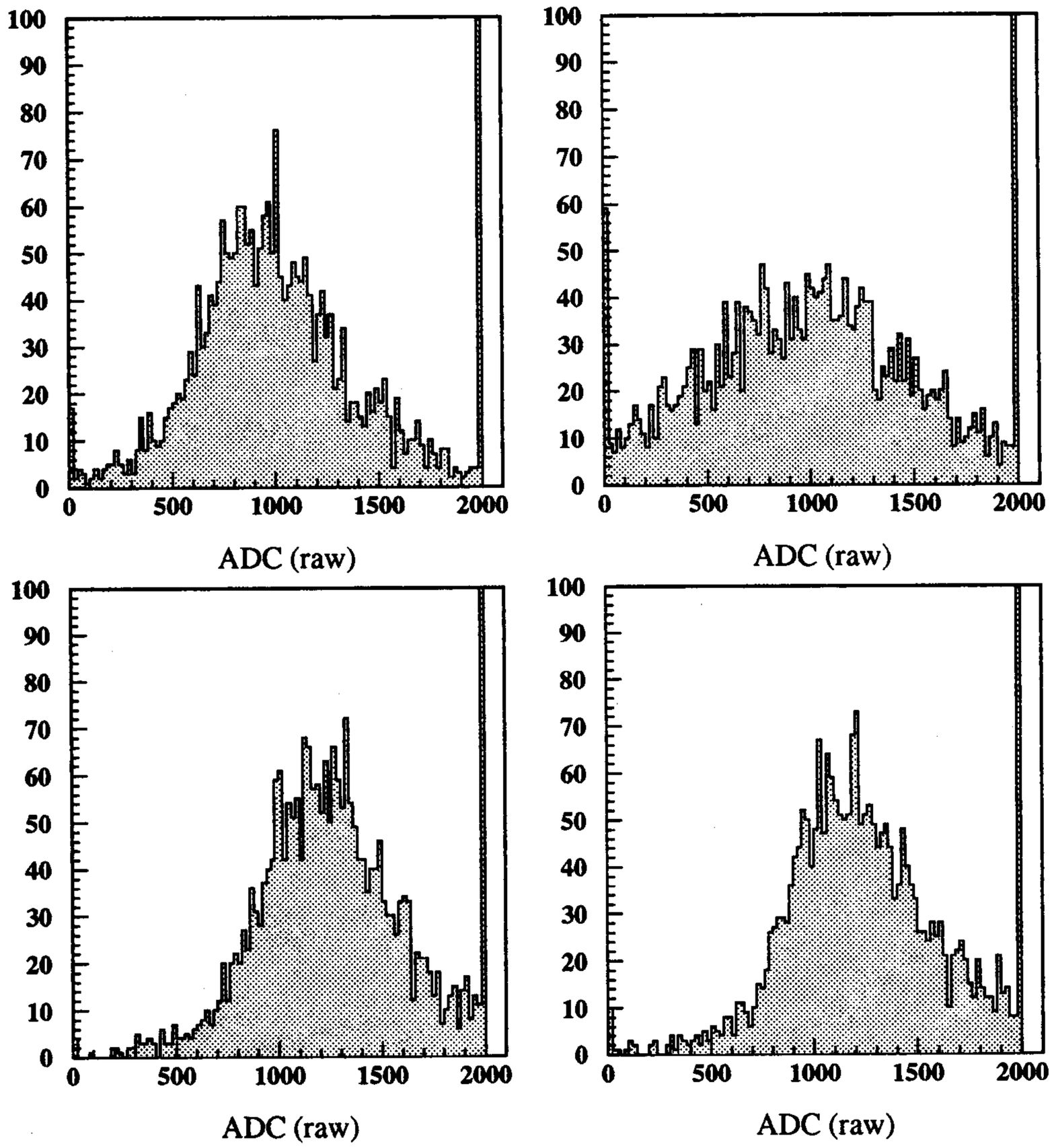

Fig. A3.2. ADC spectra for cells 13,14,18,19, prot.0.1

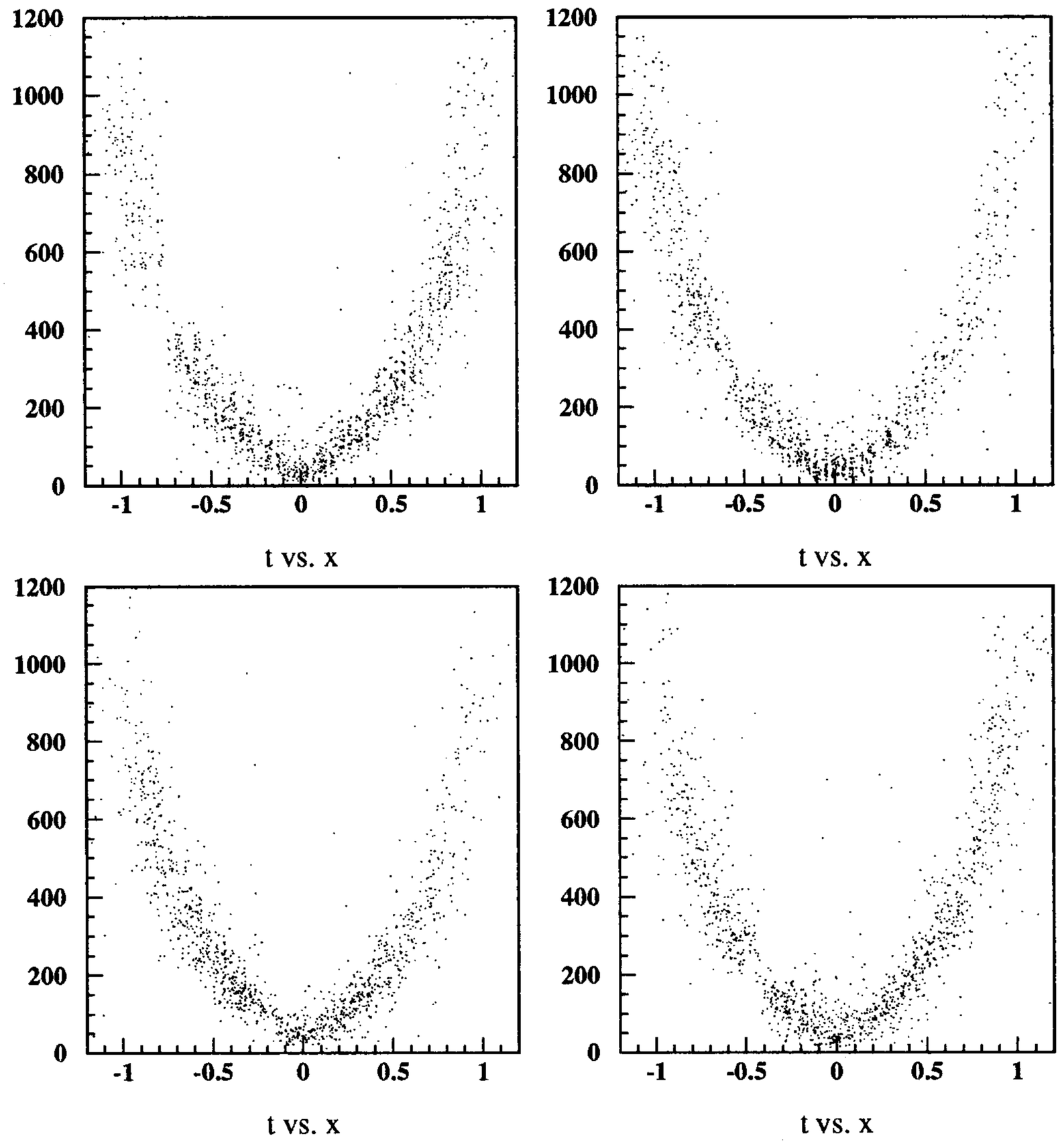

Fig. A3.3. Space-time correlations for cells 13,14,18,19, prot.0.2

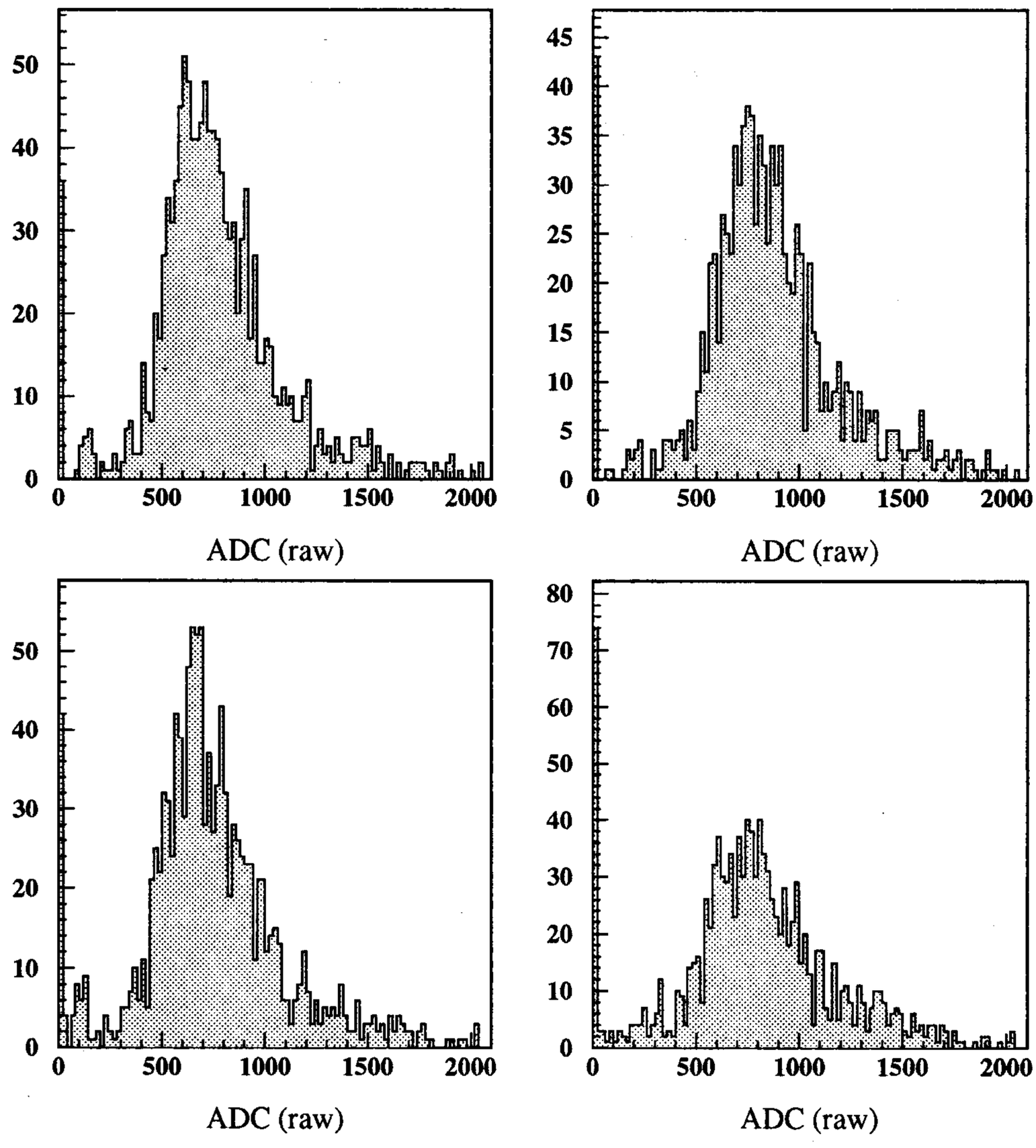

Fig. A3.4. ADC spectra for cells 13,14,18,19, prot.0.2

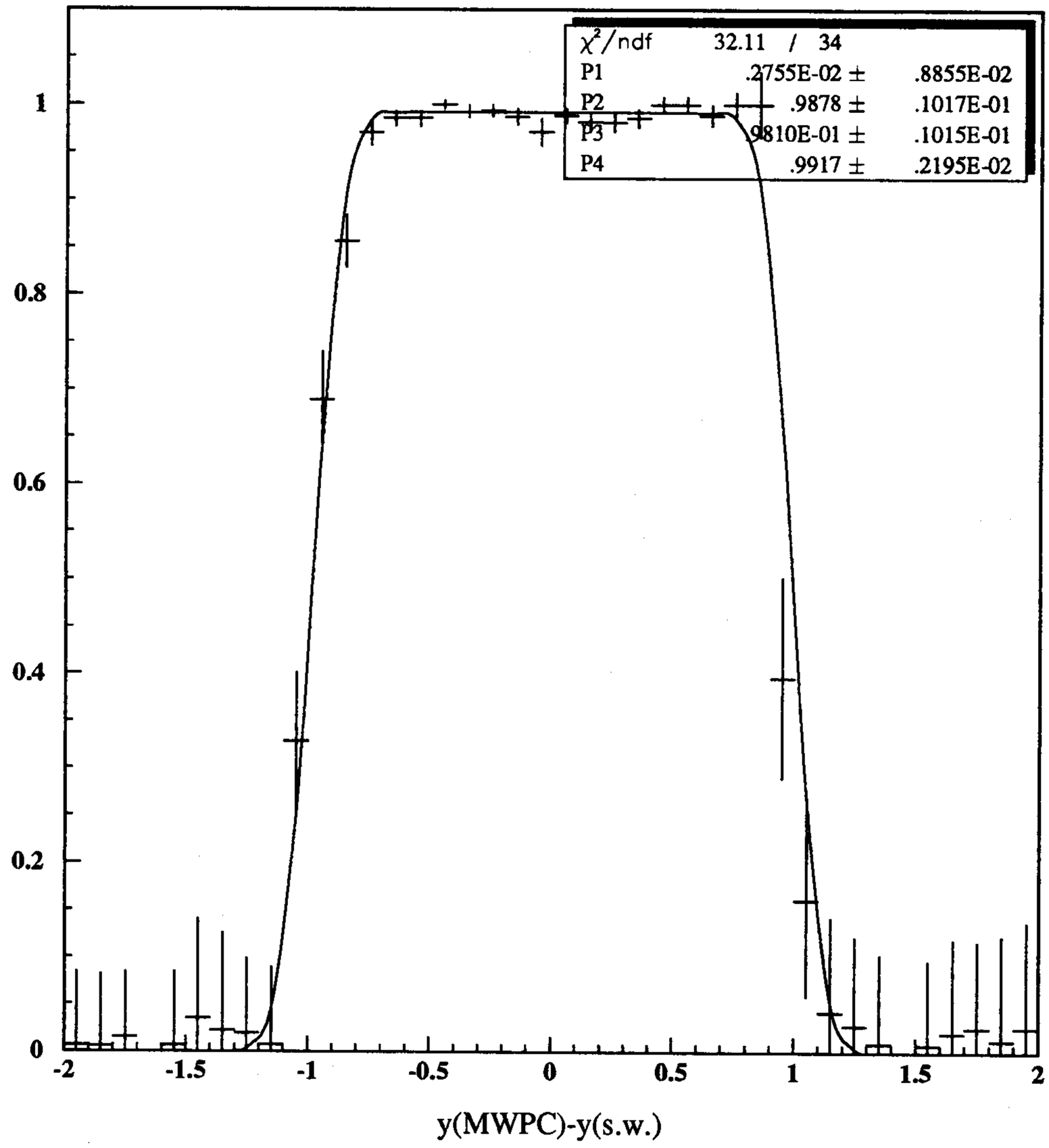

Fig. A3.5. Efficiency profile, prot.0.1

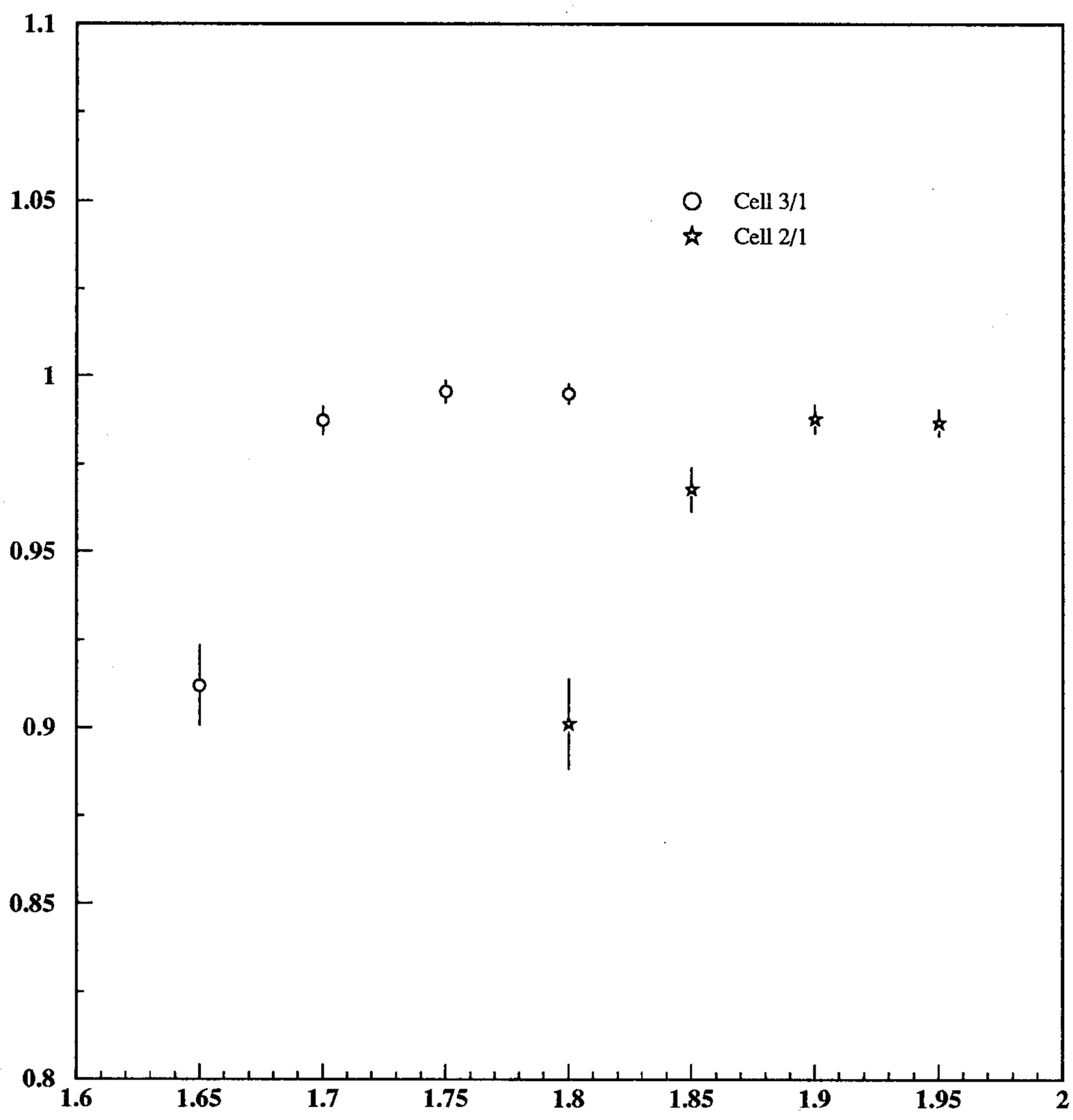

Fig. A3.6. H.V. Efficiency curves

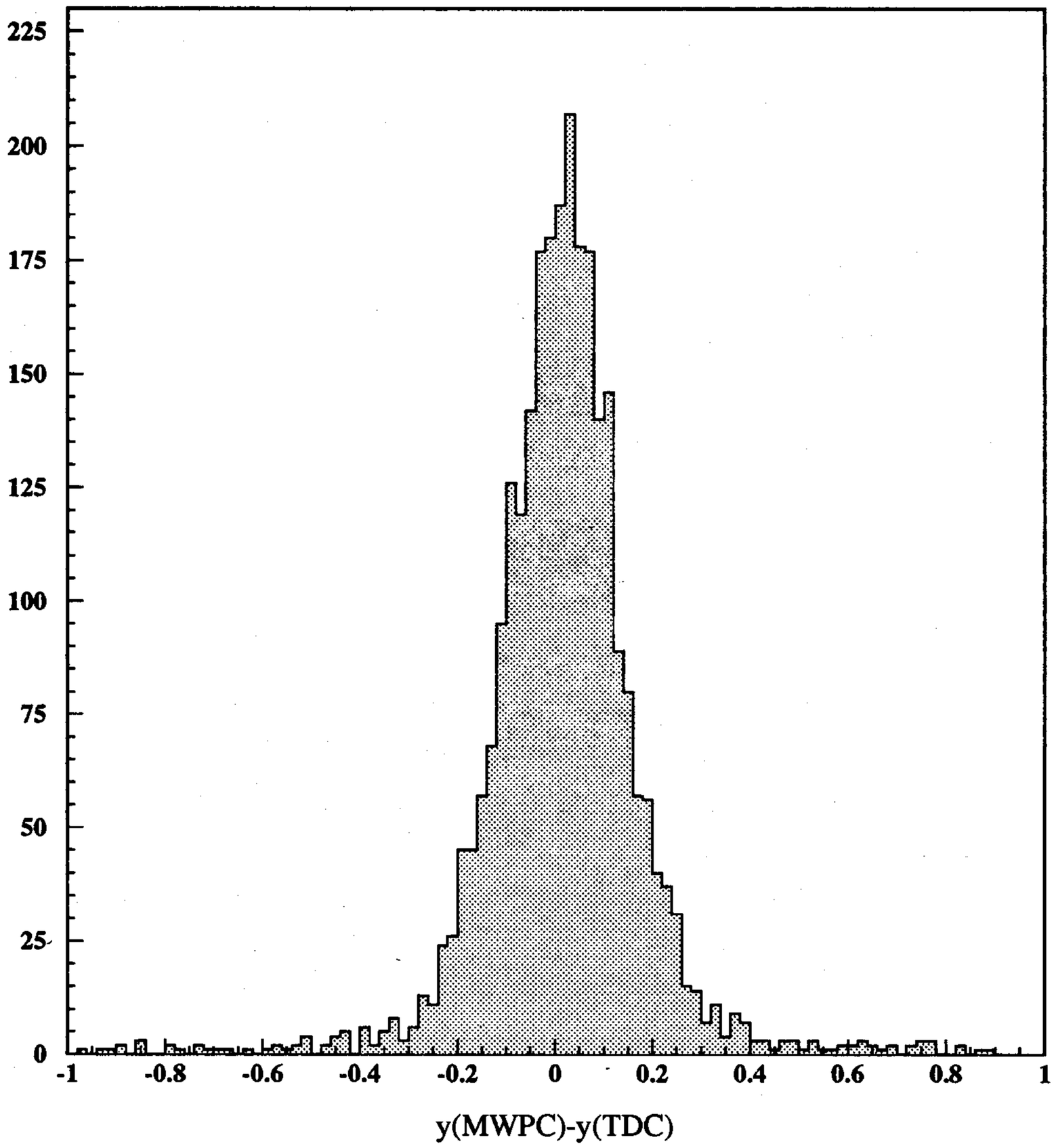

Fig. A3.7. Resolution from MWPC's alone(see text)

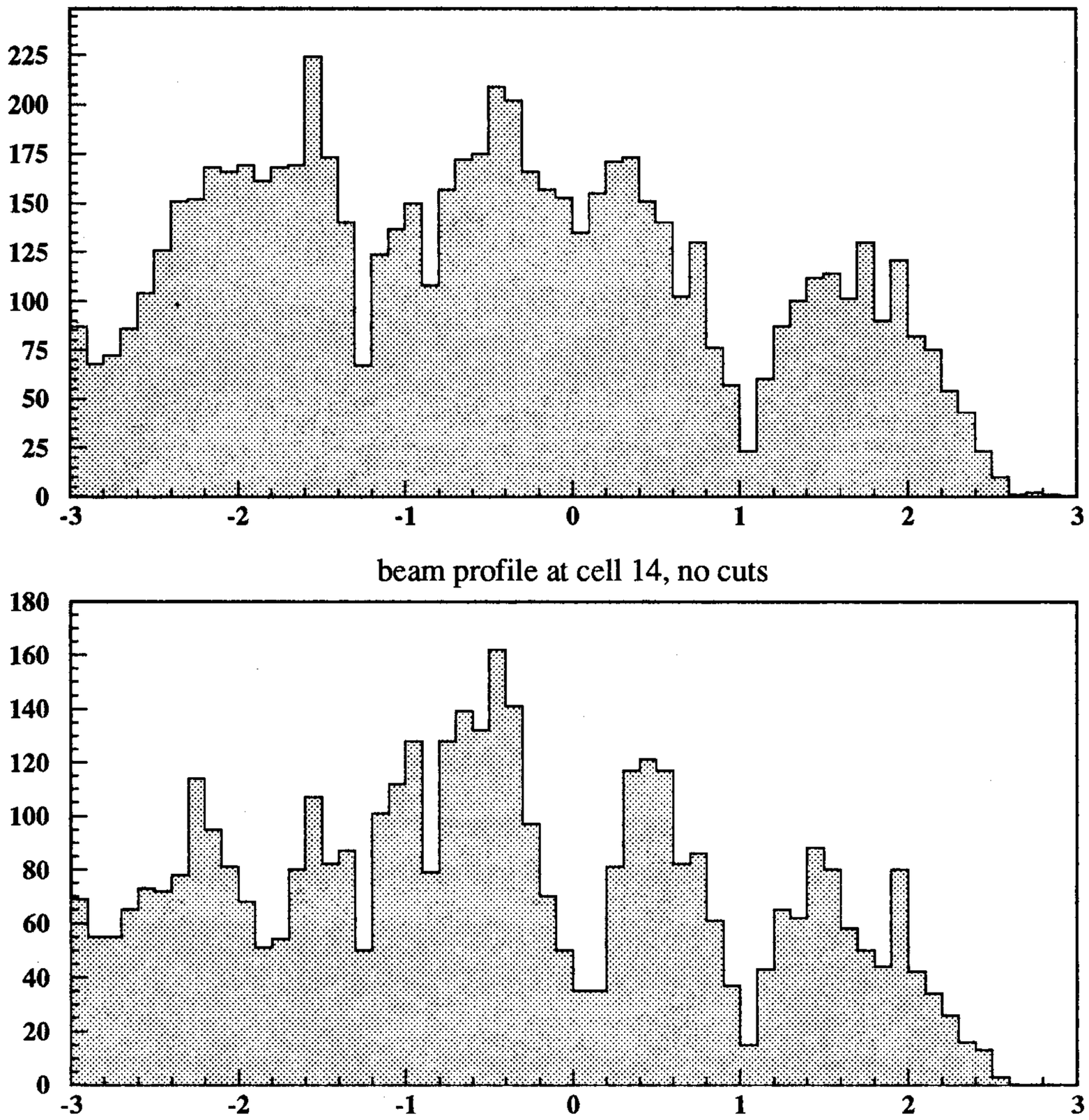

Fig. A3.8. Beam profile from MWPC, before and after a χ^2 cut

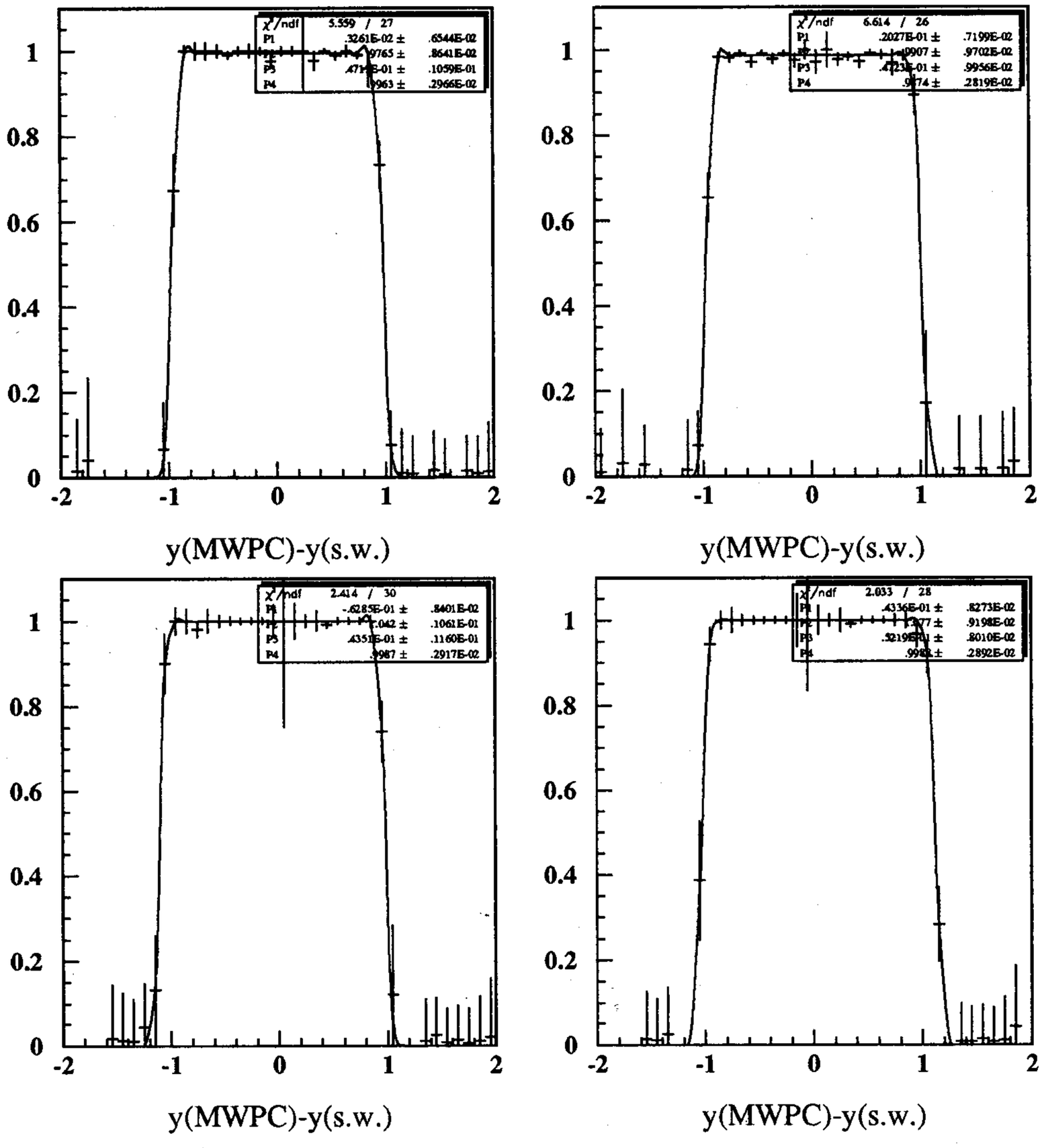

Fig. A3.9. Efficiency profiles: cells 13,14 prot 0.1(above) and prot 0.2(below)

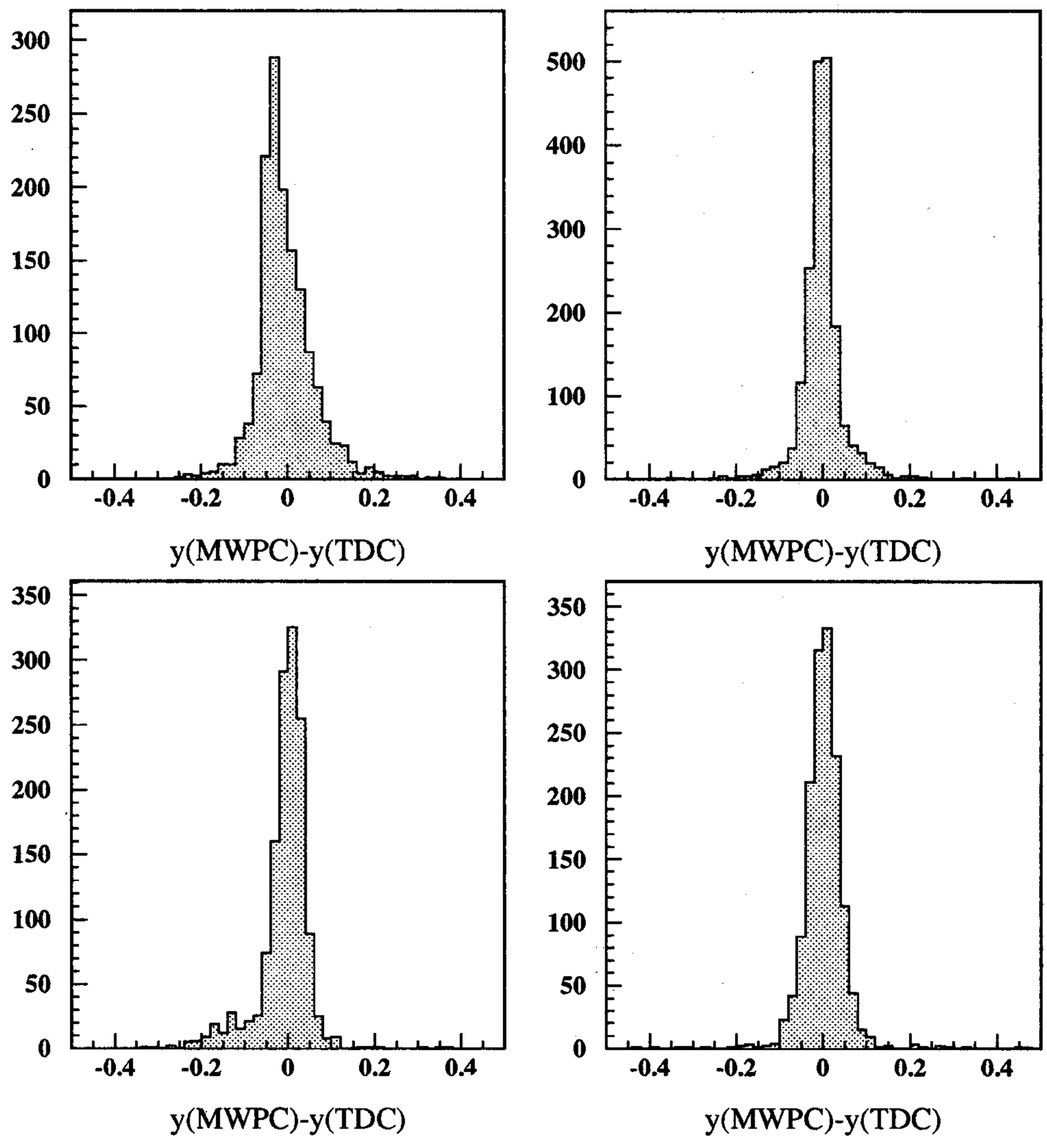

Fig. A3.10. Fit residuals for cells 13,14 prot.0.1(above) and prot.0.2(below)

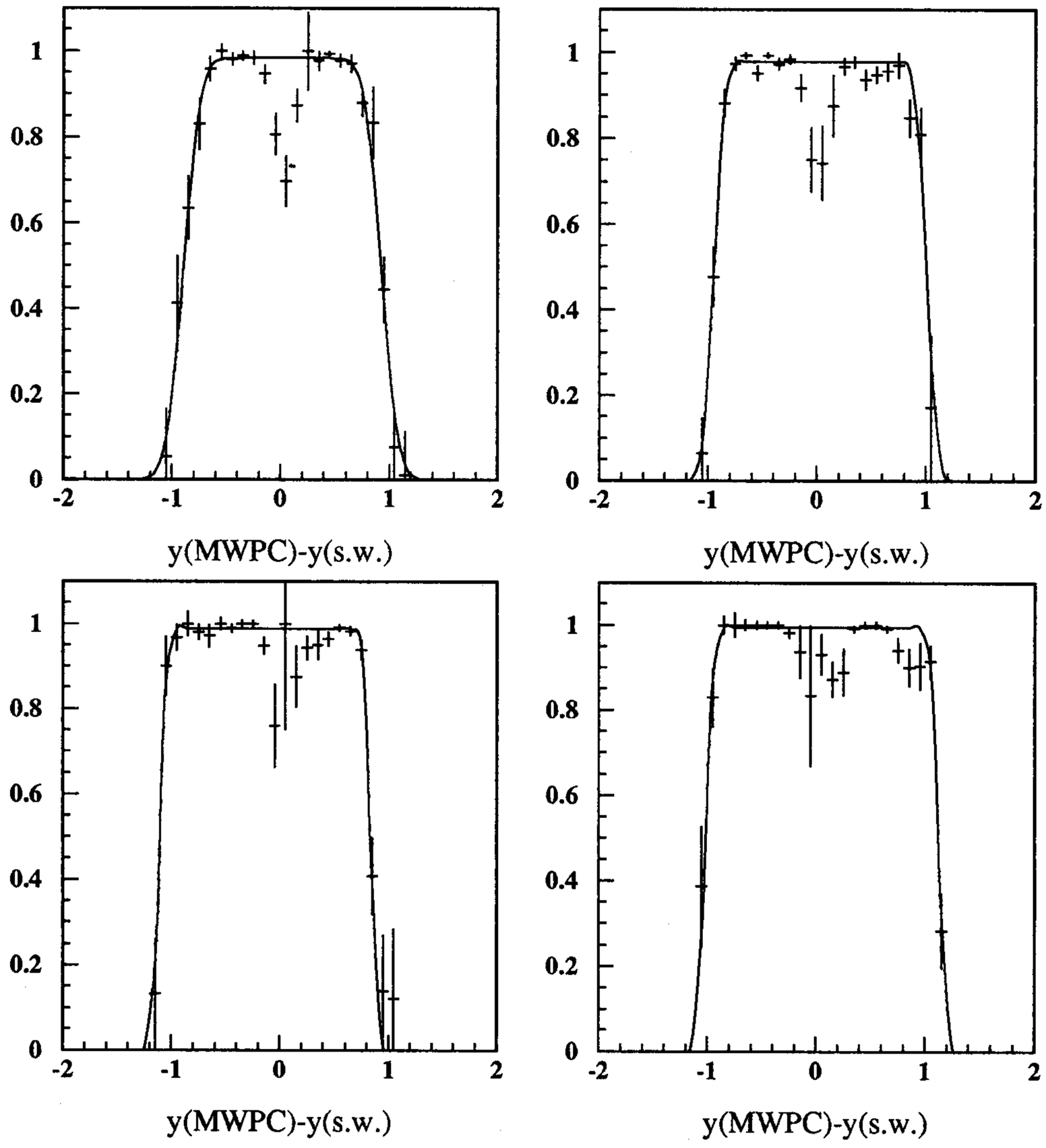

Fig. A3.11. Efficiency profiles after cut on fit residuals

INFN - Laboratori Nazionali di Frascati
P.O.Box 13, I-00044 Frascati (Italy)

KLOE Note No. 92
March 1994

APPENDIX A4.

A measurement of the spatial resolution in square drift cells via the stagger method

Giuseppe Finocchiaro

ABSTRACT

An analysis of the data collected at P.S.I. on *prototype 0.1* and *prototype 0.2* is presented. The space-time relation is determined from the drift time distribution and from the space-time correlation. The stagger method is used to measure the spatial resolution, which is found to be within the design specification of 200 μm.

A4.1 Introduction

A test at P.S.I. has been performed during summer '93 in order to measure the performances of two small prototypes with square cells of the KLOE drift chamber. A detailed description of the prototypes, of the test beam setup and of the trigger and DAQ system is given elsewhere.[43] In fig. A4.1 the layout of the cell configuration is shown. The arrangement of the prototypes in the beam is given in fig. A4.2. Tracks coming from below in fig. A4.3 are defined to have 0° incidence angle, tracks from the right 90°.

Stimulated by the fact that in the early days of the test the MWPC were not working properly, we developed a method for measuring the space-time relation and the spatial resolution based exclusively on the drift time information. This method is presented here, toghether with another one, based as well on the stagger among different cells.

A4.2 The space-time relation

In order to transform the drift time measurement into the space coordinates necessary to fit tracks inside the drift chamber, a space-time relation must be given. In this section we describe the two methods adopted to determine the parameters of the space-time relation.

The space-time relation from the time spectrum.

Making the assumption that the cells are uniformly illuminated by the beam,[1] the time spectrum measured in a single cell can be written as

$$\frac{\partial N}{\partial t} = \frac{\partial N}{\partial x} \cdot \frac{\partial x}{\partial t} \simeq \mathcal{K} \frac{\partial x}{\partial t}.$$

thus being proportional to the drift velocity $\partial x/\partial t$, which in He-based mixtures is far from being saturated. Choosing therefore a functional form $t(x)$ for the space-time relation, its parameters can be determined from a fit to the cell time spectrum with the function $|\partial t(x)/\partial x|^{-1}$. The normalization constant $\mathcal{K}$ can be determined requiring that the number of events between times t_1 and t_2 be equal to the integral of the function between the same extremes.

From previous analysis on prototype 0,[44] it is found that a parabolic approximation of the space-time relation:

$$\mathrm{t} = \mathrm{t_0} + \mathrm{A}(\mathrm{r} - \mathrm{r_{wire}})^2 + \mathrm{B}|\mathrm{r} - \mathrm{r_{wire}}| \qquad \text{(A4.1)}$$

adequately describes a symmetric field configuration. Parameter B has the simple interpretation of the inverse of the drift velocity near the anode wire (i.e. for high electric fields). The method is illustrated for 3 cells of *prototype 0.1* in figure A4.4, where the fitting function is the inverse of eqn. (A4.1).

Events entering the histograms in fig. A4.4 pass a selection cut based on the total charge released along the track length inside the cell: an event is defined as 'good' if, for all the 5 cells in the row, the ADC value exceeds the pedestal by 3 sigmas. As can be seen from the ADC spectra in fig. A4.5, this allows a rather clean selection, since the pedestal and signal peaks are well separated.

A few remarks are in order about the fits in fig. A4.4:

1 Only parameters A and B of eqn. (A4.1) are fitted: $\mathrm{x_{wire}}$ does not play any role here, the drift time being sensitive only to $|\mathrm{x} - \mathrm{x_{wire}}|$; $\mathrm{t_0}$ is determined (not fitted!) from the initial region of the time spectrum.

2 The fitted parameters are consistent among different cells and with previous measurements,[44] although the errors are rather large.

3 Since the assumed functional dependence is symmetric, the fit should be performed in a region sufficiently close to the anode wire, where symmetry is actually expected. Given the measured drift velocity in the gas mixture 90% He - 10% $\mathrm{iC_4H_{10}}$, the maximum drift distance in the cell ($\simeq L/2 \simeq 10$ mm) correspond to $\simeq (400 \div 500)$ ns drift time, as can be seen from the rather sharp decrease in fig. A4.4. In this respect, 350 ns is a reasonable limit for the fit. To illustrate this point, a calculation of the electric field as a function of the distance from the sense wire for tracks at a) 0°, b) 90° respectively, in cell 13 of

1 For several runs this is actually true only for the central cells.

prototype 0.1 is shown in fig. A4.5.[2] A high degree of symmetry is observed in the first case due to the field wires at the sides of the cell. On the contrary, 'up' and 'down' field wires are slightly displaced in cell 13 (see fig. A4.6), which results in the asymmetry of fig. A4.5b for drift distances $\geq$ 0.6 mm.

This fit method cannot be applied equally well to any cell configuration. The heaviest limitations are for *prototype 0.2*, due to its particular wire configuration. Referring to fig. A4.6, clusters originated from a track traversing *prototype 0.2* at 90° see a 'closed' cell, like in *prototype 0.1*. On the other hand, clusters from 0° tracks follow the drift lines of an open cell. The different potential configuration is shown in fig. A4.7. The drift time distribution for tracks at 0° in *prototype 0.2* is shown for one cell in fig. A4.8. The cell borders are no longer well defined as in *prototype 0.1*. In fact we did not succeed in fitting *prototype 0.2* time spectra at 0°.

The space-time relation from the space to time correlation.

Having at our disposal a tracking system, the most natural way to study the space-time relation is of course to correlate the measured drift time with the projected distance of closest approach (DCA) of the track to the anode wire. The combined efficiency of the 2 MWPC's is $\simeq$ 40%. Examples of correlations are shown in fig. A4.9 for both prototypes.

Two effects have to be considered, both related to the intrinsic lower limit of the time distribution near the wire:

1 The finite distance between ionization clusters ($\simeq$ 800 μm in He-based mixtures with $\geq$ 90% He) distorts the drift time distribution near the wire (getting far from the wire, the effect levels off according to the Pythagorean theorem). One way to correct for this is to replace the DCA coordinate x with

$$x' = \sqrt{x^2 + (\lambda/2)^2},$$

where the mean distance between clusters λ is extrapolated from the measured value to the β of the particle.

2 The resolution of the tracking system smears the DCA distribution.[3] For tracks sufficiently far from the anode wire, the mean value of the time distribution is not affected. On the contrary, for clusters released close to the wire the mean value does change, due to the tails caused by events at relatively large time, but whose reconstructed distance is smeared to small x. We found that the bulk of this effect is accounted for by *fixing* independently the t_0. Actually, if one tries to include t_0 in the fit, its value is overestimated (compare the profile histograms with the scatter plots in fig. A4.9), and correspondigly overestimated is the drift velocity.

An example of parameters fitted in this way is shown in fig. A4.10.

---

2 The simulation is done by means of the program GARFIELD.[45]

3 In our case the spatial resolution of the tracking system is of the order of 1 mm, due to the combined effect of the intrinsic resolution of the MWPC's ($\simeq$ 500 μm), the material traversed by the low momentum pion beam ($\simeq$ 600 μm), and the relative disalignment between the prototypes and the MWPC's.

A4.3 Spatial resolution

In order to measure the spatial resolution in our prototypes, we compared the spatial measurements in several cells. The main advantage of this method is that one automatically gets rid of both any disalignment with respect to the tracking system and the effect of multiple scattering (the cells are typically few cm. – in He – apart).

The correction for the track slope, mandatory to consistently compare the spatial measurements, can be accomplished in two ways. The first method, illustrated in fig. A4.11, uses only the drift time information from the prototypes themselves. The plot of the quantity

$$\Delta x_{\text{stag}} = \frac{x(t_1) + x(t_3)}{2} - x(t_2) \tag{A4.2}$$

is shown in fig. A4.12. Tracks are selected requiring 5 hits in the row of interest and only 1 hit in each column of cells. A hit is defined 'good' if the collected charge is at least 3 sigmas above the pedestal, and the drift time is lower than 1.5 μs. The branches of fig. A4.12 correspond to different configurations of the track with respect to the 3 cells. The difference in height between two the straight branches is twice the stagger between the mean of cells 11 and 15 and cell 13. Examples of Gaussian fits to 500 μm slices of these branches are shown in fig. A4.13. The half-distance between the peaks is 2.15 mm, to be compared with the nominal 2.20 mm. The space scale is therefore correcly reconstructed.

The spread around the mean value is the convolution of the spatial resolution of the 3 cells. An example of a fit to the resolution curve (upper branch of fig. A4.12 is shown in fig. A4.13. For each cell the diffusion, the 'instrumental' and the ionization contribution to the spatial resolution have been taken into account. The fitted values are consistent with previous measurements;[44] it has to be noted however that, just because of the stagger, the data reach at most $|r| \simeq (7 \div 8)$ mm from the anode wire, where the sensitivity to the diffusion coefficient is reduced.

The spatial resolution has been measured also correcting for the track slope by means of the MWPC information (for nearby cells the errors induced by the telescope slope is negligible). This method has to be used when measuring the resolution comparing the reconstructed distance in cells where the stagger has not the simple interpretation of fig. A4.11. The mean value of the residuals is shown in figure fig. A4.14 as a function of the drift distance. The curve is basically flat (as it has to be) and the residuals are contained inside a ± 200 μm band. This gives an *a posteriori* justification for the correctness of using a symmetric function in our drift cells: only at the very border the asymmetry starts to be apparent.

In figures A4.15 and A4.16 examples are shown of resolution curves from the stagger method for different values of high voltage, angle and beam momentum. In all the configurations the mixture 90% He - 10% iC_4H_{10} gives results within design specifications.

A4.4 Conclusions

We analyzed test beam data on the 2 square cell prototypes of the KLOE drift chamber. The space-time relation has been determined in two different ways, yelding consistent results. Typical errors on fitted parameters in the most precise determination are $O(5 \div 10)\%$. The spatial resolution has been measured for both prototypes, both at 0° and at 90° and for different beam momenta and operating voltages, and it has been found to be within the design specifications of 200 μm.

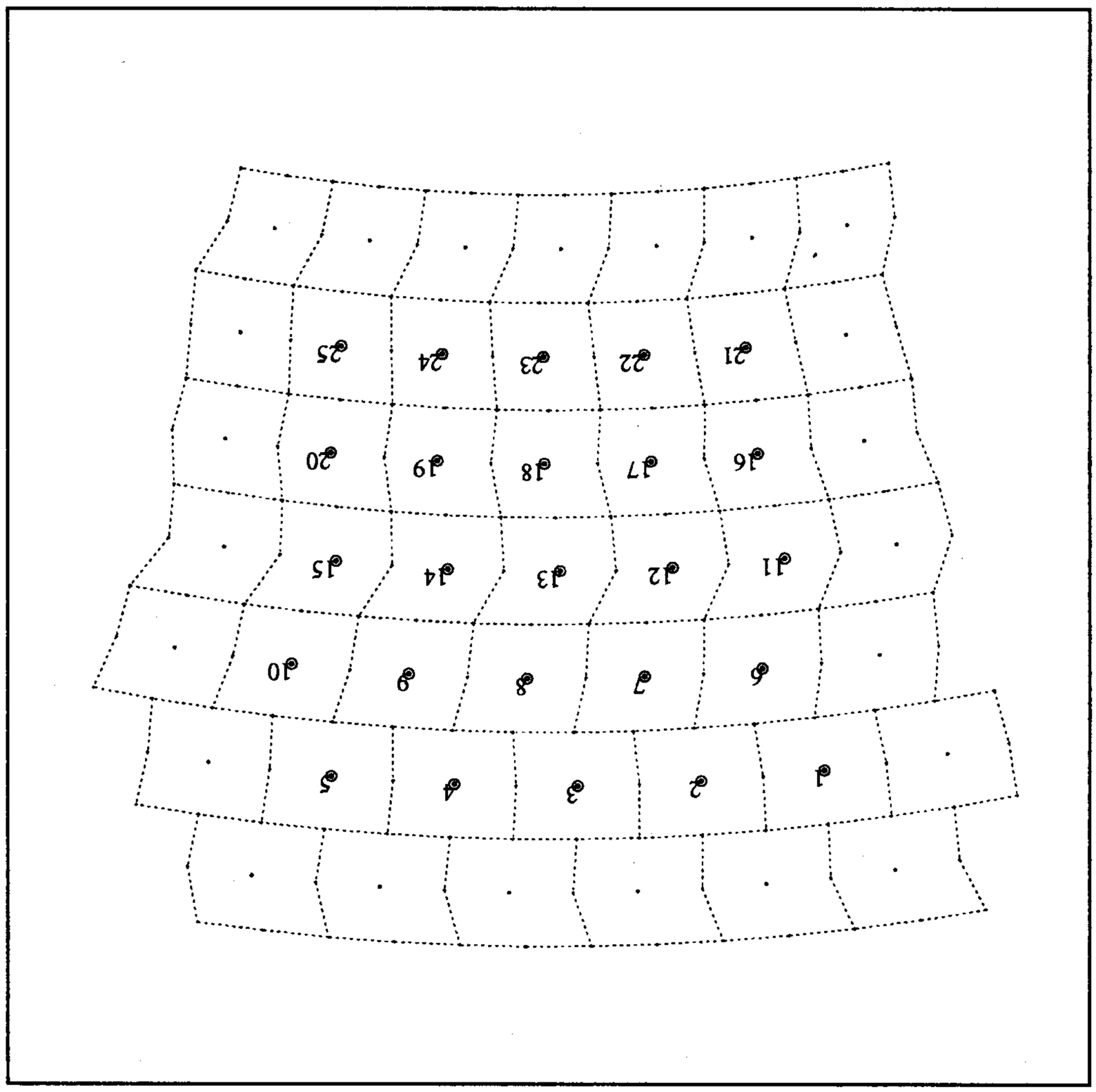

Fig. A4.1. Sketch of the geometry of *prototypes 0.1* and *0.2*. The numbering corresponds to that conventionally assigned to the equipped cells. The field wires on the lateral cell sides are actually there only for *prototype 0.1*.

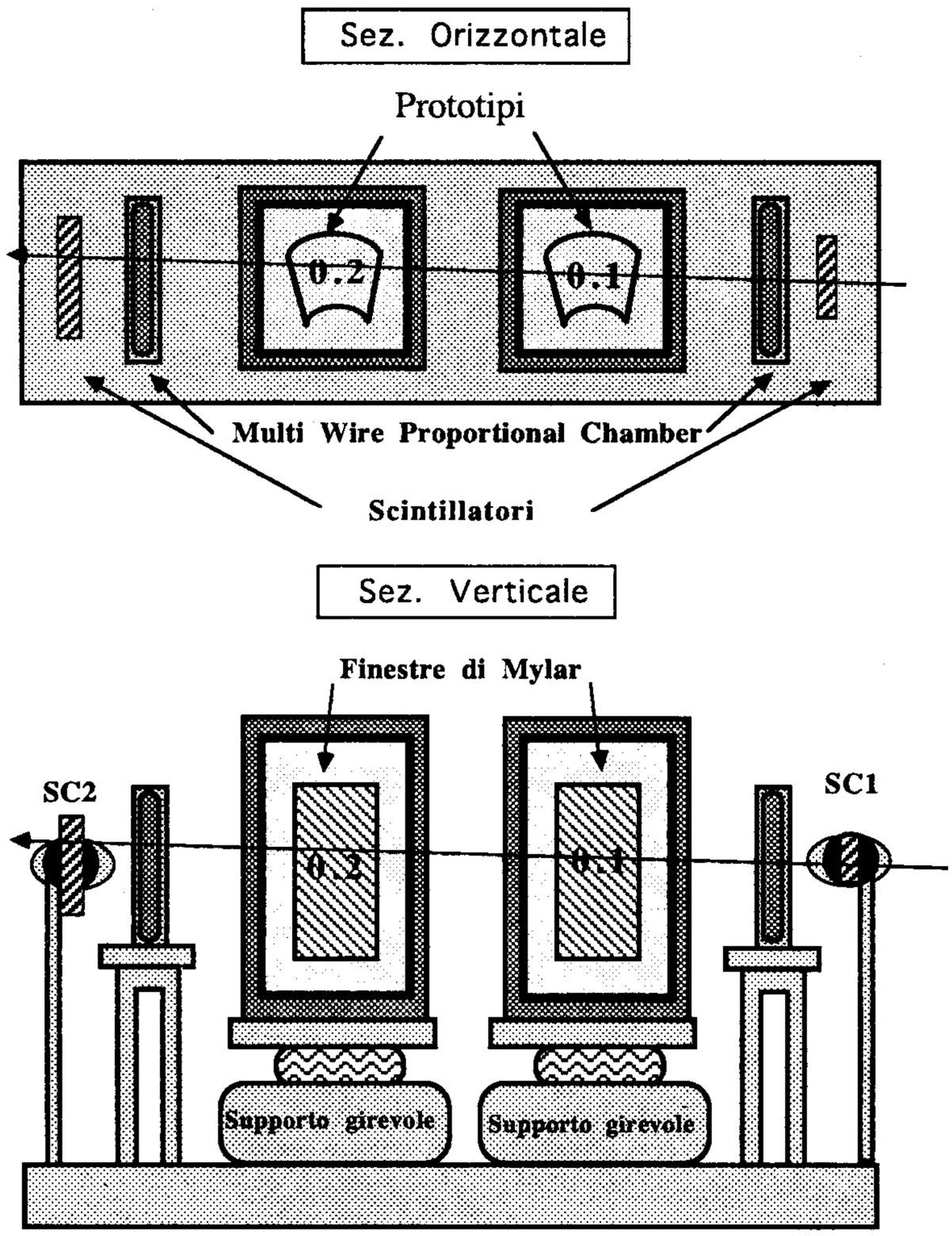

Fig. A4.2. Scheme of the setup at the P.S.I. test.

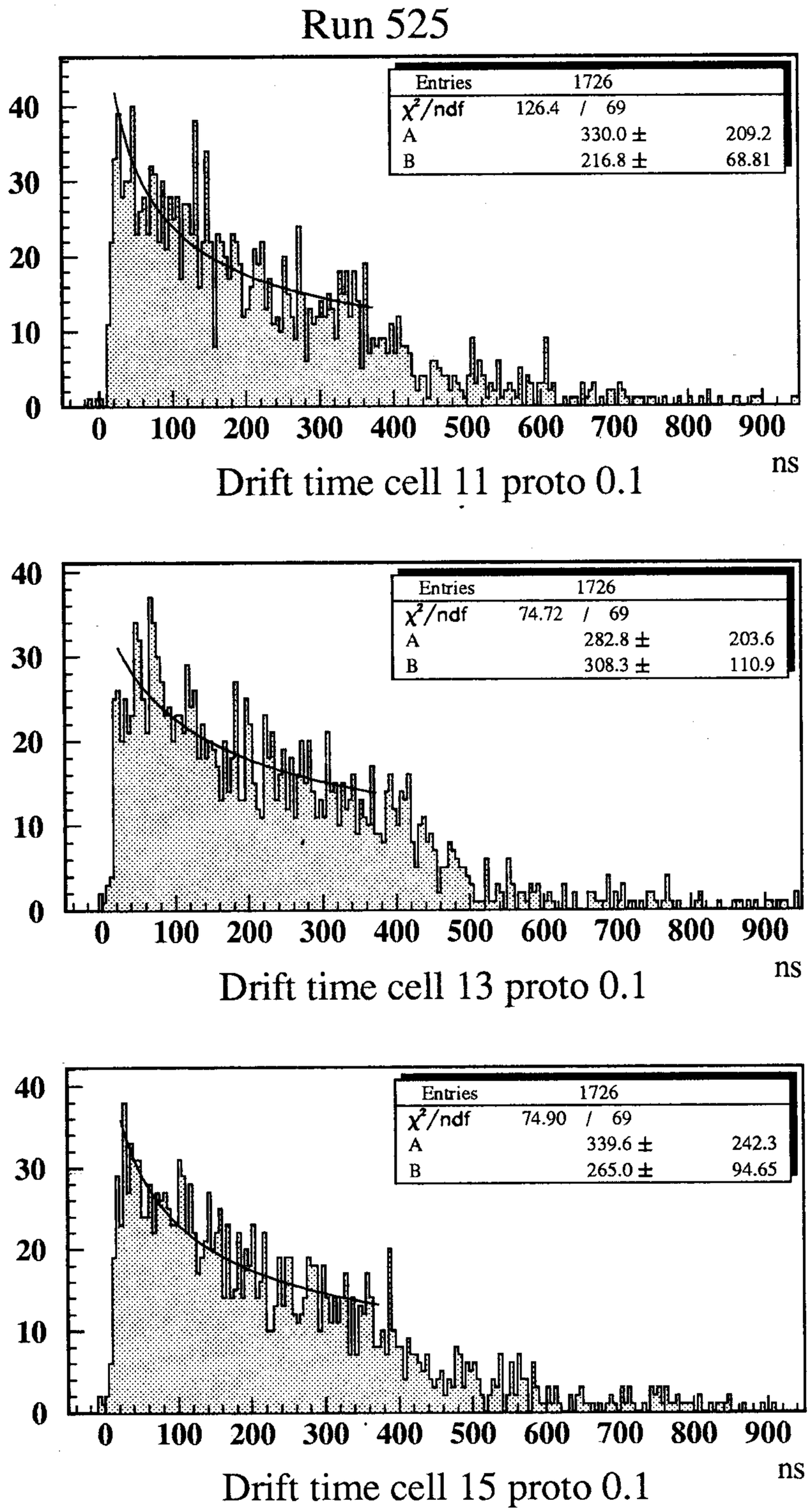

Fig. A4.3. Parabolic fit to the time spectra for 3 cells of *prototype 0.1* $\phi_1 = 90°$, HV_1=1800 V. The gas mixture is 90% He - 10% iC_4H_{10} .

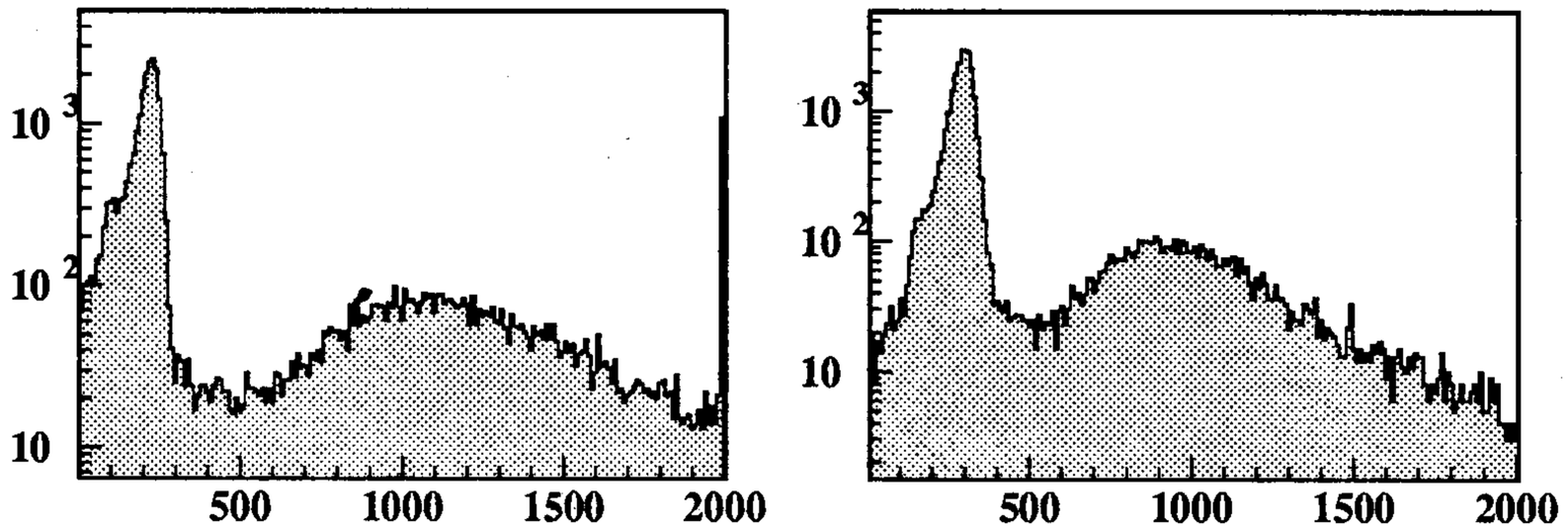

Fig. A4.4. ADC spectra for one cell in each of the two prototypes.

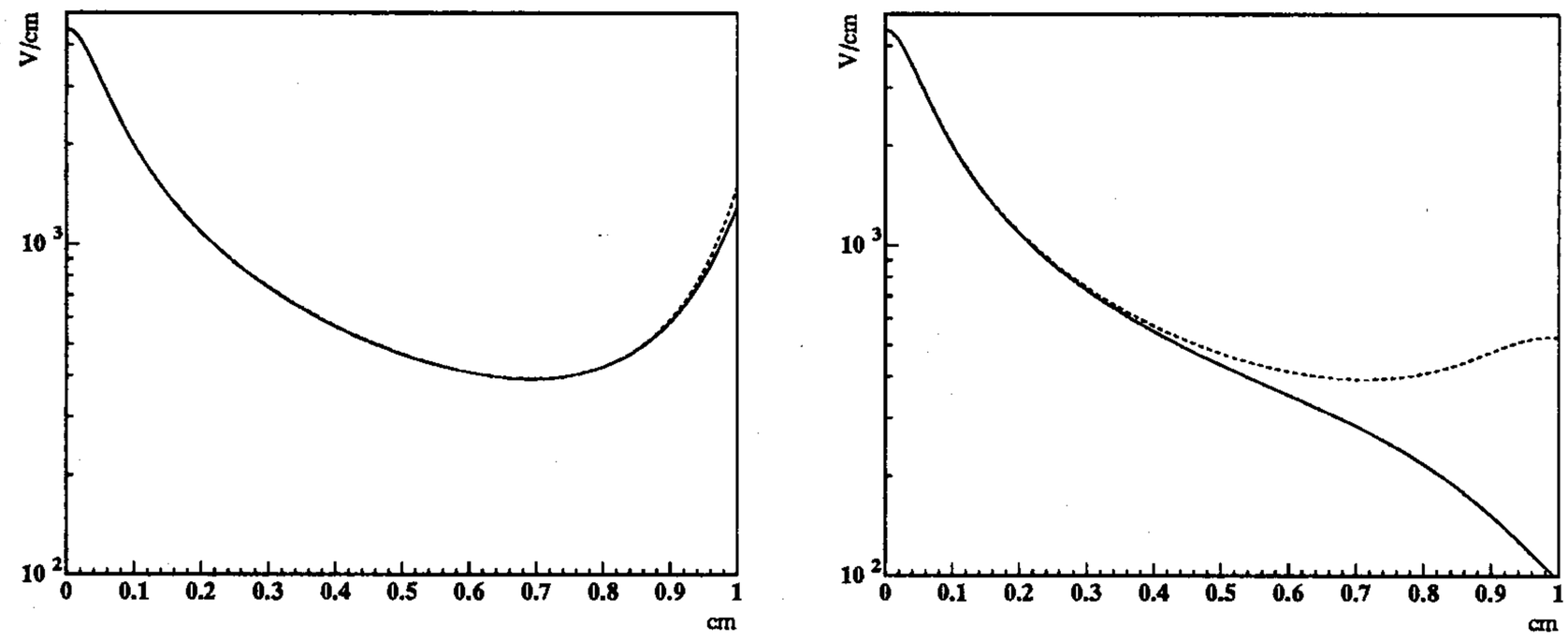

Fig. A4.5. Profile of the electric field inside cell 13 of *prototype 0.1*. Continuous lines refer to tracks at x $(y) \geq 0$, dashed lines to tracks at x $(y) \leq 0$. HV=1850 V.

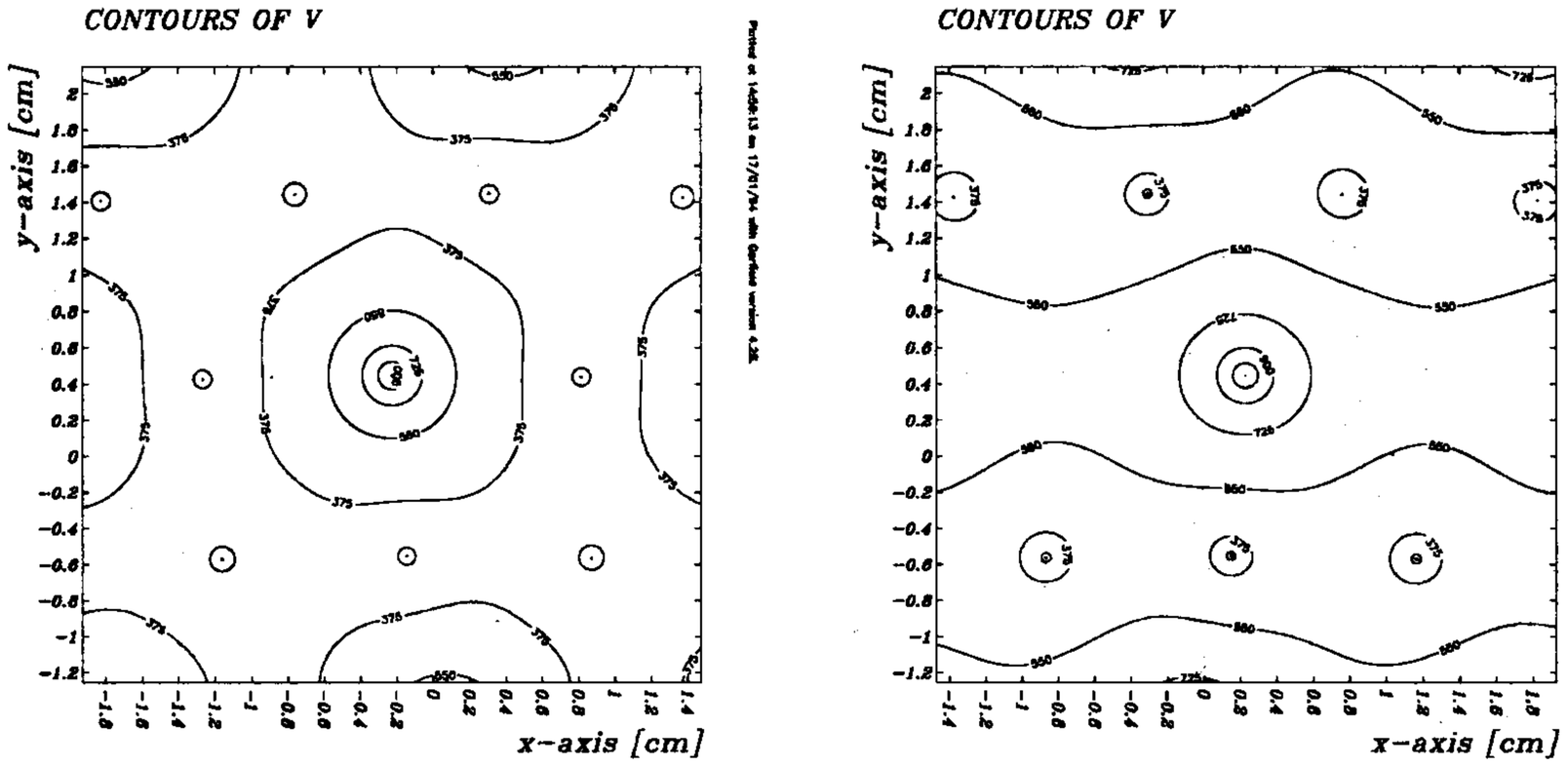

Fig. A4.6. Equipotential lines in the 2 prototypes. The 'opening' of *prototype 0.2* is apparent.

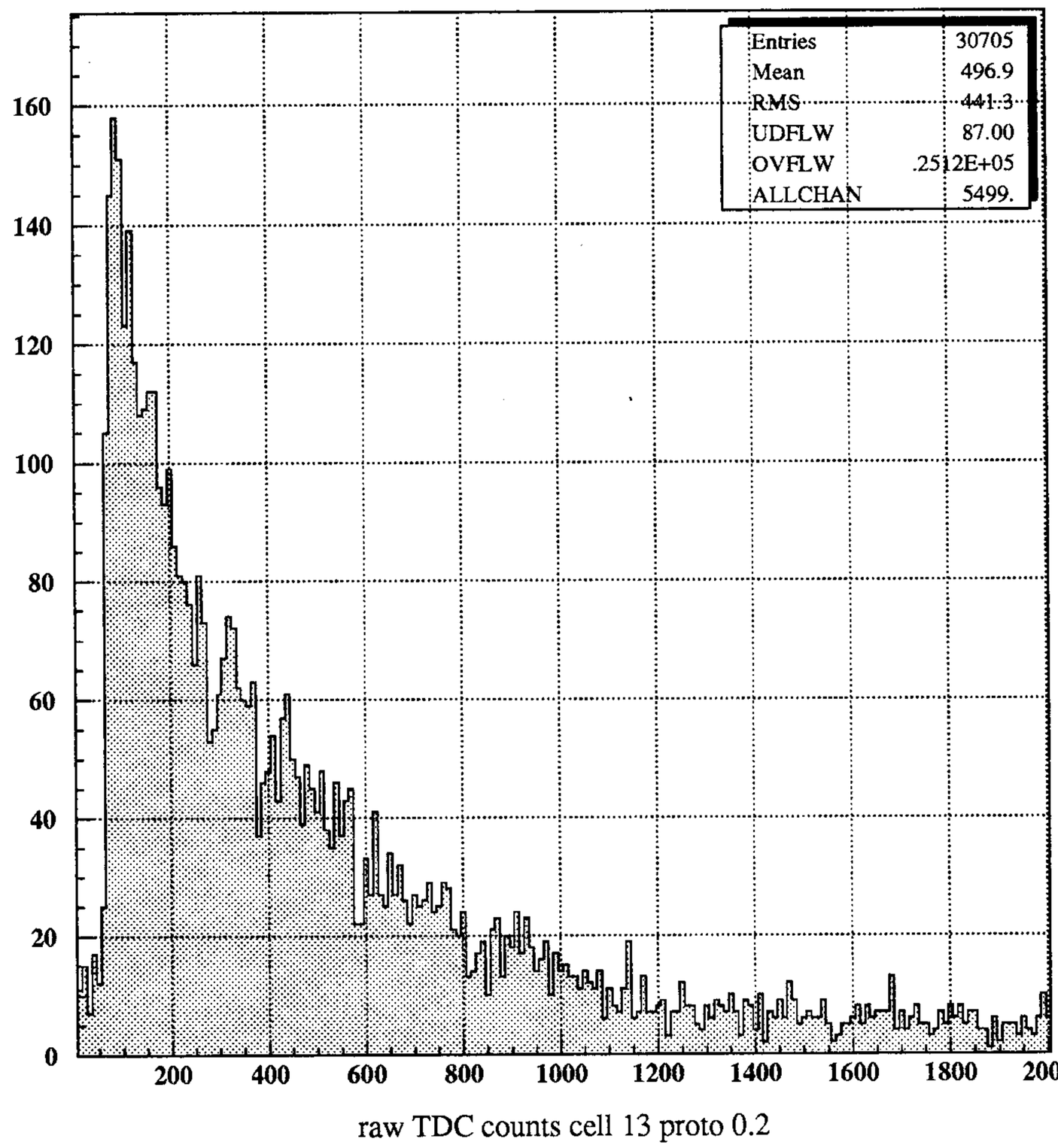

Fig. A4.7. Time spectrum for 0° tracks in *prototype 0.2*

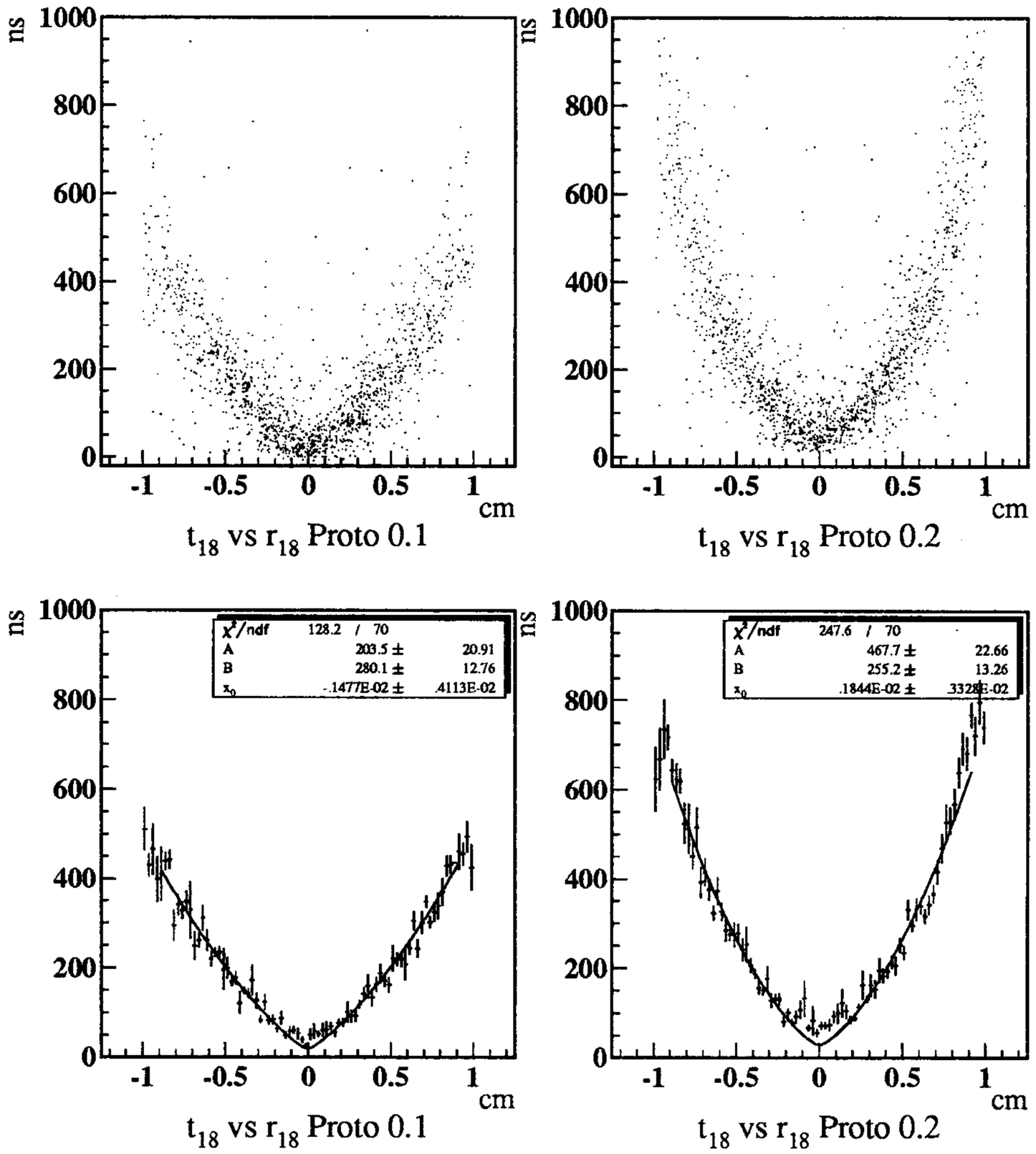

Fig. A4.8. Space-time relations for the same cell of *prototype 0.1* and *prototype 0.2*. Near the cell borders, drift times are considerably longer in *prototype 0.2*. Fits with the parabolic function (A4.1), performed in the region $|r - r_{wire}| \leq 0.9$ cm, consistently give the same drift velocity close to the wire (1/B).

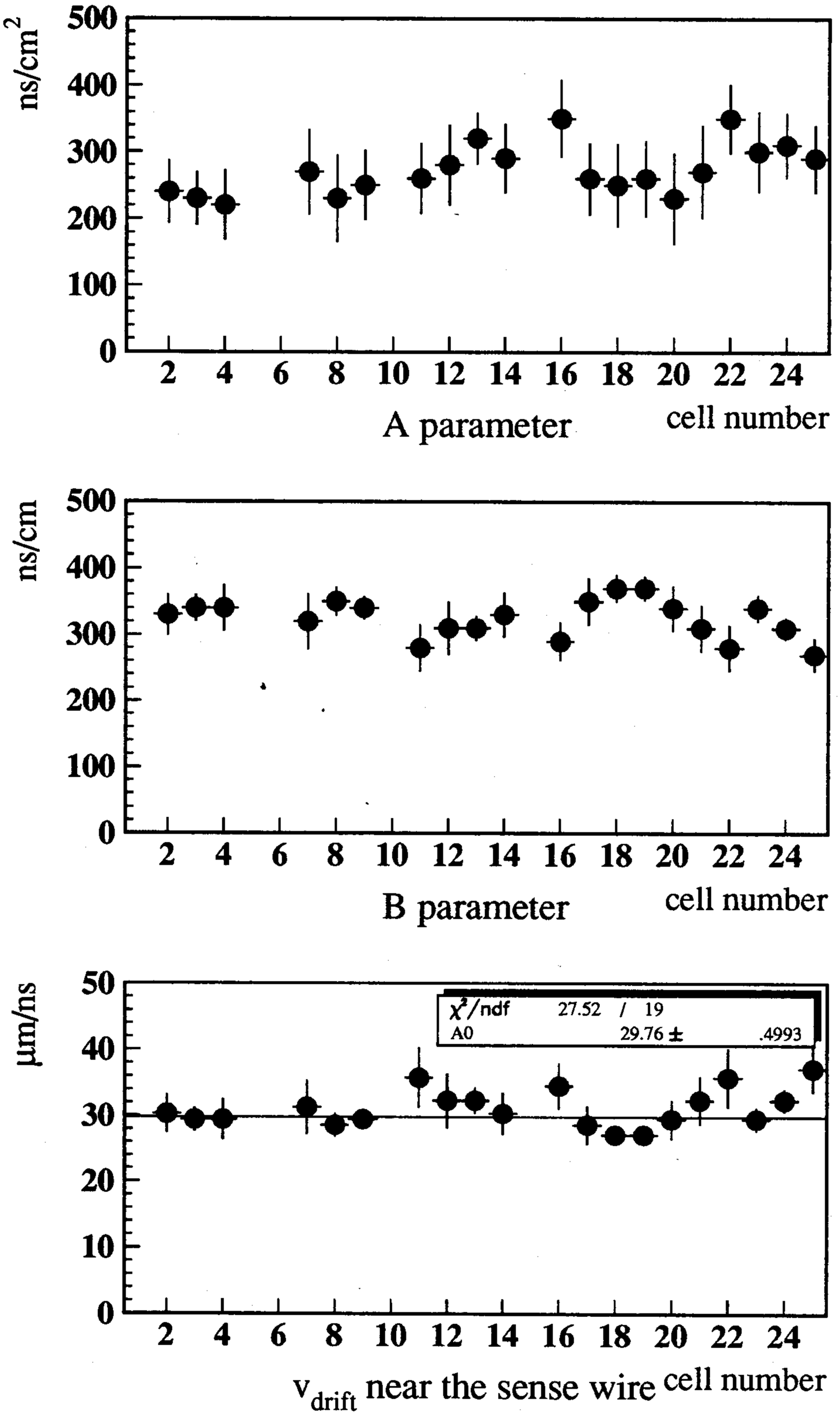

Fig. A4.9. A, B and drift velocity close to the wire from the parabolic fit for the *prototype 0.2* cells. Points related to cells non completely illuminated are excluded from the fit.

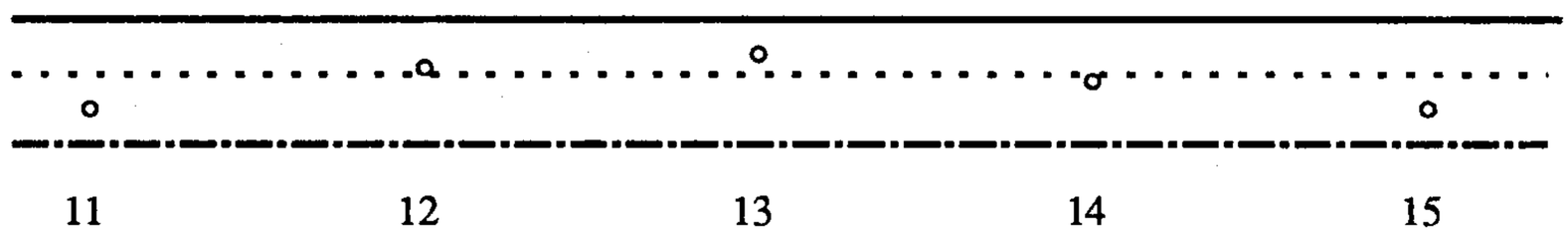

Fig. A4.10. Illustration of the stagger method using only the time information inside the prototypes. The little circles represent the wire positions in the central row of the prototypes. The lines stand for different track configurations (see fig. A4.11).

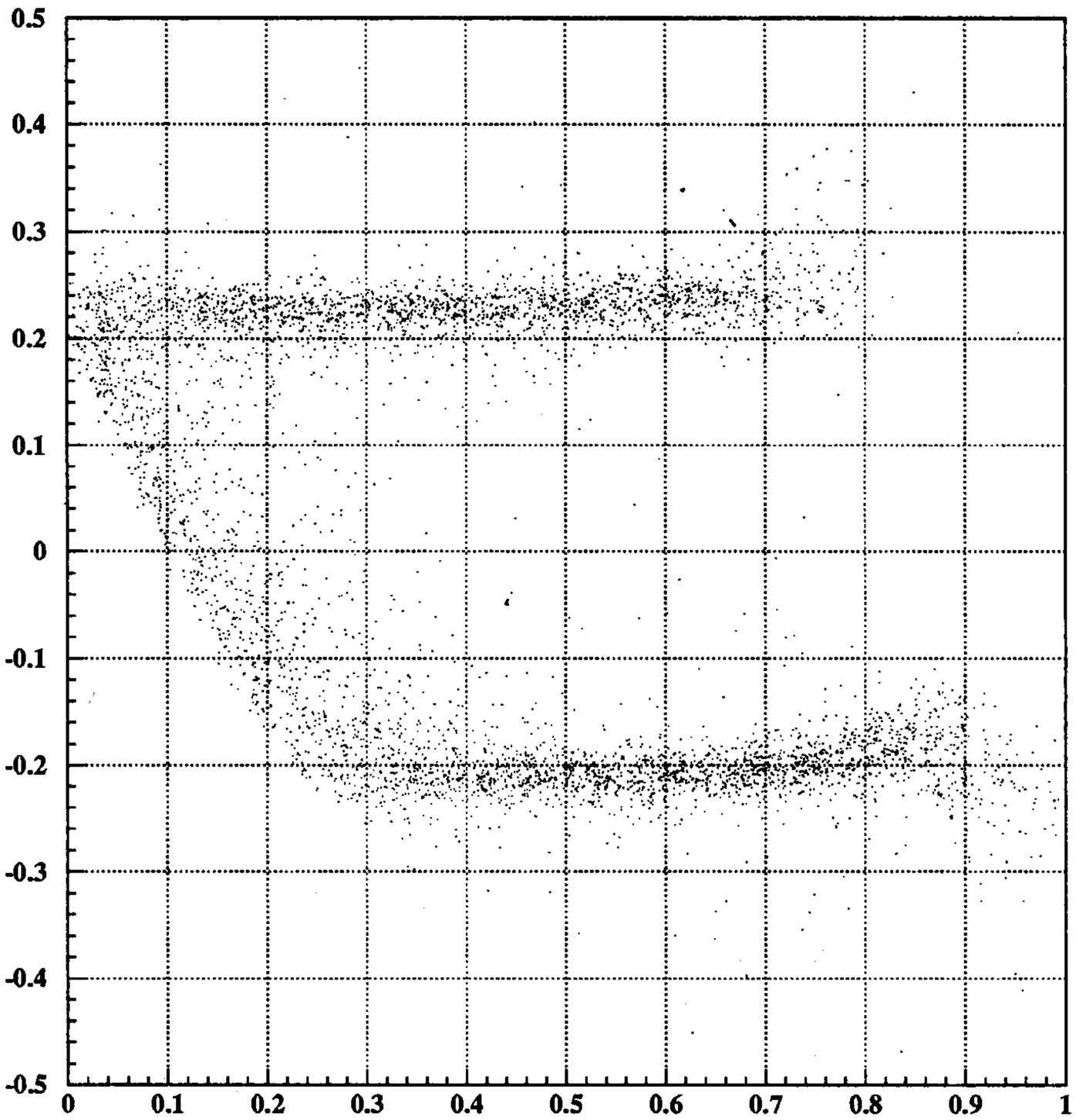

Fig. A4.11. Scatter-plot of the stagger vs. r_{13} (eqn. A4.2). The upper branch refers to tracks passing like the continuous line in fig. A4.10, the lower branch to the dashed-dotted line, the branch between them to tracks passed between the central wire and the two lateral ones (dotted line in fig. A4.10). The scales are in cm.

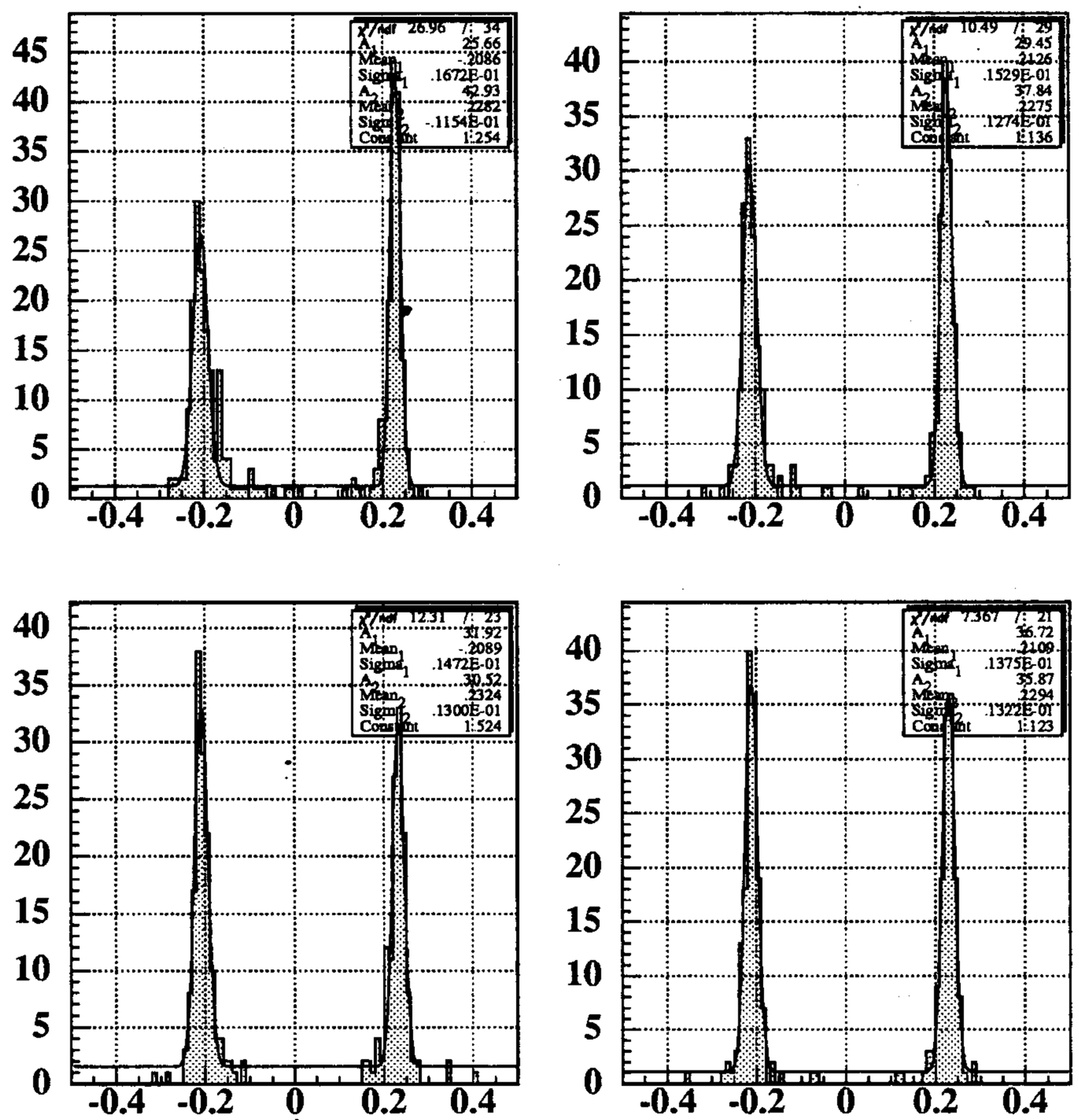

Fig. A4.12. Gaussian fits to slices ($r_{13} = (4 \div 6)$ mm) of the previous figure. Horizontal scales are in cm.

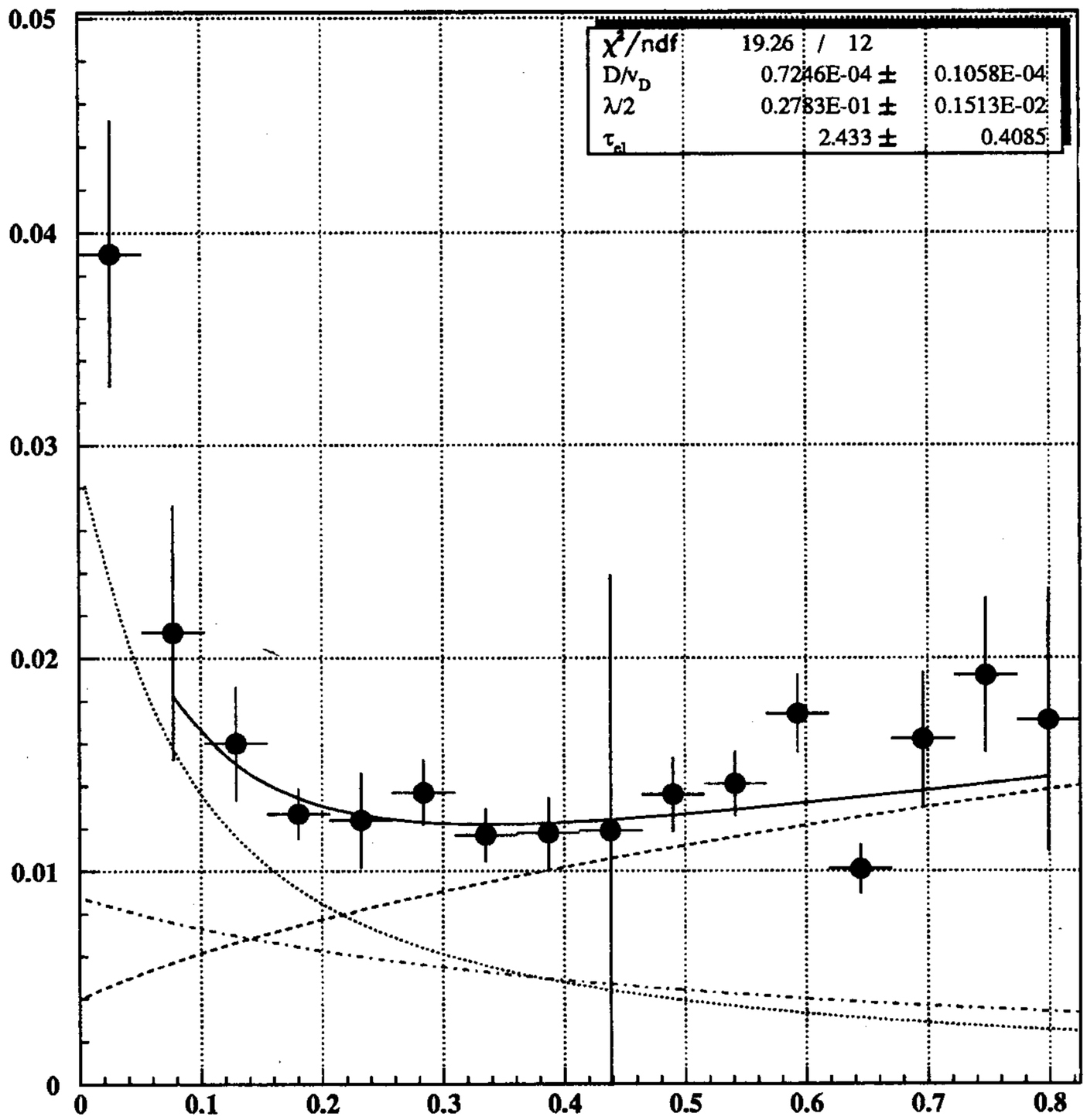

Fig. A4.13. Fit to the resolution curve for *prototype 0.1*. HV_1=1800 V, $\phi_1 = 0°$, $p_{beam} = 150$ MeV/c. The scales are in cm.

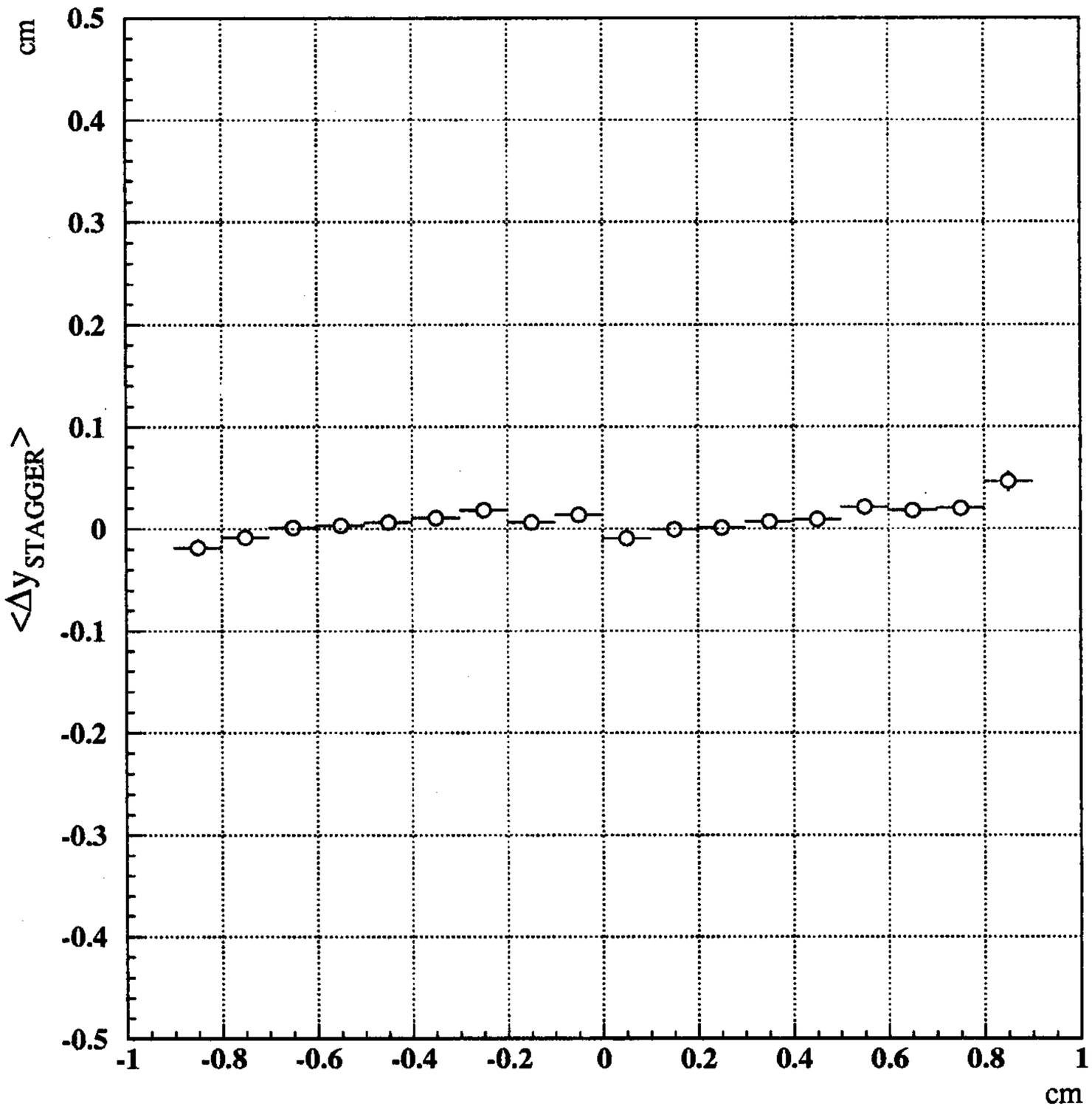

Fig. A4.14. Mean value of the residuals vs. track DCA in *prototype 0.1* for $\phi_1 = 0°$, HV=1800 V.

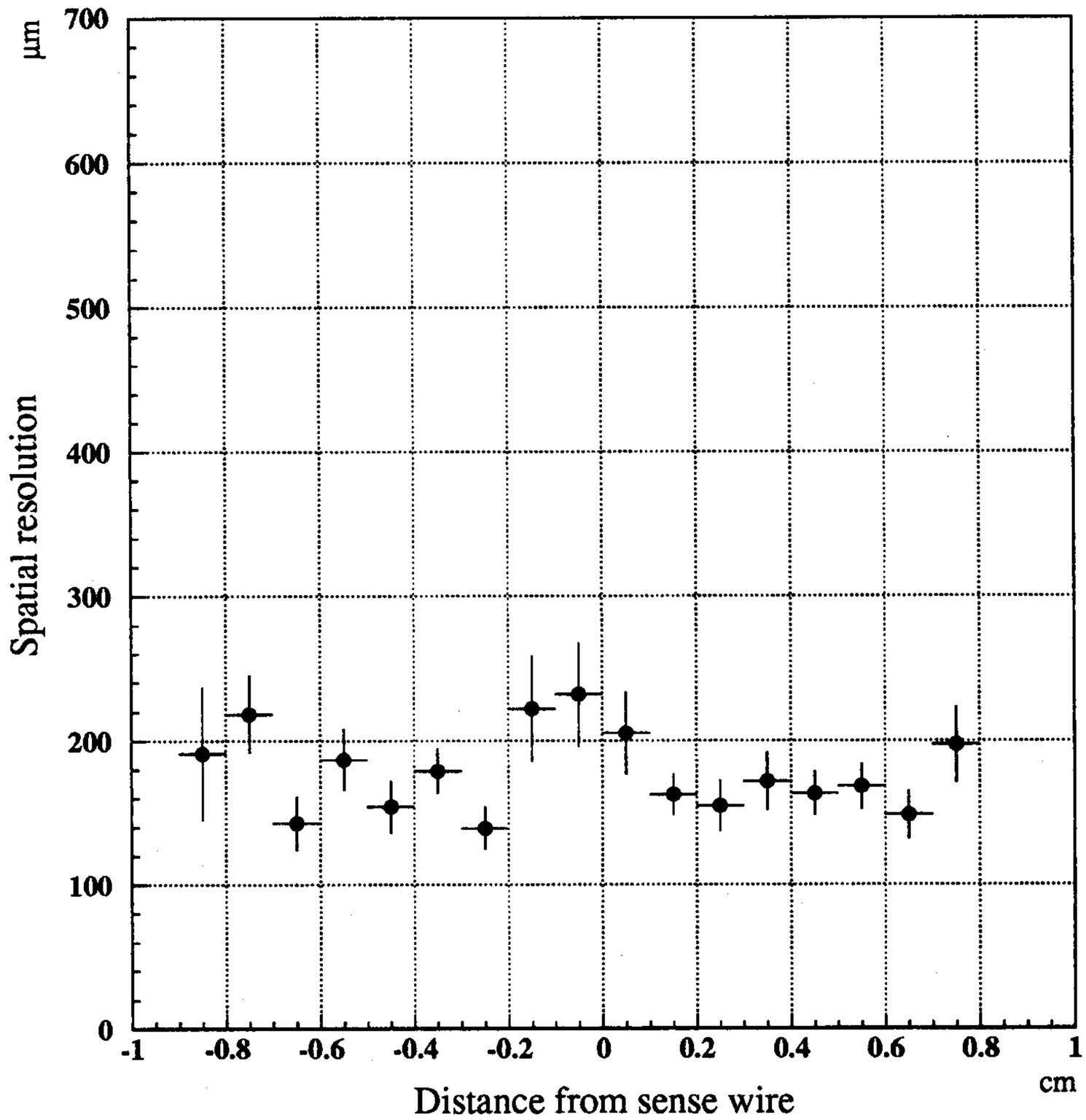

Fig. A4.15. Resolution curve in *prototype 0.1* for $\phi_1 = 0°$, HV=1800 V, p_{beam} = 250 MeV/c.

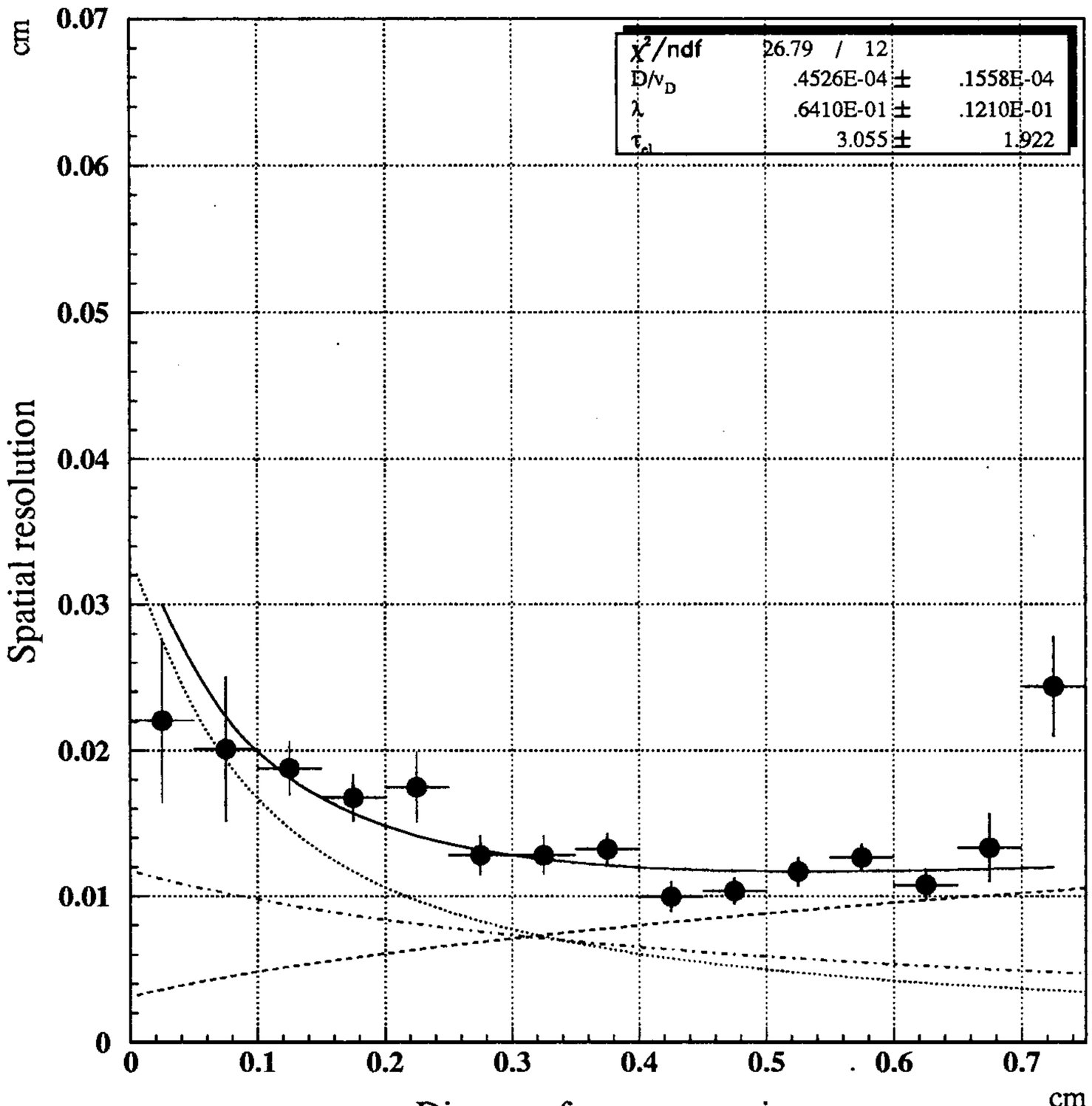

Fig. A4.16. Resolution curve in *prototype 0.1* for $\phi_1 = 90°$, HV=1800 V, p_{beam} = 250 MeV/c.

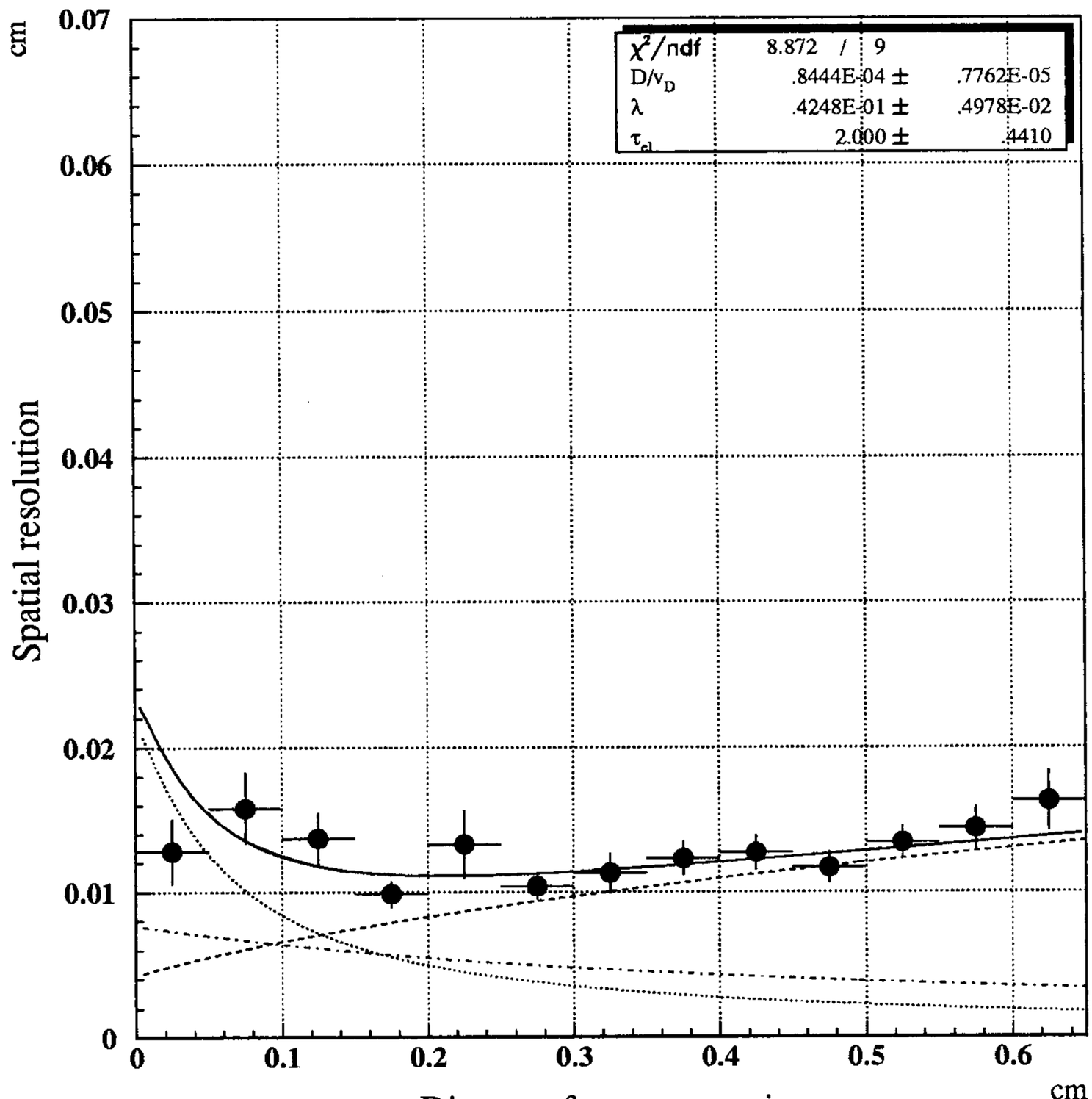

Fig. A4.17. Resolution curve in *prototype 0.2* for $\phi_2 = 90°$, HV=1950 V, p_{beam} = 150 MeV/c.

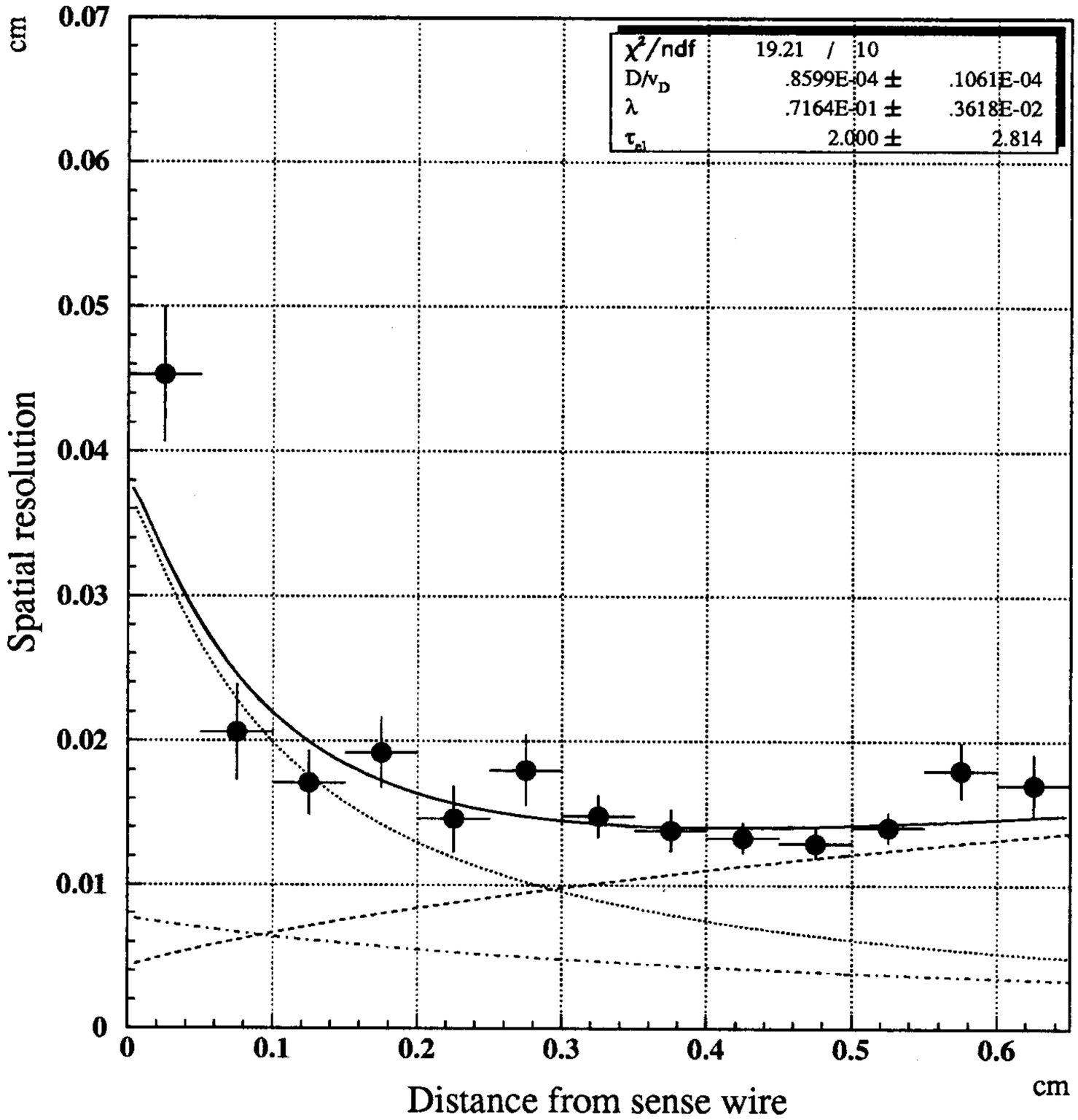

Fig. A4.18. Resolution curve in *prototype 0.2* for $\phi_2 = 90°$, HV=1950 V, p_{beam} = 350 MeV/c. Spatial resolution is marginally worse with respect to previous figure due to the reduced number of cluster/cm released along the track, because of the different beam momentum.

KLOE Note N. 97
March 13, 1994

APPENDIX A5.

Measurement of the space point resolution the drift chamber prototypes

Riccardo de Sangro

ABSTRACT

We have tested two small drift chambers with different square cell configurations in a test beam of energies between 150 and 350 MeV with various helium based gas mixtures. In this work we show that a resolution of $\leq 200\mu m$ can be achieved with a 90% He - 10% iC_4H_{10} gas mixture.

A5.1 Introduction

In this paper we report on the tests that have been made to get an experimental confirmation of the practical possibility to achieve some of the goal performances of the KLOE drift chamber. A more detailed discussion of the physics motivations for the required performances and the design solutions adopted to reach them can be found in refs.[46] [47] . In the following we will just briefly mentions the aspects more relevant to this work.

The main design goals are a resolution on transverse momentum of $\sim$0.3%, which is based on assuming $\sim 200\mu m$ for the point resolution in the transverse plane, and a high ($\geq$ 98%) tracking reconstruction efficiency for the CP violating decay $K_L \rightarrow \pi^+\pi^-$. Both of them depends on the drift gas chosen and on the geometry of the cell.

The low ($\sim$150-250 MeV/c) particle momenta involved in the decays of interest, result in the multiple Coulomb scattering being the dominating contribution to the momentum resolution, which compels one to use the lightest possible materials throughout the chamber. The transparency of the chamber is also needed to preserve the high detection efficiency for low energy photons in the electromagnetic calorimeter outside it, which is needed to detect the neutrals. Widespread use of special materials such as carbon fibers, characterized by their strength and low radiation length, is therefore foreseen for the construction of the mechanical structure of the chamber and very light, helium based drift gas mixtures are under study. Also, the number of sense and field wires will have to be kept to a minimum.

Since the charged tracks from the decays of can originate anywhere inside the chamber volume and leave in all directions, an interaction region pointing geometry is not the most efficient and thus the whole chamber volume will be uniformly filled with closely packed cells.

The z coordinate measurement along the wires is done with stereo layers. In the present design, the chamber will have all layers stereo, alternating positive and negative angles. To realize such a layout and to minimize the number of wires per cell, a square cell has been adopted.

To test both the cell geometry and the relatively little known gas mixtures, we have built two small drift chamber prototypes with square cells: *Prototype 0.1* with a 3:1 ratio of field to sense wires, and *Prototype 0.2* with a ratio of 2:1 (see fig. A5.1).

about 2 cm wide, differing between them only for the fact that *Prototype 0.1* has one more wire on each of the vertical sides of the squares. Table A5.1 lists the principal characteristics of the two devices.

Wire length	50 cm
Wire diameter	sense: $20\mu m$/ field: $80\mu m$
Wire material	sense: Cu-Be / field: Al
Cell shape/size	square/ $(2x2)cm^2$
Field to sense wire ratio	Prot 0.1 : 3:1 – Prot 0.2 : 2:1

Table A5.1. Prototypes main characteristics.

In fig. A5.2 the layout of the cells is shown and in fig A5.3 the details of the two cells showing the differences between the two geometries.

Only the innermost 5x5 sense wires are instrumented, while the outer ones are set at the proper high voltage only to reduce the distortion of the electric field in the cells under study. All the field wires are grounded. The signals from the wires are amplified by a transresistance amplifier developed in Frascati as a first prototype of the final front-end read out for the final chamber.[48]

A5.2 Test Beam Setup

The two prototypes have been exposed to a particle beam (mostly pions) of energies between 150 and 350 MeV made available in the $\pi\mu 3$ experimental area of PSI[49] . A sketch of the experimental setup is shown in fig. A5.4.

The beam entered from the right first traversing the $(4x4)cm^2$ scintillator S1, then the first of two multiwire proportional chambers, MWPC 1 and MWPC 2, positioned immediately before and after the two prototypes *Prototype 0.1* and *Prototype 0.2* . A second $(12x12)cm^2$ scintillator S2 followed MWPC 2.

The prototypes were sitting vertically (wires running vertically) on two revolving supports that enabled us to rotate them about their axis and study their response to different incident beam angles.

The MWPCs are made of two orthogonal planes of 128 wires with a 1 mm pitch. The signals above a set threshold constituted a digital hit; adjacent hit wires were then grouped in clusters. After this operation one was left with a cluster list with the coordinates of the clusters for each plane, which was written to disk. The resolution on the position thus obtained is expected to be $\sim 300\mu m$.

The two MWPCs therefore gave two position measurements of the incident tracks, one for each of the two projection planes X,Y and X,Z as defined in the reference system chosen for the analysis and shown in fig. A5.4. From these measurements we could determine the incident particles straight trajectories in the prototypes.

The coincidence S1*S2 of the two scintillators formed a trigger. The CAMAC acquired signals included one TDC and one ADC value for each sense wire (100 channels), the MWPC latches (128x4 channels), two ADC value for the scintillators plus a number of scaler channels with various rates. Also, the time of flight of the beam particles going from the production target to the setup was acquired in order to get some information on the type of beam particle (π , μ , e, p etc.).[50]

The CAMAC was read out with a PC running an acquisition software developed at PSI and the data stored on a μVAX disk connected to the PC. The program allowed on line histogramming of the acquired data for monitoring, and performed the clustering of the MWPC hits. The data was then transferred to tape for the off-line analysis. In fig. A5.5an event is shown; the solid line represents the external track, the others represent the tracks fitted with the two prototypes individually and the track obtained with a combined fit of the two. A profile of the beam and a measure of its angular dispersion as measure in the MWPCs is shown in fig. A5.6.

A5.3 Data Analysis

The test beam data has been collected in two one-week periods in June and July of 1993. Different runs have been taken with different combinations of gas mixture, beam incidence angle and operating voltage of the chambers. The different mixtures tested included 90% He - 10% iC_4H_{10} , 95% He - 5% iC_4H_{10} , 60% He - 40% CH_4 , 80% He - 20% CO_2 and 60% Ar - 40% iC_4H_{10} .

In this paper we report on the data taken with 90% He - 10% iC_4H_{10} , a summary of which is given in Table A5.2.

RUN #	Φ angle (degrees) Proto 0.1	Proto 0.2	All Runs:
513	0	0	Gas mixture 90% He - 10% iC_4H_{10}
519	0	90	Beam Energy: 250 MeV
520	0	60	HV Proto 0.1: 1800 V
522	30	30	HV Proto 0.2: 1950 V
523	60	0	
525	90	0	

Table A5.2. Summary of the data runs used in the present analysis

Track Fit

The main scope of this analysis is to study how well could one reconstruct the beam particles trajectories inside the chambers, and more precisely with what spatial resolution one could measure the impact parameters of *real* tracks inside the cells.

To do this one needs to first determine which wires were hit by the particle, then apply some function to translate the time measurements to a distance, and finally perform a fit with these points to a straight line. The residuals of this fit give an estimate of this resolution.

Hit Selection

The first selection criterium applied to the data to look for events with a good track, was to ask for a MWPCs track, being it defined as two one-cluster hits in each of the two MWPCs Y projections. These points give the *external track*'s parameters. This requirement already cuts about 40% of the events, due to a somewhat low MWPCs efficiency (~80% each).

In the events selected, the external track is used to determine which cells had been traversed by the particle. Its distance of closest approach to all the cells with a TDC reading in range is calculated, and compared to the R_d obtained from the time measurement of the cells. All the hits in which the two differed by more than 1.2 cell radii are discarded. The ADC reading of all the others are then required to be 3σabove the pedestals.

For all the events in which there are at least 4 hits in each prototype, a fit is attempted.

Fit Procedure

Since the time measurements can only be translated in radial distances from the wires and not to single points in space x_i, y_i, the fit is done by looking for straight lines which are simultaneously tangent to all the circles centered in the positions of the hit wires, and with radii proportional to the drift times via the space-to-time relation.

Both parameters of the fitting line are varied and the distances of closest approach ρ_i to all the fitted cells calculated at each iteration. The fit is required to minimize the χ^2 :

$$\chi^2 = \sum_i \frac{(\rho_i^M - \rho_i)^2}{\sigma_i^2}$$

where the ρ_i^M are the measured starting values, and σ_i are the errors of each cell, which are expected to be a function of the distance from the wires. The error function used is shown in fig. A5.7. A difficulty inherent to this position measurement is that of left-right ambiguities: the time gives only the distance from the wire but not the *direction* the ionization is coming from. Such ambiguities are resolved by the fit most of the times because the cells are slightly staggered, but there still remain some cases in which the fit results in a bad track giving a good χ^2 .

We have tried to resolve this problem using the information of the external track to decide which side of the wire a particular track had crossed. It turns out that is very difficult to implement such a thing in our 'circles' fit. We have therefore also tried a simple least square fit to a straight line, in which the x_i were fixed to the nominal coordinates of the wires and the y_i were the y nominal coordinates of the wires $\pm$ measured drift distances, where the sign was chosen based on where the external track was. The error in fixing the x_i's is not significant because the tracks are almost horizontal, thus the x point of closest approach has a coordinate which is indeed $x_{doca} \sim X_{wire}$.

Althoug we have indeed seen a slight improvment in the χ^2 distribution with this linear fit, we have decided not to rely too much on the extra information given by the external tracking in order not to obtain results that may turn out to be too optimistic, and decided to use only the 'circles' fit.

It is worth noting at this point that the external tracking has in fact been used in the track fit only to select the 'good' hits, and only because we did not want to spend any time with the pattern recognition of beam tracks.

It is important to notice that to apply this procedure one has to know the space to time relation to a very good precision, as well as the relative position of the chambers, MWPCs etc.

Set-up Alignment

So the first thing to do to obtain a good time to distance relation is to check the relative alignment between the MWPCs and the prototypes.

The origin of the reference system is chosen to be exactly in the middle of the two prototypes in X, and in the center of the MWPCs active region in Y. The relative Y offset between the two MWPCs was measured to be zero in a survey of the setup, as was expected given the precision of their mechanical assembly. Note that any small deviation from the nominal value of the X coordinate of either the MWPCs and/or the prototypes, produces a negligible effect on the

determination of the position of the tracks relative to the wires, because the tracks are almost horizontal, i.e. aligned with X.

The MWPCs are therefore aligned in Y and what we need to do is only to find the position of the two prototypes with respect to them. Starting from the nominal positions of each prototype obtained with the survey measurements, the small deviations from them can be reduced to a rotation about their vertical axis and an offset in their Y coordinate.

These deviations were measured by comparing, event by event, the offset and angular coefficients of the external track with those of the two tracks independently fitted starting from the prototypes hit cells[1] . A systematic shift from zero in the distribution of the difference between the angular coefficients indicates a rotation in the XY plane of the prototype with respect to the chambers. After correcting for it, we repeated the fit and then plotted the difference between the Y coordinate extrapolated from the external track in a given cell and that extrapolated in the same cell from the prototype fitted track. Again, a shift in this distribution indicates a systematic offset of the prototype with respect to its nominal position. That this is a real overall displacement of the whole prototype is confirmed by the fact that the same offset is simultaneously observed in different cells in the prototype. In fig. A5.8we show these distributions. The procedure has been repeated for both prototypes independently and for all of the analyzed runs.

Space to Time Relations

The time-to-distance relation is the relation between the measured time of arrival of the ionization signal on the prototypes wires (that is the drift time, t_d) and the position where the ionization was produced by the particle inside the corresponding cell. If one knows the real distance of closest approach to the wire (R_d) of the track, this can be done relatively easily by correlating the drift time t_d to the known R_d , and then fitting a function which will give the distance corresponding to each measured time.

In our setup, the real R_d was obtained by using the particle track trajectory measured with the MWPCs, which we have already called *external track* because is determined independently from the prototypes.

Time-to-Distance Fit

After all the position corrections have been applied, the fits to the space to time functions have been repeated. In fig. A5.9the t_d Vs R_d correlation is shown for a cell of the two prototypes for ϕ=0° and 90° . The sign of R_d has been assigned based on whether the tracks passed above the wire ($Y_{trk} \geq Y_{wire}$, $R_d \geq 0$) or below it ($Y_{trk} \leq Y_{wire}$, $R_d \leq 0$). From the 0° plots one can clearly see the effect of the missing field wire on the sides cell structure of *Prototype 0.2* , namely the lengthening of the drift time of the 2:1 with respect to the 3:1 cell near the border, which is due to its lower electric field in this region. They also show that tracks entering the 2:1 cell at 90° see a cell very similar to the 3:1, and that the latter is identical for tracks at 0° or 90° as expected.

To perform the fit, a profile histogram was obtained from these scatter plots. This is shown superimposed to the scatter plot before (fig. A5.10b) and after (fig. A5.10c) applying the cuts

1 A 0^{th} order space-to-time relation can be obtained before any alignment is made, and used to perform a first track fit in the prototypes.

shown in fig. A5.10a aimed at removing some of the background noise; fig. A5.10d shows the comparison of the two profiles. As it is apparent from these plots, without the cuts the profile histogram does not adequately reproduce the shape of the scatter plot neither very close to the wire nor closer to the cell border.

The function used to fit the profile is the parabola:

$$t_d = AR_d^2 + B|R_d| + t_0$$

where the parameter t_0 takes into account any small errors in the evaluation of the TDC pedestals which are due to the unavoidable delay of the signals in the cables, electronics etc. These pedestals are estimated for every cell by looking at the beginning of the raw TDC time distributions, then subtracted from the raw TDC reading before the conversion to ns. Inverting this function one gets the drift distance for any measured t_d .

The correct choice of t_0 is very important because it affect the track fit near the wires, and at the same time is difficult because there are many effects to take into account when the track get close to the wire.

Firstly, even at zero impact parameter the time of arrival of the first cluster is not always zero, but on the average is $\lambda/2$, if λ is the mean distance between ionization clusters, divided by the drift velocity. This is due to the very low ionization density of the gas mixture, and the effect becomes negligible very soon going away from the wire (see fig. A5.11). This effect can and has been corrected for.

A second effect is due to the finite resolution in the extrapolation of the tracks position in the cells, which is due to a combination of multiple Coulomb scattering of the beam particles in air and other materials and the MWPCs resolution, and amounts to $\sim 600\mu m$. Given the fact that the time measurements cannot fluctuate to values below a minimum (which is the starting point of the time spectrum) when we take the average time of those tracks whose position extrapolates to a very small distance from the wire, we get a number that remains greater than zero, even when the distance is zero. This situation is very clear by looking at the t_d Vs R_d correlation plots in the proximity of $R_d = 0$, where the profile histogram obtained by doing such an average is clearly away from $t_d = 0$.

At this point there are two possible approaches: either one fixes t_0 to the value corresponding to the beginning of the spectrum (which after all is the *real* t_0 , because the TDC measured a zero drift time), or one fit the t_0 . In the first case the space-to-time relation is not reproduced very well, especially near the wire, but the gas parameters like the drift velocity at the wire (which is directly given by the inverse of the fitted parameter B) assume values that are in good agreement with the expectations.[2] In the second case the space-to-time relations get reproduced much better, both closer to the wire and towards the cell's border, but in this case the drift velocities at the wires turn out about a factor of two higher than expected. It is not too surprising though, given the external tracking extrapolation resolution, that we cannot measure these parameters near the wire.

If the space-to-time relation is not correct, the effect appears as a bias in the mean value of the distributions of the residuals of the track fit that depend on the distance from the wire.

---

2 See the discussion in G.Finocchiaro, KLOE Note N.92, March 1994 and references therein

An example of this is shown in fig. A5.12, where a comparison is made of the two fits, labeled NEW (fitted t_0) and OLD (fixed t_0); the two cases also differ in the cuts applied to the t_d Vs R_d correlation plot before fitting. These systematic effects in the determination of the space-to-time relations make it very difficult to assign the correct error to the measurement and therefore lead to a χ^2 distribution which is not very good.

In fig. A5.13we compare the χ^2 distributions for the two cases in the two prototypes, and they both have a rather high average value. In fig. A5.14we show as an example how the average resolution for cell 8 compares for the two cases. The gaussian fits give a $\dot{\sigma}$of $\sim 340\mu m$ for *Prototype 0.1* and $\sim 310\mu m$ for *Prototype 0.2* , and were made to have an idea of the size of the errors to be used in computing the χ^2 . The fact that the χ^2 /dof average value is still higher than one is clearly due to the fact that the distributions are not gaussian and have rather long tails.

The space-to-time relations can in principle be corrected for, and with a few iterations it should be possible to cope with this problem. The reason why we observe a bigger improvement for *Prototype 0.2* is because the fit for *Prototype 0.1* had been already worked on several times, albeit using always the same fitting method. This improvement is also reflected in the width of the $\Delta\Phi$ distributions, as is shown in fig. A5.15. The difference in angle between the external and the fitted tracks is basically due to the measurement error in the prototypes, and its rather large size is due to the short (10 cm) lever arm of the measurement. The width of $\sim 6.6mrd$ correspond to an average cell error of $\sim 330\mu m$, that is in fair agreement with what is observed above.

Resolution Vs drift distance

It is an important point to note that this error is averaged over the whole cell and, as we have already seen, is mainly due to the systematics. By looking at the residuals as a function of R_d one can measure the resolution that could in principle be achieved once the space-to-time relations are well modeled for all R_d , and all the systematic effects have been understood and corrected for.

In fig. A5.16and fig. A5.17the plots of the residuals of the fit as a function of R_d for the two prototypes are shown. The residuals plotted for each given cell are calculated from fits which include the cell itself, and is therefore an optimistic estimate of the real resolution. For the cell of the figure, one could take $\sim 160\mu m$ as an average value throughout the cell, excluding the region very close to the wire and very far from it; this number would translate in a resolution of $\sim 190\mu m$.

The different curves are obtained for different track incidence angles, and different space-to-time relations have been used for each different angle; the resolution is very similar at all angles in both prototypes.

We have obtained similar results for other cells. In fig. A5.18and fig. A5.19we have plotted the resolution as a function of R_d for 5 different cell for each prototype. The cells are all in one column and for the run chosen, the tracks all traversed the prototypes entering from cell 23 and exiting from cell 3, at 0 incidence angle. The resolutions are very similar to those above.

A5.4 Conclusions

We have analyzed the test beam data taken at PSI in July 1993, measured the time-to distance relations in each prototype and reconstructed the beam tracks in the prototypes. This analysis has shown that the design goal resolution of $\leq 200\mu m$ can be achieved in both cell configurations 3:1 and 2:1.

A comparison of runs taken at different beam incidence angles has not shown any dependence of the resolution on such angle in either of the prototypes.

Within the present measurement errors, we observe no significant difference in the resolution of the two cell types in any of the situations analised.

The main sources of error are the systematic effects due to the imprecise knowledge of the space-to-time relations, which is in turn due to the error in the tracks extrapolation inside the prototypes. We have no reason to believe that these effects could not be eliminated in the future, with an improved external tracking, or even in the present data by applying some iterative correction procedure.

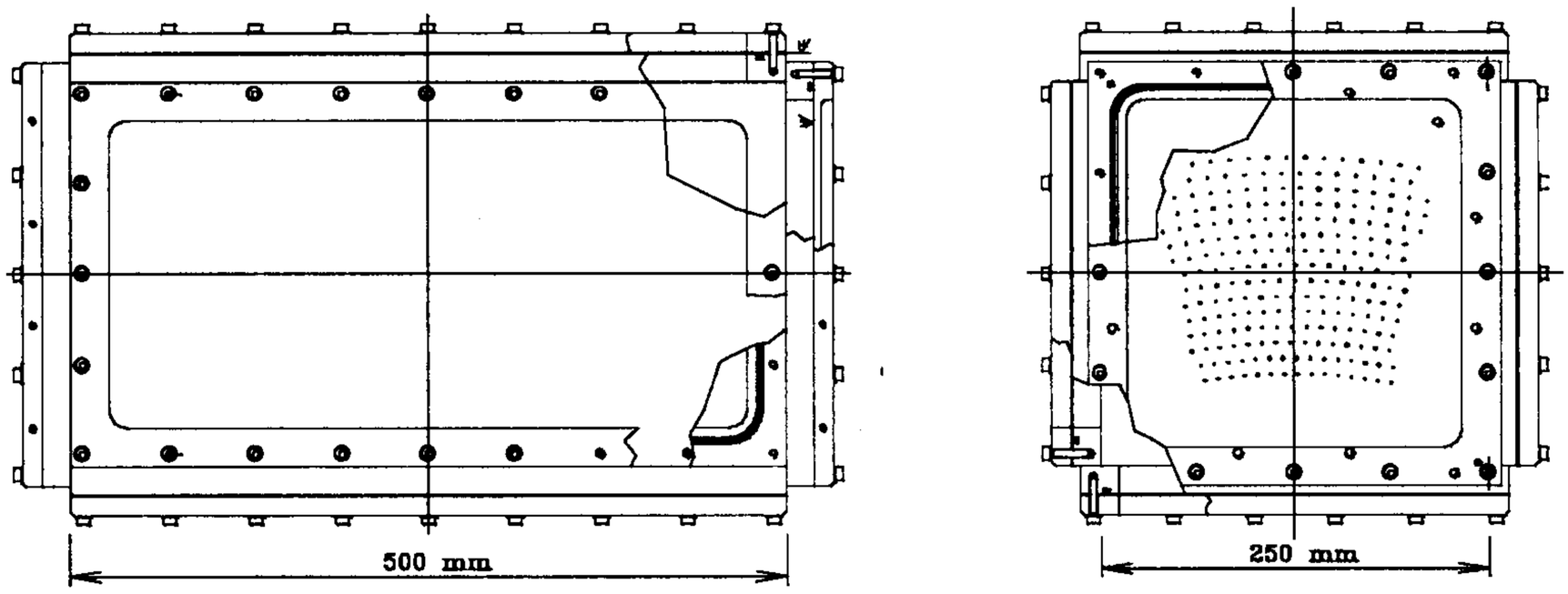

Fig. A5.1. Mechanical skecth of the prototype chambers built.

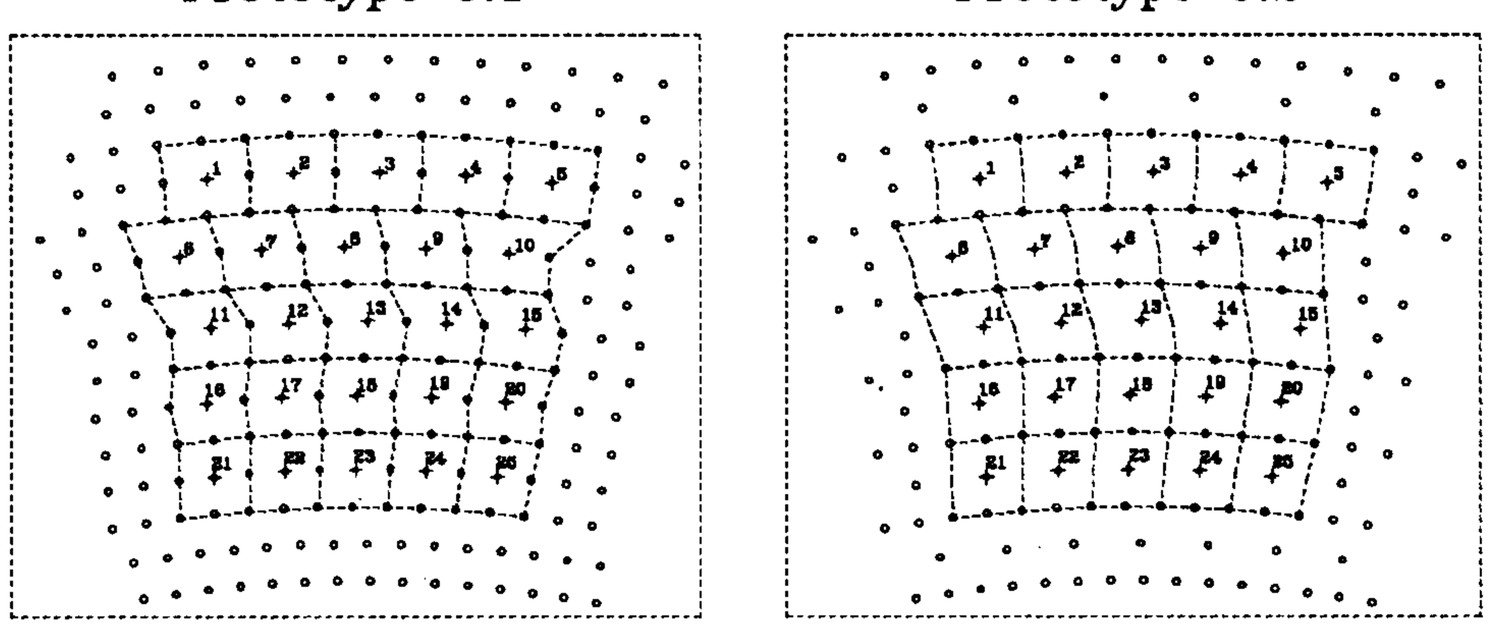

Fig. A5.2. Cells layout in the two prototypes.

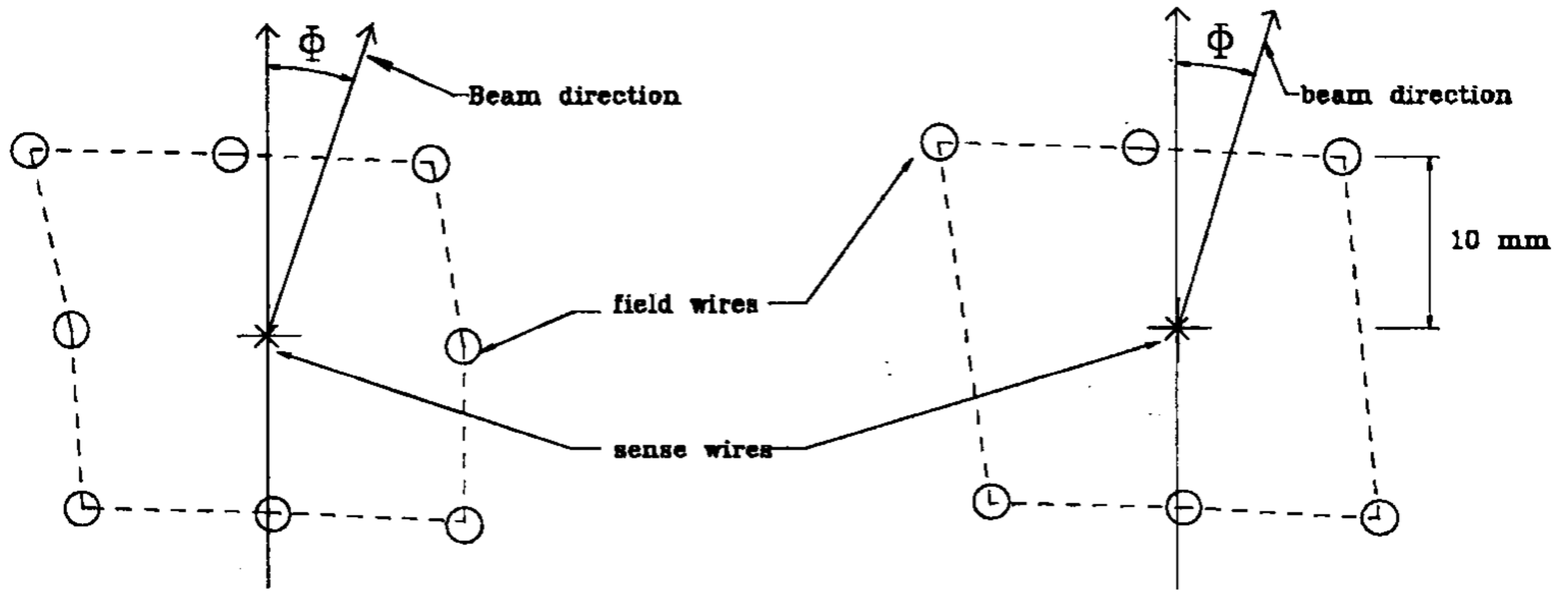

Fig. A5.3. Detail of the two cells.

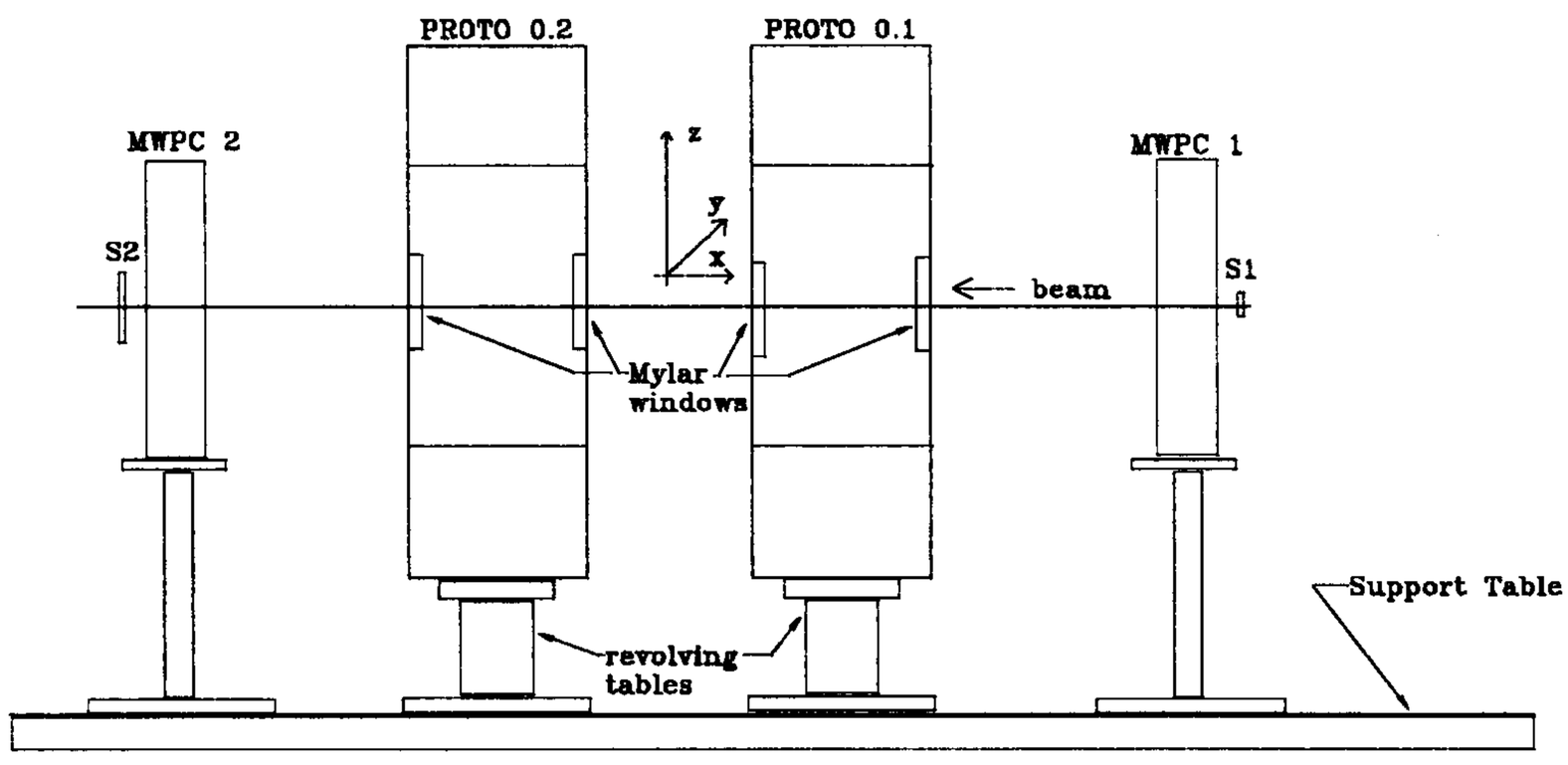

Fig. A5.4. Sketch of the experimental setup at PSI. The coordinate system used in the analysis is also shown.

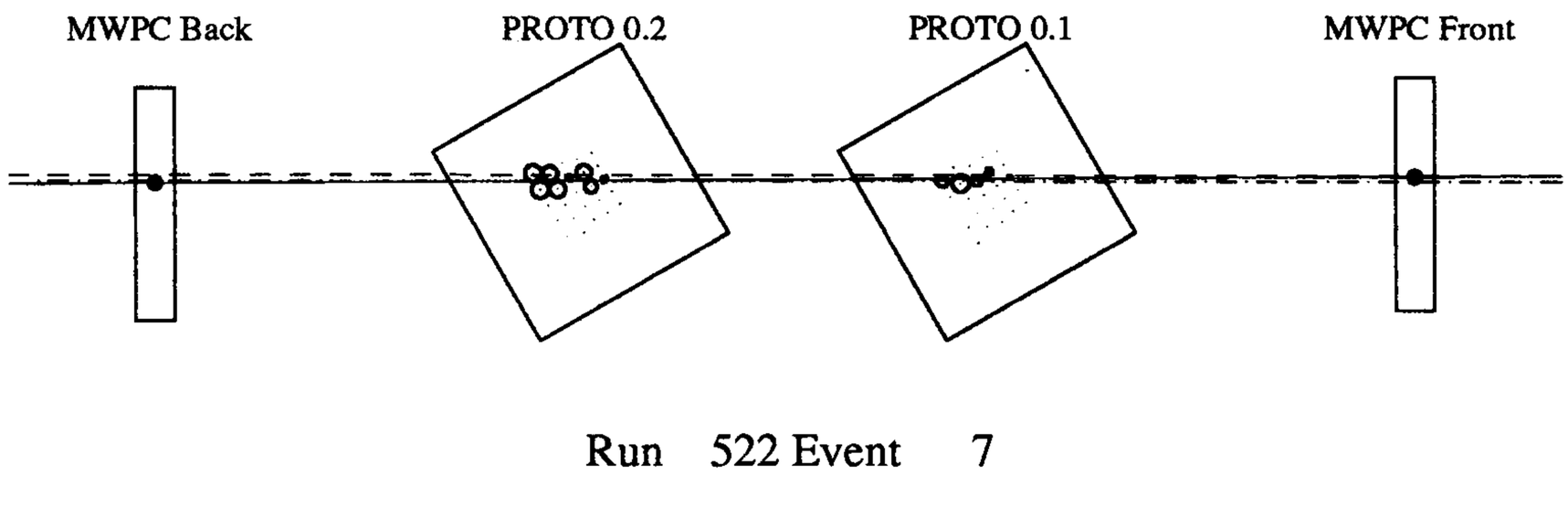

Fig. A5.5. Display of one event of a run taken at $\Phi = 30°$.

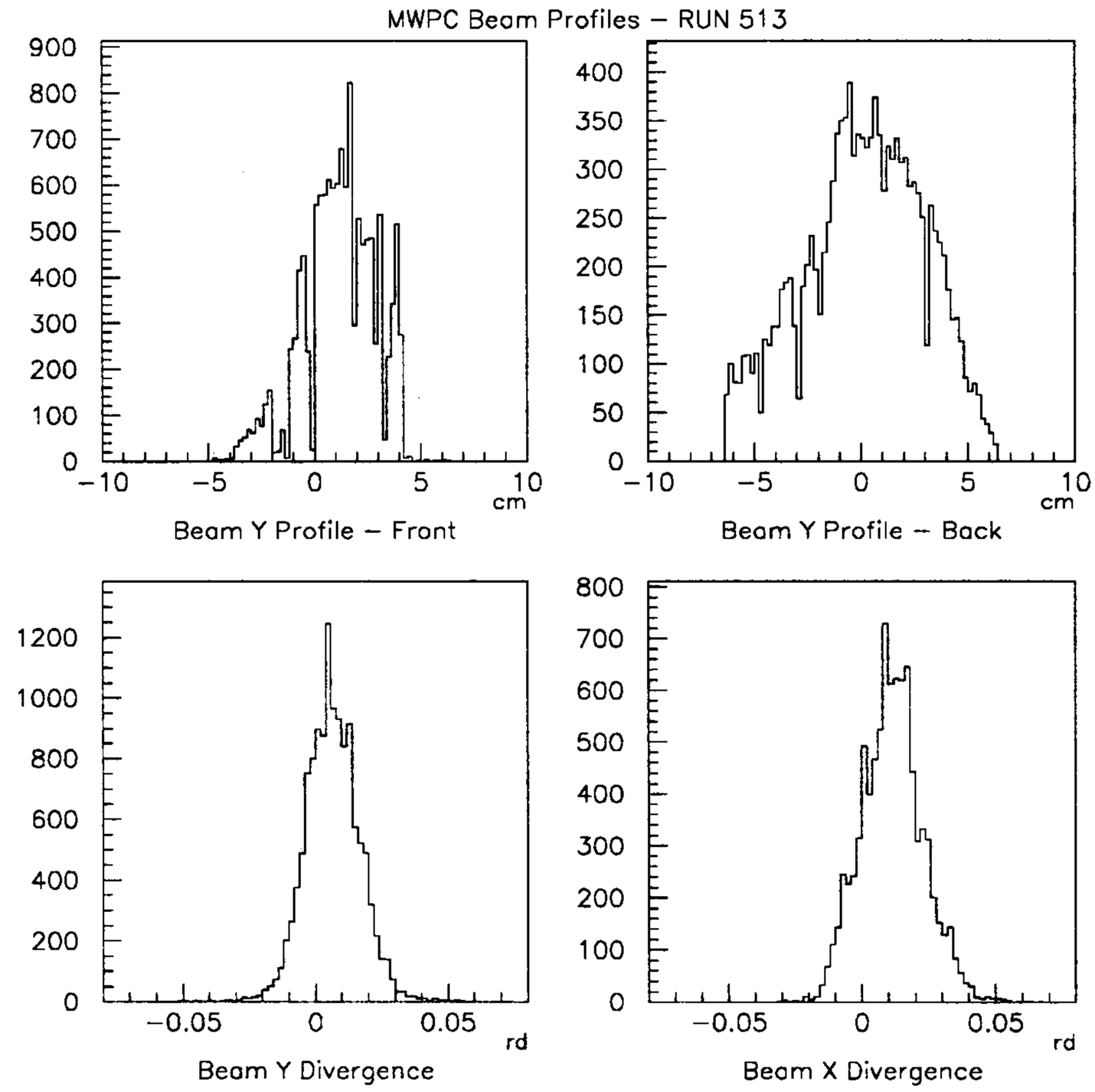

Fig. A5.6. Beam profile obtained with the MWPCs.

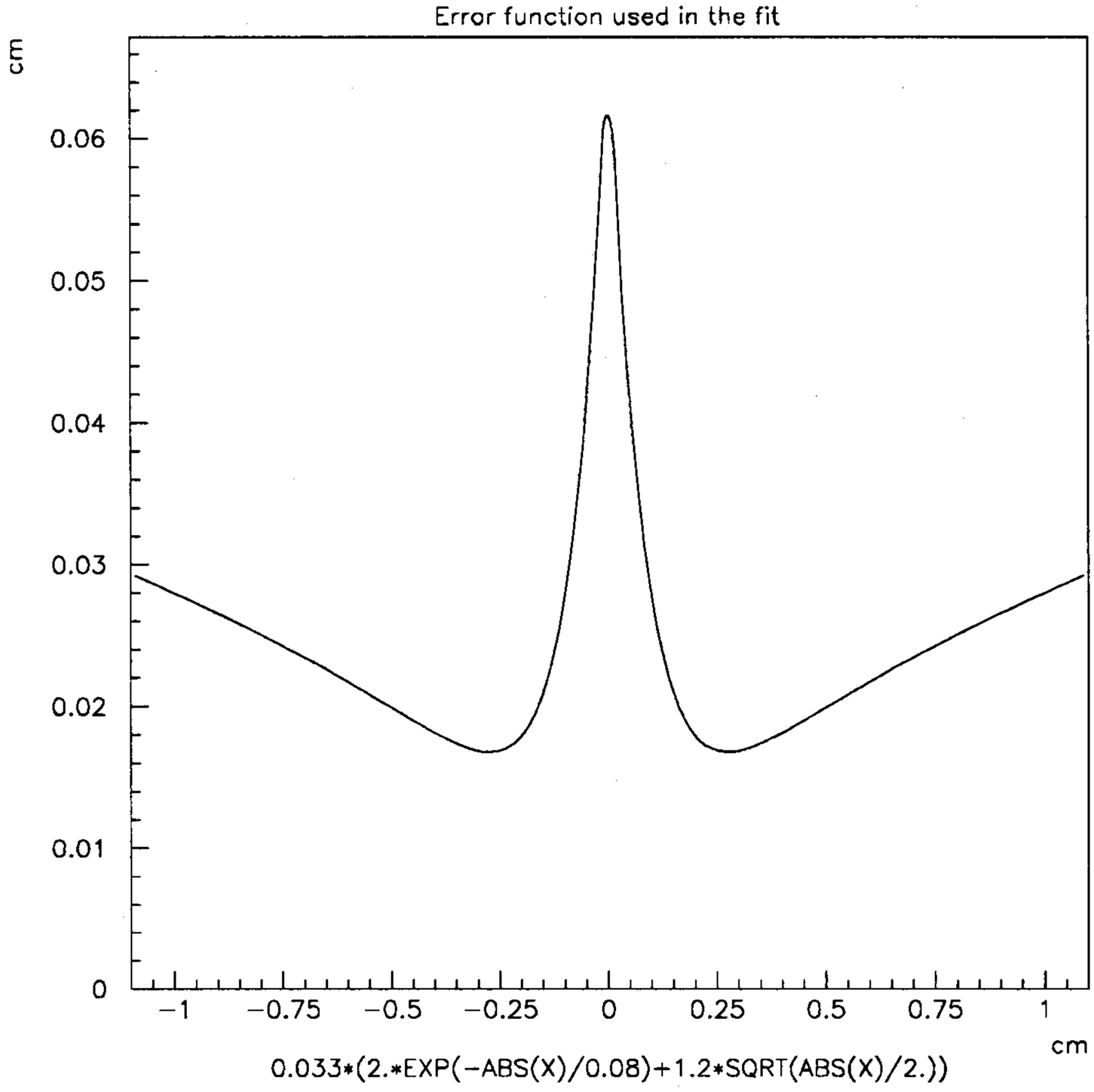

Fig. A5.7. Function used to represent the point measurement error as a function of R_d .

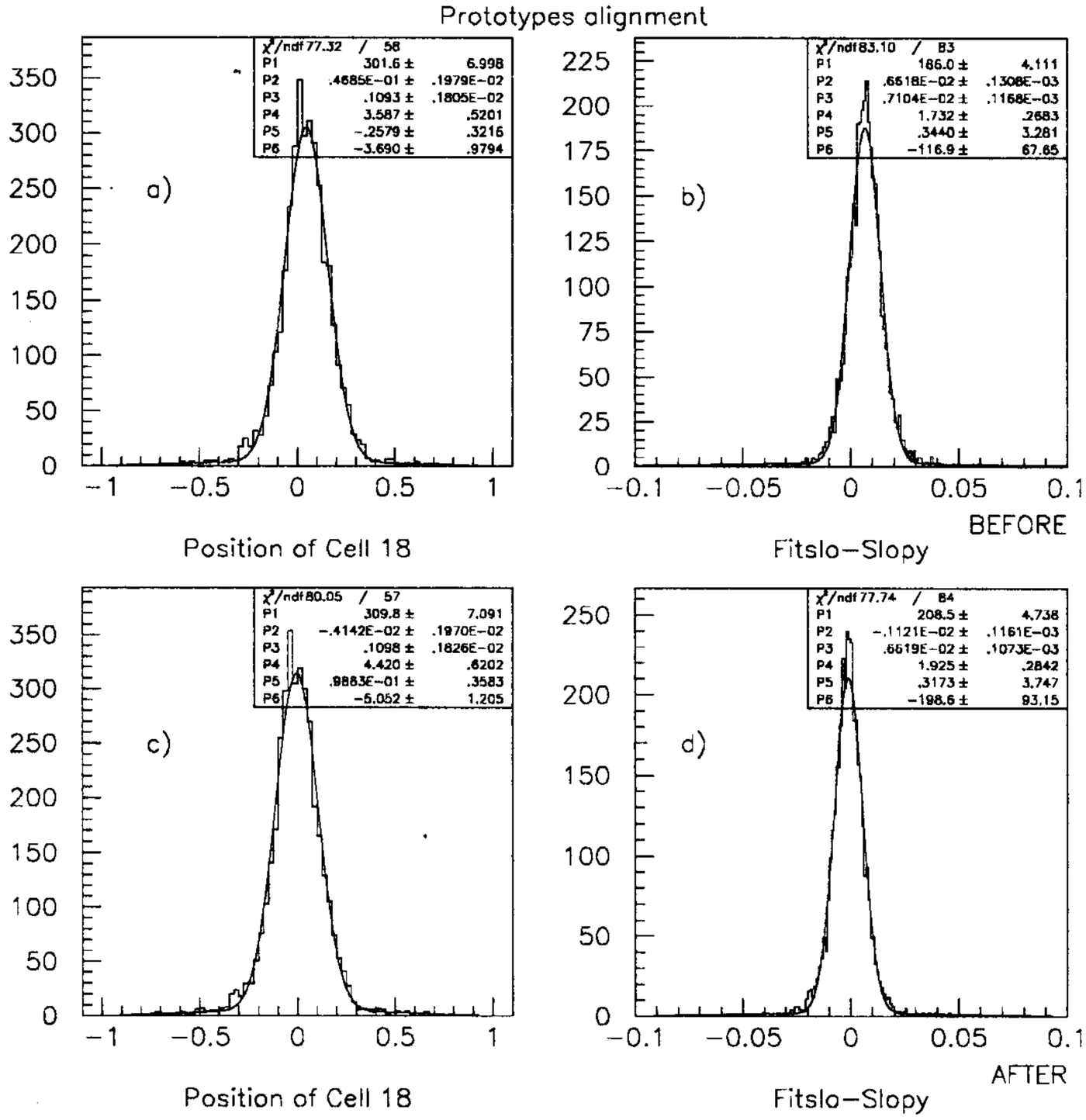

Fig. A5.8. Plots showing the effect of the alignment procedure. a) Φ offset before corrections; b) Y displacement after the Φ correction; c),d) ΔY and $\Delta\Phi$ after corrections.

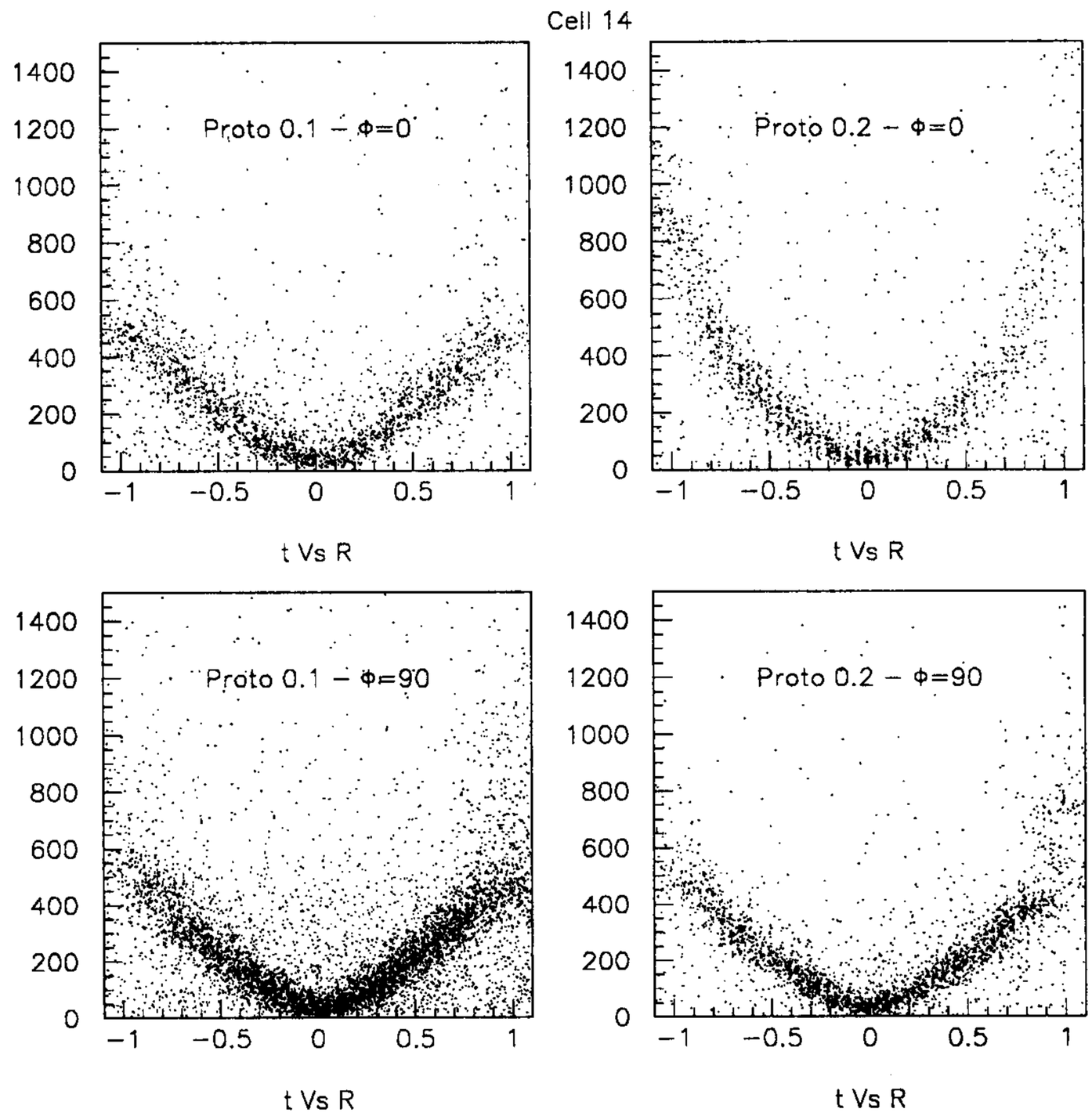

Fig. A5.9. Plots showing the effect time-to-distance correlation.

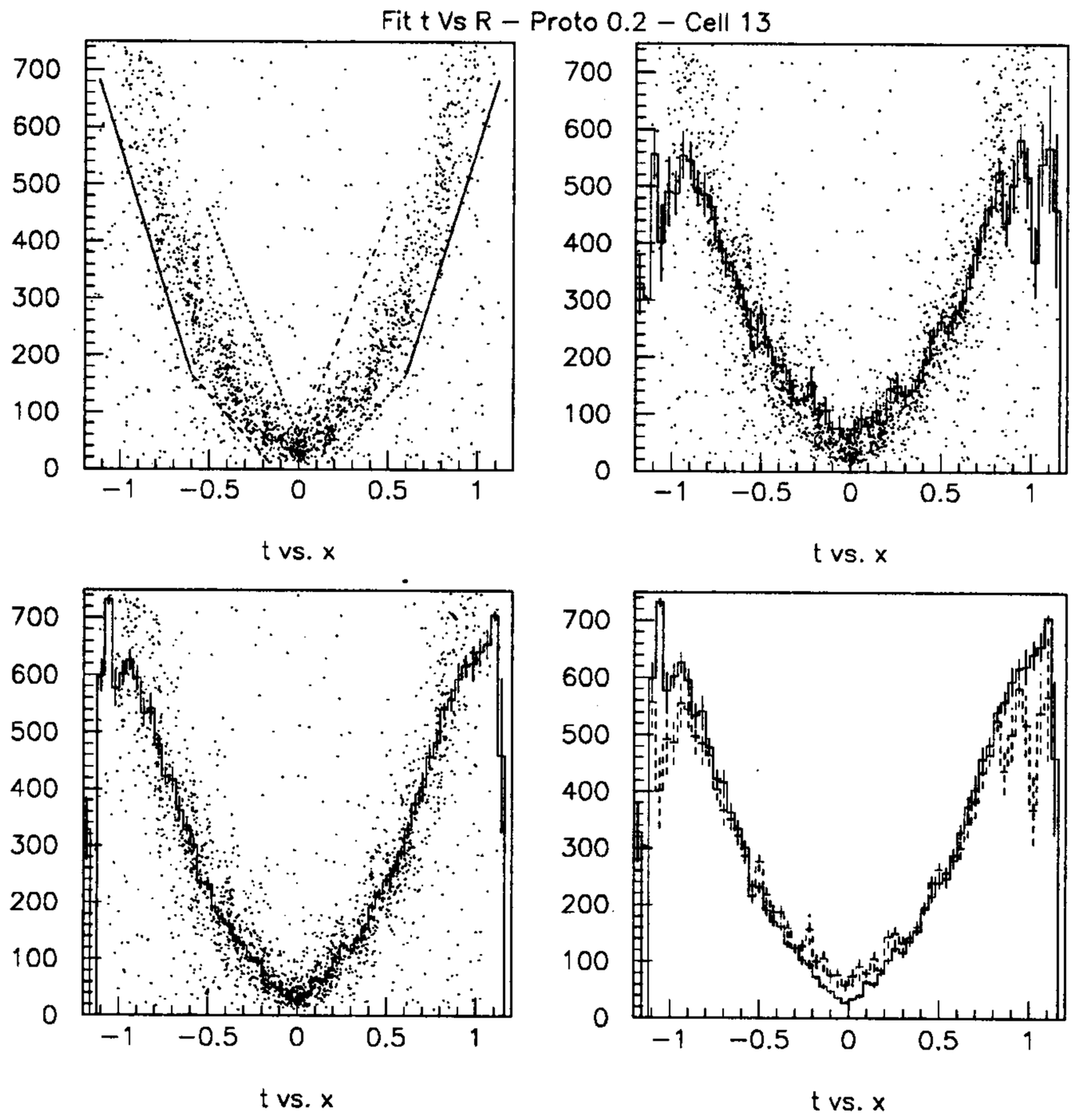

Fig. A5.10. Fit of the time-to-distance correlation plots (see text).

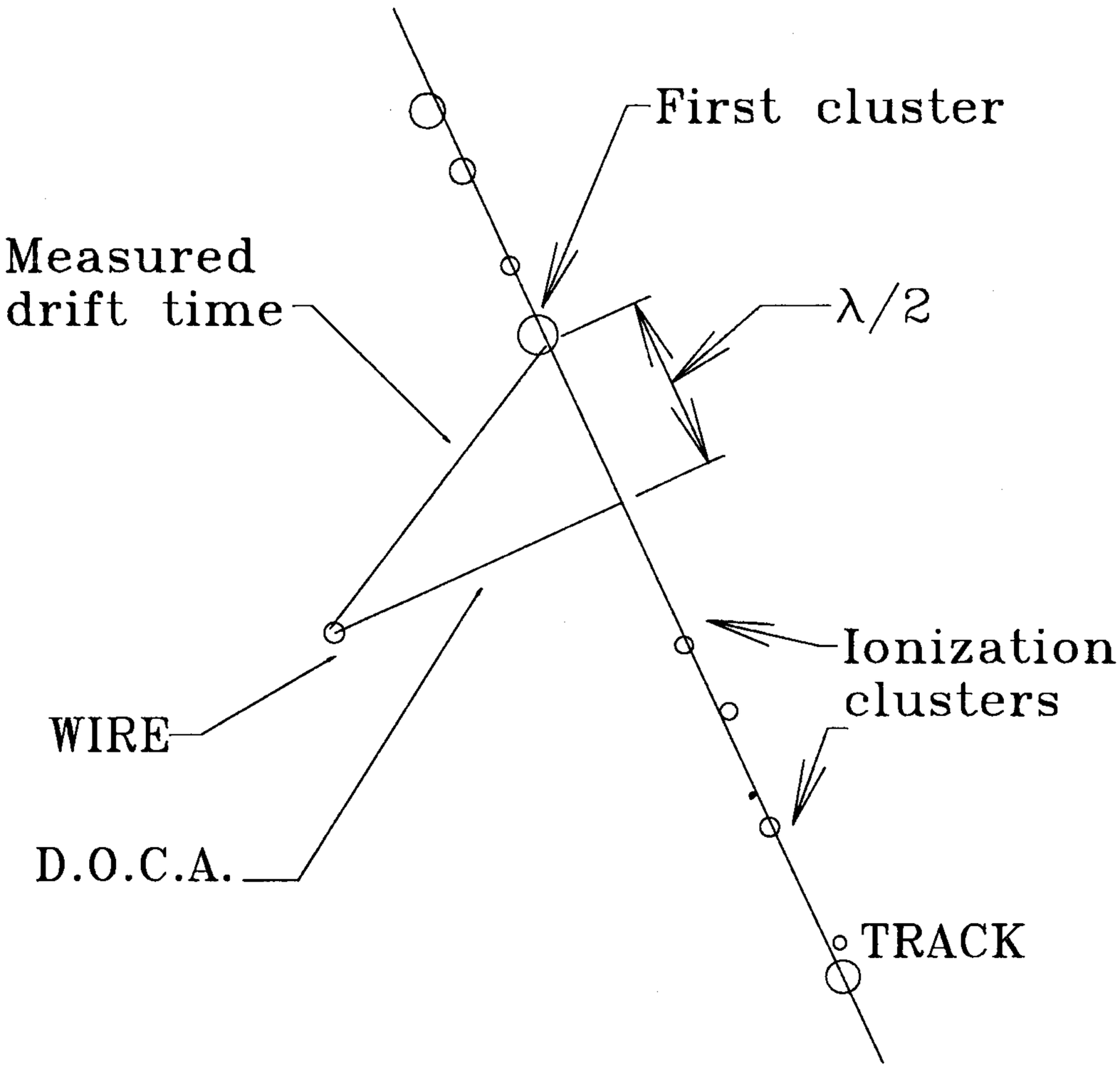

Fig. A5.11. Effect of the ionization statistics on the time of arrival of the signal on the wires.

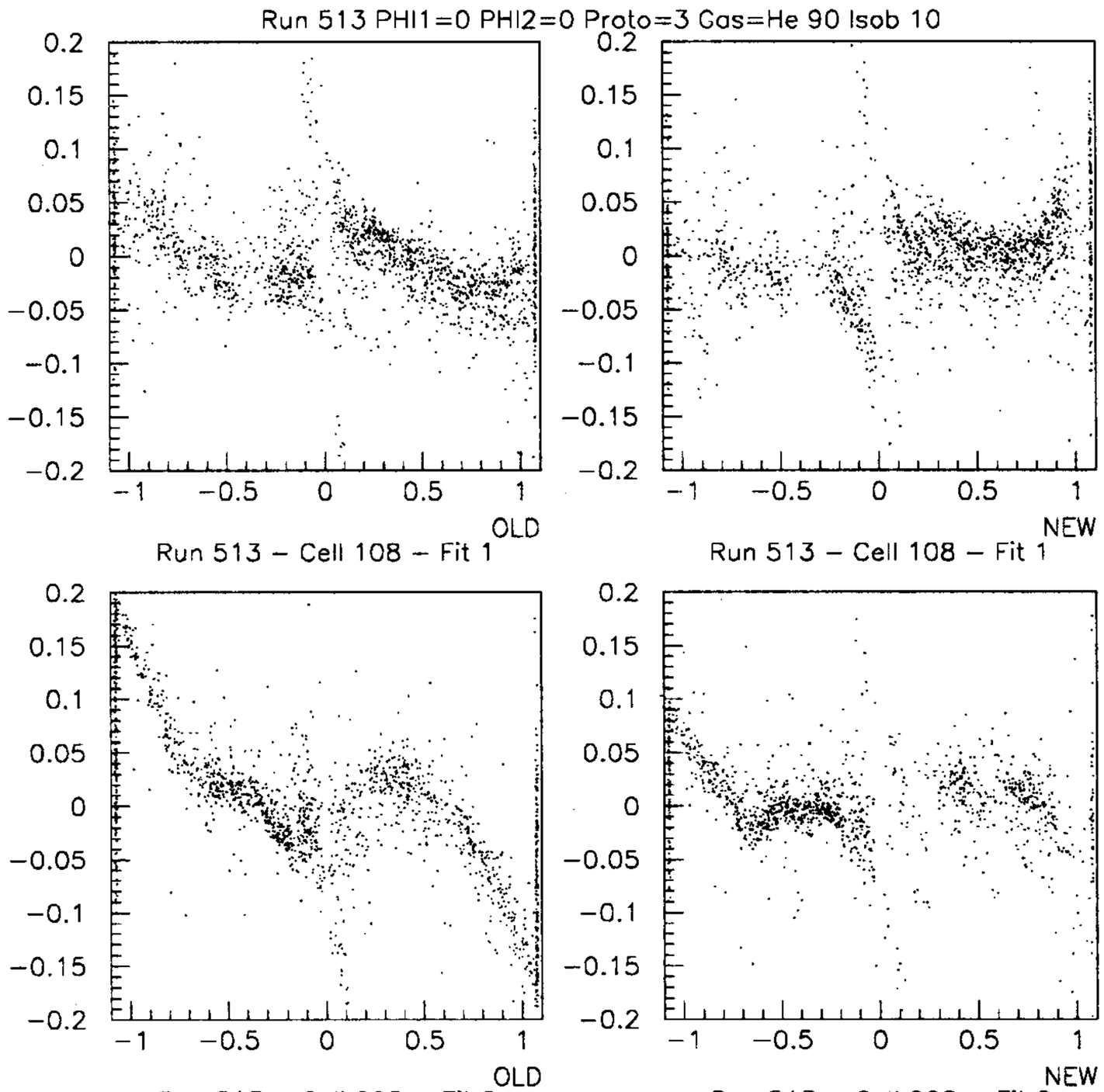

Fig. A5.12. Comparison of the residuals as a function of R_d for the two fits, with t_0 fixed or fitted.

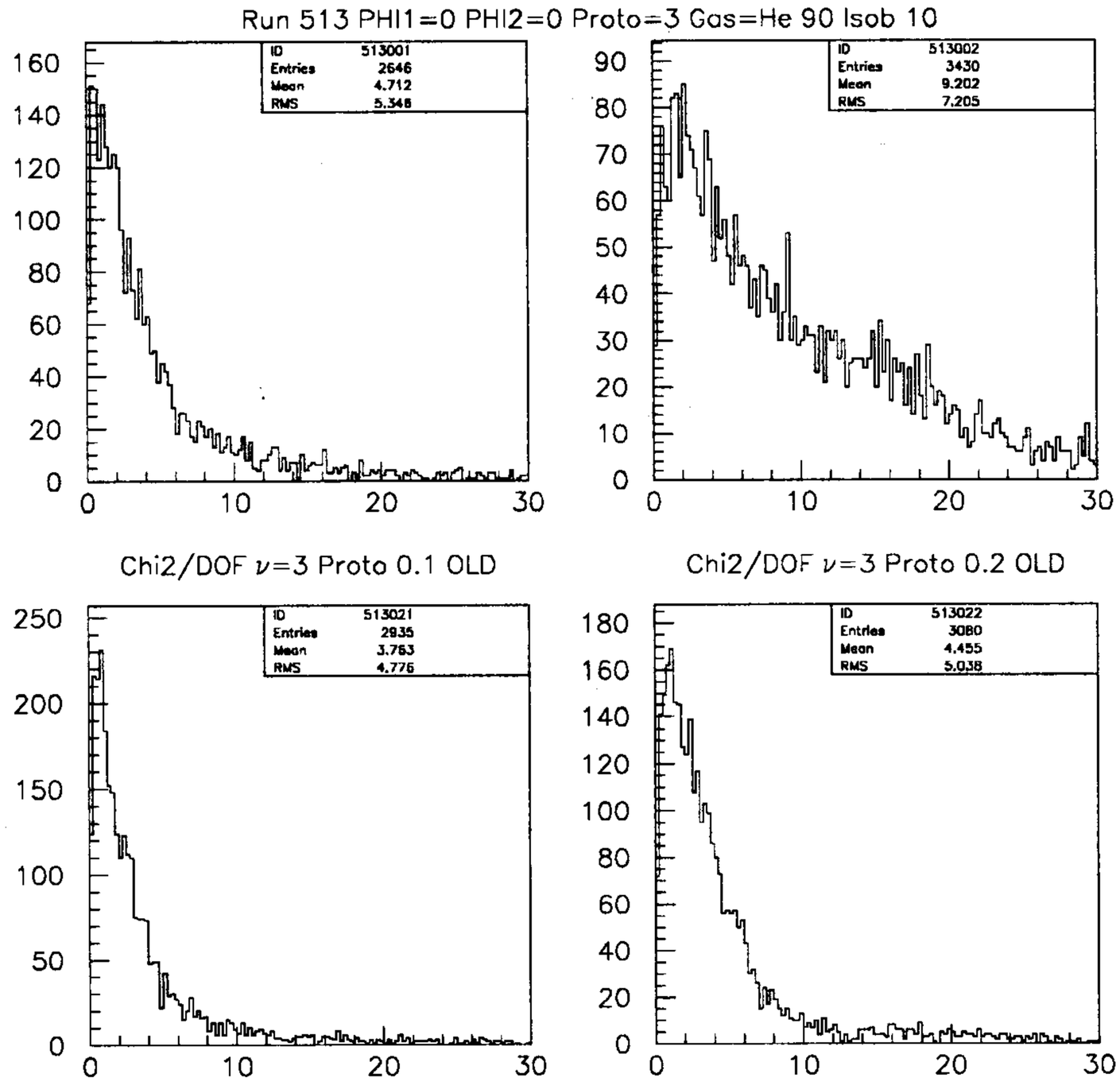

Fig. A5.13. Comparison of the χ^2 for the two fits.

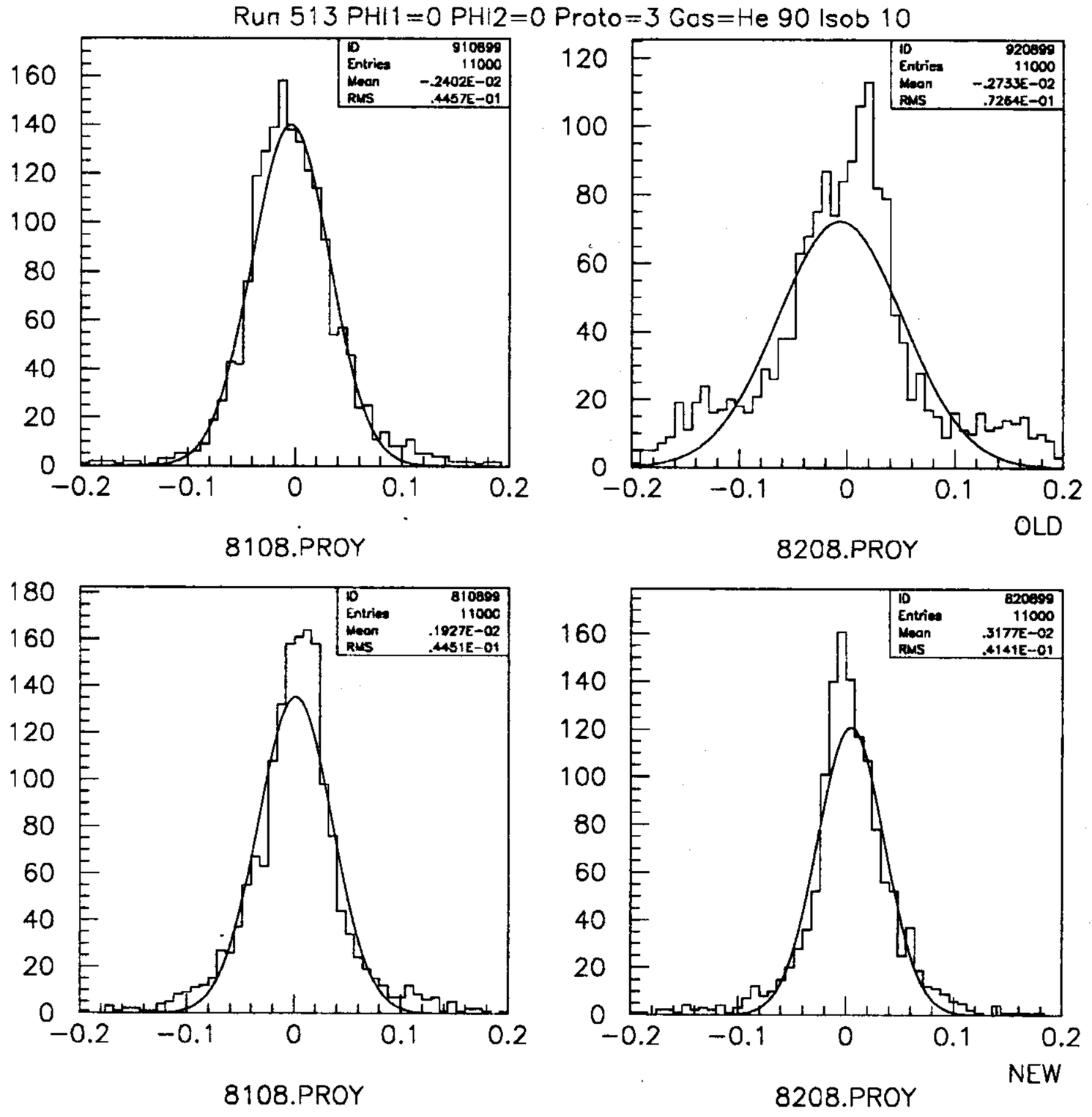

Fig. A5.14. Comparison of the fit residuals averaged over the whole cell.

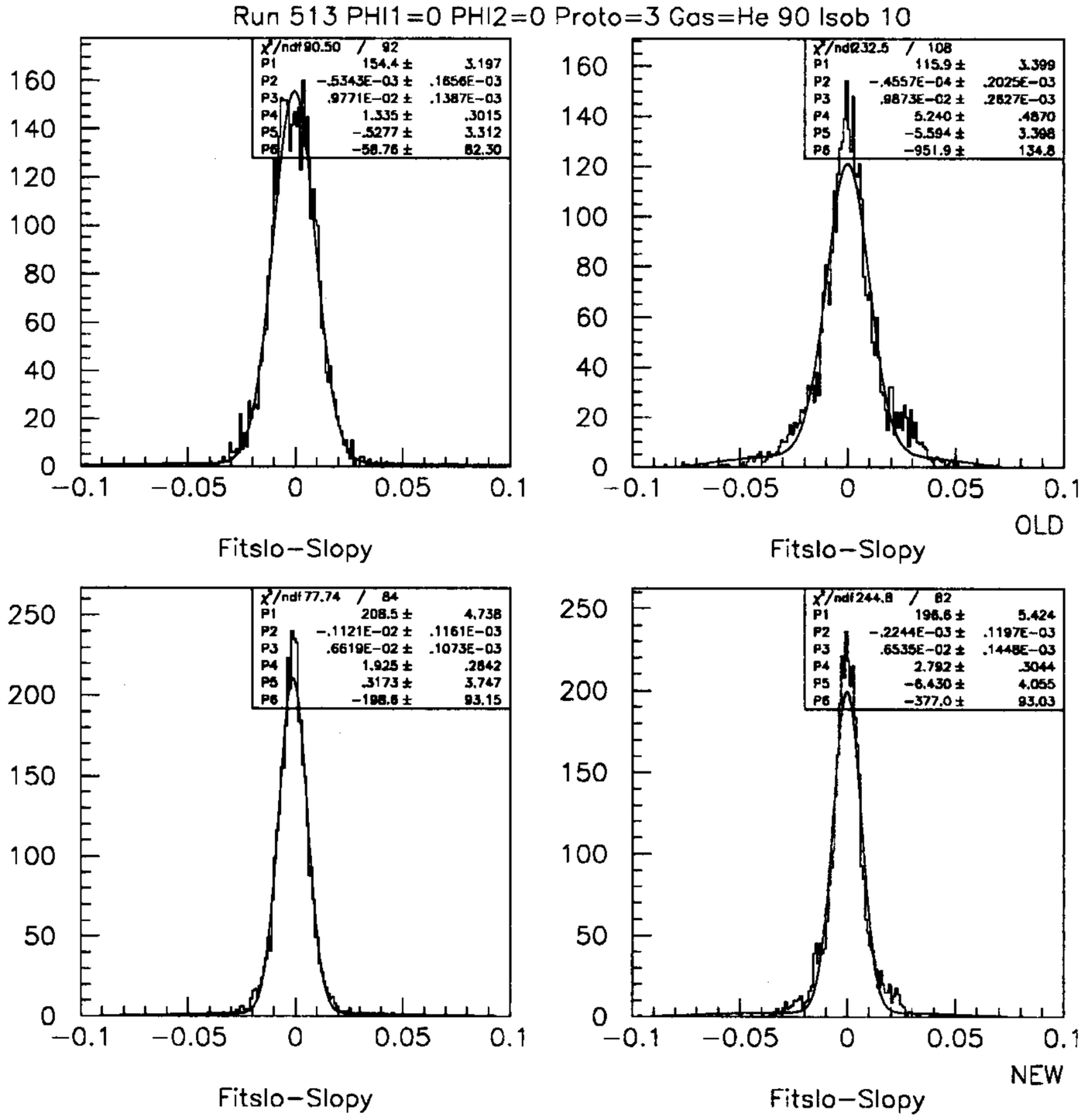

Fig. A5.15. Comparison of the $\Delta\Phi$ distributions for the two fits.

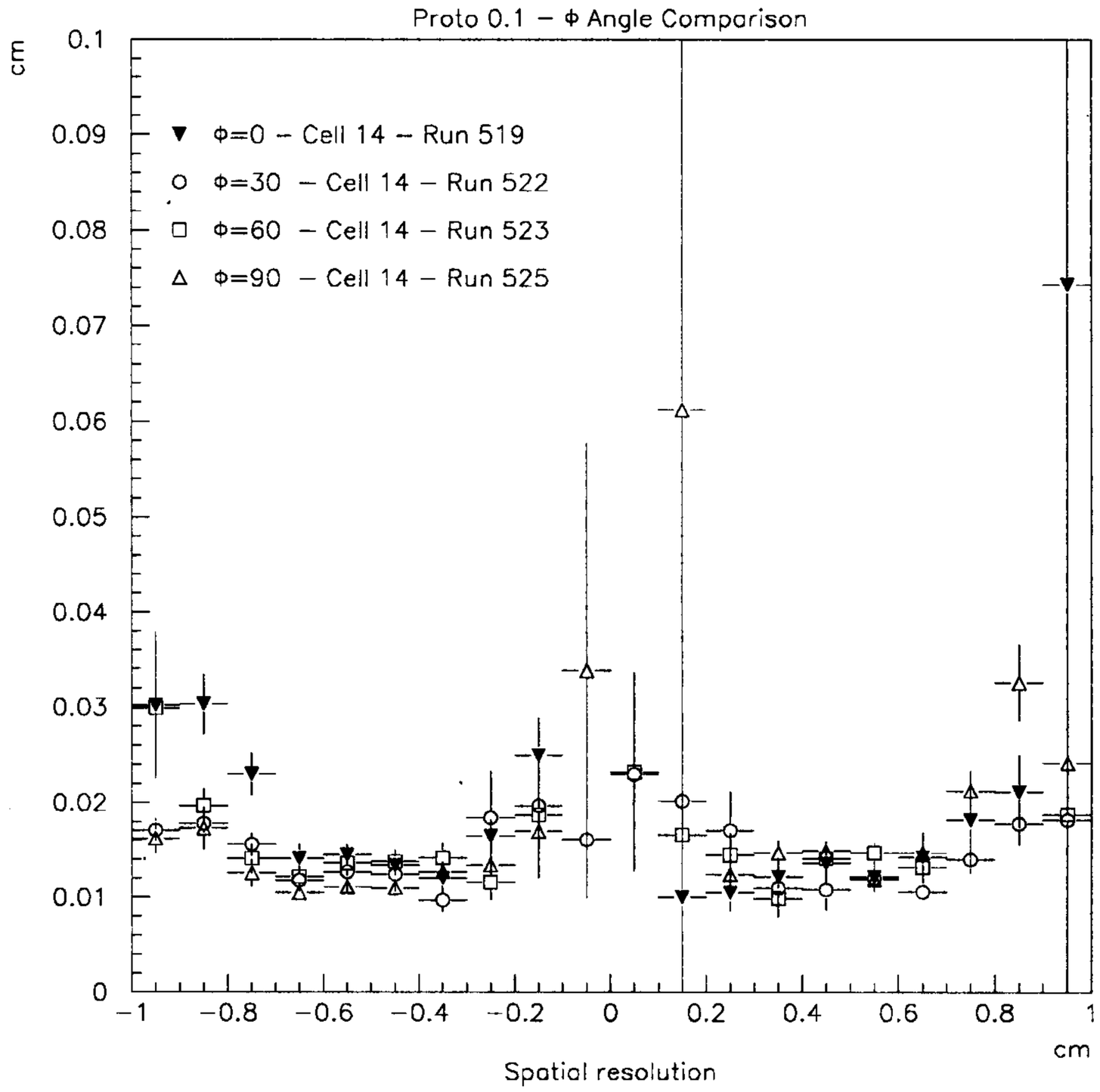

Fig. A5.16. Fit residual as a function of R_d for different Φ angles in *Prototype 0.1*

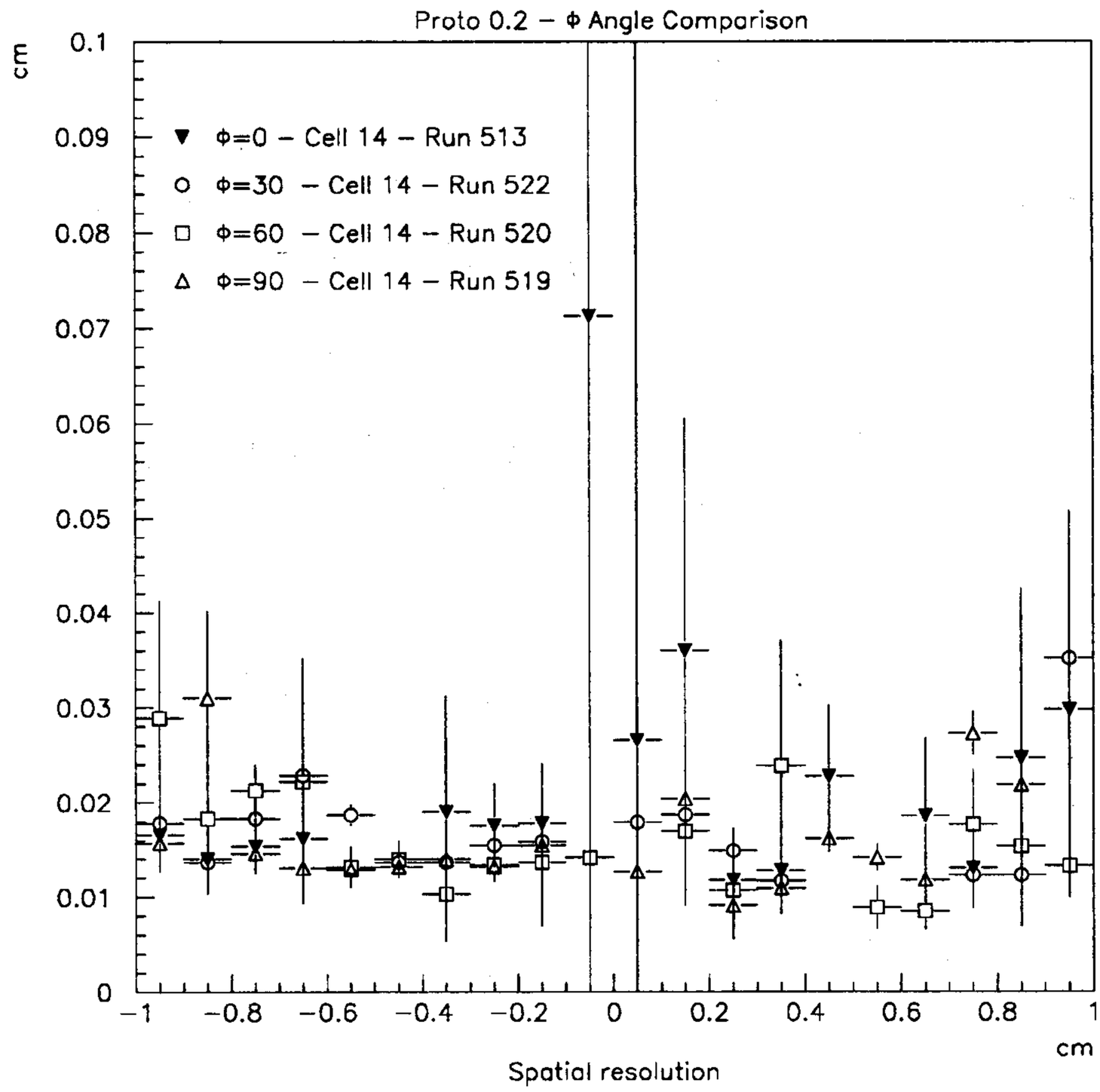

Fig. A5.17. Fit residual as a function of R_d for different Φ angles in *Prototype 0.2*

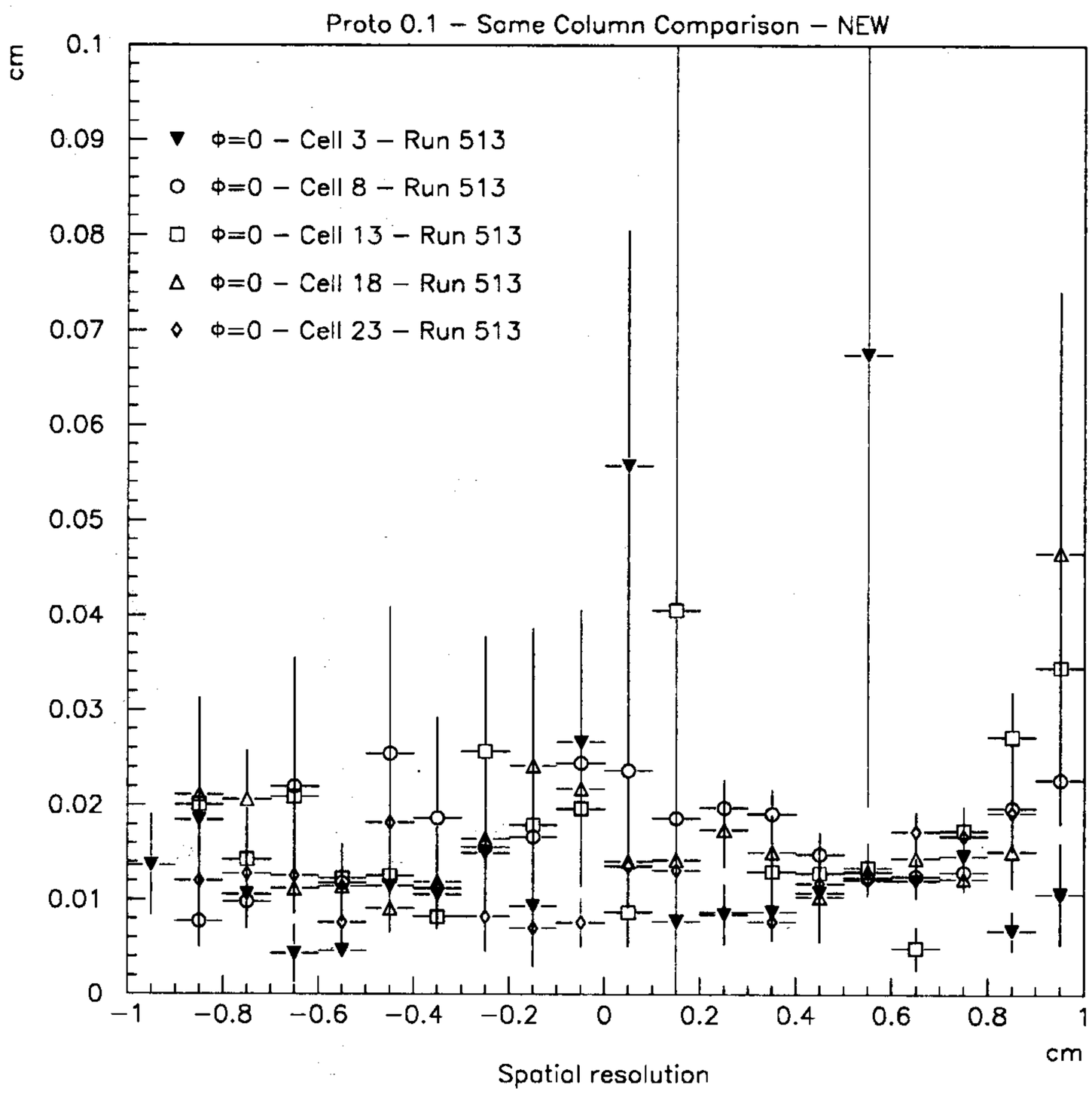

Fig. A5.18. Fit residual as a function of R_d for different cells at the same Φ angle in *Prototype 0.1* .

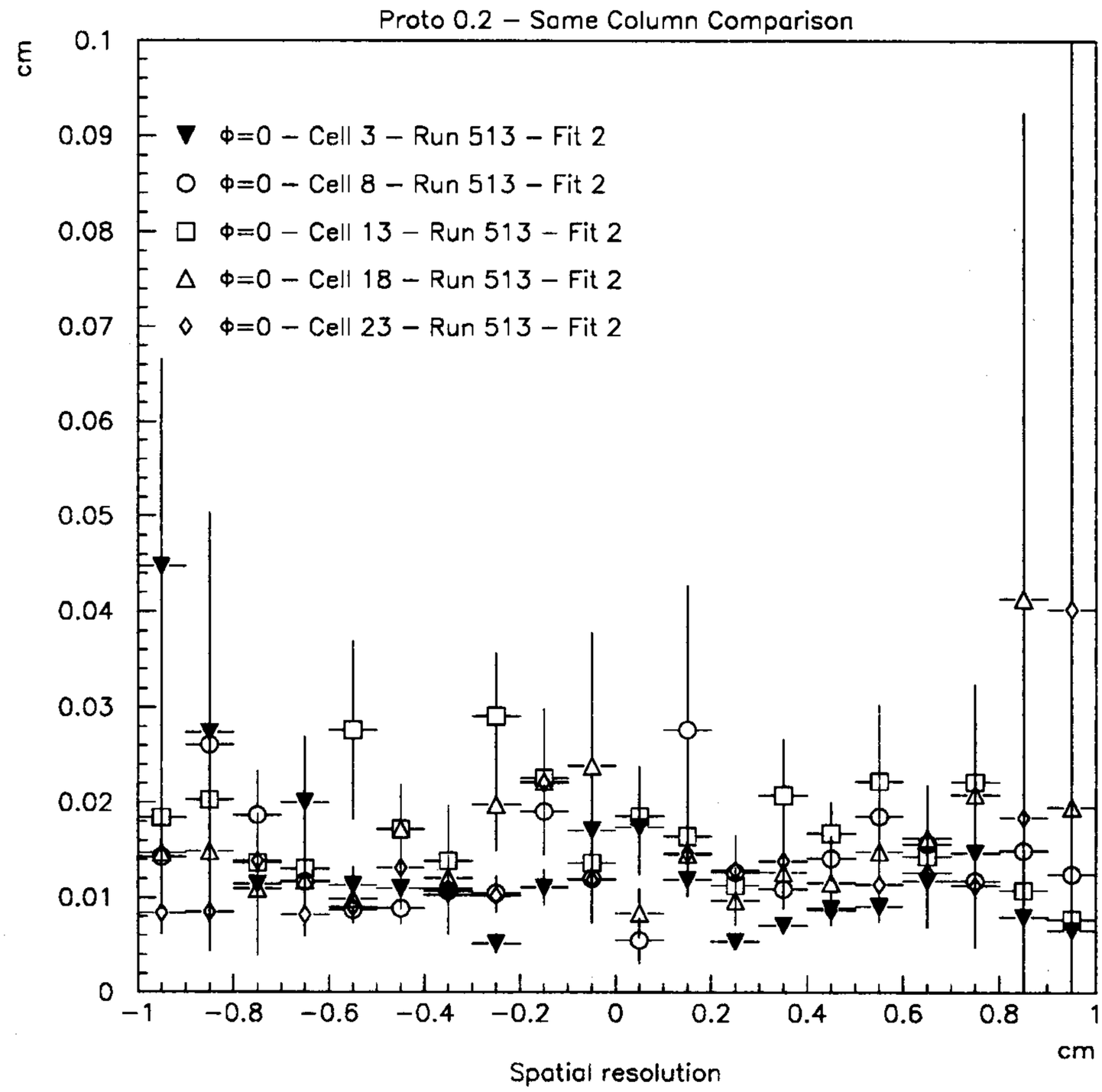

Fig. A5.19. Fit residual as a function of R_d for different cells at the same Φ angle in *Prototype 0.2* .

REFERENCES

1. W. Zimmerman *et al.*, Nuc. Inst. Meth. **A243**, 86, 1986. The first suggestion of the use of Helium as drift chamber gas in experiments at dedicated 'factories' appears in F. Grancagnolo, A Helium Drift Chamber as the Central Tracker of a B-Factory, proc. Workshop on Heavy Quarks Factory and Nuclear Physics Facility with Superconducting Linacs, Courmayeur, 1987, eds. E. de Sanctis, M. Greco, M. Piccolo and S. Tazzari (Atti di conferenze, Società Italiana di Fisica, Bologna, 1987, p. 599). A helium based chamber is used at PSI in the Sindrum experiment, K. G. Nekrasov, JINR-p13-92-513, and they have been recently subject of many investigations, see Boyarski *et al.*, in Proc. of the 6th Wire Chamber Conf. NIM **A323**, 267, 1992; I. Yadigaroglu *et al.*, *Ibid.* 322, and the KLOE collaboration, notes # 07.
2. Aluminum wires have been used with success in the CLEO-II, Y. Kubota *et al.*, NIM **A320**, 66, 1992 and the SLD chamber, M. Piccolo, private communication.
3. Helena, H. Albrecht *et al.*, DESY -92-041.
4. See for instance tests performed by the SLD group, J. P. Venuti and G. B. Chadwick, IEEE Transaction on Nuclear Science, Vol. 36, No. 1, 595, 1989.
5. D.G.Cassel et al., Nucl. Instr. and Meth. **A252**, 325 (1986)
6. R. J. Roark, W. G. Young, Formulas for stress and strain, Mc Graw Hill (1985).
7. A. Gaddi, S. Moccia, R. Baldini, Kloe note, in preparation
8. S. Miscetti *et al.*, KLOE Calorimeter Test Results, Elba Conference on Calorimetry, 1994.
9. G.Bencivenni et al., Wire and Feed-Through Study for the KLOE Drift Chamber, KLOE note # 107.
10. R.D.Heuer, A.Wagner, Nucl. Instr. and Meth. A265 (1988) 11.
11. H. Fischle et al., Nucl. Instr. Meth. A301 (1991) 202.
12. KLOE Collab., LNF-92/019(IR).
13. U. Becker in Instrumentation in High Energy Physics, ed. F. Sauli World Scientific Publishing Co. (1992).
14. Review of Particle Properties, Phys. Lett. B239 (1990).
15. F. Grancagnolo, U. von Hagel, M. Primavera, KLOE note in preparation.
16. Labview 2, Nat. Instr. Corp. (1992).
17. A. Sharma, F. Sauli, 'Low mass gas mixture for drift chamber operation' CERN PPE/93-51 February 10,1993.
18. S.F. Biagi, Nucl. Instr. Meth. A283 (1989) 716.
19. M. Carletti, G.Felici, P.Locchi , Chamber front-end status report, KLOE note 66.
20. R. J. Yarema et al., A high performance multi-channel preamplifier ASIC IEEE Transaction on Nuclear Science, vol 39, NO. 4, 1992.
21. M.Primavera and S.Spagnolo, Kloe Note in preparation.
22. F. Lacava et al., KLOE Note, in preparation
23. "KLOE a general purpose detector for DAFNE", the KLOE Collaboration LNF Report, 92/019 (1992)
24. A. Antonelli et al. KLOE note N. 3 (1991) and N. 23 (1992)
25. R. Brun et al. , CERN GEANT 3 User's Guide, DD/ee/84-1 (1987)
26. "GARFIELD, a drift-chamber simulation program" CERN program library entry W5050.
27. R. de Sangro "Measurement of the space point resolution of the drift chamber prototypes" KLOE Note 97/1994
28. G. Bencivenni et al. "The prototype 0 of the KLOE tracking chamber" KLOE note n. 79
29. KLOE note in preparation
30. A. Andryakov, "Charge track reconstruction and drift chamber optimization", KLOE Note #48 (1993).
31. H. Albrecht *et al.*, (ARGUS Collaboration), Nucl. Instr. Meth. **A275** (1989) 1.
32. R. J. Haydar, "Study of $K^+ \to \pi^+\pi^0$ with Geanfi" KLOE Note #82 (1994)

33. P. Franzini, in "Workshop on Physics and Detectors for DAΦNE" (Frascati,1990) edited by G. Pancheri p. 733
34. A. Andryakov, V. Patera "$K_{\mu 3}$ rejection via kinematical cuts", KLOE note N. 51, Feb. 1993
35. A. Andryakov, KLOE Note # 106 in preparation
36. 'Garfield, a drift-chamber simulation program' CERN program library entry W5050.
37. R. de Sangro KLOE note # 97.
38. G. Bencivenni et al.:'The prototype 0 of the KLOE tracking chamber' KLOE note n. 79
39. KLOE note in preparation
40. V. Patera KLOE note # 103.
41. A. Andryakov KLOE note in preparation
42. A. Calcaterra, KLOE Note # 95.
43. G.Bencivenni, A.Calcaterra, M.Carletti, R.de Sangro, G.Felici, G.Finocchiaro, M.Piccolo, P.Santantonio, KLOE note 79/93 (1993).
44. Garfield, a drift-chamber simulation program, CERN program library entry W5050.
45. "The KLOE detector technical proposal", The KLOE Collaboration, LNF-93-002 (IR); January 21, 1993.
46. Proposal for a ϕ-Factory, The ϕ-factory study group, LNF-90/031(R); April 30, 1990
47. G.Felici *et al.*, 'Front end chamber electronics status report'. KLOE Note N.66, Oct 1993.
48. Paul Scherrer Institute, now become Inst. for Intermediate Energy Physics of ETH, Villigen, Zurich, Switzerland.
49. M.Pollack, "Energy loss measurement in Prototype 0.1', KLOE Note N. 85, Jan 1994